AWARD NUMBER: W81XWH-15-1-0572

TITLE: Prostate Cancer Grade Mapping with Transrectal Electrical Impedance Tomography

PRINCIPAL INVESTIGATOR: Kofi Odame
Ryan Halter

CONTRACTING ORGANIZATION: Trustees of Dartmouth College
Hanover, NH 03755-1404

REPORT DATE: December 2019

TYPE OF REPORT: Final

PREPARED FOR: U.S. Army Medical Research and Materiel Command
Fort Detrick, Maryland 21702-5012

DISTRIBUTION STATEMENT: Approved for Public Release;
Distribution Unlimited

The views, opinions and/or findings contained in this report are those of the author(s) and should not be construed as an official Department of the Army position, policy or decision unless so designated by other documentation.

REPORT DOCUMENTATION PAGE

Form Approved
OMB No. 0704-0188

Public reporting burden for this collection of information is estimated to average 1 hour per response, including the time for reviewing instructions, searching existing data sources, gathering and maintaining the data needed, and completing and reviewing this collection of information. Send comments regarding this burden estimate or any other aspect of this collection of information, including suggestions for reducing this burden to Department of Defense, Washington Headquarters Services, Directorate for Information Operations and Reports (0704-0188), 1215 Jefferson Davis Highway, Suite 1204, Arlington, VA 22202-4302. Respondents should be aware that notwithstanding any other provision of law, no person shall be subject to any penalty for failing to comply with a collection of information if it does not display a currently valid OMB control number. **PLEASE DO NOT RETURN YOUR FORM TO THE ABOVE ADDRESS.**

1. REPORT DATE	2. REPORT TYPE	3. DATES COVERED
December 2019	Final	09/15/2015 - 09/14/2019

4. TITLE AND SUBTITLE
Prostate Cancer Grade Mapping with Transrectal Electrical Impedance Tomography

5a. CONTRACT NUMBER

5b. GRANT NUMBER
W81XWH-15-1-0572

5c. PROGRAM ELEMENT NUMBER

6. AUTHOR(S)
Kofi Odame; Ryan Halter

E-Mail: odame@dartmouth.edu; ryan.j.halter@dartmouth.edu

5d. PROJECT NUMBER

5e. TASK NUMBER

5f. WORK UNIT NUMBER

7. PERFORMING ORGANIZATION NAME(S) AND ADDRESS(ES)
Trustees of Dartmouth College
AND ADDRESS(ES)
Office of Sponsored Projects
11 Rope Ferry Road #6210
Hanover, NH 03755-1404

8. PERFORMING ORGANIZATION REPORT NUMBER

9. SPONSORING / MONITORING AGENCY NAME(S) AND ADDRESS(ES)

U.S. Army Medical Research and Development Command
Fort Detrick, Maryland 21702-5012

10. SPONSOR/MONITOR'S ACRONYM(S)

11. SPONSOR/MONITOR'S REPORT NUMBER(S)

12. DISTRIBUTION / AVAILABILITY STATEMENT

Approved for Public Release; Distribution Unlimited

13. SUPPLEMENTARY NOTES

14. ABSTRACT
The primary objective of this research is to combine advanced integrated electronics with transrectal electrical impedance tomography (TREIT) and electrical impedance sensing biopsy (EIS-Bx) devices to improve TRUS-guided prostate biopsy procedures and help to address the challenge of distinguishing aggressive from indolent disease in men newly diagnosed with prostate cancer. The novelty in this program falls into two categories: 1) we aim to couple our single point EIS-Bx measurement device with an array of electrodes adhered to a standard end-fired TRUS probe (Halter's team) and 2) we aim to develop a custom application specific integrated circuit (ASIC) that will enable us to measure these electrical properties over a wide frequency range (optimal for distinguishing high- from low-grade prostate cancer) and at high frame rates (required for real-time prostate biopsy procedures) (Odame's team). During the first two years of this study, we focused on designing, implementing and validating (1) a small form-factor EIT based on a custom ASIC chip (2) an EM-tracking approach to capture the surface of the prostate during TRUS, (3) finite element method meshing approaches and reconstruction algorithms for imaging the electrical properties of prostate during an TREIT + EIS-Bx procedure. Year 3 focused on further phantom studies and the development of a second version (20-channel) of a miniaturized EIT system. A no-cost-extension period of Year 4 focused on clinical data acquisition from a series of ex vivo human prostates.

15. SUBJECT TERMS electrical impedance sensing; prostate biopsy

16. SECURITY CLASSIFICATION OF:			17. LIMITATION OF ABSTRACT	18. NUMBER OF PAGES	19a. NAME OF RESPONSIBLE PERSON
a. REPORT	b. ABSTRACT	c. THIS PAGE			USAMRMC
Unclassified	Unclassified	Unclassified	Unclassified	137	19b. TELEPHONE NUMBER *(include area code)*

TABLE OF CONTENTS

Page

INTRODUCTION 4

KEYWORDS 4

ACCOMPLISHMENTS 5

IMPACT 17

CHANGES/PROBLEMS 17

PRODUCTS 18

PARTICIPANTS & OTHER COLLABORATING ORGANIZATIONS 22

SPECIAL REPORTING REQUIREMENTS 24

APPENDICES 24

INTRODUCTION

This research project addresses the challenge of distinguishing aggressive from indolent disease in men newly diagnosed with prostate cancer. The goal is to improve transrectal ultrasound (TRUS)-guided prostate biopsy by combining it with advanced integrated electronics, transrectal electrical impedance tomography (TREIT) and electrical impedance sensing biopsy (EIS-Bx). The novelty in this program falls into two categories: (1) we aim to couple our single point EIS-Bx measurement device with an array of electrodes adhered to a standard end-fired TRUS probe (Halter's team) and (2) we aim to develop a custom application specific integrated circuit (ASIC) that will enable us to measure these electrical properties over a wide frequency range and at high frame rates (Odame's team). During the first two years of this project, we focused on designing, implementing and validating (1) a small form-factor EIT based on a custom ASIC chip (2) an EM-tracking approach to capture the surface of the prostate during TRUS, (3) finite element method meshing approaches and reconstruction algorithms for imaging the electrical properties of prostate during an TREIT + EIS-Bx procedure. Year 3 focused on further phantom studies and the development of a second version (20-channel) of a miniaturized EIT system. A no-cost-extension period of Year 4 focused on clinical data acquisition from a series of ex vivo human prostates.

KEYWORDS

Trans-rectal electrical impedance tomography; prostate biopsy; custom biomedical integrated circuits.

ACCOMPLISHMENTS

What were the major goals of the project?

There were four major goals of the project, namely:
1. To develop TREIT hardware for prostate imaging (Odame)
2. To develop TREIT imaging algorithms for prostate imaging (Halter)
3. To validate TREIT through phantom studies (Halter/Odame)
4. To evaluate TREIT using a sample of ex-vivo prostates (Halter)

What was accomplished under these goals?

Goal #1: To develop TREIT hardware for prostate imaging

The goal was to design and validate a small form-factor TREIT instrumentation system that would integrate into a standard end-fired transrectal ultrasound probe. The proposed miniaturized TREIT instrumentation consisted of an application specific integrated circuit (ASIC) that would eliminate many of the challenges (i.e. cabling, signal cross-talk, channel-to-channel variations, parasitic capacitances, etc.) associated with the typical bench-top EIT system.

The specific objective under this goal was to develop EIT instrumentation that provides the high frequency, high SNR and high frame rate performance necessary for TREIT applications. To achieve the above objective, we performed the following activities: designed and fabricated an EIT instrumentation ASIC; designed and fabricated a printed circuit board (PCB) for the ASIC, controller unit and other peripherals, to form a complete miniaturized TREIT system; performed electrical benchtop validation of the miniaturized TREIT system.

Under this goal, our activities resulted in two key outcomes. First, we produced the first-ever ASIC for high frequency, high SNR EIT instrumentation (Fig. 1). Second, we produced an ASIC-based 20-channel TREIT system (Fig. 2), which is the first miniaturized TREIT system capable of delivering a measurement SNR of up to 72 dB over a 1 MHz frequency range (Fig. 3).

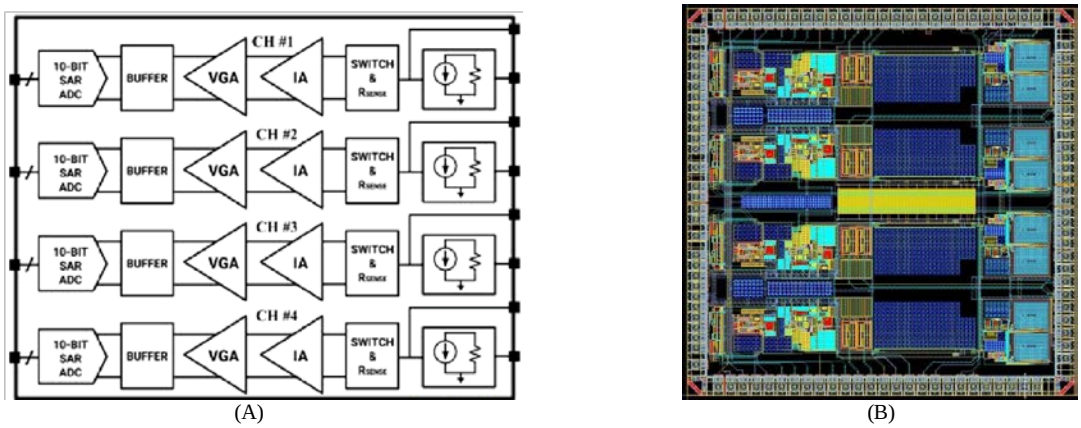

(A) (B)

Figure 1: EIT instrumentation ASIC containing 4 channels that can each perform current injection, current sink and voltage readout. On-chip multiplexing is included to switch the channels between the three operation modes. (A) Simplified floorplan of ASIC, depicting analog-digital-converter ("10-bit SAR ADC"), ADC driver ("buffer"), variable gain amplifier ("VGA"), instrumentation amplifier ("IA"), multiplexing circuitry ("switch") and current driver (right-most column). (B) Screenshot of ASIC layout, just prior to extraction and submission to semiconductor foundry for fabrication. (Adapted from 2016-2017 Annual Report)

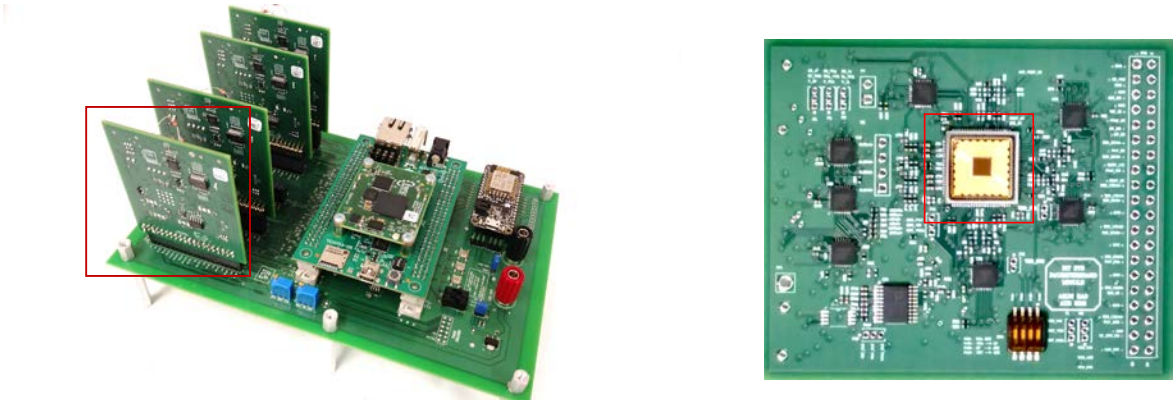

(A) (B)

Figure 2: Miniaturized TREIT system. We have designed a modular, 4 channel small form-factor PCB to house the ASIC and support circuitry. Our design is based on a motherboard-daughterboard system. The motherboard PCB houses an FPGA for central control, multiple daughterboards, a UART communication unit, and a Wi-Fi module. The UART communication unit is used to download initial FPGA configuration settings from a laptop. The Wi-Fi module is used to send EIT impedance measurements back to the laptop. Each daughterboard implements a complete channel, which includes our ASIC (for current source/sink and voltage readout), switches, voltage references and power management circuitry. (A) Photograph depicts horizontal motherboard and 4 of the 5 daughter boards (red border) that comprise the system. Total dimensions are 5.5"(W) x 8.25"(L) x 3.25" (H) (B) Detail of daughter board, showing 4-channel ASIC (red border; see Fig. 1 for layout details) and peripheral components. (Adapted from 2017-2018 Annual Report)

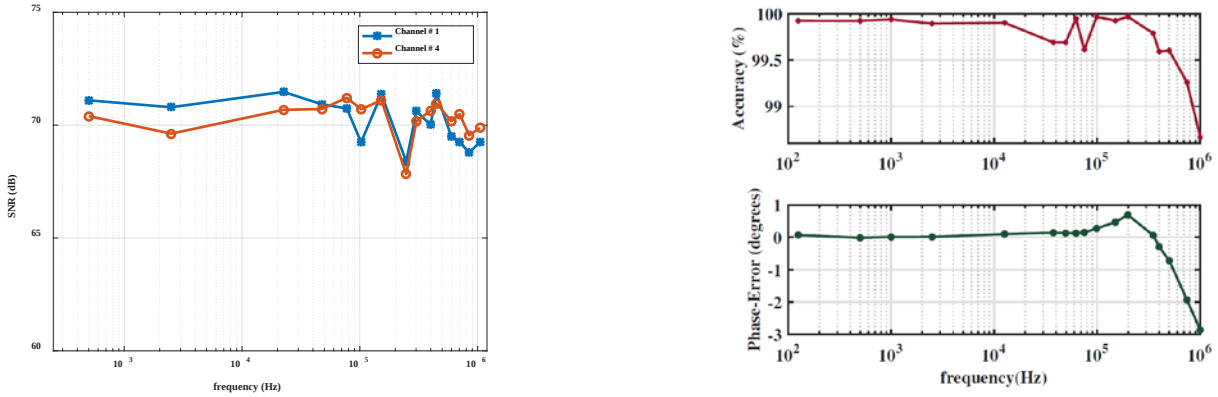

(A) (B)

Figure 3: Validation of the small form-factor TREIT system. The TREIT system was used to measure the impedance of a known test load (120 Ohms in series with a parallel combination of 47 Ohms and 300 nF) across the frequency range 100 Hz to 1 MHz. Two of the main system specification requirements of an EIT device are the precision, or signal-to-noise ratio (SNR), and accuracy. We measure the SNR of the ASIC by performing hundreds of load impedance measurements under nominally-identical conditions. The SNR is calculated as the ratio of the mean squared over the variance of these repeated measurements. (A) Signal-to-noise ratio of the measured amplitudes, tested on two representative channels. (B) Accuracy of measured amplitude (top panel) and phase error (bottom panel). (Adapted from 2017-2018 Annual Report)

Goal #2: To develop TREIT imaging algorithms for prostate imaging

Under this goal, we aimed to develop electrical impedance imaging algorithms that are able to couple impedance measurements recorded from an electrical impedance sensing biopsy needle and electrodes adhered to an end-fired TRUS probe. These images would be overlaid directly onto a gray scale TRUS image to provide enhanced feedback to the clinician regarding cancer grade.

The specific objectives were to implement TREIT meshing and reconstruction algorithms to (1) accurately model an end-fired probe geometry, (2) embed a 3D prostate surface into the FEM mesh, and (3) insert multiple internal sensing nodes into FEM meshes based on identified needle locations. To achieve the above objectives, we performed the following activities: optimized and manufactured TREIT electrode arrays and EIT-Bx needles; developed 3D prostate meshing through EM-tracked TRUS; developed custom image reconstruction software for TREIT-based prostate biopsy.

Our activities under this goal resulted in a number of key outcomes. We developed an FEM model of our TRUS/TREIT probe (Fig. 4), that has a depth of sensitivity to > 20 mm. We also developed a dual mesh approach for use in estimating the electrical properties within the prostate with a combination of TREIT and EIS-Bx electrodes (Fig. 5). This approach was validated with simulations to explore the sensitivity of the coupled system when different sets of current patterns are used (i.e. when just the TRUS electrodes are used or when just the EIS-Bx electrodes are used, or when some combined patterns are used (Fig. 6).

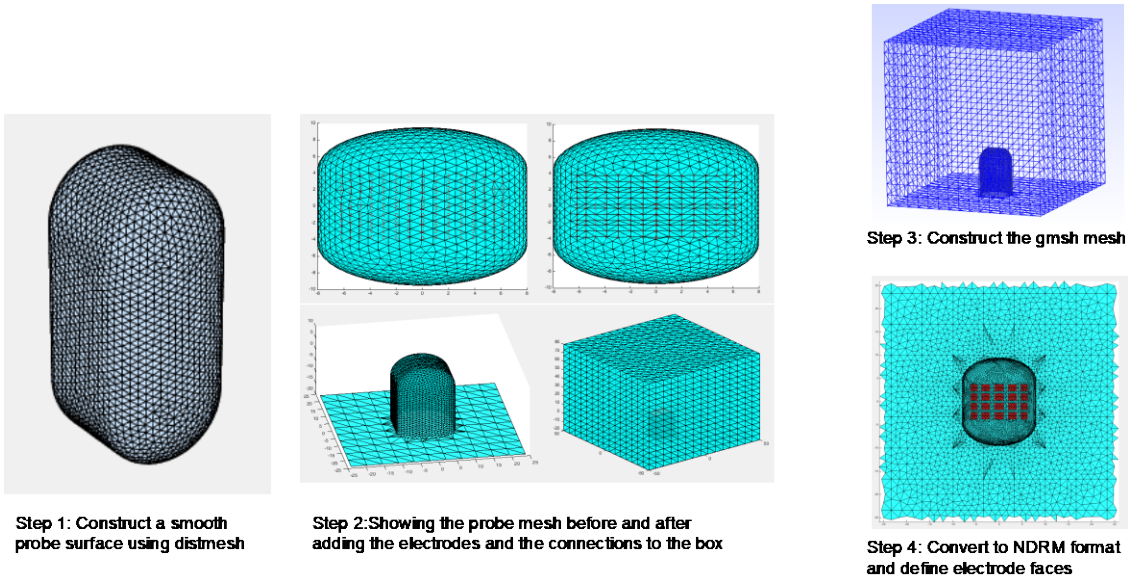

Figure 4: These images display the process used to generate a custom FEM mesh that matches the dimensions of our TRUS probe with the electrode array embedded on the probe. These types of meshes will be used for phantom and clinical studies. (Adapted from 2015-2016 Annual Report)

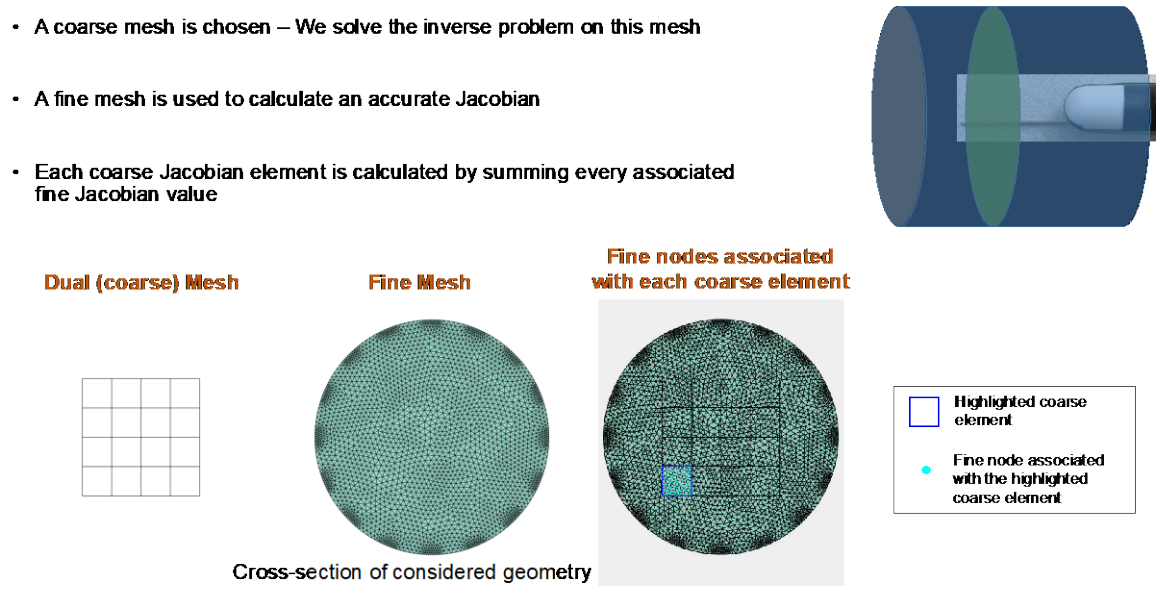

Figure 5: Summary of our multi-mesh approach to reconstructing electrical properties within the domain of interest (the prostate in the case). The domain includes the TRUS probe and the biopsy needle. (Adapted from 2016-2017 Annual Report)

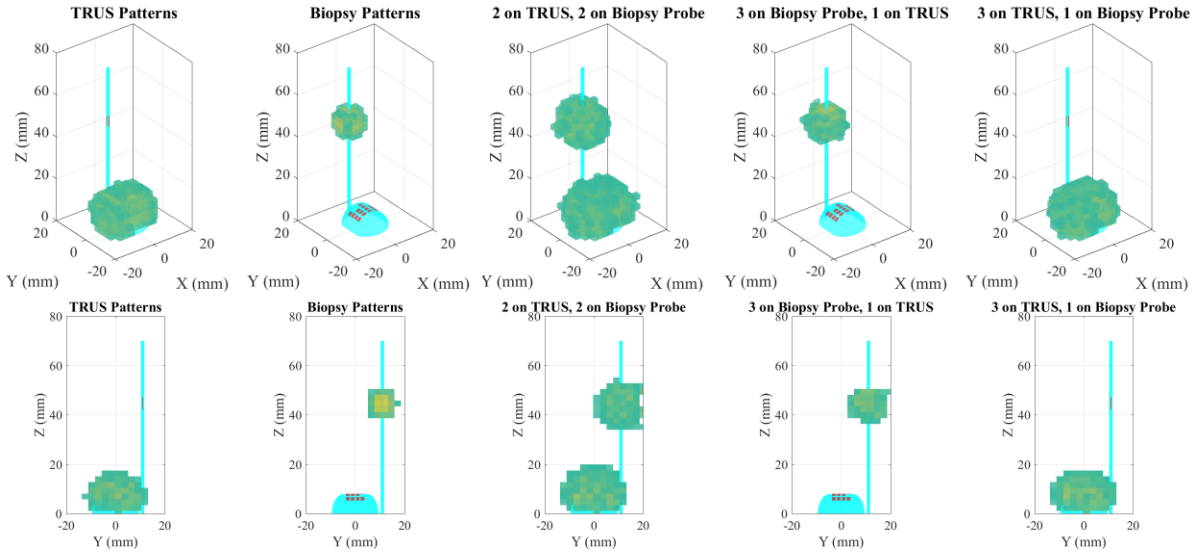

Figure 6: Sensitivity plots for different electrode combinations. Jacobian elements (i.e. sensitivity) of greater than 1/1000 of the maximum value are plotted (signifying what our system can actually sense). The green volume denote the regions in which we can identify a small conductivity perturbation within a homogenous background. Important to note is that this represent a single biopsy location. By combining data recorded from multiple biopsy locations we expect to increase our total volume of sensitivity to encompass the entire prostate. (Adapted from 2016-2017 Annual Report)

Goal #3: To validate TREIT through phantom studies

The goal was to conduct phantom imaging trials using gels and other biological substances to impersonate the prostate, and to use these studies to validate the imaging capabilities of the novel TREIT system.

The specific objective for this goal was to fully characterize our TREIT-TRUS system in terms of accuracy and image sensitivity. The major activity for achieving this objective was to evaluate TREIT with liquid phantoms, ex-vivo bovine tissue and with anatomically-accurate phantoms.

Some key outcomes resulting from pursuing this goal were: construction of a saline tank and validation of our reconstruction algorithms (Fig. 7); validation of our ASIC and miniaturized EIT system (Fig. 8). For preparation for the ex-vivo prostate study, 3D printed parts were produced to hold the TRUS probe, EIS-Bx needle, and biopsy gun (Fig. 9). Further, a rig was developed to hold the prostate (Fig. 10), which also held phantoms (gelatin prostates and bovine samples), which provided registration points for the EM tracking. This rig was additionally used to hold the sample within the MRI for further validation. TREIT reconstructions of gelatin prostate with graphite inclusions (Fig. 11) and a bovine sample (Fig. 12) show that the algorithm qualitatively working very well and was specifically able to 1) detect inclusions and 2) roughly discriminate adipose from muscle tissue. The gel phantom experiments resulted in reconstructions with area under the curve (AUC) values from receiver operator characteristic (ROC) curves of > 0.85 for 4 out of the 5 tests (Fig. 13A) and when incorporating inclusion boundaries resulted in absolute reconstructions yielding 1.9% and 12.2% average absolute percent errors for 3 consistent tests and all 5 tests, respectively (Fig. 13B-C).

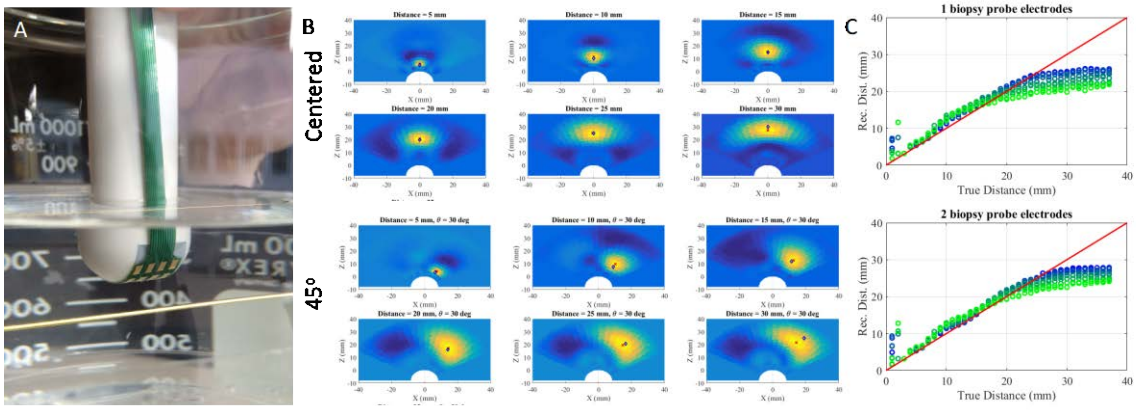

Figure 7: Saline phantom experiments exploring depth of sensitivity. (A) The TRUS/TREIT probe was submerged in a tank filled with 0.1 S/m saline and a high conductivity metal inclusion (1 mm diameter brass rod) was placed in front of the probe at different distances from the electrode array and at two angles (directly centered on the array and 45^{o} off-center). (B) Reconstructed conductivity images acquire of the inclusion shows that we can detect the rod as it moves away from the face of the probe at both angular orientations. (C) This test was carried out by extending the displacement of the rod to 35 mm from the surface of the probe. We have good linear correlation between the center of the reconstructed inclusion and the true position up to ~20 mm. This data was acquired with 1 and 2 biopsy needle electrodes. (Adapted from 2015-2016 Annual Report)

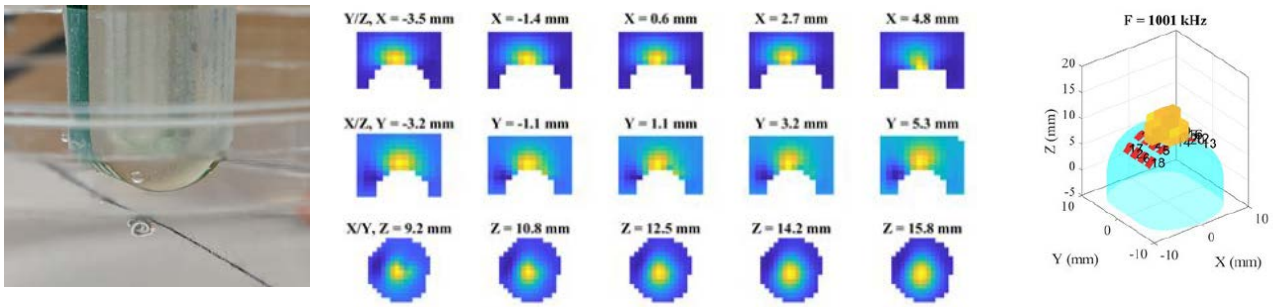

Figure 8: ASIC-based EIT system experimental setup. Left panel: Electrode array on a flexible printed circuit, immersed in a saline tank solution. Center: Impedance images obtained across frequencies for the experimental setup. Right: The yellow blocks in the reconstructed 3D images are conductivity regions that are within 70 % of the maximum measured conductivity. That is, they represent the metal inclusion.

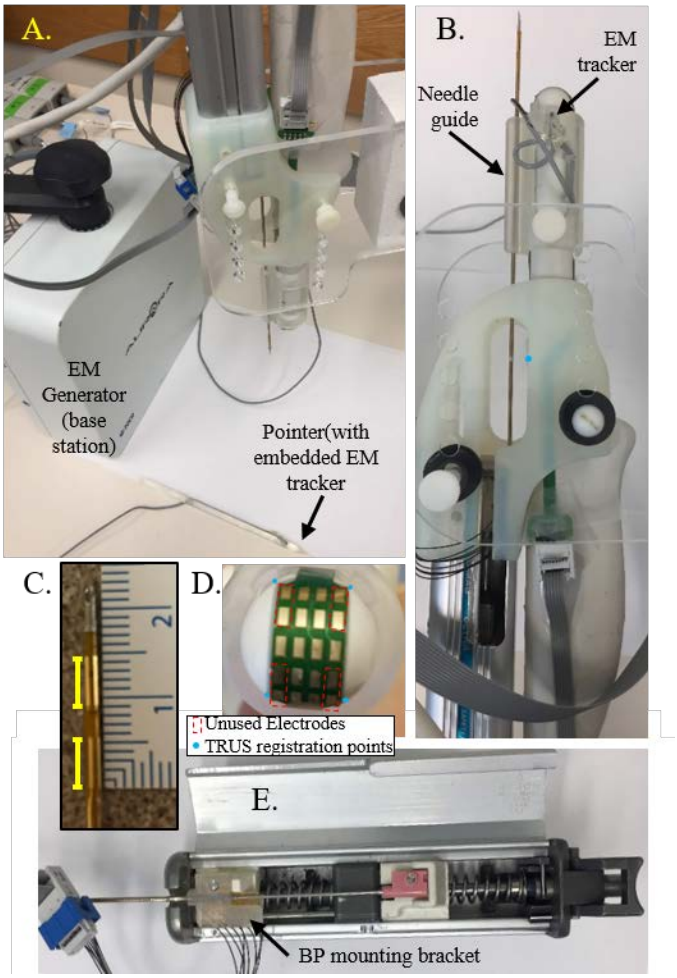

Figure 9. A. The Phillips C9-EC transrectal ultrasound probe in holder and stand with attached biopsy gun and EM generator and pointer, B. side view of the needle guide and tracker, C. BP and D. TRUS electrodes, and E. the opened biopsy gun showing mounting assembly.

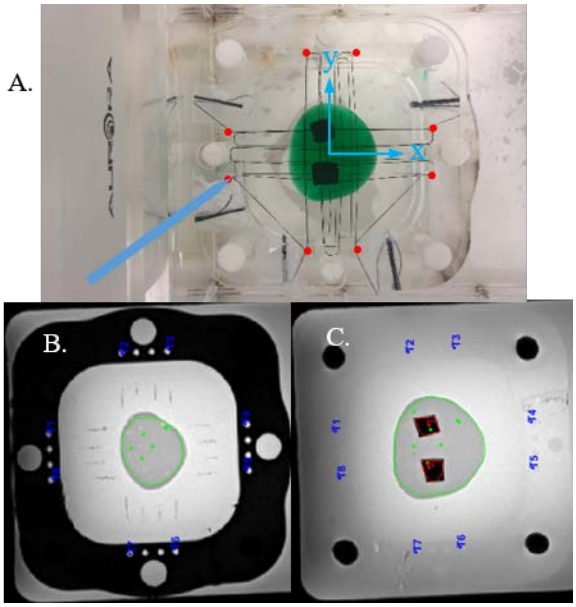

Figure 10. Illustration of A. rig, registration points, and invers frame for a gel prostate phantom with corresponding MR image (B-C) showing the segmented prostate and tumor boundaries and registration points.

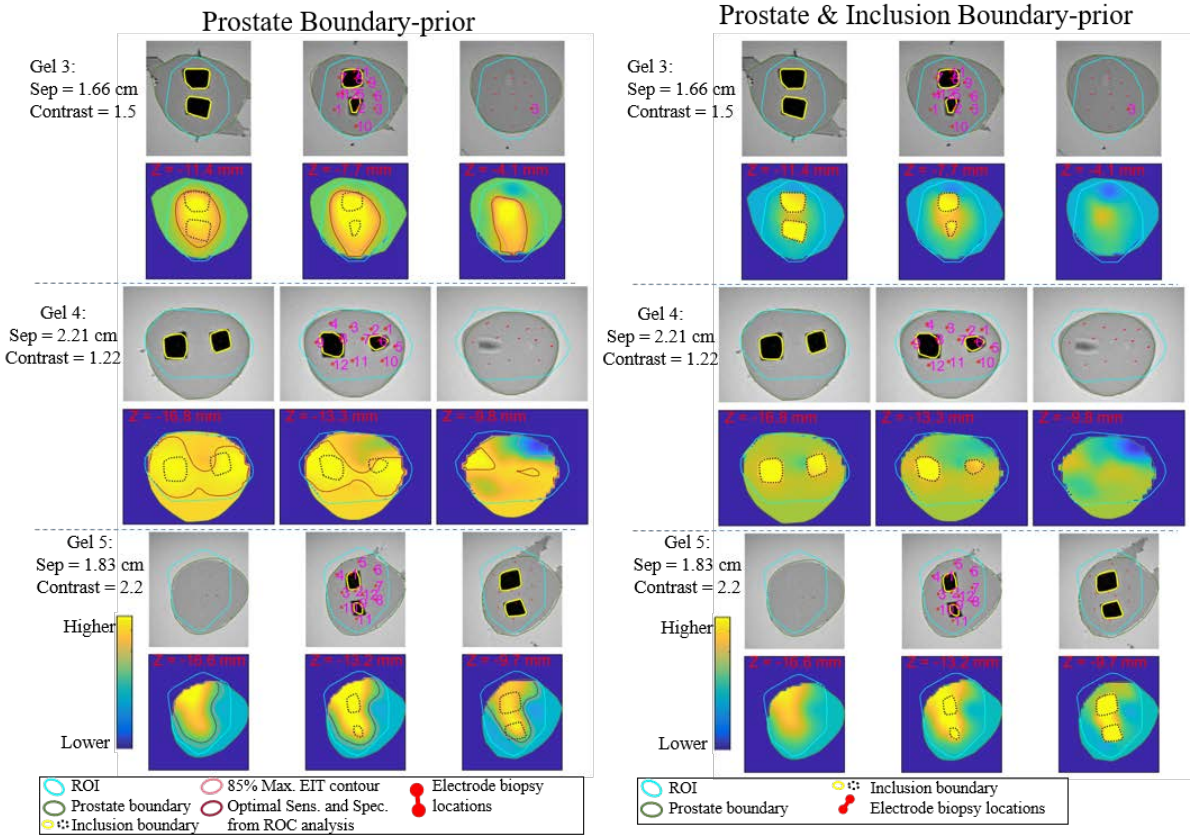

Figure 11. Absolute reconstructions (5-step) using prostate boundary (left) and prostate and inclusion boundaries as prior information in the TREIT algorithm on gel tests 3-5 at 40 kHz. The prostate (green) and inclusions (yellow or black) are clearly seen in the MR images (top row of each test) with overlaid biopsy positions, the left EIT images (bottom rows) show contours of 85% max and optimal (ROC curve), whereas the right EIT images show the exact tumor inclusion outlines.

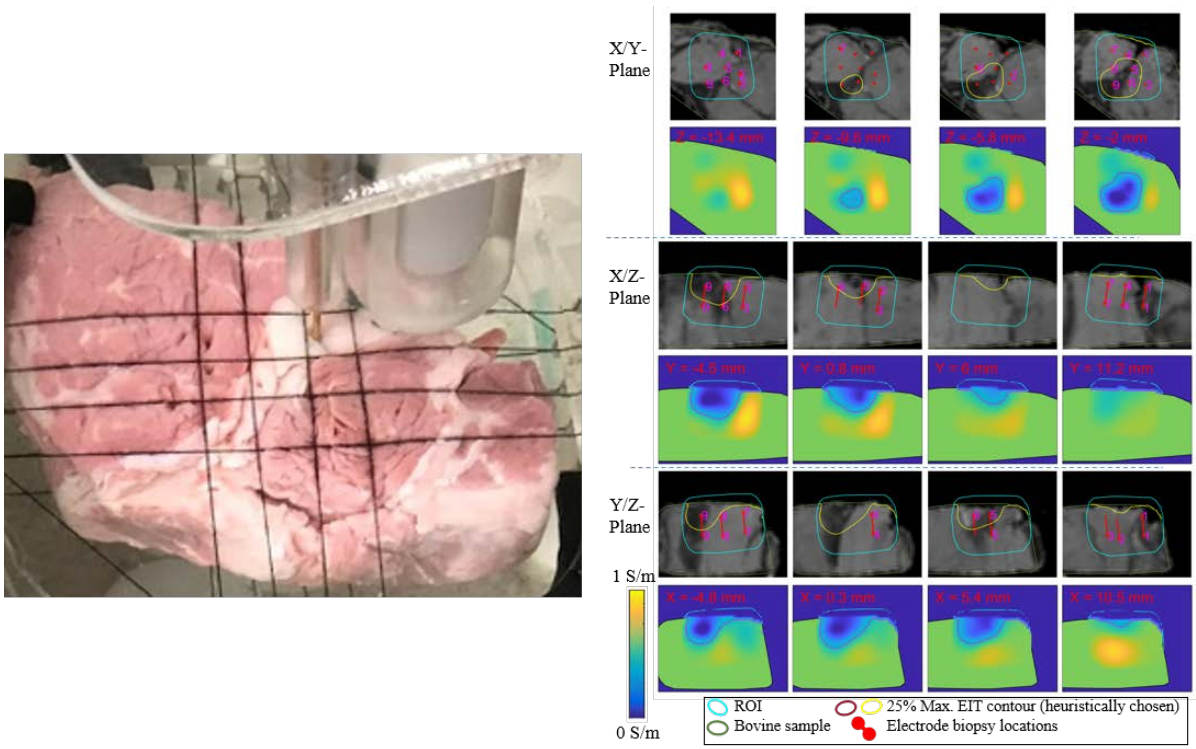

Figure 12: Left) Ex vivo bovine tissue imaging configuration. The thin electrical transparent cables secure the tissue in place. The square grid (created by the cables) indicates where biopsy cores are extracted. The TRUS probe and biopsy needle guide are placed right above the tissue. The tissue samples is submerged within a bath of 0.1 S/m saline solution to mimic the tissue surround this prostate. Right) Magnetic Resonance (MR) images are acquired of the tissue sample and registered with EIT imaging. The conductivity maps are shown below each MR slice, showing the same region. These results are very promising and highlight the strong adipose/muscle contrast visible in EIT images (yellow = muscle, blue = adipose). Note the concordance between MR muscle regions (gray) and high conductivity (yellow) regions in the EIT images and the MR adipose regions (black) and low conductivity (blue) regions in the EIT images.

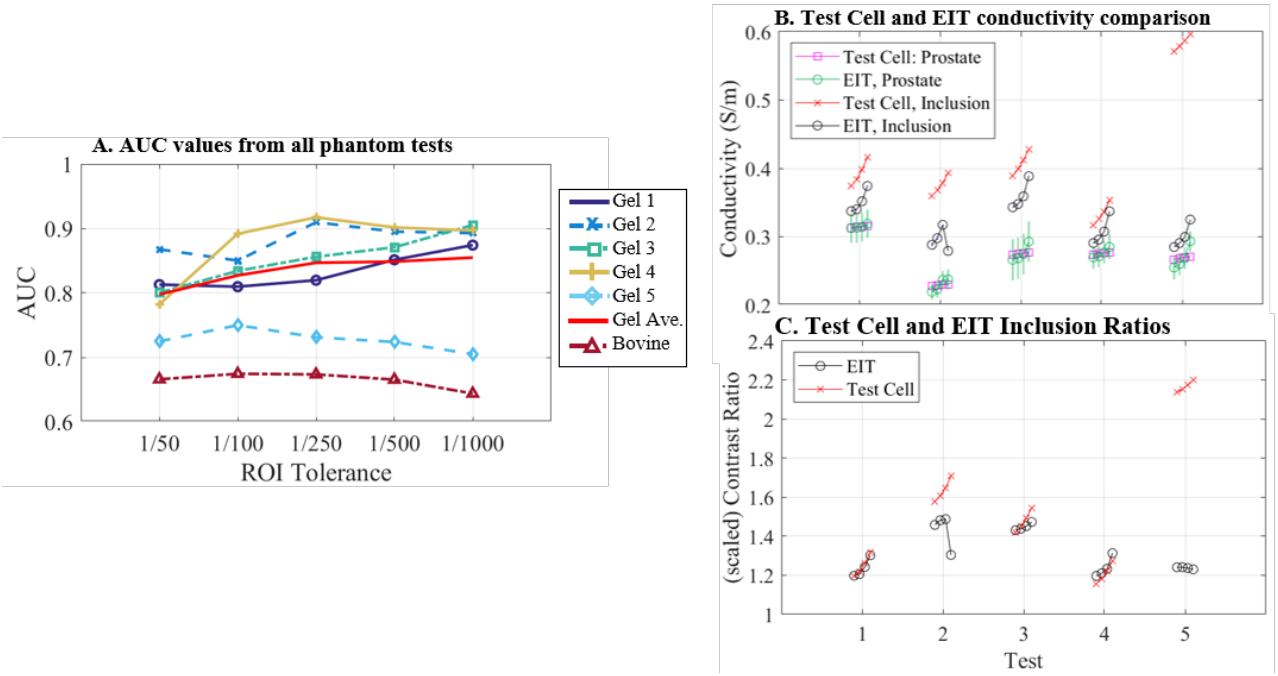

Figure 13. A. Area under the (ROC) curves (AUC) for each gel prostate phantom test, the average gel prostate phantom test AUCs, and bovine test versus the ROI tolerances (used to define the region in which the reconstruction is performed). B. Test cell (validation data) and average EIT conductivity values for the (benign) prostate and inclusions for all five gel experiments where the 4 points for each test are results at 10, 20, 40, and 80 kHz, and C. scaled contrast (inclusion-to-prostate) ratios. A scaling factor of 1.11 was used, which was calculated as a best-fit for tests 1, 3, and 4.

Goal #4: To evaluate TREIT using a sample of ex-vivo prostates

This goal involved evaluating the EIT system on a series of ex vivo prostates extracted from men undergoing radical prostatectomy. This initial ex-vivo work would provide sufficient preliminary data for extending this technology to in-vivo trials to be proposed subsequent to this project.

The specific objective for this goal was to determine if EIS-Bx or EIT can effectively differentiate benign from cancerous tissue and differentiate cancer grades. The major activity included in achieving these goals was collecting freshly excised prostates from radical prostatectomy surgeries performed at DHMC, collecting EIS-Bx data on the specimens, collecting validation data with MR and via full pathological assessment (Fig. 14). The pathology reports provided tumor boundary and grades overlaid on the MR images, providing easy registration with EIS-Bx and EIT data.

Under this goal, our activities resulted in the following key outcomes: 1) strong evidence that EIS-Bx (Fig. 15) measurements and TREIT images (Fig. 16) have an ability to separate cancerous and benign tissue, and 2) TREIT images using tumor boundary information has the potential to provide cancer grade information (Fig. 17). Receiver operator characteristic (ROC) and corresponding area under the curve (AUC) values resulted in maximum values of 0.72 and 0.82 for resistance and reactance from the EIS-Bx data at 10 kHz, and 0.75 and 0.82 for TREIT reconstructions corresponding to conductivity at 20 kHz via a pixel- and average-type analysis, respectively. Further, the linear regression of the tumor conductivity reconstruction versus tumor grade yielded adjusted R^2 values of 0.77 for tumors larger than 1.95 cm. Examples of TREIT reconstructions (Fig. 18) show that qualitatively, large tumors result in very successful reconstructions where the tumor regions appear as depressed blue regions (low conductivity areas).

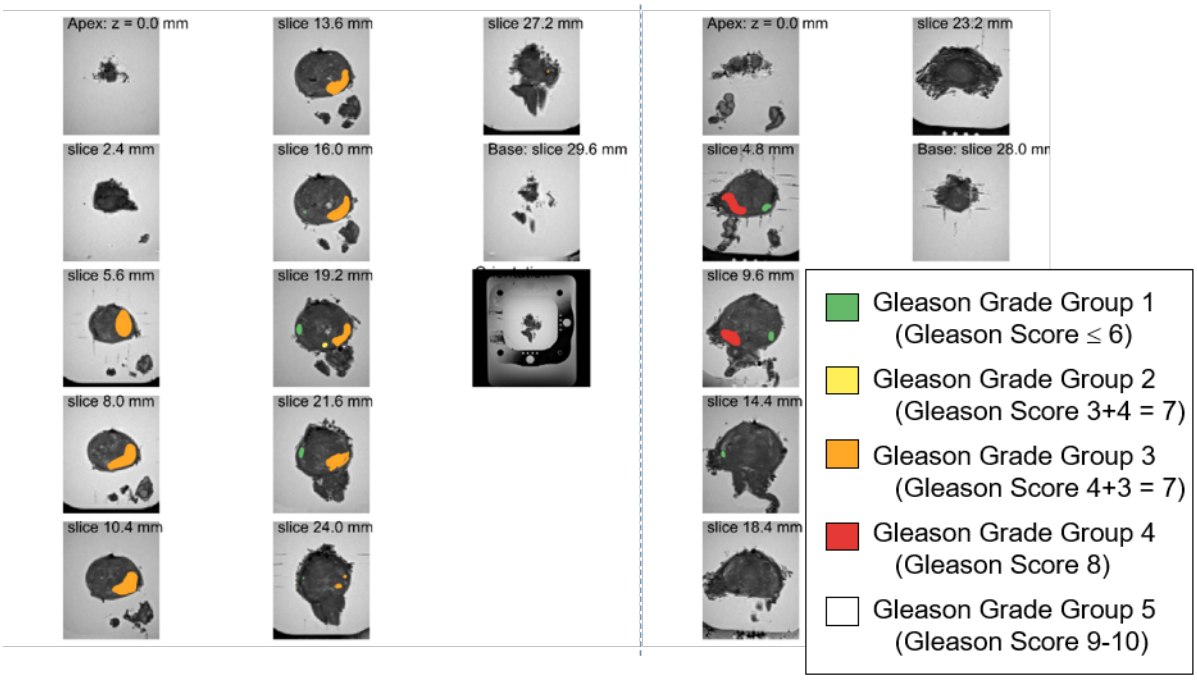

Figure 14. Overlaid pathology reports from two prostates showing examples of Gleason grade group 1 (green), 3 (orange), and 4 (red).

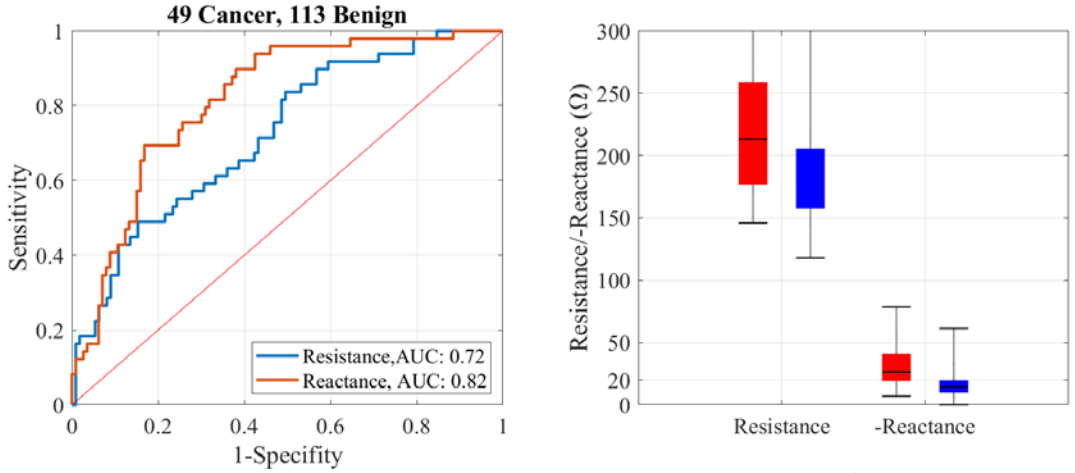

Figure 15. Receiver operator characteristic (ROC) curves corresponding to 49 cancer and 113 benign cores from the 18 ex vivo prostates studied at 10 kHz showing area under the curve (AUC) values of 0.72 and 0.82 for resistance and reactance, respectively. The right plot shows the corresponding 25-75% box and whisker plots, revealing an impressive separation for the reactance component of the data.

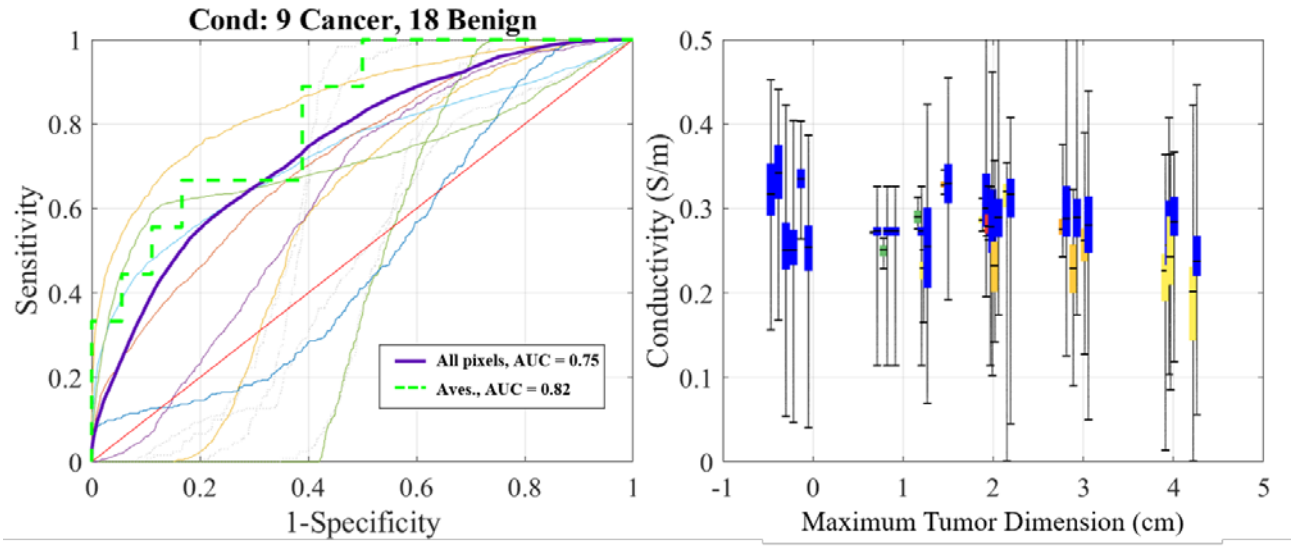

Figure 16. Receiver operator characteristic (ROC) curves corresponding to all pixels from all 18 prostates (purple), from all-pixels from individual prostates, and from average values of tumor and benign regions (green and uses 9 cancer regions) from conductivity fdTREIT reconstructions at 20 kHz. The averages include only tumors > 1.95 cm in maximum dimension. The right plot shows the 25-75% box and whisker plots for pixels from all prostates ordered from smallest to largest maximum tumor size (fully benign prostates are left of zero). Box plots show qualitative differences for larger tumors that is reduced or eliminated when the prostates get too small (~ 2cm). The fdTREIT algorithm here only assumes knowledge of the prostate outer boundary.

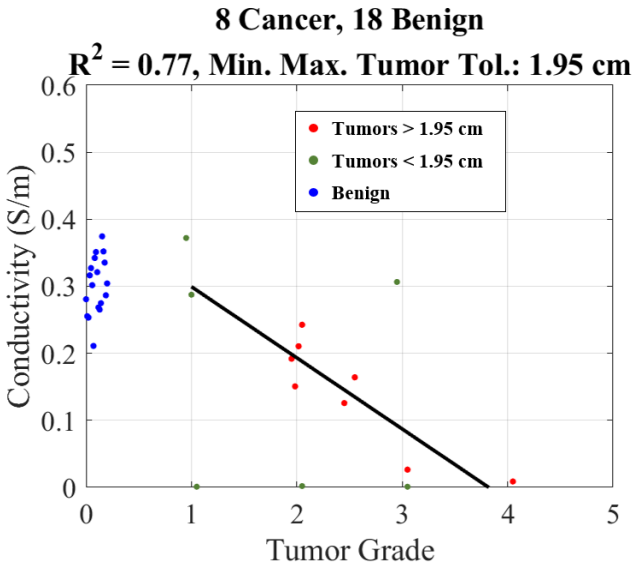

Figure 17. Linear regression of the average values of tumor regions versus tumor grade from fdTREIT reconstructions, which utilize both prostate and tumor boundaries in the method at 20 kHz. An adjusted R^2 value of 0.77 shows strong correlation for these 8 tumors, which are greater than 1.95 cm, revealing the potential for fdTREIT to differentiate cancer grade and the current minimum tumor limitation of the technique.

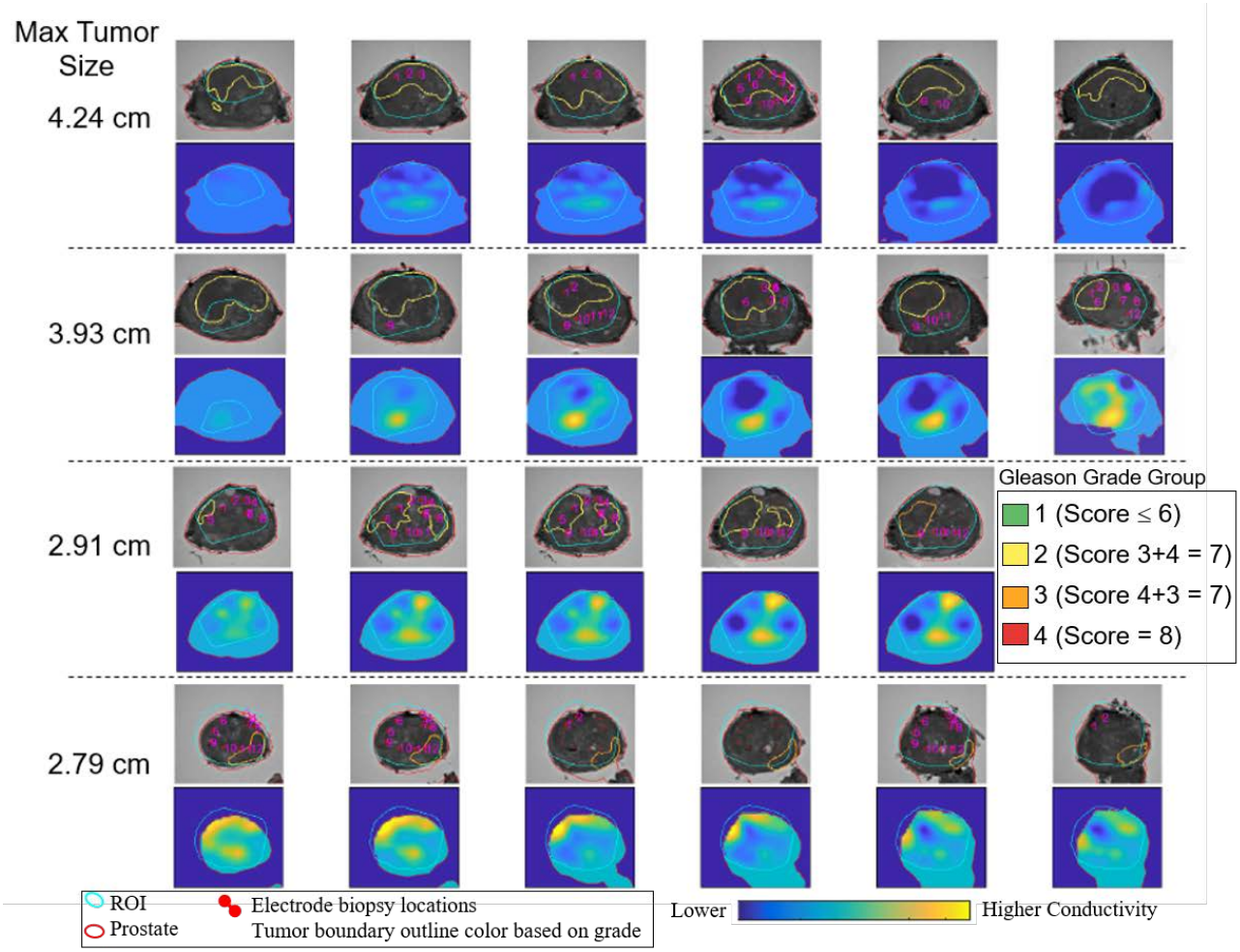

Figure 18. Example (large) fdTREIT conductivity reconstruction at 20 kHz using only prostate boundary information in the algorithm. Conductivity is expected to be lower (blue) within the tumor region, and one can see there is a qualitatively strong correlation between the outlined tumor regions in the MR images and the corresponding EIT images below for each of the 4 ex prostate examples shown.

What opportunities for training and professional development has the project provided?

Arun Rao, PhD: Worked on the project as a PhD student and benefitted from training opportunities to achieve proficiency in the following skills: integrated circuit design (analog front end and mixed signal circuits); instrumentation design for biomedical imaging; system miniaturization; FPGA programming; wireless communication; phantom experimentation and instrument validation.

Ethan Murphy, PhD: Gained clinical perspective by observing numerous radical prostatectomy procedures, continued experience in data analysis, fusion, and practical EIT probe development.

Xiaotian Wu, PhD: Worked on the project as a PhD student and benefited from training opportunities to achieve proficiency in the following skills: developing EM tracking software; user interface design; medical device development; 3D modeling and 3D printing; clinical exposure to RALP; phantom experimentation and clinical data acquisition.

Professional development activities made possible by the project included participation in the IEEE Biomedical Circuits and Systems Conference (Kofi Odame, Arun Rao), the International Conference on Biomedical Applications of Electrical Impedance Tomography (Ryan Halter, Kofi Odame, Arun Rao, Xiaotian Wu, Ethan Murphy), the Teledyne LeCroy Workshop on PCB Signal Integrity (Mohsen Shahghasemi), 2018 Biomedical Engineering Society meeting (Ethan Murphy, Ryan Halter).

Professional development activities made possible by the project also included organizing and hosting in 2017 the 18th International Conference on Biomedical Applications of Electrical Impedance Tomography (Ryan Halter)

How were the results disseminated to communities of interest?
In addition to presenting our technology development at conferences and publishing in peer-reviewed archival journals (as included in the Appendix), results were also disseminated through various other interactions as described below.

Results of the project were highlighted and presented in outreach activities to members of communities that are traditionally underrepresented in science and technology. Specifically, Kofi Odame presented this work during the Dartmouth Adventures in STEM, a weeklong summer program introducing underrepresented minority students to the exciting world of STEM. This program included guest lectures, lab visits and a mini-course that featured intriguing ideas related to on-going research. During the Adventures in STEM program, students start to form an intellectual community by engaging in intellectual improvisation and discussion motivated by challenging problems posed by Odame and other instructors, and by their own curiosity.

Several invited talks that highlighted the developments made as part of this project were presented at various venues:

1. Halter RJ "Smart devices and systems for surgical guidance: Augmenting today's surgeon," Invited speaker, Jones Seminar on Science, Technology and Society, Dartmouth College, Hanover, NH, March 2019.
2. Halter RJ, "Prostate Cancer Sensing and Imaging Technologies: From bench to bedside," Invited speaker, Norris Cotton Cancer Center Grand Rounds, Dartmouth-Hitchcock Medical Center, Lebanon, NH November 2018.
3. Halter RJ and Murphy EK "Multimodal Electrical Impedance Tomography (EIT): Advances in EIT-coupled Ultrasound Imaging," Invited Symposium Participant: *Recent innovations and new health-related applications of electrical bioimpedance* at 40th International Conf IEEE EMBS July 2018.
4. Halter RJ, "Smart Devices and Systems for Urological Guidance," Invited speaker, Urology Grand Rounds, Dartmouth-Hitchcock Medical Center, Lebanon, NH November 2017.
5. Halter RJ, "Smart Devices and Systems for Surgical Guidance," Invited speaker, Williamson Translational Research Forum, Dartmouth-Hitchcock Medical Center, Lebanon, NH August 2017.
6. Halter RJ "Surgical enhancement: Using electrical bioimpedance to improve clinical practice," Invited speaker, Surgical Planning Laboratory Seminar Series, Brigham and Women's Hospital, Boston, MA, February 2016.

What do you plan to do during the next reporting period to accomplish the goals?
Nothing to Report

IMPACT

What was the impact on the development of the principal discipline(s) of the project?
Fused Electrical Impedance Tomography: This was the first work that demonstrated how one could combined impedance measurements recorded from multiple configurations to improve volumetric impedance imaging. This approach has been extended to breast imaging applications and has the potential to be deployed for other clinical image scenarios.

Integrated Circuits for Prostate Electrical Impedance Tomography: This work produced the first application specific integrated circuit (ASIC) that can be used for in-vivo prostate electrical impedance tomography (EIT). This new capability could help improve prostate cancer diagnosis.

What was the impact on other disciplines?
Impedance Sensing Biopsy Needles: This work has demonstrated that volumetric prostate imaging can be accomplished with the use of multi-electrode biopsy needles; using these "smart" biopsy needles one can increase the volume of prostate sensed from <1% for a standard 12-core procedure to more than 75% of a standard prostate with the same number of cores. This technology represents a potential approach to improving biopsy without the need for full EIT imaging. In addition, these biopsy needles have the potential to be used for cancers other than in prostate (i.e. breast, kidney, liver, etc).

ASIC Design Methodology: We developed a formal methodology for designing application specific integrated circuits (ASICs) in EIT systems. Our methodology allows engineers to translate the high-level, biomedical imaging requirements of an EIT system to the physical design of integrated circuits.

What was the impact on technology transfer?
Nothing to Report

What was the impact on society beyond science and technology?
Nothing to Report

CHANGES/PROBLEMS

Changes in approach and reasons for change
Nothing to Report

Actual or anticipated problems or delays and actions or plans to resolve them
There were delays in completing the ex vivo data collection component of this project (PI: Halter) and in finalizing our small-form factor ASIC-based design (PI: Odame), due to two primary challenges. The first was that it took longer than expected to obtain approval for conducting the human studies component of the program. The second was that one Graduate Student working on this program during Year 1 (under PI: Halter) transitioned to another project, while another Graduate Student working on this program (under PI: Odame) participated in an off-campus internship program during Year 3. These personnel changes slowed progress down.

To resolve these issues, we (1) increased the amount of effort of a post-doctoral researcher that had been working on the program and had a new student joining the project in September 2018, (2) received approval from the U.S. Army Medical Research and Materiel Command (USAMRMC), Office of Research Protections (ORP), Human Research Protection Office (HRPO) to begin our ex vivo study, (3) used a larger EIT system in

Halter's lab for performing initial phantoms studies and (4) requested, and received approval for, a twelve-month no-cost extension through 09/14/2019.

We kept our Scientific Officer, Dr. Asif Rizwan, appraised of our progress and delays (through our submitted annual reports and email correspondence). Our mitigating actions ultimately allowed us to complete the proposed goals of the project.

Changes that had a significant impact on expenditures
Due to the personnel changes described under "*Actual or anticipated problems…,"* there were funds left over after the nominal three-year performance period of the project. We received approval for a twelve-month no-cost extension through 09/14/2019, during which the small form-factor EIT system was completed and tested, and clinical data acquisition from a series of ex vivo human prostates was performed.

Significant changes in use or care of human subjects, vertebrate animals, biohazards, and/or select agents
Nothing to Report

Significant changes in use or care of human subjects
Nothing to Report

Significant changes in use or care of vertebrate animals
Not Applicable

Significant changes in use of biohazards and/or select agents
Not Applicable

PRODUCTS

- **Publications, conference papers, and presentations**

  Journal publications:

  Author: Murphy E, Takhti M, Skinner J, Halter RJ, Odame K
  Title: Signal-to-noise ratio analysis of a phase-sensitive voltmeter for electrical impedance tomography
  Journal: IEEE Transactions on Biomedical Circuits and Systems
  Volume: 11(2)
  Year: 2016
  Pages: 360-369
  Status of Publication: Published
  Acknowledgement of Federal Support: Yes

  Author: Murphy E, Mahara A, Halter RJ
  Title: Absolute Reconstructions using Rotational Electrical Impedance Tomography for Breast Cancer Imaging
  Journal: IEEE Transactions on Medical Imaging
  Volume: 36 (4)
  Year: 892–903
  Pages: 2017
  Status of Publication: Published
  Acknowledgement of Federal Support: Yes

Author: Murphy E, Mahara A, Wu X, Halter RJ
Title: Phantom Experiments using Soft-Prior Regularization EIT for Breast Cancer Imaging
Journal: Physiological Measurement
Volume: 38(6)
Year: 2017
Pages: 1262
Status of Publication: Published
Acknowledgement of Federal Support: Yes

Author: Rao A, Teng Y, Schaef C, Murphy E, Arshad S, Halter RJ, Odame K
Title: An analog front end ASIC for cardiac electrical impedance tomography
Journal: IEEE transactions on biomedical circuits and systems
Volume: 12(4)
Year: 2018
Pages: 729-738
Status of Publication: Published
Acknowledgement of Federal Support: Yes

Author: Murphy E, Skinner J, Martucci M, Rutkove S, Halter RJ
Title: Towards Electrical Impedance Tomography Coupled Ultrasound Imaging for Assessing Muscle Health
Journal: IEEE Transactions on Medical Imaging
Volume: 38
Year: 2019
Pages: 1409-1419
Status of Publication: Published
Acknowledgement of Federal Support: Yes

Author: Murphy E, Wu X, Halter RJ
Title: Fused-data transrectal EIT for prostate cancer imaging
Journal: Physiological Measurement
Volume: 39(5)
Year: 2018
Pages:054005
Status of Publication: Published
Acknowledgement of Federal Support: Yes

Author: Rao A, Murphy E, Shahghasemi M, Odame K
Title: Current-conveyor-based wide-band current driver for electrical impedance tomography
Journal: Physiological Measurement
Volume: 40(3)
Year: 2019
Pages: 034005
Status of Publication: Published
Acknowledgement of Federal Support: Yes

Author: Murphy E, Amoh J, Arshad S, Halter RJ, Odame K
Title: Noise-robust bioimpedance approach for cardiac output measurement
Journal: Physiological Measurement
Volume: 40
Year: 2019
Pages: 074004

Status of Publication: Published
Acknowledgement of Federal Support: Yes

Author: Murphy E, Wu X, Everitt A, Halter RJ
Title: Phantom Studies of Fused-data TREIT using only Biopsy-probe electrodes
Journal: IEEE Transactions on Medical Imaging
Volume: n/a
Year: n/a
Pages: n/a
Status of Publication: Submitted December 2019
Acknowledgement of Federal Support: Yes

Author: Rao A, Murphy E, Halter RJ, Odame K
Title: A 1 MHz Miniaturized Electrical Impedance Tomography System for Prostate Imaging
Journal: IEEE Transactions on Biomedical Circuits and Systems
Volume: n/a
Year: n/a
Pages: n/a
Status of Publication: Submitted November 2019
Acknowledgement of Federal Support: Yes

Books or other non-periodical, one-time publications:

Author: Arun Rao
Title: Design of Small Form Factor Electrical Impedance Tomography System,
Year: 2019
Type of publication: Dissertation
Status of publication: Published
Acknowledgement of Federal Support: No

Other publications, conference papers and presentations.

Author: Halter RJ
Title: Surgical enhancement: Using electrical bioimpedance to improve clinical practice
Conference: Invited speaker, Surgical Planning Laboratory Seminar Series (2016)
Location: Brigham and Women's Hospital, Boston, MA
Status of Publication: Presented

Author: Halter RJ, Hartov A, Sched A, Seigne J
Title: Prostate Imaging with Transrectal Electrical Impedance Tomography
Conference: AdMeTech (2016)
Location: Boston, MA
Status of Publication: Presented

Author: Murphy E, Mahara A, Halter RJ
Title: Investigation into Improvements offered by Fused-data EIT
Conference: XVII. Conference on Electrical Impedance Tomography (2016)
Location: Stockholm, Sweden
Status of Publication: Presented

Author: Murphy E, Mahara A, Halter RJ
Title: Soft-Prior Regularization EIT for Breast Cancer Detection
Conference: XVII. Conference on Electrical Impedance Tomography (2016)
Location: Stockholm, Sweden
Status of Publication: Presented

Author: Everitt A, Pettus J, Hyams E, Halter RJ
Title: Electrical impedance sensing biopsy needle for real-time prostate cancer detection
Conference: Annual Meeting of the Biomedical Engineering Society (2017)
Location: Phoenix, AZ
Status of Publication: Presented

Author: Murphy EK, Wu X, Halter RJ
Title: Fused-data Transrectal EIT incorporating Biopsy Electrodes
Conference: International Conference on Biomedical Applications of Electrical Impedance Tomography (2017)
Location: Hanover, NH
Status of Publication: Presented

Author: Rao A, Teng Y, Odame K
Title: System on Chip Implementation for Electrical Impedance Tomography
Conference: International Conference on Biomedical Applications of Electrical Impedance Tomography (2017)
Location: Hanover, NH
Status of Publication: Presented

Author: Murphy E, Wu X, Halter RJ
Title: Absolute Phantom Reconstructions using Fused-Data EIT
Conference: International Conference on Biomedical Applications of Electrical Impedance Tomography (2018)
Location: Edinburgh, UK
Status of Publication: Presented

Author: Halter RJ and Murphy EK
Title: Multimodal Electrical Impedance Tomography (EIT): Advances in EIT-coupled Ultrasound Imaging
Conference: Annual International Conference of the IEEE Engineering in Medicine and Biology Society (2018)
Location: Honolulu, HI
Status of Publication: Presented

Author: Murphy E, Wu X, Halter RJ
Title: Fused-data Transrectal Electrical Impedance Tomography for Prostate Cancer Imaging
Conference: BMES Annual Meeting
Location: Atlanta, GA
Year: 2018
Status of Publication: Presented

Author: Murphy E, Skinner J, Martucci M, Rutkove S, Halter RJ
Title: A Coupled US/EIT System for Assessing Muscle Health
Conference: EIT conference
Location: Edinburgh, UK

Year: 2018
Status of Publication: Presented

Author: Murphy E, Wu X, Halter RJ
Title: Absolute Phantom Reconstructions using Fused-Data EIT
Conference: EIT conference
Location: Edinburgh, UK
Year: 2018
Status of Publication: Presented

Author: Everitt A, Manwaring P, Halter RJ
Title: A real-time 4-bit imaging electrical impedance sensing biopsy needle for prostate cancer detection
Conference: Proc. SPIE Medical Imaging 2018: Biomedical Applications in Molecular, Structural, and Functional Imaging
Location: Houston, TX
Year: 2018
Status of Publication: Presented

Author: Murphy EK, Hyams ES, Schned AR, Pettus J, Halter RJ
Title: Study of Separation Between ex vivo Malignant and Benign Prostatic Tissue using Magnetic Resonance-Electrical Property Tomography
Conference: SPIE Medical Imaging, (2019)
Location: San Diego, CA
Status of Publication: Presented

Author: Murphy EK, Wu X, Everitt A, Halter RJ
Title: Fused-data TREIT using an 8-electrode biopsy needle and soft priors
Conference: EIT conference 2019
Location: University College London
Status of Publication: Presented

- **Website(s) or other Internet site(s)**
  URL: https://sites.dartmouth.edu/odame/
  Description: The Analog Lab at Dartmouth website disseminates the results of research activities to a broad audience including the research community, prospective students and funding agencies.

- **Technologies or techniques**
  Nothing to report

- **Inventions, patent applications, and/or licenses**
  Nothing to report

- **Other Products**
  Nothing to report

PARTICIPANTS & OTHER COLLABORATING ORGANIZATIONS

What individuals have worked on the project?

Name: Kofi Odame

Project Role:	Principal Investigator
Nearest person month worked:	4.5
Contribution to Project:	Dr. Odame oversaw the design and testing of the EIT system (ASIC, printed circuit board, FPGA control), and maintained communication with Dr. Halter and Dr. Halter's lab to coordinate on ASIC/EIT system design requirements and performance specifications.

Name:	Ryan Halter
Project Role:	Principal Investigator
Nearest person month worked:	5
Contribution to Project:	Dr. Halter oversaw the development of fused data EIT image reconstruction, development of the multi-electrode biopsy probe and TRUS electrode array, conducting of all phantom and ex vivo imaging experiments

Name:	Arun Rao
Project Role:	Graduate Student
Nearest person month worked:	33
Contribution to Project:	Dr. Rao designed, taped-out and tested the custom application specific integrated circuit (ASIC) chips for this project. He constructed a miniaturized EIT system and integrated the various parts of the FPGA controller. Finally, he evaluated the performance of the miniaturized EIT with a TRUS probe and phantom study experiment.

Name:	Ethan Murphy
Project Role:	Research Scientist
Nearest person month worked:	30
Contribution to Project:	Dr. Murphy developed FEM meshes, EIT image reconstruction algorithms, conducted simulations to optimize TREIT system design parameters, conducted phantom experiments, and record and analyzed ex vivo prostate data.

Name:	Xiaotian Wu
Project Role:	Graduate Student
Nearest person month worked:	16
Contribution to Project:	Dr. Wu developed hardware for mounting TRUS/TREIT probe and EM-tracking sensors, approach and software for tracking instruments, developed tracking calibration protocols, conducted phantom experiments, assisted with recording and analyzing ex vivo prostate data

Has there been a change in the active other support of the PD/PI(s) or senior/key personnel since the last reporting period?
Nothing to Report

What other organizations were involved as partners?
Nothing to Report

SPECIAL REPORTING REQUIREMENTS

COLLABORATIVE AWARDS:
A partnering award (CDMRP Log No. PC140924, Grant Agreement No. W81XWH-15-1-0571) was made to Partnering PI Dr. Ryan Halter (Dartmouth College). A separate final report is being submitted for the partnering award.

QUAD CHARTS:
Not Applicable

APPENDICES

Appendix 1: IEEE TBioCAS 2016 publication
Appendix 2: IEEE TMI 2017 publication
Appendix 3: Phys Meas 2017 publication
Appendix 4: IEEE TBioCAS 2018 publication
Appendix 5: IEEE TMI 2019 publication
Appendix 6: Phys Meas 2018 publication
Appendix 7: Phys Meas 2019 publication I
Appendix 8: Phys Meas 2019 publication II
Appendix 9: IEEE TMI 2019 submitted
Appendix 10: IEEE TBioCAS 2019 submitted

Signal-to-Noise Ratio Analysis of a Phase-Sensitive Voltmeter for Electrical Impedance Tomography

Ethan K. Murphy, Mohammad Takhti, *Student Member, IEEE*, Joseph Skinner, Ryan J. Halter, *Member, IEEE*, and Kofi Odame, *Senior Member, IEEE*

***Abstract*—In this paper, thorough analysis along with mathematical derivations of the matched filter for a voltmeter used in electrical impedance tomography systems are presented. The effect of the random noise in the system prior to the matched filter, generated by other components, are considered. Employing the presented equations allow system/circuit designers to find the maximum tolerable noise prior to the matched filter that leads to the target signal-to-noise ratio (SNR) of the voltmeter, without having to over-design internal components. A practical model was developed that should fall within 2 dB and 5 dB of the median SNR measurements of signal amplitude and phase, respectively. In order to validate our claims, simulation and experimental measurements have been performed with an analog-to-digital converter (ADC) followed by a digital matched filter, while the noise of the whole system was modeled as the input referred at the ADC input. The input signal was contaminated by a known value of additive white Gaussian noise (AWGN) noise, and the noise level was swept from 3% to 75% of the least significant bit (LSB) of the ADC. Differences between experimental and both simulated and analytical SNR values were less than 0.59 and 0.35 dB for RMS values $\geq$ 20% of an LSB and less than 1.45 and 2.58 dB for RMS values $<$ 20% of an LSB for the amplitude and phase, respectively. Overall, this study provides a practical model for circuit designers in EIT, and a more accurate error analysis that was previously missing in EIT literature.**

***Index Terms*—Analog-to-digital converter (ADC), digital voltmeter, electrical impedance imaging, matched filter, random noise.**

I. Introduction

IMAGE reconstruction in electrical impedance tomography (EIT) aims to estimate the spatially varying electrical properties within a domain from a set of boundary voltage measurements. The amplitudes and phases of these measurements carry information about the internal electrical properties, and by processing them, it is possible to estimate the spatial distribution of conductivity and permittivity. Recently, EIT has been considered in a number of medical applications, and it is attractive due to its affordability, its safe non-ionizing radiation-based nature [1], and its potential for portability and miniaturization [2]–[4]. A positive trend towards EITs acceptance in medical imaging is the release of several commercial systems for lung ventilation and perfusion monitoring applications [5].

One challenge with EIT is that the image reconstruction problem is poorly conditioned and ill-posed, meaning that the boundary voltage measurements must be read out at signal-to-noise ratios (SNRs) as high as 90 dB [6]. Insufficiently high SNR makes the different impedance distributions indistinguishable from each other, resulting in EIT images that are of limited clinical value. Ordinarily, these SNR levels have challenging power and area implications for the circuit integration of a multi-channel, multi-MHz signal application such as EIT.

Fortunately, the EIT readout chain incorporates a matched filter, which makes high SNR achievable even with relatively low-precision circuit components [7]–[9]. For instance, depending on electronic circuit noise levels and the number of taps in the matched filter, a 10 bit resolution analog-to-digital converter (ADC) is sufficient for 96 dB SNR. Previous investigators (e.g., [9], [10]) have recognized this possibility, but their results do not completely take into account how electronic noise and quantization error will interact to affect SNR. Further, previous work has rarely considered the SNR of phase measurements, focusing only on amplitude. It is difficult for the circuit designer to use these previous results to make proper trade-offs and decisions between various circuit specifications to try to meet EIT performance goals. Although EIT relies on in-phase and quadrature (or real and reactive) components for performing reconstructions, we concern ourselves here with analyzing the SNR of the amplitude and phase because these are important for analyzing system performance ([11]) and in calibrating an EIT system ([6], [12]).

In this paper, we formulate the SNR of both the extracted amplitude and phase of the matched filter considering both quantization and additive electronic noise of the system. An analytic and two approximate models are developed. The approximate models are referred to as the Discrete Uniform (DU) and Continuous Uniform (CU) models. Based on simulations (validated through measurements), the DU model should fall within 2 dB and 5 dB of the median SNR measurements of signal amplitude and phase, respectively, and the CU model should fall within 6.5 dB and 11 dB of the median SNR measurements of signal amplitude and phase, respectively. Thus a circuit designer could use the, more accurate, DU model to translate a target SNR to circuit-level specifications that incorporate various parameters including electronic noise budget, ADC resolution, and number of filter taps of the matched filter. Therefore, the designer can

Manuscript received December 22, 2015; revised April 10, 2016 and July 13, 2016; accepted August 1, 2016. Date of publication November 10, 2016; date of current version March 22, 2017. This work was supported in part by the U.S. National Science Foundation (NSF) under Grant IIS-1418497, and by the U.S. National Institutes of Health under Grant 5R01CA143020, National Science Foundation under Grant 1418497, and US DoD CDMRP Grant W81XWH-15-1-0571. This paper was recommended by Associate Editor S. Chakrabartty.

The authors are with the Thayer School of Engineering, Dartmouth College, Hanover, NH 03755 USA (e-mail: ethan.k.murphy@dartmouth.edu; mohammad.takhti.th@dartmouth.edu).

Color versions of one or more of the figures in this paper are available online at http://ieeexplore.ieee.org.

Digital Object Identifier 10.1109/TBCAS.2016.2601692

1932-4545 © 2016 IEEE. Personal use is permitted, but republication/redistribution requires IEEE permission.
See http://www.ieee.org/publications_standards/publications/rights/index.html for more information.

budget the noise between different blocks prior to the matched filter, without having to over-design the system.

Determining SNR in terms of circuit-level specification is not unique to EIT; numerous works have studied closely related problems. Quantization noise due to an ADC has been thoroughly explored beginning around 1947 [13], [14]. Error propagation of noisy signals through an ADC has been considered in the area of signal processing [15], where it is referred to as non-subtractive dither. In [15], a simple expression, which corresponds to our Continuous Uniform (CU) model, is described and analyzed for when it is technically applicable. As they considered dither, noise produced from a user-specified probability distribution, their results are not directly applicable in the case of Gaussian additive noise. Error modeling and analysis of digital matched filters is also well-studied in signal-processing literature, e.g., [16], but our particular signal, additive noise (distribution and range), ADC, and matched filter appear to have not been considered.

The remainder of this paper is organized as follows; Section II describes amplitude and phase extraction using a matched filter, Section III discusses the noise resulting from analog and mixed-signal circuits, Section IV presents the analytic expressions for the SNR, and Section V discusses the DU model and its utility. The analytic model and our simulation code are validated by a set of measured data (Section IV-B), and two sets of example curves produced by the DU model illustrate how the model can aid in circuit design (Section V). Although the analytic model is very accurate, it would be unpractical to use prior to circuit construction. However, the DU model provides a real practical SNR formula that could help circuit designers achieve an SNR tolerance. Overall, the DU model yields a specific and accurate SNR formulation that provides a practical use and error description that was missing in the EIT literature.

II. Amplitude and Phase Extraction

In EIT, a low-amplitude sinusoidal current of frequency f Hz is injected into the tissue via a pair of electrodes. This injected current results in a set of boundary voltages developing across the surface of the tissue, each of which is measured with phase-sensitive voltage readout circuitry. The readout circuit provides both amplitude (A) and phase (ϕ) information, based on the in-phase and quadrature ('I' and 'Q') components of the time-dependent boundary voltage, $V_{\mathrm{BND}}(t)$

$$\begin{aligned} V_{\mathrm{BND}}(t) &= A\sin(2\pi ft+\phi) \\ &= \underbrace{A\cos(\phi)}_{V_I}\sin(2\pi ft) + \underbrace{A\sin(\phi)}_{V_Q}\cos(2\pi ft). \end{aligned} \quad (1)$$

The I/Q components, V_I and V_Q, can be extracted by multiplying the boundary voltage with orthogonal sinusoidal signals and integrating over one period, $T = 1/f$. This yields

$$V_I = \frac{2}{T}\int_0^T V_{\mathrm{BND}}(t)\sin(2\pi ft) = A\cos(\phi) \quad (2)$$

$$V_Q = \frac{2}{T}\int_0^T V_{\mathrm{BND}}(t)\cos(2\pi ft) = A\sin(\phi). \quad (3)$$

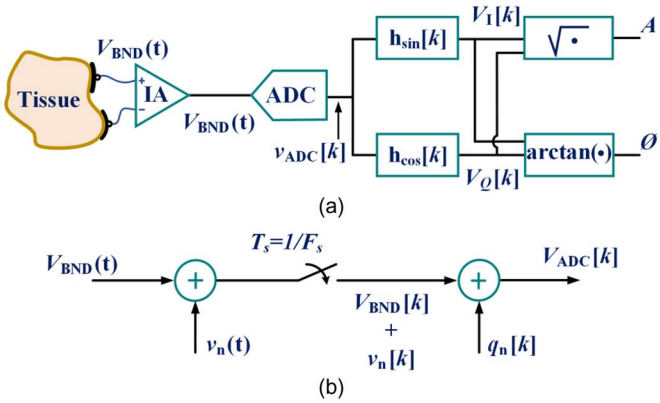

Fig. 1. (a) Simplified block diagram of a typical EIT readout channel. (b) Detail of the signal processing chain from the instrumentation amplifier (IA) input to the ADC output. The boundary voltage $V_{\mathrm{BND}}(t)$ is corrupted by electrical noise, $v_n(t)$. This noisy signal is sampled by the ADC at a rate of F_s. Finally, the sampled signal is converted to the digital value $V_{\mathrm{ADC}}[k]$, by adding a quantization noise term, $q_n[k]$.

In general, more than one period can be sampled; through averaging this can increase the SNR of the measurements. From the I/Q components, the amplitude and phase of the boundary voltage can be calculated as

$$A = \sqrt{V_Q^2 + V_I^2} \quad (4)$$

$$\phi = \arctan\left(\frac{V_Q}{V_I}\right). \quad (5)$$

Any errors in the readout circuit will affect how precisely we can measure these amplitude and phase values. In turn, measurement precision is a major factor in determining the imaging quality of the EIT system as a whole. The remainder of this paper will explore the relationship between circuit-level error and overall measurement precision. Practically, this is explored by finding the SNR of the output signal. The primary effort is in the calculation of the (variance of the) noise.

III. Noise From Analog and Mixed-Signal Circuits

Fig. 1(a) is a simplified diagram of a typical EIT readout circuit. The boundary voltage, V_{BND}, is sensed on a pair of electrodes and amplified by an instrumentation amplifier. The amplified voltage is then converted to a digital signal with an ADC. A pair of digital filters perform the I/Q extraction and additional processing calculates the amplitude and phase of the signal.

The instrumentation amplifier and the analog components of the ADC both produce random electronic noise from their component devices. The noise from all of these sources can be lumped together and modeled as a single additive white Gaussian noise (AWGN) voltage signal, $v_n(t)$, that is referred to the input of the ADC [see Fig. 1(b)]. This is a common assumption. The flicker noise and the corner frequency vary from design to design, since it is device and design dependent, and can be lowered by proper design and circuit techniques [17]. The $1/f$ corner frequency reported for commercial amplifiers shows the corner frequency as low as 500 Hz for CMOS amplifiers [18]. In EIT, $1/f$ noise can be likely ignored based on the moderately high current frequencies (1 kHz–10 MHz).

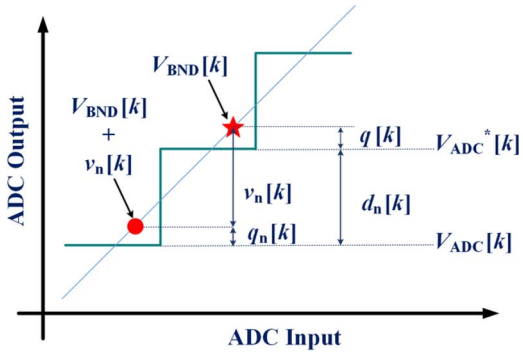

Fig. 2. Illustration of the two equivalent descriptions of the random system and quantization (ADC) noise. The ADC output is $V_{\mathrm{ADC}}[k]$, which is a quantized version of the sampled noisy input, $V_{\mathrm{BND}}[k] + v_n[k]$. If the ADC input were clean, then its output would be $V^*_{\mathrm{ADC}}[k]$, which is a quantized version of $V_{\mathrm{BND}}[k]$. The difference between this theoretical, clean ADC output and the actual (noisy) ADC output is the discrete noise term, $d_n[k]$. So, $V_{\mathrm{ADC}}[k]$ can also be written as the sum of $d_n[k]$ and $V^*_{\mathrm{ADC}}[k]$.

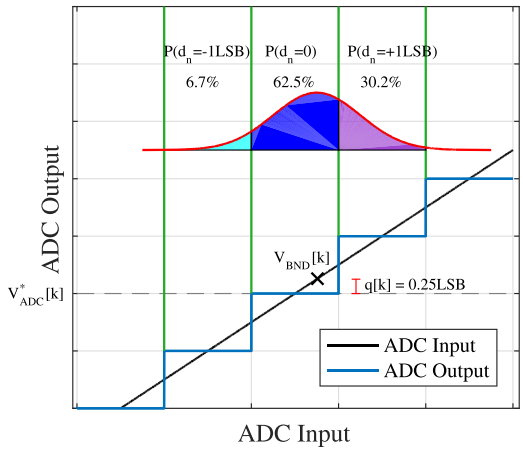

Fig. 3. Illustration of the effect that the random noise, $v_n[k]$, has on the ADC output. In this example, the signal $V_{\mathrm{BND}}[k]$ should ideally result in an output of $V^*_{\mathrm{ADC}}[k]$, which is 0.25 LSB away and is the closest ADC quantization level. However, the presence of the random noise term, $v_n[k]$, can cause the ADC output to "jump" by some multiple of an LSB away from the ideal clean output. The probability of a +1 LSB jump is 30.2%, and the probability of a -1 LSB jump is 6.7%. Also, it is possible (62.5% probability) that there will be no jump at all, and that the random noise term has no effect, ultimately, on the ADC output. The random noise $v_n[k]$ is assumed to have a normal distribution with zero mean and a standard deviation of 0.5 an LSB.

It is common to assume that electronic noise (assumed predominately to be from thermal sources) is AWGN [19], and the practice of combining different noise sources into a single term is a standard approach [19], [20]. We note that noise due to current or tissue sources are not explicitly considered in this study.

The AWGN noise is added to the otherwise clean signal, $V_{\mathrm{BND}}(t)$, and sampled by the ADC to produce $V_{\mathrm{BND}}[k] + v_n[k]$, where k is a discrete time index. The ADC then quantizes the sampled signal, which is equivalent to adding quantization noise, $q_n[k]$, to the signal. Thus, the output of the ADC can be written as

$$V_{\mathrm{ADC}}[k] = V_{\mathrm{BND}}[k] + q_n[k] + v_n[k] \tag{6}$$

where $v_n[k]$ and $q_n[k]$ are both continuous valued, random variables, with $q_n[k]$ dependent on $V_{\mathrm{BND}}[k]$ and $v_n[k]$.

Fig. 2 presents an equivalent, perhaps more tractable model of the k'th ADC output. In this model, we can think of the ADC output as the sampled clean input plus two error terms

$$V_{\mathrm{ADC}}[k] = V_{\mathrm{BND}}[k] + q[k] + d_n[k]. \tag{7}$$

Here, $q[k]$ is a quantization error that is completely deterministic; it is the difference between the clean input sample, $V_{\mathrm{BND}}[k]$ and the closest ADC quantization level, $V^*_{\mathrm{ADC}}[k]$ from Fig. 2. The second error term, $d_n[k]$ is a discrete-valued random variable of the form mLSB, where m is an integer and LSB is the least significant bit. The LSB for a b-bit ADC is defined by LSB $= V_{FS}/2^b$, where V_{FS} is the full-scale voltage. For a derivation of (7) see Appendix A.

The main advantage of expressing $V_{\mathrm{ADC}}[k]$ with (7) is that it expresses the error as a single random variable, d_n, as opposed to two correlated random variables ($q_n[k]$ and $v_n[k]$ in (6)). This means that the amount of noise in $V_{\mathrm{ADC}}[k]$ is simply given by the variance of $d_n[k]$, i.e.,

$$\begin{aligned}\mathrm{var}\left(V_{\mathrm{ADC}}[k]\right) &= \mathrm{var}\left(d_n[k]\right) \\ &= \sum_{m=-\infty}^{\infty} P\left(d_n[k] = m\mathrm{LSB}\right)\left(m\mathrm{LSB} - E\left[d_n[k]\right]\right)^2\end{aligned} \tag{8}$$

where $E[d_n[k]]$ is the expected value of $d_n[k]$, and $P(d_n[k] = m\mathrm{LSB})$ is the probability that $d_n[k]$ is equal to mLSB. We note that (8) is the definition of variance for a discrete random variable [21]. Since $q[k]$ is deterministic it has a variance of zero, and therefore does not contributed to $\mathrm{var}(V_{\mathrm{ADC}}[k])$.

Studying Fig. 2, we see that $d_n[k]$ is a discretization of the random and quantization error. We assume the random error $(v_n[k])$ to be normally distributed with a standard deviation of σ_n. Incorporating the deterministic error $q[k]$ into the random error $(v_n[k])$ is equivalent to offsetting its mean by $q[k]$. Thus the probability of $d_n[k]$ attaining a given value mLSB is determined by evaluating the probability of the normal error $(v_n[k])$ offset by the quantization error $q[k]$ being within the interval $[(m-0.5)\mathrm{LSB}, (m+0.5)\mathrm{LSB}]$, i.e., $P(d_n[k] = m\mathrm{LSB})$ is given by

$$\begin{aligned}&P\left(d_n[k] = m\mathrm{LSB}\right) \\ &\quad = P\left((m-0.5)\mathrm{LSB} < v_n[k] - q[k] < (m+0.5)\mathrm{LSB}\right) \\ &\quad = \frac{1}{\sigma_n\sqrt{2\pi}} \int_{(m-0.5)\mathrm{LSB}}^{(m+0.5)\mathrm{LSB}} \exp\left(\frac{-\left(x - q[k]\right)^2}{2\sigma_n^2}\right) dx\end{aligned} \tag{9}$$

where the variable x in the integral represents the random normal error $v_n[k]$, and the last line of (9) follows from the previous line by definition ([21]) given that $v_n[k]$ is an AWGN with standard deviation σ_n.

Fig. 3 provides an additional illustration of how the error is modeled. It shows the continuous probability distribution function (pdf) of the input random error, $v_n[k]$, offset by the deterministic error, $q[k]$, and the resulting discrete probability mass function (pmf) that represents the distribution of the output random error, $d_n[k]$, of the ADC. This illustrates the dependence of $d_n[k]$ on the width of the normal error and the offset location due to the deterministic error.

IV. Signal-to-Noise Ratio in a Phase-Sensitive Measurement System

To predict the SNR that we can expect from the readout circuit, we will consider the noise signal, $d_n[k]$, and how it propagates through the I/Q extraction to the final amplitude and phase measurements.

The SNR of the amplitude and phase of the whole chain shown in Fig. 1 can be found using the following:

$$\mathrm{SNR}_{A\backslash\phi} = 10\log_{10}\frac{(\bar{V}^2_{A\backslash\phi})}{\mathrm{var}(A\setminus\phi)} \tag{10}$$

where $\bar{V}_{A\backslash\phi}$ and $\mathrm{var}(A\setminus\phi)$ are the mean and variance, respectively, of the amplitude and phase. In the remainder of this section, equations for the amplitude and phase SNRs will be defined by finding the mean and variance of the amplitude and phase, and these equations are compared to the SNR from a set of measured data. In order to find the aforementioned mean and variance values, one needs to first calculate the mean and variance of the in-phase and quadrature components.

A. SNR Using the Analytical Model

Fig. 1 showed the I/Q extraction being performed in the digital domain; implementing the I/Q extraction in its original continuous-time form ((2) and (3)) would require costly, high-precision analog components. Instead, low cost, digital matched filters are used to approximate V_I and V_Q via

$$V_I = \frac{2}{N}\sum_{k=0}^{N-1} V_{\mathrm{ADC}}[k]\cdot\sin\left(\frac{2\pi fk}{F_{\mathrm{s}}}\right) \tag{11}$$

$$V_Q = \frac{2}{N}\sum_{k=0}^{N-1} V_{\mathrm{ADC}}[k]\cdot\cos\left(\frac{2\pi fk}{F_{\mathrm{s}}}\right) \tag{12}$$

where F_s is the ADC sample rate and N is the number of sample points in one period of the input signal, i.e., for this situation N is also the number of matched filter taps. The amount of noise in the calculated V_I and V_Q signals is given by

$$\mathrm{var}(V_I) = \frac{4}{N^2}\sum_{k=0}^{N-1}\mathrm{var}\left(d_n[k]\right)\cdot\sin^2\left(\frac{2\pi fk}{F_s}\right) \tag{13}$$

$$\mathrm{var}(V_Q) = \frac{4}{N^2}\sum_{k=0}^{N-1}\mathrm{var}\left(d_n[k]\right)\cdot\cos^2\left(\frac{2\pi fk}{F_s}\right). \tag{14}$$

Here, we have used the fact (8) that $\mathrm{var}(V_{\mathrm{ADC}}[k]) = \mathrm{var}(d_n[k])$ and the assumption that the variances, $d_n[k]$, are uncorrelated (white).

Recalling (4), the variance of the amplitude is

$$\begin{aligned}\mathrm{var}(A) &= \mathrm{var}\left(\sqrt{V_Q^2+V_I^2}\right)\\ &\approx \mathrm{var}(V_I)\cos^2(\phi)+\mathrm{var}(V_Q)\sin^2(\phi)\\ &\quad+2\mathrm{cov}(V_I,V_Q)\cos(\phi)\sin(\phi)\end{aligned} \tag{15}$$

where we have linearized the function $\sqrt{x^2+y^2}$, on the assumption that the in-phase and quadrature noise is sufficiently small. Appendix B shows the details of our derivation. Similarly, using (5), we write the variance of the phase as

$$\begin{aligned}\mathrm{var}(\phi) &= \mathrm{var}\left(\arctan\left(\frac{V_Q}{V_I}\right)\right)\\ &\approx \frac{1}{A^2}\left(\mathrm{var}(V_I)\sin^2(\phi)+\mathrm{var}(V_Q)\cos^2(\phi)\right.\\ &\quad\left.-2\mathrm{cov}(V_I,V_Q)\cos(\phi)\sin(\phi)\right).\end{aligned} \tag{16}$$

Here, too, we have used a linearization approach to arrive at a simple expression (see Appendix C for details). Further, details of the calculation of the covariance $(\mathrm{cov}(V_I,V_Q))$ are given in Appendix D.

From (15) and (16), the SNR for the amplitude and phase using (10) are therefore

$$\begin{aligned}\mathrm{SNR}_A &= 10\log_{10}(A^2)\\ &\quad-10\log_{10}\left[\mathrm{var}(V_I)\cos^2\phi+\mathrm{var}(V_Q)\sin^2\phi\right.\\ &\quad\left.+\ 2\mathrm{cov}(V_I,V_Q)\cos(\phi)\sin(\phi)\right]\end{aligned} \tag{17}$$

$$\begin{aligned}\mathrm{SNR}_\phi &= 10\log_{10}(\phi^2A^2)\\ &\quad-10\log_{10}\left[\mathrm{var}(V_I)\sin^2\phi+\mathrm{var}(V_Q)\cos^2\phi\right.\\ &\quad\left.-\ 2\mathrm{cov}(V_I,V_Q)\cos(\phi)\sin(\phi)\right].\end{aligned} \tag{18}$$

Equations (17) and (18) are purely analytical models to predict the SNR of the amplitude and phase measurements. The model depends on the amount of electronic noise, the ADC resolution, the number of matched filter taps, and the phase of the measured voltage. Therefore, if we wanted to characterize the SNR performance of an EIT system, then we could use this model as a reasonably accurate check against experimental measurement results.

B. Comparison to Measured Data

Fig. 4 are the results of comparing the analytical models, (17) and (18), to measured and simulated data. The DU and CU Models, discussed in detail in the following section, are also included in Fig. 4 for comparison. The measured and simulated SNR values are determined by calculating the mean and standard deviation values of amplitude and phase using (10). The measurement setup involved an evaluation board with an Analog Devices AD7760 24-bit sigma delta ADC, which was chosen to guarantee that the ADC has a very low-level thermal noise ($< 0.38\ \mu V_{\mathrm{rms}}$), much lower than the noise input by the signal generator. A signal generator (Agilent 33522A) input a sinusoidal signal with a frequency of 3.125 kHz (f) and a full-scale voltage, V_{FS} of 6.42 V. The effective sampling frequency was 78.125 kHz (F_S) based on the sampling frequency of 20 MHz and a decimation rate of 256 on the evaluation board. This results in 25 equally spaced points per period (N). A total of $5,000$ periods were sampled for each measurement set, i.e., these were used to numerically calculate the mean and variance in (10). White Gaussian noise was added to the signal with RMS values (σ_n) ranging from 0.5% to 75% of a 7-bit LSB using the same signal generator. The measurements

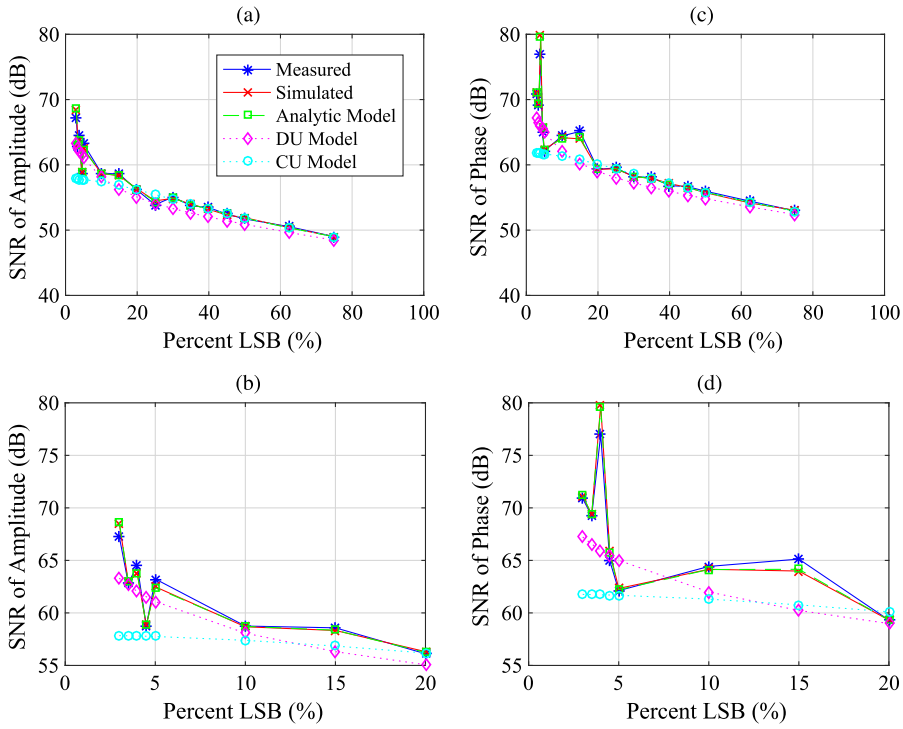

Fig. 4. Comparison of amplitude and phase SNR versus RMS for measured data, simulated data, and the analytic, DU, and CU models. (a) and (c) show ranges from 3–100%, whereas (b) and (d) zooms in on the range of 3–20%.

were reduced to 7-bit values using a straightforward reduction in bit depth using Matlab. We focus on the percent LSB of white noise error, because this is the most significant factor in how the error distribution varies. The minimum noise added to the signal corresponded to 0.5% an LSB or 0.251 mVrms, where the LSB is given by $50.156\,\text{mV} = 6.42/2^7\,\text{V}$. In order to produce 0.5% LSB increments the signal generator added noise in minimum increments of 1.154 mVrms with a bandwidth of 2.048 MHz, and a low-pass filter was used to remove noise above 64.0591 kHz. Thus reducing in-bandwidth noise. An antialiasing filter on the evaluation board of the ADC, which had a cut-off frequency of 6.97 MHz, was also used. This prevented possible folding of the noise. The simulated data was constructed in Matlab using a 7-bit sinusoidal signal with the same frequency, sampling frequency, number of samples, and added noise as the measured data.

In Fig. 4 one can see very good agreement for RMS values 20% of an LSB and higher. Specifically, maximum absolute differences between all combinations of analytic, simulated, and measured data is less than 0.59 dB and 0.35 dB for amplitude and phase measurements, respectively. For RMS values less than 20% an LSB the differences between measured and analytic data (or simulated) increases, but are less than 1.45 and 2.58 dB for amplitude and phase, respectively. The differences between simulated and analytic SNR values are less than 0.25 dB over all RMS values. The non-smooth aspects of the curves at low RMS values are due to different phase values (i.e., different deterministic quantization errors across different RMS values), which was due to the fact that the phase of the input signal was not explicitly set. Small deviations between measured and simulated (or the analytic model) appear due to phase drifts and DC offsets in the data that could not be entirely removed.

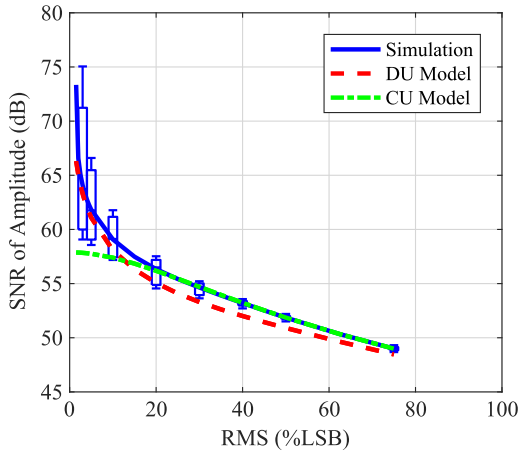

Fig. 5. Illustration of the SNR amplitude corresponding to the DU and CU models and calculated from 5,000 simulated noisy input signals which uniformly vary phase from 0 to 90 degrees with RMS values ranging from 3–75% an LSB. The input signal assumes the same scenario as the measured scenario (Fig. 4).

V. Determining Circuit-Level Specifications to Meet a SNR Target

Beyond its use to verify measurement results, the model of (17) and (18) would be a powerful design tool, if, given a target SNR, it could provide a corresponding set of required circuit design specifications (e.g., noise budget, ADC resolution, number of filter taps) that must be met. Unfortunately, (17) and

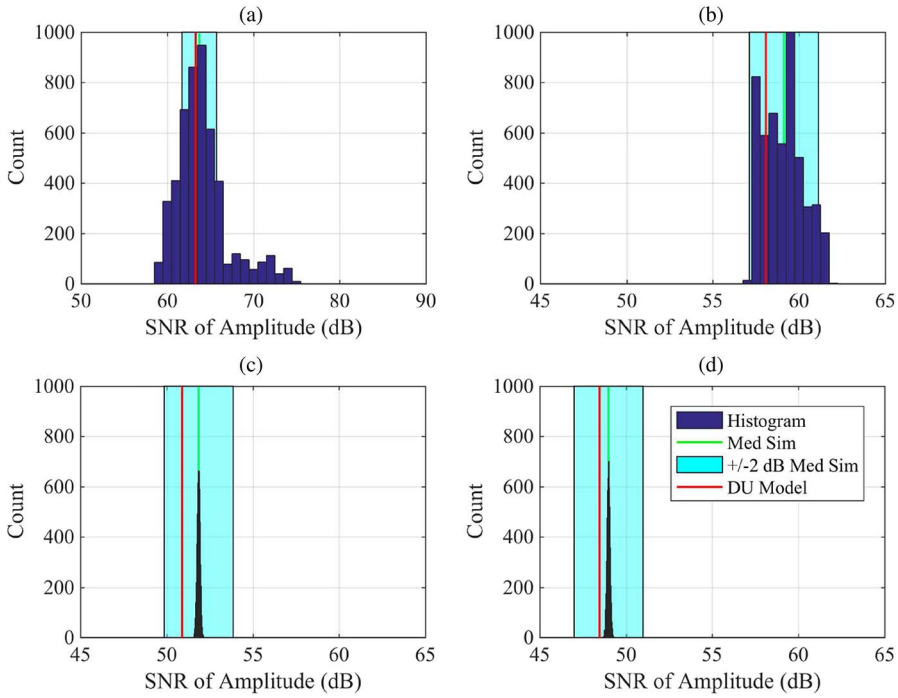

Fig. 6. Illustration of the distribution of the amplitude SNR for RMS values of 3%, 10%, 50%, and 75% of an LSB. The DU model falls within +/−2 dB of the median (Med) SNR. The distributions were constructed from 5,000 SNR values calculated from simulated (Sim) noisy signals with phase values uniformly ranging from 0 to 90 degrees. The input signal assumes the same scenario as the measured scenario (Fig. 4). (a) RMS $= 3\%$ an LSB. (b) RMS $= 10\%$ an LSB. (c) RMS $= 50\%$ an LSB. (d) RMS $= 75\%$ an LSB.

(18) are unhelpful in this regard, because they are based on (9), which depends on the phase of a boundary voltage that will be known only *after* the circuit has been designed and deployed in a functioning EIT system.

Even though the individual sample values are unknown during circuit design, we do have an idea about their statistics. In particular, we know that the quantization error resembles a random variable with a uniform distribution between -0.5 LSB and 0.5 LSB. We refer to this as the Discrete Uniform (DU) model. Using this assumption, we can recalculate the probability function (9) giving us

$$P\left(d_n^{DU} = m\text{LSB}\right) = \frac{1}{\text{LSB}} \int_{-\text{LSB}/2}^{+\text{LSB}/2} \frac{1}{\sigma_n\sqrt{2\pi}} \times \int_{(m-0.5)\text{LSB}}^{(m+0.5)\text{LSB}} \exp\left(\frac{-(x-z)^2}{2\sigma_n^2}\right) dxdz \quad (19)$$

where we have averaged (integrated) over all possible $q[k]$ values, which also has the effect of removing the dependence on k. In (19), z is associated with $q[k]$ and x is associated with $v_n[k]$. Next, one can calculate the variance of the error in the DU model, $\text{var}(d_n^{DU})$ similarly to (8). Since there is no longer a k dependence, (13) and (14) simplify to

$$\text{var}\left(V_{I/Q}^{DU}\right) = 2/N \times \text{var}\left(d_n^{DU}\right) \quad (20)$$

and the covariance term, $\text{cov}(V_I, V_Q)$, is zero. The covariance is zero because once the d_n terms can be pulled out of the summations in (A.21) and (A.24) the sine and cosine terms sum to zero. Thus the SNR equations of the DU model are given by

$$\text{SNR}_A^{DU} = 10\log_{10}\frac{A^2\left(\frac{N}{2}\right)}{\text{var}\left(d_n^{DU}\right)} \quad (21)$$

$$\text{SNR}_\phi^{DU} = 10\log_{10}\frac{\phi^2\left(\frac{A^2N}{2}\right)}{\text{var}\left(d_n^{DU}\right)}. \quad (22)$$

Given a particular set of design parameters, the DU model of (21) and (22) is able to predict a reasonably representative value for SNR (Figs. 4 and 5). The actual SNR might vary over a wide range, but in practice (and in our simulated experiments) it is expected to fall within ± 2 dB of the median value; the DU model provides an estimated SNR that is within this window (see Fig. 6). As the SNR can vary due to the phase of the signal, this bound was determined by investigating simulations of SNR based on 5,000 phase values uniformly ranging from 0 to 90 degrees with all other parameters taken to be the same as the measured scenario (Section IV-B). Therefore, a circuit designer can use this model to translate a target SNR to circuit-level specifications. Fig. 7 illustrates two sets of curves that show the various combinations of electronic noise budget (RMS), ADC resolution and number of filter taps (N) that could be used to achieve an SNR of 80 dB. Specifically, Fig. 7(a) compares an 8-, 10-, and 12-bit ADC with $N = 25$, and, Fig. 7(b) compares 10, 100, and 1,000 filter taps for a 10-bit ADC. Both plots consider RMS values ranging from 10 μV to 10 mV, which covers 1–100% an LSB for each curve. We note that Figs. 5–7 illustrate SNR of the amplitude but similar properties and utility are applicable for the phase. The phase has a bound of ± 5 dB

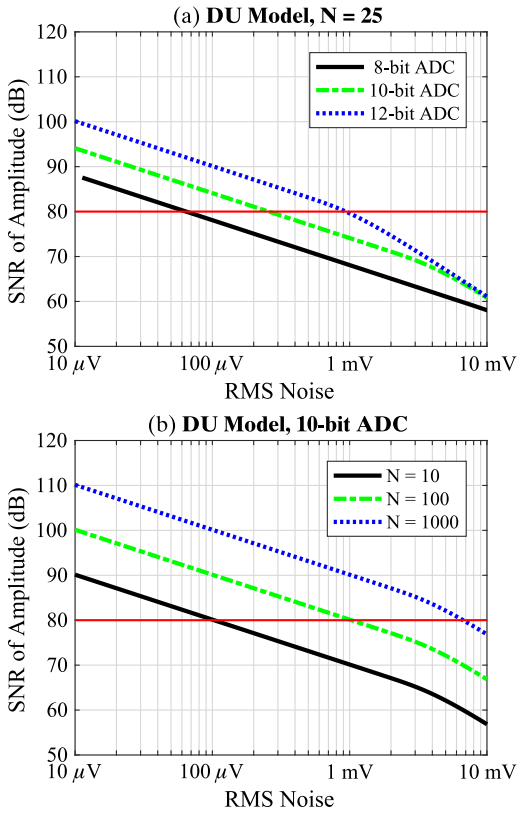

Fig. 7. Different combinations of circuit-level design choices that will achieve a measurement precision of 80 dB SNR. (a) A 10-bit ADC, followed by a 25-tap matched filter, can meet the 80 dB SNR specification as long as the total circuit noise (input-referred to the ADC) is 300 μV_{rms} or less. With the same 25-tap matched filter, a 12 bit ADC design can tolerate up to 1 mV_{rms} of noise and still meet the SNR target. (b) The number of taps in the matched filter can be traded off with the amount of circuit noise in order to achieve a desired SNR target. In this example with a 10 bit ADC, a system with a 10 tap filter would require a total noise level(input-referred to the ADC) of 100 μV_{rms} or less in order to achieve 80 dB SNR. Increasing the number of filter taps (and hence ADC sampling rate) by a factor of 100 will relax the noise specification to 6 mV_{rms}.

tolerance based on simulations as opposed to the ± 2 dB for the amplitude.

It is worth mentioning an alternative simplified model that can be constructed from two points of view. First, one can construct the model directly considering the sampled signal $V_{\text{ADC}}[k]$, assuming that the error terms $v_n[k]$ and $q_n[k]$ are independent of each other, the quantization error $q_n[k]$ is uniformly-distributed error over $-$LSB/2 to LSB/2, and $v_n[k]$ is a normally distributed error with a variance of σ_n^2. Alternatively, one can arrive at this model by taking the DU model but allowing for continuous output values, as opposed to discrete LSB factors. We refer to this simplified model as the Continuous-Uniform (CU) model. The variance of the CU model is given by

$$\text{var}\left(d_n^{CU}\right) = \text{LSB}^2/12 + \sigma_S^2 \tag{23}$$

which was the modeling approach used in [15] for a similar problem. The SNR formulae for the CU model is equivalent to the DU model, i.e., (21) and (22), except one needs to substitute in (23) in place of $\text{var}(d_n^{DU})$. As a further connection between the CU and DU model, one could interpret the double integrals in (19) as the convolution of two pdfs, which is equivalent to the addition of two random variables, e.g.,

$$P\left(d_n^{DU} = m\text{LSB}\right) = P\left(m - \frac{1}{2} < \frac{d_n^{CU}}{\text{LSB}} < m + \frac{1}{2}\right). \tag{24}$$

Figs. 4 and 5 shows the predicted SNR values using this model compared to the measurement data and a large set of simulated data and the DU model, respectively. Based on the simulation results, the CU model is expected to fall within 6.5 dB and 11 dB of the median SNR measurements of signal amplitude and phase, respectively. More specifically, the CU model is very accurate for high levels of noise, but substantially underestimates the SNR for lower levels of noise. For instance, the differences between the CU model and the mean simulated SNR amplitude values are less than 0.16 dB for RMS values $\geq 20\%$ an LSB, and the maximum difference for RMS values $< 20\%$ an LSB is 6.3 dB. In contrast, the analytic model and the DU model developed are accurate across all levels of noise (see Fig. 4). Quantitatively the difference between simulated data and the analytic model is less than 0.25 dB across all RMS values considered, and for the DU model the differences between the simulated mean and DU model from Fig. 5 are less than 1.35 dB over all RMS values considered. However, we note that if one is interested in larger % LSB RMS values (say greater than 20%), then the CU model may be desirable to use because of its added simplicity and its better accuracy in this error region. The CU model is more accurate than the DU model for RMS values greater than 20% an LSB (Fig. 4) because at these noise levels it is more accurate to assume that the AWGN is independent of the ADC noise (CU model) than to consider discrete mLSB-valued noise (DU-model). Further, in the low RMS region ($< 20\%$ an LSB) the DU model is more accurate, which implies the discrete mLSB-valued noise is a better assumption. We note the region of low RMS (thermal) noise is important for applications that use low- to moderate-resolution ADCs, since these are not thermal noise limited [22].

VI. Conclusion

In conclusion this study has derived an analytical model to accurately describe the SNR of the amplitude and phase of an EIT measurement that considers both quantization caused by the ADC and additive system noise (prior to the ADC) that was not previously described in EIT literature. The analytical model (and our simulation code) was validated by a set of measured data. Furthermore, a practical model (DU model) was developed that a circuit designer could use as a tool to translate a target SNR to circuit-level specifications. The models developed here are being used in the design and development of analog readout front ends for an EIT system. Use of these tools within this design process will be reported.

Appendix A
Detailed Derivation of (7)

Assume that ADC$(\cdot)$ is a function denoting the ADC process. The output of the ADC is given by

$$V_{\text{ADC}}[k] = \text{ADC}\left(V_{\text{BND}}[k] + v_n[k]\right). \tag{A.1}$$

The deterministic error is defined as the difference between the ADC output of the noise-free input ($V^*_{\mathrm{ADC}}[k] = \mathrm{ADC}(V_{\mathrm{BND}}[k])$) and the noise-free input, i.e.,

$$q[k] = V^*_{\mathrm{ADC}}[k] - V_{\mathrm{BND}}[k]. \tag{A.2}$$

The probabilistic error is defined as the difference between the ADC output of the noisy signal and the ADC output of the noise-free signal, i.e.,

$$d_n[k] = V_{\mathrm{ADC}}[k] - V^*_{\mathrm{ADC}}[k]. \tag{A.3}$$

A simple check can verify that (A.1) is equal to $V_{\mathrm{BND}}[k]$ plus (A.2) and (A.3), which verifies and explicitly defines each term in (7).

Appendix B
Derivation of Variance of Amplitude

The amplitude is given in terms of the in-phase and quadrature component of the signal, i.e., (4). Thus we are interested in determining the following:

$$\mathrm{var}(A) = \mathrm{var}\left(\sqrt{V_I^2 + V_Q^2}\right). \tag{A.4}$$

In order to derive the variance of the amplitude, (A.4), we use two linear approximations. The first is used to approximate V_I^2 and V_Q^2, and the second is used to approximate the square root function. The linearization of $y = x^2$ centered at the point a is given by

$$y(a + \Delta x) \approx a^2 + 2a\Delta x. \tag{A.5}$$

In terms of V_I the approximation is given by

$$V_I^2 = (\bar{V}_I + e_{VI})^2 \approx \bar{V}_I^2 + 2\bar{V}_I e_{VI} \tag{A.6}$$

where the bar represents the mean of the in-phase component, and e_{VI} is the error associated with V_I. One can obtain a similar approximation for the V_Q component. Putting the approximations for V_I^2 and V_Q^2 together one has the following:

$$V_I^2 + V_Q^2 \approx \bar{V}_I^2 + \bar{V}_Q^2 + 2(\bar{V}_I e_{VI} + \bar{V}_Q e_{VQ}). \tag{A.7}$$

Next, a linear approximation to the square root function is used, centered at the point $a = \bar{V}_I^2 + \bar{V}_Q^2$. The general form of the approximation is given by

$$y(a + \Delta x) \approx \sqrt{a} + \frac{1}{2\sqrt{a}}\Delta x. \tag{A.8}$$

In our application $\Delta x = 2(\bar{V}_I e_{VI} + \bar{V}_Q e_{VQ})$. Thus inserting our specific forms of a and Δx into (A.8) we have

$$\sqrt{V_I^2 + V_Q^2} \approx \sqrt{\bar{V}_I^2 + \bar{V}_Q^2} + \frac{2(\bar{V}_I e_{VI} + \bar{V}_Q e_{VQ})}{2\sqrt{\bar{V}_I^2 + \bar{V}_Q^2}}. \tag{A.9}$$

One can now return to (A.4) by taking the variance of both sides of (A.9), i.e.,

$$\mathrm{var}(A) = \mathrm{var}\left(\sqrt{V_I^2 + V_Q^2}\right) \approx \mathrm{var}\left(\frac{\bar{V}_I e_{VI} + \bar{V}_Q e_{VQ}}{\sqrt{\bar{V}_I^2 + \bar{V}_Q^2}}\right). \tag{A.10}$$

Next by using standard identities we have

$$\mathrm{var}(A) \approx \frac{\bar{V}_I^2 \mathrm{var}(V_I) + \bar{V}_Q^2 \mathrm{var}(V_Q) + 2\bar{V}_I \bar{V}_Q \mathrm{cov}(V_I, V_Q)}{\bar{V}_I^2 + \bar{V}_Q^2} \tag{A.11}$$

where we have assumed that $\mathrm{var}(V_I) = \mathrm{var}(e_{VI})$ and $\mathrm{var}(V_Q) = \mathrm{var}(e_{VQ})$. One can then use (2) and (3), which should be equivalent to the average V_I and V_Q values, to simplify (A.11) to our final expression for the variance of the amplitude, i.e., (15).

Appendix C
Derivation of Variance of Phase

The phase derivation follows in a similar fashion. In this case we use two linear approximations in order to estimate the following:

$$\mathrm{var}(\phi) = \mathrm{var}\left(\arctan\left(\frac{V_Q}{V_I}\right)\right). \tag{A.12}$$

The first linear approximation is with regards to the ratio, V_Q/V_I, and the second is with regards to the inverse tangent function. We begin by taking a first order approximation of the function $y = 1/x$. In general, this approximation is given by

$$y(a + \Delta x) \approx \frac{1}{a} - \frac{1}{a^2}\Delta x. \tag{A.13}$$

In our case we have

$$\frac{\bar{V}_Q + e_{VQ}}{\bar{V}_I + e_{VI}} \approx \frac{\bar{V}_Q + e_{VQ}}{\bar{V}_I} - (\bar{V}_Q + e_{VQ})\frac{e_{VI}}{(\bar{V}_I)^2} \tag{A.14}$$

where e_{VI} and e_{VQ} are small errors with regard to the in-phase and quadrature components. We drop the second order term, i.e., $e_{VQ}e_{VI}/\bar{V}_I^2$. Next, using a linear approximation to the inverse tangent function, $y = \arctan(x)$, which can be written as

$$y(a + \Delta x) \approx \arctan(a) + \frac{1}{1 + a^2}\Delta x. \tag{A.15}$$

Assuming that $a = \bar{V}_Q/\bar{V}_I$, we have that

$$\arctan\left(\frac{V_Q}{V_I}\right) \approx \arctan\left(\frac{\bar{V}_Q}{\bar{V}_I}\right) + \frac{\Delta x}{1 + \left(\frac{\bar{V}_Q}{\bar{V}_I}\right)^2}. \tag{A.16}$$

Noting that $\Delta x = e_{VQ}/\bar{V}_I - e_{VI}\bar{V}_Q/\bar{V}_I^2$, we can use (A.16) to approximate (A.12) by the following:

$$\mathrm{var}(\phi) \approx \mathrm{var}\left(\frac{\left(\frac{e_{VQ}}{V_I} - \frac{e_{VI}\bar{V}_Q}{\bar{V}_I^2}\right)}{1 + \left(\frac{\bar{V}_Q}{\bar{V}_I}\right)^2}\right). \tag{A.17}$$

Pulling out the denominator from the variance, $\mathrm{var}(aX) = a^2\mathrm{var}(X)$, and performing some simple manipulation of terms

gives us

$$\mathrm{var}(\phi) \approx \left(\frac{\bar{V}_I^2}{\bar{V}_I^2+\bar{V}_Q^2}\right)^2 \mathrm{var}\left(\frac{e_{VQ}}{\bar{V}_I} - \frac{e_{VI}\bar{V}_Q}{\bar{V}_I^2}\right), \quad \frac{1}{\left(\bar{V}_I^2+\bar{V}_Q^2\right)^2}\mathrm{var}(e_{VQ}\bar{V}_I - e_{VI}\bar{V}_Q). \quad \text{(A.18)}$$

Further simplification yields the following:

$$\mathrm{var}(\phi) \approx \frac{1}{\left(\bar{V}_I^2+\bar{V}_Q^2\right)^2}\left[\bar{V}_I^2\mathrm{var}(V_Q) + \bar{V}_Q^2\mathrm{var}(V_I) - 2\bar{V}_I\bar{V}_Q\mathrm{cov}(V_I,V_Q)\right]. \quad \text{(A.19)}$$

Similar to the amplitude variance calculation, we can then use (2) and (3) to simplify (A.19) to our final expression for the variance of the phase, i.e., (16).

Appendix D
Covariance Calculation

First note the standard definition of the covariance

$$\mathrm{cov}(V_I,V_Q) = \mathrm{E}[V_IV_Q] - \mathrm{E}[V_I]\mathrm{E}[V_Q]. \quad \text{(A.20)}$$

The independent expectations of the in-phase and quadrature components, i.e., $E[V_I]$ and $E[V_Q]$, can be computed using similar equations to (13) and (14), which follows from the standard formula for the expectation from a discrete probability distribution, i.e.,

$$\mathrm{E}[V_I] = \frac{2}{N}\sum_{k=0}^{N-1}\mathrm{E}\left[d_n[k]\right]\sin\left(\frac{2\pi fk}{F_S}\right) \quad \text{(A.21)}$$

where each $\mathrm{E}[d_n[k]]$ can be calculated by the following:

$$\mathrm{E}\left[d_n[k]\right] = \sum_{m=-\infty}^{\infty}\mathrm{P}\left(d_n[k]=m\mathrm{LSB}\right)m\mathrm{LSB}. \quad \text{(A.22)}$$

The joint expectation, $\mathrm{E}[V_IV_Q]$ is calculated by the following:

$$\mathrm{E}[V_IV_Q] = \mathrm{E}\left[\left(\frac{2}{N}\sum_{k=0}^{N-1}d_n[k]\sin\left[\frac{2\pi fk}{F_S}\right]\right)\times\left(\frac{2}{N}\sum_{m=0}^{N-1}d_n[m]\cos\left[\frac{2\pi fm}{F_S}\right]\right)\right] \quad \text{(A.23)}$$

which can be simplified to

$$\mathrm{E}[V_IV_Q] = \frac{4}{N^2}\sum_{k,m=0}^{N-1}\mathrm{E}\left[d_n[k]d_n[m]\right]\times\sin\left[\frac{2\pi fk}{F_S}\right]\cos\left[\frac{2\pi fm}{F_S}\right]. \quad \text{(A.24)}$$

If k and m are different, then the errors should be independent and one can say that

$$\mathrm{E}\left[d_n[k]d_n[m]\right] = \mathrm{E}\left[d_n[k]\right]\mathrm{E}\left[d_n[m]\right]. \quad \text{(A.25)}$$

Each of the $\mathrm{E}[d_n[k]]$ can be calculated using (A.22). If k and m are the same then we need to calculate $\mathrm{E}[(d_n[k])^2]$, which was essentially already calculated in (8).

Acknowledgment

The authors would like to enumerate individual authors contributions. These contributions are as follows: E. K. Murphy developed the analytic and DU models and drafted the paper, M. Takhti worked on mathematical modeling/simulation including the deriving the CU model, and designed the measurement device, J. Skinner assembled hardware, performed measurements, and contributed to resolving phase drift issues, and R. J. Halter and K. Odame directed the research and provided important editorial and technical insights.

References

[1] R. H. Bayford, "Bioimpedance tomography (electrical impedance tomography)," *Annual Rev. Biomed. Eng.*, vol. 8, pp. 63–91, 2006.
[2] S. H. Arshad, J. S. Kunzika, E. K. Murphy, K. Odame, and R. J. Halter, "Towards a smart phone-based cardiac monitoring device using electrical impedance tomography," in *Proc. IEEE BioCAS Conf.*, Oct. 22–24, 2015.
[3] D. Holder, *Electrical Impedance Tomography*. Bristol, U.K.: Inst. Physics, 2005.
[4] D. S. Holder, "Electrical impedance tomography of brain function," in *Proc. IEEE World Automation Congress*, 2008.
[5] A. Adler *et al.*, "Whither lung EIT: Where are we, where do we want to go and what do we need to get there?" *Phys. Meas.*, vol. 33, pp. 679–694, 2012.
[6] R. J. Halter, A. Hartov, and K. D. Paulsen, "A broadband high-frequency electrical impedance tomography system for breast imaging," *IEEE Trans. Biomed. Eng.*, vol. 55, no. 2, pp. 650–659, 2008.
[7] R. W. M. Smith, I. L. Freeston, B. H. Brown, and A. M. Sinton, "Design of a phase-sensitive detector to maximize signal-to-noise ratio in the presence of Gaussian wideband noise," *Meas. Sci. Technol.*, vol. 3, pp. 1054–1062, 1992.
[8] N. Liu, G. J. Saulnier, and J. C. Newell, "A multichannel synthesizer and voltmeter for electrical impedance tomography," in *Proc. 25th Annu. Int. Conf. IEEE EMBS*, Cancun, Mexico, Sep. 17–21, 2003.
[9] N. Liu, "ACT4: A High-Precision, Multi-Frequency Electrical Impedance Tomograph," Ph.D. dissertation, Rensselaer Polytechnic Inst., Troy, NY, USA, 2007.
[10] G. Saulnier, "Hardware," in *Electrical Impedance Tomograph*, D. Holder, Ed. Bristol, U.K.: Inst. Physics, 2005.
[11] S. Kahn, P. Manwaring, A. Borsic, and R. J. Hlater, "FPGA-based voltage and current dual drive system for high frame rate electrical impedance tomography," *IEEE Trans. Med. Imaging*, vol. 34, no. 4, pp. 888–901, 2015.
[12] H. Wi, H. Sohal, A. L. McEwan, E. J. Woo, and T. I. Oh, "Multi-frequency electrical impedance tomography system with automatic self-calibration for long-term monitoring," *IEEE Trans. Biomed. Circuits Syst.*, vol. 8, no. 1, pp. 119–128, 2014.
[13] A. G. Clavier, P. F. Panter, and D. D. Grieg, "Distortion in a pulse count modulation system," *Trans. Amer. Inst. Electr. Eng.*, vol. 66, no. 1, pp. 989–1005, 1947.
[14] W. R. Bennett, "Spectra of quantized signals," *Bell Syst. Tech. J.*, vol. 27, no. 3, pp. 446–472, 1948.
[15] R. A. Wannamaker, S. P. Lipshitz, J. Vanderkooy, and J. N. Wright, "A theory of nonsubtractive dither," *IEEE Trans. Signal Process.*, vol. 48, no. 2, pp. 499–516, 2000.
[16] G. L. Turin, "An introduction to digitial matched filters," *Proc. IEEE*, vol. 64, no. 7, pp. 1092–1112, 1976.
[17] W. Sansen, *Analog Design Essentials*. New York, NY, USA: Springer, 2006.

[18] P. Lee, "Low noise amplifier selection guide for optimal noise performance," Analog Devices, Appl. Note 940, 2009.
[19] P. R. Gray *et al.*, *Analysis and Design of Analog Integrated Circuits*. Hoboken, NJ, USA: Wiley, 2001.
[20] D. A. Johns and K. Martin, *Analog Integrated Circuit Design*. Hoboken, NJ, USA: Wiley, 2008.
[21] S. M. Ross, *Introduction to Probability Models*. San Diego, CA, USA: Academic, 2000.
[22] B. Murmann, "Energy limits in A/D converters," *Proc. IEEE Faible Tension Faible Consommation*, 2013.

Ethan K. Murphy received the B.S. and M.S. degrees from Worcester Polytechnic Institute, Worcester, MA, USA, in 2002, and the Ph.D. degree in mathematics from Colorado State University, Fort Collins, CO, USA, in 2007.

Currently, he is a Research Associate at Thayer School of Engineering, Dartmouth College, Hanover, NH, USA. He has worked in industrial and academic positions since arriving at Dartmouth in 2014. His interests are in inverse problems, especially EIT, medical imaging, data fusion, and error analysis.

Mohammad Takhti (S'09) received the B.S. degree in electrical engineering from the University of Dezful, Dezful, Iran, and the M.S. degree in electrical engineering from the K. N. Toosi University of Technology (KNTU), Tehran, Iran.

Currently, he is working toward the Ph.D. degree in electrical engineering at the Thayer School of Engineering, Dartmouth College, Hanover, NH, USA. His research interests include low-power analog and mixed-mode IC design for biomedical wearable and portable applications. He was a Research Assistant in the Research Laboratory for Integrated Circuits and Systems (ICAS) at KNTU from 2007 to 2010 and an Associate Researcher from 2010 to 2013.

Joseph Skinner is a Research Engineer at the Thayer School of Engineering, Dartmouth College, Hanover, NH, USA. His primary interest is in hardware level integrated circuit layout and design. This work is most frequently applied to low power medical sensing devices in addition to other sampling systems used in medical settings.

Ryan J. Halter (M'04) is an Assistant Professor of Biomedical Engineering at the Thayer School of Engineering, Dartmouth College, Hanover, NH, USA. His research interests are in the fields of medical device development and medical imaging. He primarily focuses on exploring the use of electrical impedance spectroscopy and tomography in clinical applications including cancer detection and imaging, surgical margin assessment, and cardiac imaging.

Kofi Odame (S'06–M'08–SM'15) is an Associate Professor of Electrical Engineering at the Thayer School of Engineering, Dartmouth College, Hanover, NH, USA. His primary interest is in analog integrated circuits for nonlinear signal processing. This work has applications in low-power electronics for implantable and wearable biomedical devices, as well as in autonomous sensor systems.

Absolute Reconstructions Using Rotational Electrical Impedance Tomography for Breast Cancer Imaging

Ethan K. Murphy,* Aditya Mahara, and Ryan J. Halter

***Abstract*— A rotational Electrical Impedance Tomography (rEIT) methodology is described and shown to produce spatially accurate absolute reconstructions with improved image contrast and an improved ability to distinguish closely spaced inclusions compared to traditional EIT on data recorded from cylindrical and breast-shaped tanks. Rotations of the tank without altering the interior conductivity distribution are used to produce the rEIT data. Quantitatively, rEIT was able to distinguish two inclusions that were 1.5 cm closer together than traditional EIT could achieve for inclusions placed 2 to 3 cm from the center for the cylindrical tank, and rEIT was able to distinguish two tumor-like inclusions where traditional EIT could not reliably do so. Mathematical analysis showed that rEIT improves the number of stable singular vectors by up to 4.2 and 4.7 times than that of traditional EIT for the cylindrical and breast-shaped tanks, respectively, which is an indication of improved resolution. Direct investigations into measurements revealed minimum rotation angles that should yield data uncorrupted by noise. Two inverse approaches (one that inverts then fuses the data (I/DF) and one that fuses the data then inverts (DF/I)) and two mesh modeling approaches were considered. It was found that DF/I produces far better results compared to I/DF and a rotated-mesh approach produces further improvements. The ability to obtain improved absolute reconstructions using rEIT on a practical clinical scenario (breast-shaped tank experiment) is an important step towards using rEIT to improve previous EIT results in medical applications.**

***Index Terms*— Data fusion, electrical impedance tomography, finite element method, inverse problem, singular value decomposition.**

I. Introduction

ELECTRICAL impedance tomography (EIT) is an imaging modality that aims to estimate the electrical property distribution within a domain of interest using currents and voltages measured on the domain's boundary. It has been considered in a number of medical [1] and industrial applications [2]. Medical applications include ventilation and perfusion imaging [3], brain imaging [4], and cancer detection applied to breast [5], prostate [6], and cervical [7] tissues. It is attractive for medical applications due to its affordability, safe non-ionizing radiation-based nature [1], and potential for portability and miniaturization [8].

Several recent studies ([9]–[13]) in both industrial and medical applications have explored fusing together multiple sets of data with the objective of improving image quality. These approaches have been termed EIT with non-stationary electrodes [9], scanning EIT (SEIT) ([10], [11]), rotational EIT (rEIT) [12], and rotary planar electrical impedance mammography (RPEIM) [13]. SEIT has been applied to rotating electrodes in a tank [10] and to translating electrodes across a surface [11]. All of these techniques aim to fuse sets of traditional EIT data together in order to produce an improved image with higher resolution and accuracy. However, there are questions of how best to fuse the data and which modeling approaches should be used to maximize these improvements.

EIT is a severely ill-posed inverse problem [14], which partially explains the moderately low resolution of EIT, i.e. the low sensitivity 'far' from the electrodes limits the accuracy of the electrical property estimation. Another factor limiting the resolution is the relatively low number of measurements typically available in clinical EIT systems. This stems from the cost and complexity of designing high channel-count systems and the practical challenges of applying a large number of electrodes given a fixed surface area constrained by the anatomy being imaged; this latter challenge is especially important since larger electrodes are preferred because they increase the signal to noise ratio [15] and reduce contact impedances [16]. By combining multiple sets of measurements together these fusion EIT approaches have the potential to create a better-posed inverse problem and improve resolution without expensive/complex hardware upgrades.

There are two methods for solving the inverse problem in fusion EIT approaches. The first approach, used by ([9]–[12]), is to stack all measurements together in a single measurement vector over which the appropriate inversion is performed. Alternatively, the RPEIM approach [13] calculates the inverse reconstruction for each rotation and then fuses the data together through an averaging technique. We refer to the two methods as the data fusion then inversion (DF/I) and the inversion then data fusion (I/DF) techniques.

Manuscript received August 23, 2016; revised December 5, 2016; accepted December 12, 2016. Date of publication December 15, 2016; date of current version April 1, 2017. This work was supported in part by the U.S. National Institutes of Health under Grant 1R01CA143020-01A1 and Department of Defense Congressionally Directed Medical Research Program under Grant W81XWH-15-1-0102. *Asterisk indicates corresponding author.*

*E. K. Murphy is with the Thayer School of Engineering, Dartmouth College, Hanover, NH 03755 USA (e-mail: ethan.k.murphy@dartmouth.edu).

A. Mahara is with the Thayer School of Engineering, Dartmouth College, Hanover, NH 03755 USA (e-mail: aditya.mahara.th@dartmouth.edu).

R. J. Halter is with the Thayer School of Engineering and Geisel School of Medicine, Dartmouth College, Hanover, NH 03755 USA (e-mail: ryan.halter@dartmouth.edu).

Digital Object Identifier 10.1109/TMI.2016.2640944

0278-0062 © 2016 IEEE. Personal use is permitted, but republication/redistribution requires IEEE permission.
See http://www.ieee.org/publications_standards/publications/rights/index.html for more information.

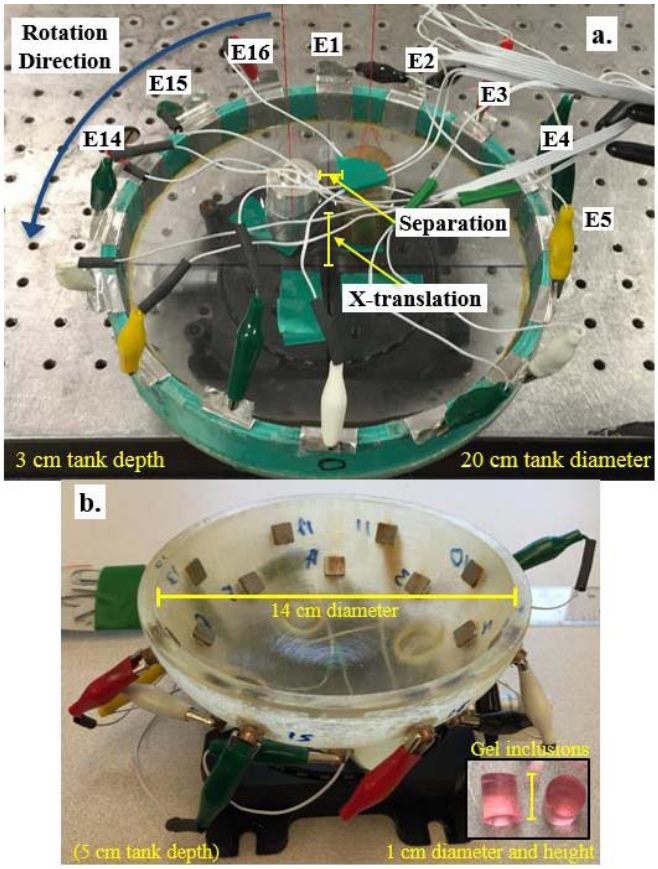

Fig. 1. Two 16-electrode tanks used in this study, a. cylindrical tank and b. a breast-shaped tank (half-ellipsoid). The tanks are rotated counter clockwise while suspended inclusions remain fixed.

For each inversion approach, the mesh used to define the domain geometry and electrodes can either be 1) a single mesh that encodes all of the electrodes from all states (or rotations) within the boundary, or 2) a single standard mesh with electrodes defined for one particular state (i.e. 0° rotation) that is transformed (or rotated) to each of the states considered. We refer to these mesh types as the 1-mesh and rotated-mesh approaches, respectively.

In this study, we explored rEIT for breast cancer imaging. Absolute reconstructions, i.e. reconstructions that estimate the true conductivity distribution of the tissue without the need of a reference measurement, are essential for this application [17]. We developed a rEIT modeling approach that achieves improved absolute reconstructions compared to traditional EIT and quantitatively assessed the improvements and limitations offered by rEIT. These improvements and limitations are evaluated through 1) analysis of the mathematical formulation of the inverse problem, 2) analysis of image reconstructions produced from rotating tank experiments (each rotation denotes an additional dataset), and 3) analysis of raw voltage measurements acquired from bench-top experiments. Although rEIT has been studied previously ([10], [12]), this study 1) appears to be the first to produce absolute images with measured data, and 2) demonstrates more explicitly the qualitative and quantitative improvements offered by rEIT.

Bench-top imaging experiments were conducted to evaluate rEIT using a cylindrical and a breast-shaped tank (see Fig. 1a-b). In both experiments, two inclusions within the domain were kept stationary while the tanks were rotated. The full-set of traditional EIT measurements is recorded at each rotation, which is referred to as a *dataset*. rEIT uses a certain number of datasets, referred to as *fused datasets*, to produce a reconstruction. The mathematical analysis revealed an improvement of up to 4.2 and 4.7 times the number of stable singular vectors on the cylindrical and breast-shaped tank, respectively. This analysis enables one to quantify the improved resolution or *added information* provided by rEIT. Absolute imaging with rEIT was able to distinguish two inclusions that were 1.5 cm closer together than traditional EIT could achieve for inclusions placed 2 to 3 cm from the center of the cylindrical tank; likewise, rEIT was able to better distinguish two tumor-like inclusions within the breast tank, when compared to traditional EIT. Qualitative analysis of the reconstructions and quantitative analysis of the distinguishability and spatial metrics and inclusion contrasts revealed that the DF/I technique and rotated-mesh approach is the preferred method for rEIT. Lastly, analysis of voltage measurements was used to illustrate important limitations of rEIT, i.e. the minimum rotational step size, $\Delta\theta$, that should yield added information was determined.

The remainder of the paper continues as follows. *Section II* includes a description of the forward problem, the meshing techniques, the inverse methods, the mathematical tools used to quantify the amount of information added by rEIT, and the description of the experiment, measurement system, and metrics used for analysis. *Section III* describes the results of the mathematical analysis, experiments, and direct investigation into measured voltage data. Section IV discusses the contributions of this study to literature, further discusses the clinical applications of rEIT, specifically those explored here, and includes a short discussion on modeling approaches.

II. Methods

This section describes the forward problem, two approaches for modeling tank rotations, two data fusion approaches used to perform the inversion, and three mathematical approaches used to investigate how much additional information can be gained through use of rEIT.

A. Forward Problem

The forward problem computes the electric potential within the domain and the electrode voltages on the boundary given a specified current injection distribution. The complete electrode model (CEM) [18] has been found to produce the most accurate simulated voltage measurements [19] and is defined by the following:

$$\nabla \cdot (\sigma \nabla \mathrm{u}) = 0, \quad x \in \Omega, \tag{1}$$

$$\mathrm{u} + \mathrm{z}_l \sigma \frac{\partial u}{\partial n} = U_l, \quad x \in \mathrm{E}_l, l = 1, 2, \ldots L \tag{2}$$

$$\int_{E_l} \sigma \frac{\partial u}{\partial n} ds = I_l, \quad x \in \mathrm{E}_l, l = 1, 2, \ldots L \tag{3}$$

$$\sigma \frac{\partial u}{\partial n} = 0, \quad x \in \partial\Omega \backslash \bigcup_{l=1}^{L} E_l, \tag{4}$$

where σ is the conductivity, u is the electric potential, Ω denotes the domain, L is the number of electrodes, and U_l, I_l, z_l represent the voltage, current, and contact impedance on the lth electrode, E_l. Using the variational formulation of these equations [18] one can solve in 3D using the finite element method (FEM) [20]. We use a 3D Matlab implementation of the CEM and FEM using tetrahedral elements and linear basis functions for calculations [21]. A 3D mesh defining the domain of interest is constructed using gmsh [22]. Electrodes are defined within the mesh by specifying their boundaries using the nodes and edges. Therefore, each electrode is defined by a set of tetrahedral faces or 2D triangles.

The forward problem was modeled in two ways, referred to as the *1-mesh* and *rotated-mesh* approaches. In the 1-mesh approach, a single FEM mesh was constructed that encoded the electrodes from *all* rotations. When calculating voltages corresponding to a single rotation, one needs to simply use the triangles that represent the electrodes for that rotation. In a sense the mesh is composed of overlapping electrodes. In contrast, the rotated-mesh approach is composed of a single mesh with the electrodes from a zero-degree rotation encoded in it, and one obtains meshes for different rotations by rotating the nodes of this mesh.

B. Inverse Problem

The inverse approach is based on the standard Gauss-Newton algorithm employing a generalized Tikhonov regularization scheme. After a linearization step ([23]) about an initial estimate of the conductivity, $\tilde{\sigma}_0$, the error to be minimized is given by

$$E(\boldsymbol{\delta\sigma}) = \|\boldsymbol{J}\boldsymbol{\delta\sigma} - \Delta\boldsymbol{V}\|_2^2 + \lambda^2 \|\boldsymbol{L}\boldsymbol{\delta\sigma}\|_2^2 \tag{5}$$

where $\delta\boldsymbol{\sigma}$ is the conductivity update, $\boldsymbol{J}$ is the Jacobian, $\boldsymbol{L}$ is the regularization matrix, λ is the Tikhonov regularization factor, and $\Delta\boldsymbol{V}$ is the vector difference between measured, $\boldsymbol{V}_{Meas}$, and simulated voltages, $\boldsymbol{V}_{Sim}(\tilde{\sigma}_0)$. In this study $\boldsymbol{L}$ is taken to be a Laplace smoothing regularization matrix. The solution to (5) can be written as

$$\delta\tilde{\sigma} = \left(\boldsymbol{J}^T\boldsymbol{J} + \lambda\boldsymbol{L}^T\boldsymbol{L}\right)^{-1}\boldsymbol{J}^T\left(\boldsymbol{V}_{Meas} - \boldsymbol{V}_{Sim}(\tilde{\sigma}_0)\right). \tag{6}$$

If an appropriate regularization matrix and Tikhonov factor are chosen, then the augmented Jacobian, $\boldsymbol{J}^T\boldsymbol{J} + \lambda\boldsymbol{L}^T\boldsymbol{L}$, is positive definite and therefore invertible [24]. *Absolute imaging* assumes (as stated in (6)) that $\boldsymbol{V}_{Sim}(\tilde{\sigma}_0)$ is simulated, whereas *difference imaging* uses a measured reference set in place of $\boldsymbol{V}_{Sim}(\tilde{\sigma}_0)$. Difference imaging can only be used when an appropriate reference set can be acquired. Equation (6) yields an update for the conductivity estimate throughout the domain, $\tilde{\sigma}_1 = \delta\tilde{\sigma} + \tilde{\sigma}_0$, and the whole process can be iterated to improve the quality and accuracy of the absolute reconstructions.

Our inverse implementation uses the dual-mesh method [25], which allows one to solve the Jacobian on a fine mesh while estimating the conductivity on a much coarser inverse mesh. This approach yields an electrical potential with high accuracy throughout the domain and enables one to reconstruct on any chosen inverse mesh. We note that this fine mesh is the same mesh used to simulate the voltages, $\boldsymbol{V}_{Sim}(\tilde{\sigma}_0)$, in (6).

In rEIT, datasets recorded from multiple tank rotations are combined to produce an improved reconstruction. For each of the N_R rotations one has a distinct Jacobian $\boldsymbol{J}(\theta)$, measured data vector $\boldsymbol{V}_{Meas}(\theta)$, and simulated voltages $\boldsymbol{V}_{Sim}(\sigma_0, \theta)$. There are two approaches that one may use when combining the data. The first approach is to compute the inverse problem for each rotation (i.e. solve (6)) and then fuse the reconstructions (I/DF), and the second approach is to fuse all the data and solve the inverse problem simultaneously for all rotations (DF/I).

1) Inversion Then Data Fusion (I/DF): In this method, an estimate of the conductivity, $\tilde{\sigma}(\theta)$, is calculated for each rotation and these individual reconstructions are averaged to yield a final reconstruction, $\tilde{\sigma}_{I/DF}$. Each individual reconstruction is performed on the same inverse mesh. Thus the fusion is a direct average over each node, i.e.

$$\tilde{\sigma}_{I/DF}(x_i) = \frac{1}{N_R}\sum_{n=1}^{N_R}\tilde{\sigma}(x_i, \theta_n). \tag{7}$$

The I/DF technique was used in [13]; however, in [13] coarser and separate distinct meshes were used for each individual rotation compared to the final fused mesh (similar to the rotated-mesh approach).

2) Data Fusion Then Inversion (DF/I): In this approach the data is first fused and then inversion is performed simultaneously using all of the data. The data is fused in the error function such that

$$E(\boldsymbol{\delta\sigma}) = \frac{1}{N_R}\sum_{n=1}^{N_R}\|\boldsymbol{J}(\theta_n)\boldsymbol{\delta\sigma} - \Delta\boldsymbol{V}(\theta_n)\|_2^2 + \lambda^2\|\boldsymbol{L}\boldsymbol{\delta\sigma}\|_2^2. \tag{8}$$

Equation (8) is the average error between the model and measured data while including the same regularization scheme as traditional EIT, i.e. identical second term as in (5). The averaging maintains the same relative error and regularization norms regardless of the number of rotations due to the $1/N_R$ factor. Thus a single Tikhonov factor can be used when comparing reconstructions across different numbers of fused datasets. One can rewrite (8) in the following equivalent form

$$E(\boldsymbol{\delta\sigma}) = \frac{1}{N_R}\|\boldsymbol{J}_{\mathbf{FD}}\boldsymbol{\delta\sigma} - \Delta\boldsymbol{V}_{\mathbf{FD}}\|_2^2 + \lambda^2\|\boldsymbol{L}\boldsymbol{\delta\sigma}\|_2^2, \tag{9}$$

where $\boldsymbol{J}_{\mathbf{FD}}$ and $\Delta\boldsymbol{V}_{\mathbf{FD}}$ represent the concatenated fused-data (FD) Jacobian and voltage data, e.g. $\boldsymbol{J}_{\mathbf{FD}}$ is defined by

$$\boldsymbol{J}_{\mathbf{FD}} = \left[\begin{array}{cccc}\boldsymbol{J}^T(\theta_1) & \boldsymbol{J}^T(\theta_2) & \cdots & \boldsymbol{J}^T\left(\theta_{N_R}\right)\end{array}\right]^T. \tag{10}$$

Using the same method to solve (5), the solution to (8) or (9) is given by

$$\delta\tilde{\sigma}_{DF/I} = \left(\frac{1}{N_R}\boldsymbol{J}_{\mathbf{FD}}^T\boldsymbol{J}_{\mathbf{FD}} + \lambda\boldsymbol{L}^T\boldsymbol{L}\right)^{-1}\left(\frac{1}{N_R}\boldsymbol{J}_{\mathbf{FD}}^T\boldsymbol{\Delta V}_{FD}\right). \tag{11}$$

C. Mathematical Tools for Analyzing the Inversion

We use singular value decomposition (SVD) to analyze the additional information obtained via fused datasets. In general, the matrix $\boldsymbol{A}$, size $m \times n$, can be decomposed into three matrices, i.e. $\boldsymbol{A} = \mathbf{U}\boldsymbol{S}\boldsymbol{V}^T$, where $\boldsymbol{U}$ is $m \times n$, $\boldsymbol{V}$ *is* $n \times n$ with orthonormal columns, and $\boldsymbol{S}$ is a diagonal matrix with nonnegative elements (singular values) [26]. Analyzing the singular values gives the numerical rank of $\boldsymbol{A}$ and the expected number of singular vectors (columns of $\boldsymbol{V}$) that can be used in inverting the matrix (page 56 of [27]). One can then use the Picard condition to estimate the number of stable singular vectors (see [9], [26]).

The matrix of interest in the context of rEIT is the Jacobian, $\boldsymbol{J}_{\mathbf{FD}}$. The analysis of the singular values of $\boldsymbol{J}_{\mathbf{FD}}$ was considered in [12], and the analysis of the Picard condition in terms of the least square problem, $\|\boldsymbol{J}_{FD}\boldsymbol{\delta\sigma} - \Delta\boldsymbol{V}_{\mathbf{FD}}\|_2$ was considered in [9]. A third method of analyzing the problem can be found by first rewriting (9) in an equivalent form,

$$E(\delta\sigma) = \left\| \begin{bmatrix} \frac{1}{\sqrt{N_R}}\boldsymbol{J}_{\mathbf{FD}} \\ \lambda\boldsymbol{L} \end{bmatrix} \boldsymbol{\delta\sigma} - \begin{bmatrix} \frac{1}{\sqrt{N_R}}\Delta\boldsymbol{V}_{\boldsymbol{SR}} \\ \mathbf{0}_{N_C} \end{bmatrix} \right\|_2^2, \quad (12)$$

referred to as a stacked form (page 68 of [27]), where we refer to the stacked matrix as $\boldsymbol{B} = [\boldsymbol{J}_{\mathbf{FD}}^{\boldsymbol{T}}/\sqrt{N}_R \quad \lambda\boldsymbol{L}^{\boldsymbol{T}}]^T$. An analysis of the singular values (SV) of $\boldsymbol{B}$ indicate the number of singular vectors that are directly associated with the Jacobian in the final regularized inverse solution. By using an empirically best-fit Tikhonov factor this analysis also incorporates the decay of the singular values and the measurements.

D. Description of Experiments

This section describes the experiments designed to reveal the practical improvements offered by rEIT and details of the measurements, measurement system, and reconstruction parameters. The experiments were conducted on a 16-electrode cylindrical tank (diameter 20 cm, depth of 3 cm) and a breast-shaped tank (half-ellipsoid: x/y-diameter 14 cm, and z-semi-principle axis/depth 5 cm) with two rows of 8 electrodes, offset by 45° (Fig. 1). The cylindrical tank electrodes were 3 cm in height and 2.0 cm in width and the square breast tank electrodes were $1cm \times 1cm$. The cylindrical tank was filled with 0.1 S/m saline and cylindrical metal inclusions (25.4 mm diameter) were used. The breast tank was filled with 0.05 S/m (near adipose tissue) and gel inclusions (1 cm diameter and 1 cm height with a 0.22 S/m conductivity) were placed in the solution as tumor surrogates ([28]).

Based on the results from [12] we aimed to use as many rotations as possible. Our manual rotation stage allowed accurate rotations down to 1 degree. Based on the electrode spacing there was a maximum turn of 22° and 44° before a repeated geometry would occur for the cylindrical and breast-shaped tanks, respectively. For the 1-mesh approach, rotations that resulted in nearly intersecting electrode boundaries (intersections within 0.15 cm) needed to be excluded to prevent ill-shaped mesh elements. Considering these factors and assuming 1° rotations for the cylindrical tank and using a simple greedy algorithm to find least overlapping electrode boundaries for the breast-shaped tank the parameters for the experiments were selected (Table I).

TABLE I
ROTATIONS USED IN TANK EXPERIMENTS

Tank	No. of Datasets	Minimum Rotation (°)	Rotations (°)
Cylinder	1	-	0
	2	7	0, 7
	4	3	0, 3, 6
	8	1	0, 1, 2, 3, 4, 5, 6, 7
Breast	1	-	0
	2	24	0, 24
	4	7	0, 7, 24, 31
	6	3	0, 3, 7, 24, 27, 31
	8	2	0, 3, 5, 7, 24, 27, 29, 31

1) Measurement System: Impedance data was recorded using a custom designed EIT system [29]. All data was sampled at 10 kHz. A total of 1,456 tetrapolar measurements for the cylindrical tank and 1,320 tetrapolar measurements for the breast tank were recorded from each rotation, i.e. for each *dataset*. Each tetrapolar measurement is specified as the differential voltage measured between two electrodes created due to a pair of current injecting electrodes. We define each measurement as an IIVV pattern where II represents the current injection electrode pair (I_1, I_2) and VV represents the differential voltage sensing pair of electrodes (V_1, V_2). The IIVV patterns are composed of 0-skip through 6-skip patterns for cylindrical tank and composed of combinations of 0-skip through 3-skip patterns from both rows of the breast-shaped tank. No bi-polar measurements were used. The n-skip patterns are all combinations of current and voltage electrodes that have n electrodes between current carrying and voltage measurement electrodes. For example, two IIVV patterns using 0- and 2-skips are [1 2 3 4] and [1 4 8 11], respectively. The average standard deviation across all voltage measurements and tests at a rotation of 0 degrees for the system, $\overline{SN}$, was 0.21 mV for cylindrical tank and 0.10 mV for the breast-shaped tank. A saline calibration step was performed on all measurements [30].

2) Reconstructions: All reconstructions are absolute using (6) or (12). The number of fine mesh nodes and elements, the coarse inverse mesh grid and number of nodes, the number of inverse algorithm steps, and the Tikhonov factors for both experiments are listed in Table II. The L-curve approach was investigated [26], but in an attempt to find the point at which the two inclusions were most distinguishable it was empirically found that the optimal Tikhonov factor was slightly above the corner of the L-curve.

3) Distinguishability Experiments: These experiments were conducted to illustrate how rEIT provides more resolved imaging. Specifically, the experiment explored the minimum separable distance needed to distinguish two objects.

In each measurement configuration, two inclusions were placed within the tank. The inclusions were positioned so that their centers had an x-translation from the tank center of 2 to 5 cm in 1 cm steps in the cylindrical tank and

TABLE II
MESH AND RECONSTRUCTION PARAMETERS

Parameter	Value	
	Cylinder	Breast shaped
No. fine mesh nodes	97,211	121,040
No. fine mesh elements	448,832	616,680
Inverse mesh grid	40 x 40 x 1	40 x 40 x 5
No. inverse mesh nodes	1,264	4,163
Tikhonov parameter	10	100
No. of iterations	8	6

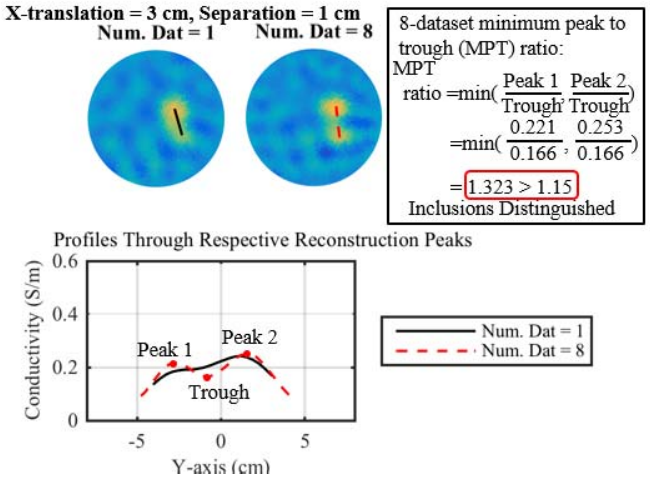

Fig. 2. Illustration of the minimum peak to trough (MPT) ratio via two example reconstructions (1 dataset and 8 fused datasets using the DF/I technique and 1-mesh approach) and their respective profiles through the reconstructed peaks.

2 to 4 cm in 0.5 cm steps in the breast-shaped tank, and the inclusions were separated in the y-direction by 0.5 to as much as 3 cm in 0.5 cm steps in both experiments (see Fig. 1a for an illustration of the x-translation and separation). The inclusions were suspended so that when the tank was rotated the inclusions remained fixed in place. In the breast-shaped tank the inclusions were centered at a depth of 2.5 cm.

Distinguishability Metric. A distinguishability metric was developed that incorporated a minimum peak to trough (MPT) ratio and a background noise (BN) measure. The inclusions were considered distinguishable if the MPT ratio was above a tolerance of 1.10 or 1.15, i.e. the minimum peak was 10% or 15% larger than the trough. Two tolerances were chosen because distinguishability is a subjective measure and these two values both help to illustrate the differences in reconstructions between the methods and number of combined datasets. A peak was required to be three times larger than the background noise, 3BN. The BN is defined to be the standard deviation of the reconstructed conductivity on nodes whose x-value was less than -1 cm, i.e. the background from the left side of the reconstructions in Fig. 2. The trough was defined to be the minimum point on the line joining the two peaks. If two peaks were not found, then the MPT ratio was assigned a value of 1. Fig. 2 provides an illustration of the MPT ratio and distinguishability metric on two example reconstructions (1 dataset and 8 fused datasets using the DF/I technique and 1-mesh approach). The reconstruction

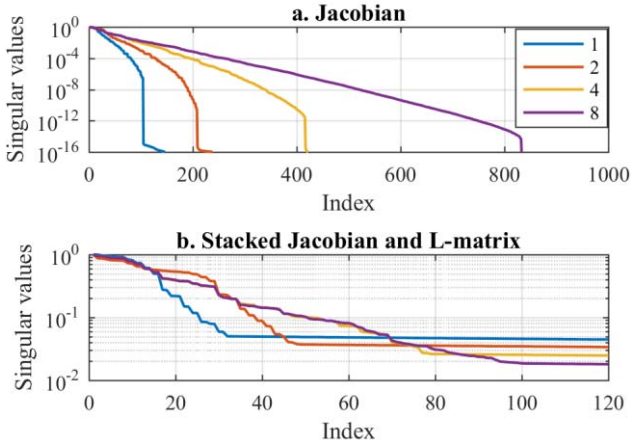

Fig. 3. Illustration of the normalized singular vectors from a. the Jacobian, $\boldsymbol{J}_{FD}$ (10) and b. the stacked Jacobian and regularization matrix, $\boldsymbol{B}$, for 1, 2, 4, and 8 fused datasets.

from the 8 fused datasets provides sufficient separation to quantitatively and qualitatively distinguish the inclusions, while the single dataset reconstruction yields a blurred region that does not clearly distinguish the inclusions. This approach to quantifying distinguishability is similar to that used in [31].

Other Metrics. In addition to the distinguishability metric, an x-translation error and separation error were used. The separation error was only calculated if two peaks were identified. Additionally, the background conductivity error and inclusion contrast, defined by the mean peak value divided by the mean background conductivity, was used to quantitatively evaluate the recovered conductivity values and the potential of absolute imaging.

III. RESULTS

The benefits of rEIT were evaluated using mathematical tools (i.e. SVD analysis), qualitative and quantitative analysis of images reconstructed from a series of experiments, and direct analysis of the raw voltage measurements. All data is measured and all reconstructions are absolute.

A. Mathematical Analysis of the Inversion (SVD Analysis)

The mathematical tools described in Section II-C were used to analyze the potential improvement associated with the fused datasets. This analysis is only applicable for the DF/I technique, since the inverse step remains the same for all data sets in the case of the I/DF technique.

First, SVs of the fused-data Jacobian, $\boldsymbol{J}_{FD}$, and the stacked Jacobian and regularization matrix, $\boldsymbol{B}$, for 1, 2, 4 and 8 fused datasets are computed (Fig. 3) for the cylindrical tank and 1-mesh approach. The SVs of $\boldsymbol{J}_{FD}$ drop to numerical precision ($\sim 1 \times 10^{-16}$) at $N_R \times L$ *(L-3)/2*, which is the product of the number of rotations and the maximum number of independent measurements possible in an L-electrode tetrapolar measurement system (Fig. 3a). As expected, this suggests that rEIT provides significantly more information as additional datasets are fused. Similar findings were reported in [12]. Although the SVs will always decay exponentially, the *degree of ill-posedness* (page 8 of [26]) is reduced (rate of decay

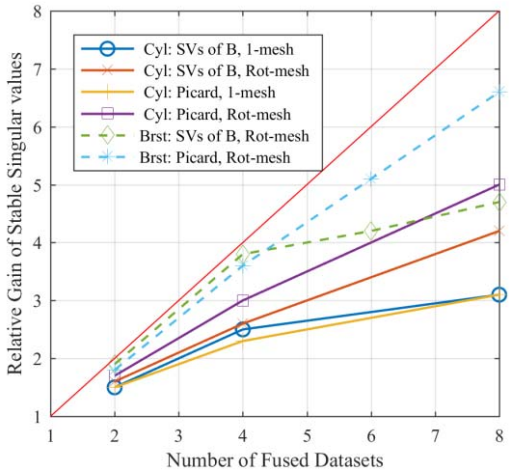

Fig. 4. The relative gain in stable singular vectors as a function of number of fused datasets for the cylindrical (Cyl) and breast-shaped (Brst) tanks and the 1-mesh and rotated-mesh approaches predicted by the singular vector analysis of B (SVs of B) and the Picard condition.

of SVs is slower) when more fused datasets are used. The SVs that correspond to the stacked Jacobian and regularization matrix, $\boldsymbol{B}$, decrease exponentially until the SVs are influenced by the regularization (Fig. 3b). While only the first 120 SVs are shown, the SVs only drop to approximately 1×10^{-3} which implies the $\boldsymbol{B}$ matrices are each numerically well-conditioned. The index at which the SVs level off signifies the point at which the regularization becomes dominant. In other words, there are only 32, 48, 79, and 100 SVs that are directly related to the Jacobian for the 1, 2, 4, and 8 fused datasets, respectively. Analysis via Picard's condition revealed 71, 105, 163, and 218 stable SVs for inversion when combining 1, 2, 4, and 8 fused datasets, respectively.

The results for the SVs of $\boldsymbol{J}_{FD}$ are overly optimistic, as they do not consider the stability of the singular vectors. The improvements in terms of relative gain of singular vectors are shown in Fig. 4 for the other two methods (SV analysis of B and the Picard condition) corresponding to both tanks and the 1-mesh and rotated-mesh approaches. The analyses from the SVs of $\boldsymbol{B}$ (Fig. 3b) and Picard condition exhibit nearly the same improvement factor for the 1-mesh approach, whereas the Picard condition analysis results in slightly higher gains than the SVs of B analysis for the rotated-mesh approach. The analysis of the SVs of B is more relevant since they are directly linked to the regularization, which has been tuned to provide the best reconstruction results. Overall, these analyses suggest multiple fused datasets provide a relative gain of as much as 4.2 and 4.7 times the number of singular vectors as compared to a single dataset for the cylindrical and breast-shaped tank, respectively (Fig. 4). The gain using 8 fused datasets (4.2 and 4.7) is similar to what one would ideally expect by doubling the number of electrodes (4.46); additionally, the gain is decreasing in slope as more datasets are fused, which implies there is likely an upper limit to the possible gains.

B. Cylindrical Tank: Distinguishability Experiment

This experiment illustrates the ability of rEIT to distinguish two metal inclusions in a cylindrical tank using three methods;

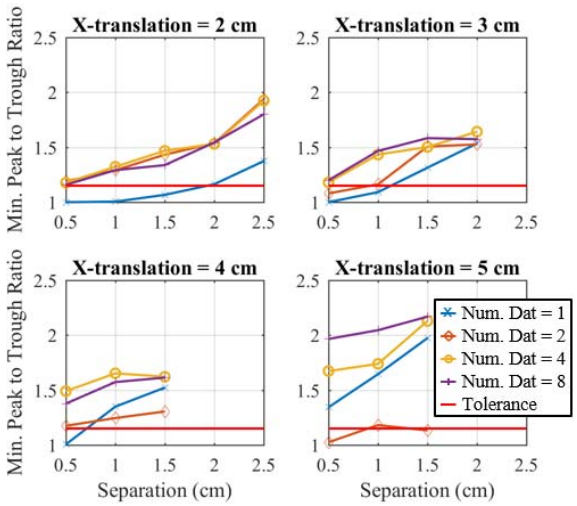

Fig. 5. Plots of the minimum peak to trough (MPT) ratios for 1, 2, 4, and 8 fused datasets using the DF/I technique and rotated-mesh approach. The MPT ratio increases as the inclusions are moved apart. One can see that the fusion of datasets increases the MPT ratio.

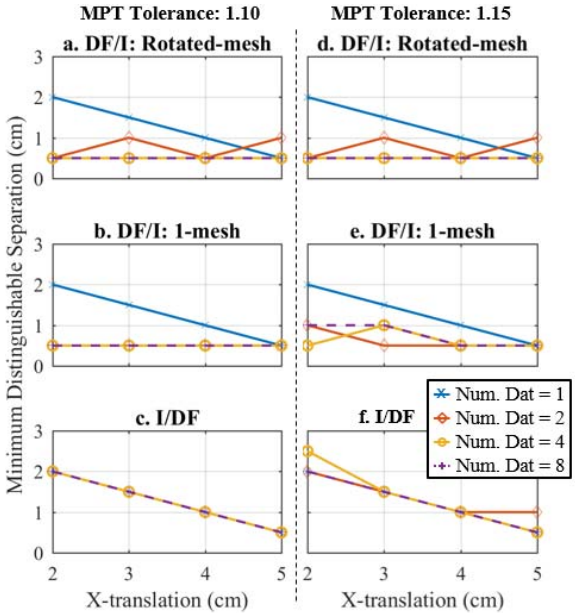

Fig. 6. Plot of the minimum distinguishable separation for 1, 2, 4, and 8 fused datasets using the a/d. DF/I technique and rotated-mesh approach, b/e. DF/I technique and 1-mesh approach, and c/f. I/DF technique, which is determined by finding the minimum separation that yields an MPT ratio of 1.10 (a-c) or 1.15 (d-f) (see Fig. 5).

1) DF/I technique using the rotated-mesh approach, 2) DF/I technique using the 1-mesh approach, and 3) the I/DF technique. We verified that the I/DF technique produced equivalent images for both the 1-mesh and rotated-mesh approaches. We show example plots of the MPT ratio versus separation for each x-translation in Fig. 5 and compare the minimum distinguishable separation using each method (Fig. 6) assuming tolerances of 1.10 and 1.15. The best reconstructions (assuming a tolerance of 1.15) are illustrated (Fig. 7) and compared to the other methods (Fig. 8). Finally, the spatial metrics and the inclusion contrasts are used to further evaluate these absolute reconstructions (Fig. 9).

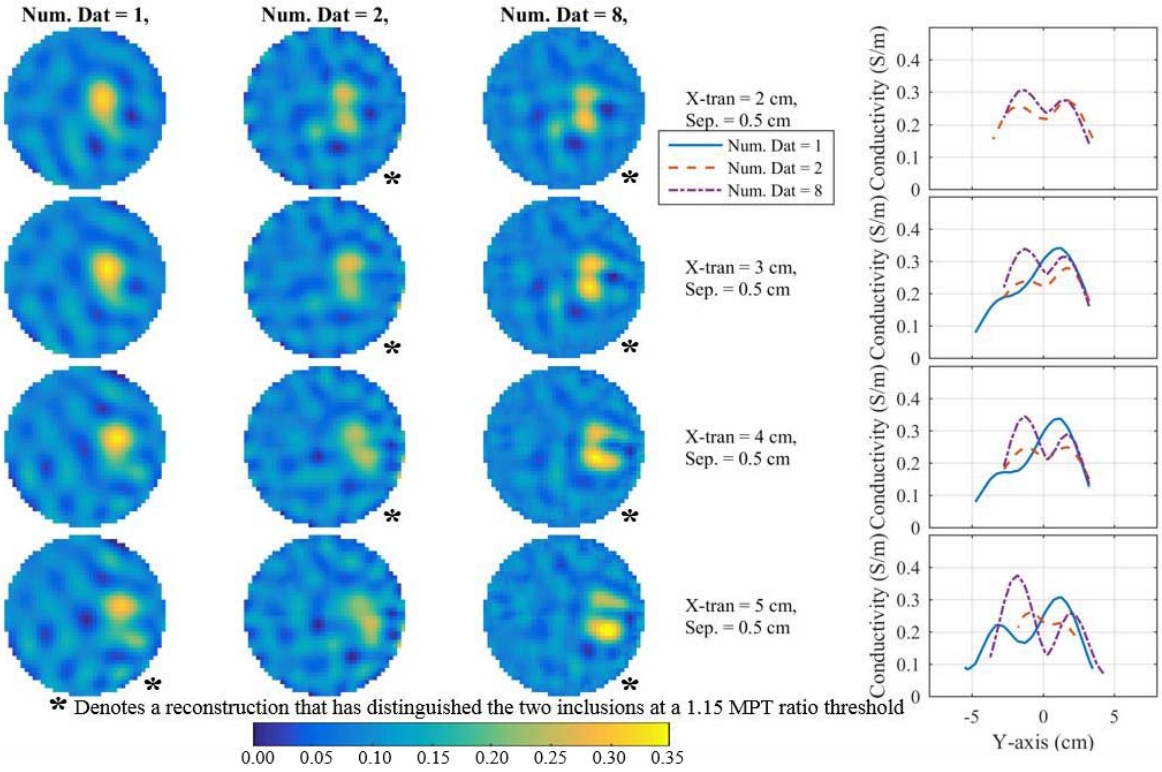

Fig. 7. Reconstructions (using the DF/I and rotated-mesh approach) corresponding to the smallest distinguishable separation (across number of fused datasets) at each x-translation for 1, 2, and 8 fused datasets (first three columns) along with profiles through their respective peaks (last column). The profiles are the reconstructed conductivities over the line connecting the two peaks. If there is no profile for a number of fused datasets then two peaks were not detected.

Fig. 5 shows the MPT ratio as a function of inclusion separation for each x-translation considered when a DF/I technique and rotated-mesh approach were used for reconstructions. The right end-point of the curves represents the maximum separation tested for the particular x-translation. The MPT ratio increases as the inclusions are spaced further apart, which implies an increased distinguishability. Visually, there is a significant improvement observed when incorporating fused datasets. It is interesting to note that as the inclusions are moved closer to the center the differences between combining 2, 4, and 8 datasets becomes much smaller.

The curves in Fig. 5 with the chosen tolerances of 1.10 and 1.15 are used to determine the minimum distinguishable separation for each x-translation, shown in Fig. 6 for all methods. As expected the minimum distance at which two inclusions can be distinguished decreases as the inclusions approach the tank boundary (Fig. 6) where EIT is most sensitive. The best method is clearly the DF/I technique using the rotated-mesh approach. It is able to distinguish the two inclusions at a separation of 0.5 cm for all x-translations when 4 or more datasets are fused using the larger/more challenging tolerance of 1.15. We suspect the 2 combined datasets performs worse because of (dual) inverse mesh artifacts (discussed in Section IV), which are reduced by averaging over more datasets. Overall and using the more challenging tolerance of 1.15, the rEIT technique is able to distinguish two inclusions 1.5 cm closer together than traditional EIT (1 dataset) could achieve for inclusions placed 2 to 3 cm from the center. In the remainder of this subsection, the tolerance of 1.15 is assumed.

There is a significant difference between the DF/I and I/DF techniques. There appears to be no added ability to distinguish the inclusions using the I/DF technique compared to traditional EIT (Fig. 6 c/f). The two DF/I techniques in contrast are quite similar. It appears that either 2- or 4- fused datasets is best for the 1-mesh approach (Fig. 6e).

Fig. 7 shows the reconstructions corresponding to the smallest overall distinguishable separation at each x-translation for 1, 2, and 8 datasets along with their corresponding conductivity profiles through the peaks using the best approach (DF/I using the rotated-mesh approach). Combinations of 4 datasets are omitted because they are nearly indistinguishable from the 8-dataset reconstructions. Combining 2 or 8 datasets provides better distinguishability between the two inclusions as compared to a traditional EIT (1 dataset). In fact, for x-translations of 2 to 4 cm the 1 dataset reconstructions only recovered a single peak (assuming separations from Fig. 7). The three methods are directly compared using each of their best number of fused datasets corresponding to the best method's smallest distinguishable separation at each x-translation (Fig. 8). The first three columns show the reconstructions and the final column shows their corresponding profiles through the peaks. In each row, the inclusions reconstructed with DF/I are qualitatively more resolved than I/DF.

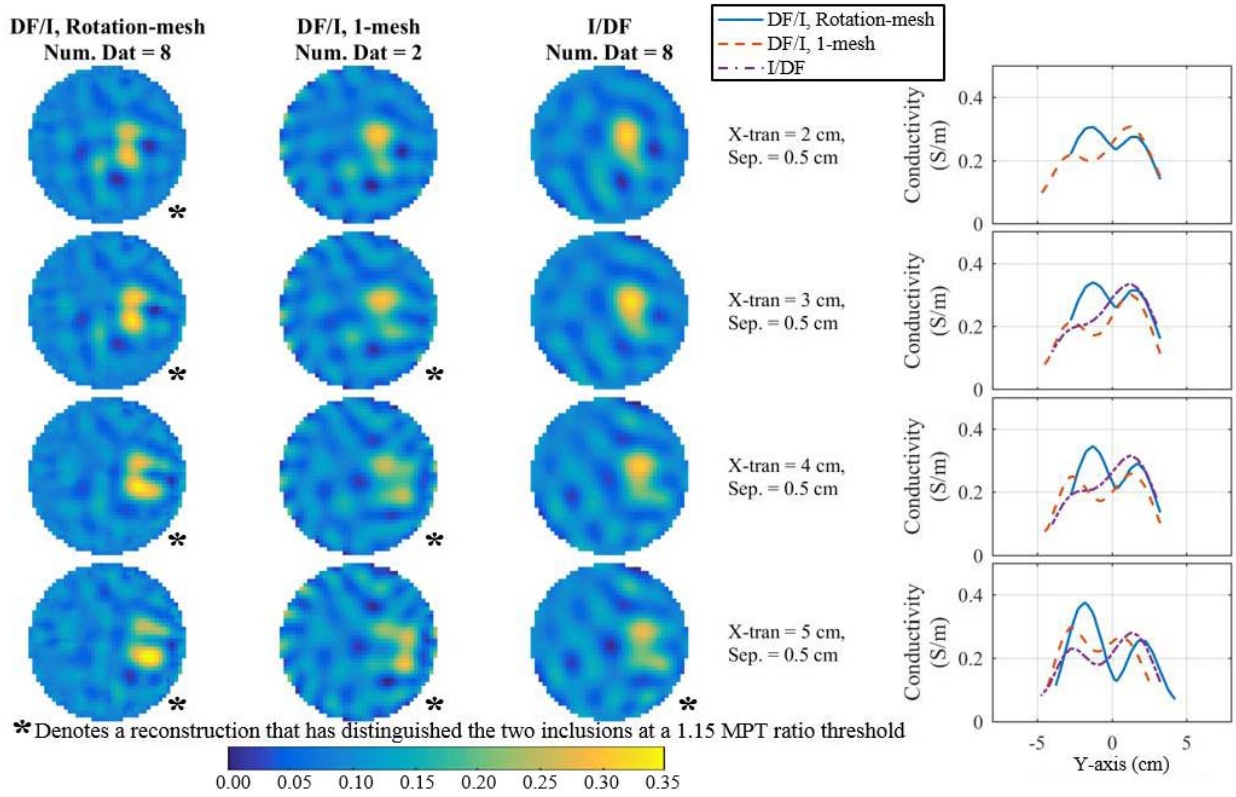

Fig. 8. Reconstructions comparing DF/I to the I/DF technique for 8 fused datasets corresponding to the DF/I's smallest distinguishable separation at each x-translation. The first three columns show the reconstructions and the final column shows the corresponding profiles through the peaks. If there is no profile for a number of fused datasets then two peaks were not detected.

Likewise, the I/DF approach is only able to quantitatively distinguish the two inclusions for an x-translation of 5 cm. The difference between the two DF/I techniques are more subtle, but qualitatively the rotated-mesh reconstructions have much more consistent contrast in the inclusions and the inclusions are more aligned vertically as expected based on the geometry of the measured data.

In Fig. 9 the spatial and contrast metrics are shown for the same reconstructions of Fig. 8. One can see that the DF/I and rotated-mesh approach is nearly always better in terms of each metric (except the smallest x-translation in the x-translation error metric). This reinforces the qualitative appearance of more accurately located and separated inclusions in Fig. 8 using this technique. We note that the separation error can only be calculated if two inclusions were detected. Thus x-translations of less than 3 cm could not be calculated for the I/DF technique. The contrast plot illustrates the convergence of the approach and the improvements one achieves using absolute imaging (3.4 contrast) compared to 1 iteration (2.2), i.e. a 1.5x improvement in contrast. The background conductivity error was 3.3%, 6.1%, and 4.8% for the reconstructions shown in Fig. 9 using the DF/I and rotated-mesh approach, DF/I and 1-mesh approach, and the I/DF technique, respectively.

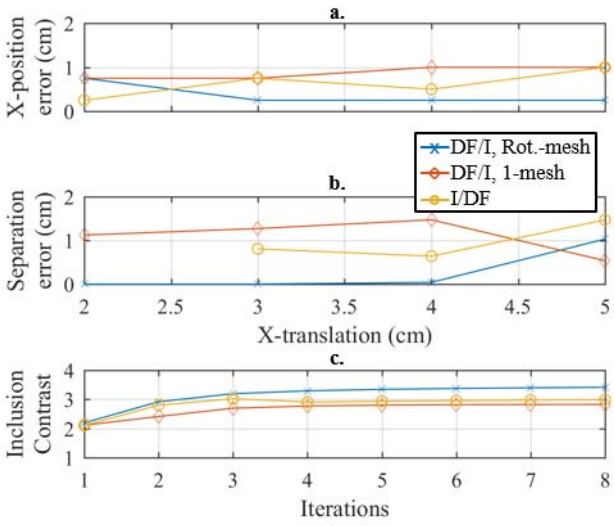

Fig. 9. Illustration of the a. X-position error and b. separation error, versus x-translation and the c. inclusion contrast (averaged across x-translations) versus iteration across each reconstruction method. The true separation at each x-translations corresponds to the reconstructions shown in Figs. 7 and 8.

C. Breast Tank: Distinguishability Experimental

The second experiment was performed on a breast-shaped tank (Fig. 1b), which is a realistic potential clinical geometry with tumor and saline conductivities chosen similar to a fatty breast [28]. Essentially the same experiment was performed as with the cylindrical tank, but here the geometry is more complicated, multiple rows of electrodes are used, and the inclusions are of a smaller size and contrast more closely representing typical tumor sizes and conductivities.

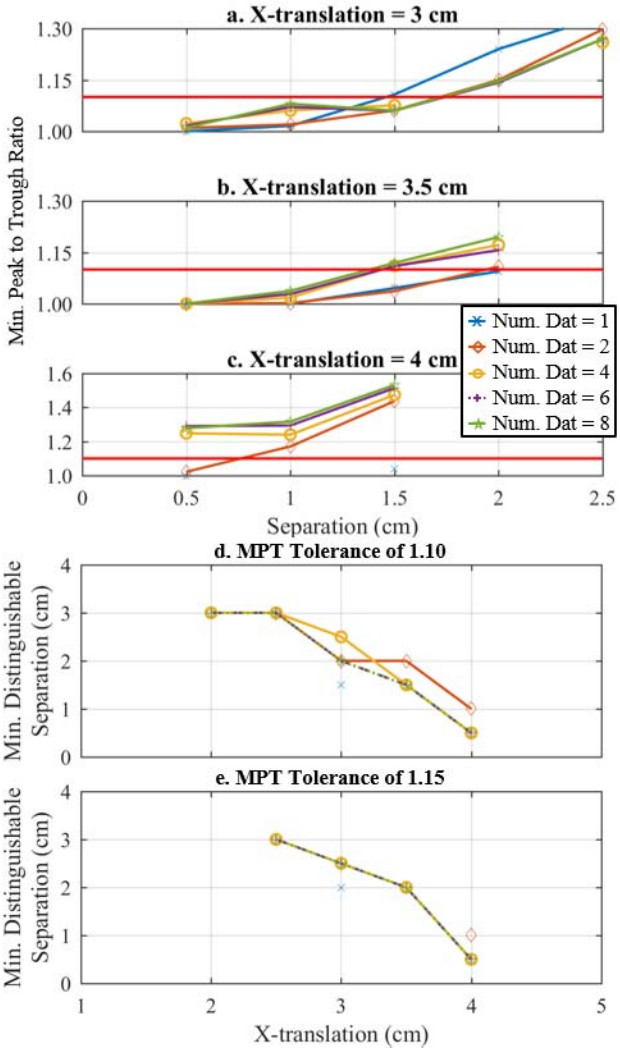

Fig. 10. Minimum peak to trough ratios versus separation for x-translation of a. 3 cm, b. 3.5 cm, and 4. cm from the tank center. Based on these MPT ratios and tolerances of 1.10 and 1.15, d. and e. show the resulting minimum distinguishable separation versus x-translations for 1, 2, 4, 6, and 8 combined datasets, respectively.

Reconstructions were performed using the DF/I technique with the rotated-mesh approach. The minimum distinguishable separations are determined (Fig. 10d-e) using the MPT ratio (Fig. 10a-c) with tolerances of 1.10 and 1.15. The reconstructions at the minimum distinguishable separation (assuming a tolerance of 1.10) using 1, 2, and 8 combined datasets are compared qualitatively in Fig. 11 and quantitatively in Fig. 12.

One can see a clear improvement when using 6 and 8 combined datasets by the MPT ratio plots at 3.5 and 4.0 cm x-translations (Fig. 10b-c) and the overall minimum distinguishable separation curves in Fig. 10d assuming a tolerance of 1.10. We prefer using the tolerance of 1.10 opposed to 1.15 because the 1.10 tolerance better illustrates the subtle changes between the different numbers of combined datasets used (compare Fig. 10d to 10e). In the remainder of this subsection, we assume a tolerance of 1.10. Regardless, the minimum distinguishable separations are much larger than the cylindrical tank experiment (Fig. 6a,d), which is expected because of the smaller sized inclusions and significantly reduced inclusion-to-background contrast. It is surprising that according to the MPT ratio the 1-combined dataset outperforms the 2, 4, 6, and 8 combined datasets at an x-translation of 3 cm (Fig. 10d). However, if one inspects the reconstructions (Fig. 11) and the spatial metrics (Fig. 12), it is apparent that the inclusions spatial locations and separations have significant errors. In terms of the contrast metric, one again sees the best contrast by taking multiple iterations (absolute imaging) and by combining 8-datasets (1.27). Unfortunately, it is significantly less than the ideal contrast 4.4 (=0.22/0.05). This significant underestimate is likely caused by the ill-posed nature of the problem and the combination of the Laplace smoothing regularization and the small size of the inclusions. Regardless, it is a 7% improvement compared to 1-iteration and a 5% improvement compared to traditional EIT (using 6 iterations). The background conductivity error was very accurate in this experiment, i.e. less than 0.5% for each reconstruction shown in Fig. 12. Overall, the 8 fused datasets appears best when considering together the minimum distinguishable separations (assuming a 1.10 tolerance), qualitative analysis of the reconstructions, and the spatial and contrast metrics.

D. Measurement Limitations on Distinguishability

Finally, the hardware specification of the data acquisition system will impact the potential improvements provided by rEIT. Fig. 13 shows the average weighted voltage difference (AWVD) between measurements recorded at rotations of θ and 0 degrees at a fixed inclusion separation of 1 cm for both experiments, which can be written as

$$AWVD(\theta) = \sum_{n=1}^{1,456} \frac{|\boldsymbol{V}_{Meas}(\theta)_{\boldsymbol{n}} - \boldsymbol{V}_{Meas}(0)_{\boldsymbol{n}}|}{SN_n}, \quad (13)$$

where SN_n n is the standard deviation of the system noise for the nth measurement. Points below the $3\overline{SN}$ line are on average more likely to be corrupted by noise than those above $3\overline{SN}$. As expected, measurements are above this noise threshold when the inclusions are closer to the boundary and when there are larger changes in the rotation, $\Delta\theta$. For instance, in the cylindrical experiment (Fig. 13a) at x-translations of 2 and 3 cm, a minimum $\Delta\theta$ of 3 and 4 degrees, respectively, is required to on average detect a measureable change in voltage. Based on how the datasets have been combined here, this implies that reconstructions using only 2 datasets are expected to be best (i.e. a 7 degree rotation change) as opposed to 4- and 8-fused dataset reconstructions (i.e. 2 and 1 degree rotations, respectively) for x-translations of 2 and 3 cm. The 2-fused dataset reconstructions do indeed appear to be better than 4- and 8-fused dataset reconstructions when using the DF/I and 1-mesh approach (Fig. 4b) at these x-translations. In the case of the breast-shaped tank (Fig. 13b), larger rotations were considered, and therefore most of the rotations result in average weighted voltage differences above the $3\overline{SN}$ threshold. One can see, e.g. that for an x-translation of 2 cm on average the 2 and 3-degree rotations are corrupted by noise, but the DF/I technique using the rotated-mesh approach appears robust to this. Regardless the overall importance of this analysis is to illustrate that there is a clear limit on the number of rotations (fine-ness of rotations that can be used), which would expect

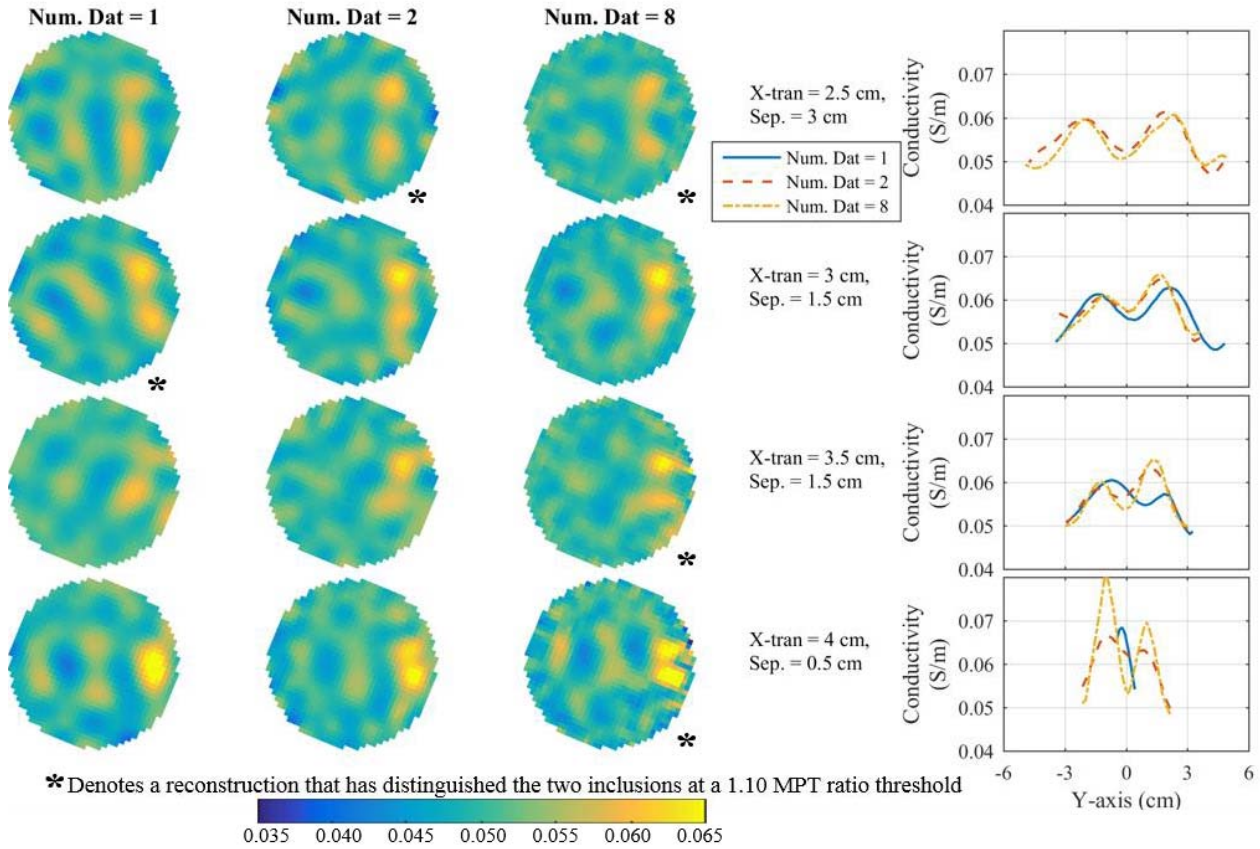

Fig. 11. Reconstructions of the breast-shaped tank (Fig. 1b) (using the DF/I and rotated-mesh approach) corresponding to the smallest distinguishable separation at each x-translation for 1, 2, and 8 combined datasets (first three columns) along with profiles through their respective peaks (last column). The profiles are the reconstructed conductivities over the line connecting the two peaks. If there is no profile for a number of fused datasets then two peaks were not detected.

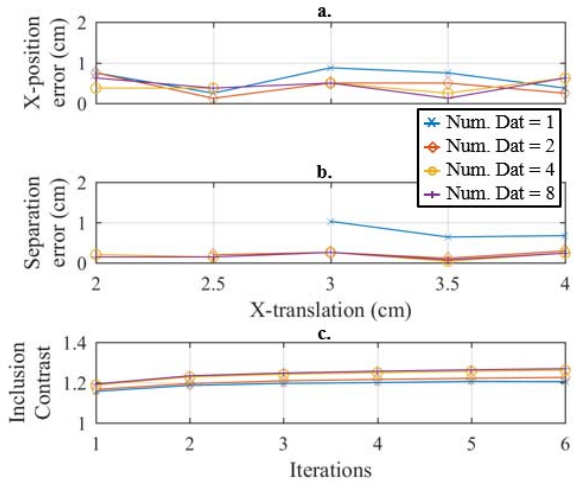

Fig. 12. Illustration of the a. x-position error and b. separation error, versus x-translation and the c. inclusion contrast (averaged across x-translations) versus iteration across 1, 2, 4, and 8 combined datasets of the breast-shaped tank. The true separation at each x-translations corresponds to the reconstructions shown in Fig. 10.

to add information and that this should be considered when designing a rEIT system.

IV. Discussion

This study reports 1) experimental evidence that illustrates the improvements offered by rEIT, and 2) provides the first rEIT (or fused-data EIT) study that has produced absolute images (with relatively large electrodes) for a realistic clinical application. In this section we discuss the modeling of the 1-mesh versus rotated-mesh approach and the above two points.

1-Mesh versus Rotated-Mesh Approaches. The 1-mesh approach was developed to minimize (dual) inverse mesh artifacts. Standard FEM mesh artifacts are well-studied and are known to potentially cause significant artifacts [32]. However, the dual mesh artifacts are different. An element of the inverse mesh is composed of numerous tetrahedra making up the same volume within the fine FEM mesh. A particular coarse element within the stationary inverse mesh will incorporate a different set of fine mesh elements for each rotation of the rotated-mesh approach, while the inverse element will consist of the same fine elements for all rotations when the stationary 1-mesh approach is used. These small variations can lead to artifacts in electrical property estimation. We believe this is why gains are limited for the rotated-mesh approach when only 2 datasets are used; the two different rotations could represent quite different sets of fine elements within each inverse mesh element. Despite this, we found that with a larger number of datasets the rotated-mesh approach in general performed better than the 1-mesh approach. We hypothesize that this slight jitter introduced on the volume of each inverse mesh element is beneficial to rEIT reconstructions, especially in improving spatial accuracy.

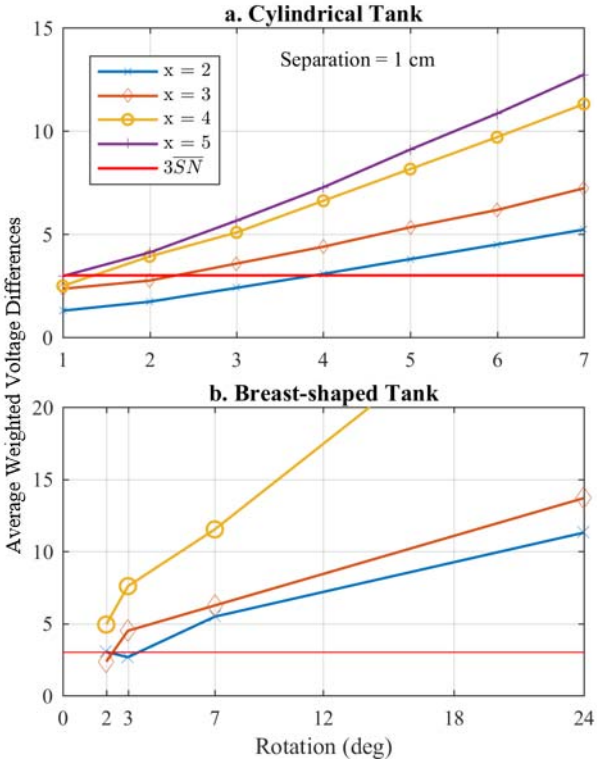

Fig. 13. Plot of the average weighted differences between a rotation of θ and 0 degrees for each x-translation and a separation of 1 cm. Points above $3\overline{SN}$, on average, should provide information whereas points below fall within the noise of the system.

Experimental Evidence of Improvements offered by rEIT. This study was motivated by a lack of clarity on how much improvement rEIT can provide ([10], [12]). In these prior studies there appeared to be overly optimistic improvements that could have been caused by poor modeling choices (Figs. 12–13 in [12]), and the remaining illustrations did not clearly quantify the improvements (e.g. improvement versus distance from tank edge). This study provides a rigorous evaluation of rEIT that 1) gives guidance on the preferred modeling approach (DF/I technique using a rotated-mesh approach), 2) clearly describes the inversion approach, and 3) quantifies the improvements via singular value analysis and two experiments that clearly show how rEIT improves the reconstructions qualitatively and quantitatively.

Absolute Imaging and Clinical Applications of rEIT. It is essential that absolute imaging is achievable using rEIT for clinical applications such as breast cancer imaging ([17]). This study has established absolute imaging using rEIT on two tank experiments. Although tank experiments are more controlled compared to clinical situations it is an important step. Our prior studies in breast imaging ([5], [33]) involved an EIT system in which the woman would lie on a custom examination table with her breast hanging pendant. Four rings of 16 electrodes were then lightly pressed against the breast. It was very challenging to obtain accurate boundary information ([34]), which is needed for absolute imaging ([35]). To overcome this problem and to utilize the potential of rEIT, we envision a slight modification of the system in which the breast is compressed into a shallow tank with embedded electrodes. This scenario/system 1) can give accurate knowledge of the domain (and electrode positions), 2) is applicable for rEIT, and 3) could be combined with other modalities such as an automated whole breast ultrasound system ([36]). This system would be similar to [13], except in its use of relatively large electrodes, which are preferable ([15], [16]), and in the combination with ultrasound. The possible addition of a bi-modal system is important for data registration and could provide further improvements to reconstructions (e.g. [37]). Practical solutions such as a properly chosen ultrasound gel or a shallow saline bath could ensure proper electrode contact (with minimal shunting) and ease of tank rotations. This study represents an important step towards the development of such a system.

In ongoing research we are investigating a fused-data EIT approach for prostate cancer imaging applications by fusing multiple sets of transrectal EIT (TREIT) ([38], [39]) data together to form an improved reconstruction and we may investigate this approach in a related project, intraoperative surgical margin assessment ([6]). The analysis of modeling approaches performed here provides important lessons that can be used to better design and deploy EIT systems and potentially help to translate this technology to the clinic.

V. Conclusions

In conclusion this study 1) developed a method capable of obtaining spatially accurate absolute rEIT reconstructions with improved image contrast and an improved ability to distinguish between closely spaced inclusions compared to traditional EIT, 2) clearly illustrated improvements due to rEIT via mathematical analysis and qualitative and quantitative assessments from two tank experiments, and 3) demonstrated through direct analysis of the measured data clear limitations in the minimum rotation step that add new information. The ability to perform absolute reconstructions using rEIT on a practical clinical scenario (breast-shaped tank experiment) and clearly showing its improvements over traditional EIT are important steps towards using rEIT to improve previous EIT results in medical applications.

Acknowledgements

This work was supported in part by the U.S. National Institutes of Health under Grant 1R01CA143020–01A1 and DoD CDMRP Grant W81XWH-15-1-0102.

The authors would also like to thank Xiaotian Wu for his construction of the breast-shaped tank.

References

[1] R. H. Bayford, "Bioimpedance tomography (electrical impedance tomography)," *Annu. Rev. Biomed. Eng.*, vol. 8, pp. 63–91, Aug. 2006.
[2] T. York, "Status of electrical tomography in industrial applications," *J. Electron. Imag.*, vol. 10, no. 3, p. 608, 2001.
[3] S. Leonhardt and B. Lachmann, "Electrical impedance tomography: The holy grail of ventilation and perfusion monitoring?" *Intensive Care Med.*, vol. 38, no. 12, pp. 1917–1929, 2012.
[4] K. Y. Aristovich, G. S. dos Santos, B. C. Packham, and D. S. Holder, "A method for reconstructing tomographic images of evoked neural activity with electrical impedance tomography using intracranial planar arrays," *Phys. Meas.*, vol. 35, no. 6, pp. 1095–1109, 2014.
[5] R. J. Halter, A. Hartov, and K. D. Paulsen, "A broadband high-frequency electrical impedance tomography system for breast imaging," *IEEE Trans. Biomed. Eng.*, vol. 55, no. 2, pp. 650–659, Feb. 2008.

[6] A. Mahara, S. Khan, E. K. Murphy, A. R. Schned, E. S. Hyams, and R. J. Halter, "3D microendoscopic electrical impedance tomography for margin assessment during robot-assisted laparoscopic prostatectomy," *IEEE Trans. Med. Imag.*, vol. 34, no. 7, pp. 1590–1601, Jul. 2015.

[7] A. Cherepenin, Y. V. Gulyaev, A. V. Korjenevsky, S. A. Sapetsky, and T. S. Tuykin, "An electrical impedance tomography system for gynecological application GIT with a tiny electrode array," *Phys. Meas.*, vol. 33, no. 5, pp. 849–862, 2012.

[8] S. H. Arshad, J. S. Kunzika, E. K. Murphy, K. Odame, and R. J. Halter, "Towards a smart phone-based cardiac monitoring device using electrical impedance tomography," in *Proc. IEEE BioCAS*, Oct. 2015, pp. 1–4.

[9] S. C. Murphy and T. A. York, "Electrical impedance tomography with non-stationary electrodes," *Meas. Sci. Technol.*, vol. 17, pp. 3042–3052, Oct. 2006.

[10] C. N. Huang, F. M. Yu, and H. Y. Chung, "The scanning data collection strategy for enhancing the quality of electrical impedance tomography," *IEEE Trans. Instrum. Meas.*, vol. 57, no. 6, pp. 1193–1198, Jun. 2008.

[11] J. Liu, H. Xiong, L. Lin, and G. Li, "Evaluation of measurement and stimulation patterns in open electrical impedance tomography with scanning electrode," *Med. Biol. Eng. Comput.*, vol. 53, no. 7, pp. 589–597, 2015.

[12] C.-N. Huang, F.-M. Yu, and H.-Y. Chung, "Rotational electrical impedance tomography," *Meas. Sci. Technol.*, vol. 18, no. 9, pp. 2958–2966, 2007.

[13] X. Zhang, C. Chatwin, and D. C. Barber, "A feasibility study of a rotary planar electrode array for electrical impedance mammography using a digital breast phantom," *Phys. Meas.*, vol. 36, no. 6, pp. 1311–1335, 2015.

[14] D. S. Holder, Ed., *Electrical Impedance Tomography: Methods, History and Applications*. Philadelphia, PA, USA: IoP, 2005.

[15] D. G. Gisser, D. Isaacson, and J. C. Newell, "Electric current computed tomography and eigenvalues," *SIAM J. Appl. Math.*, vol. 50, no. 6, pp. 1623–1634, 1990.

[16] E. T. McAdams, J. Jossinet, A. Lackermeier, and F. Risacher, "Factors affecting electrode-gel-skin interface impedance in electrical impedance tomography," *Med. Biol. Eng. Comput.*, vol. 34, no. 6, pp. 397–408, 1996.

[17] B. H. Brown, "Electrical impedance tomography (EIT): A review," *J. Med. Eng. Technol.*, vol. 27, no. 3, pp. 97–108, 2003.

[18] E. Somersalo, M. Cheney, and D. Isaacson, "Existence and uniqueness for electrode models for electric current computed tomography," *SIAM J. Appl. Math.*, vol. 52, no. 4, pp. 1023–1040, 1992.

[19] K.-S. Cheng, D. Isaacson, J. C. Newell, and D. G. Gisser, "Electrode model for electric current computed tomography," *IEEE Trans. Biomed. Eng.*, vol. 36, no. 9, pp. 918–924, Sep. 1989.

[20] P. J. Vauhkonen, M. Vauhkonen, T. Savolainen, and J. P. Kaipio, "Three-dimensional electrical impedance tomography based on the complete electrode model," *IEEE Trans. Biomed. Eng.*, vol. 46, no. 9, pp. 1150–1160, Sep. 1999.

[21] A. Borsic, A. Hartov, K. D. Paulsen, and P. Manwaring, "3D electric impedance tomography reconstruction on multi-core computing platforms," in *Proc. Annu. Int. Conf. IEEE Eng. Med. Biol. Soc.*, Dec. 2008, pp. 1175–1177.

[22] T. Lee, M. Leok, and N. H. McClamroch, "Geometric numerical integration for complex dynamics of tethered spacecraft," in *Proc. Amer. Control Conf.*, May 2011, pp. 1885–1891.

[23] W. R. B. Lionheart, "EIT reconstruction algorithms: Pitfalls, challenges and recent developments," *Phys. Meas.*, vol. 25, no. 1, pp. 125–142, 2004.

[24] A. Borsic, *Regularisation Methods for Imaging From Electrical Measurements by Andrea Borsic*. 2002.

[25] A. Borsic, R. Halter, Y. Wan, A. Hartov, and K. D. Paulsen, "Electrical impedance tomography reconstruction for three-dimensional imaging of the prostate," *Phys. Meas.*, vol. 31, no. 8, pp. S1–S16, 2010.

[26] P. C. Hansen, *Rank-Deficient and Discrete Ill-Posed Problems*. 1998.

[27] J. L. Mueller and S. Siltanen, *Linear and Nonlinear Inverse Problems With Practical Applications*. 2012.

[28] J. Jossinet and M. Schmitt, "A review of parameters for the bioelectrical characterization of breast tissue," *Ann. New York Acad. Sci.*, vol. 873, pp. 30–41, Oct. 1999.

[29] S. Khan, P. Manwaring, A. Borsic, and R. Halter, "FPGA-based voltage and current dual drive system for high frame rate electrical impedance tomography," *IEEE Trans. Med. Imag.*, vol. 34, no. 4, pp. 888–901, Apr. 2015.

[30] N. K. Soni, H. Dehghani, A. Hartov, and K. D. Paulsen, "A novel data calibration scheme for electrical impedance tomography," *Phys. Meas.*, vol. 24, no. 2, pp. 421–435, 2003.

[31] M. Yasin, S. Böhm, P. O. Gaggero, and A. Adler, "Evaluation of EIT system performance," *Phys. Meas.*, vol. 32, no. 7, pp. 851–865, 2011.

[32] A. Nissinen, V. P. Kolehmainen, and J. P. Kaipio, "Compensation of modelling errors due to unknown domain boundary in electrical impedance tomography," *IEEE Trans. Med. Imag.*, vol. 30, no. 2, pp. 231–242, Feb. 2011.

[33] S. P. Poplack *et al.*, "Electromagnetic breast imaging: Results of a pilot study in women with abnormal mammograms," *Radiology*, vol. 243, no. 2, pp. 350–359, 2007.

[34] J. Forsyth, A. Borsic, R. J. Halter, A. Hartov, and K. D. Paulsen, "Optical breast shape capture and finite-element mesh generation for electrical impedance tomography," *Phys. Meas.*, vol. 32, no. 7, pp. 797–809, 2011.

[35] V. Kolehmainen, M. Vauhkonen, P. A. Karjalainen, and J. P. Kaipio, "Assessment of errors in static electrical impedance tomography with adjacent and trigonometric current patterns," *Phys. Meas.*, vol. 18, no. 4, pp. 289–303, 1997.

[36] K. M. Kelly and G. A. Richwald, "Automated whole-breast ultrasound: Advancing the performance of breast cancer screening," *Seminars Ultrasound*, vol. 32, no. 4, pp. 273–280, 2011.

[37] G. Steiner, M. Soleimani, and D. Watzenig, "A bio-electromechanical imaging technique with combined electrical impedance and ultrasound tomography," *Phys. Meas.*, vol. 29, no. 6, pp. S63–S75, 2008.

[38] H. Syed, A. Borsic, A. Hartov, and R. J. Halter, "Anatomically accurate hard priors for transrectal electrical impedance tomography (TREIT) of the prostate," *Phys. Meas.*, vol. 33, no. 5, pp. 719–738, 2012.

[39] Y. Wan, A. Borsic, A. Hartov, and R. Halter, "Incorporating a biopsy needle as an electrode in transrectal electrical impedance imaging," in *Proc. Annu. Int. Conf. IEEE Eng. Med. Biol. Soc. (EMBS)*, Aug. 2012, pp. 6220–6223.

Physiological Measurement

IPEM Institute of Physics and Engineering in Medicine

PAPER

Comparative study of separation between *ex vivo* prostatic malignant and benign tissue using electrical impedance spectroscopy and electrical impedance tomography

To cite this article: Ethan K Murphy *et al* 2017 *Physiol. Meas.* **38** 1242

View the article online for updates and enhancements.

Related content

- Genetic and least squares algorithms for estimating spectral EIS parameters
  Ryan J Halter, Alex Hartov, Keith D Paulsen et al.
- Anatomically accurate hard priors for transrectal electrical impedance tomography (TREIT) of the prostate
  H Syed, A Borsic, A Hartov et al.
- Electrical impedance tomography reconstruction for 3D imaging of the prostate
  A Borsic, R Halter, Y Wan et al.

This content was downloaded from IP address 129.170.195.65 on 28/09/2017 at 10:16

IOP Publishing | Institute of Physics and Engineering in Medicine Physiological Measurement

Physiol. Meas. **38** (2017) 1242–1261 https://doi.org/10.1088/1361-6579/aa660e

Comparative study of separation between *ex vivo* prostatic malignant and benign tissue using electrical impedance spectroscopy and electrical impedance tomography

Ethan K Murphy[1], Aditya Mahara[1], Shadab Khan[2,3], Elias S Hyams[4,5], Alan R Schned[4,5], Jason Pettus[4,5] and Ryan J Halter[1,5]

[1] Thayer School of Engineering, Dartmouth College, 14 Engineering Drive, Hanover, NH 03755, United States of America
[2] Boston Children's Hospital, Boston, MA 02115, United States of America
[3] Harvard Medical School, Boston, MA 02115, United States of America
[4] Dartmouth-Hitchcock Medical Center, Lebanon, NH 03766, United States of America
[5] Geisel School of Medicine, Dartmouth College, Hanover, NH 03755, United States of America

E-mail: ethan.k.murphy@dartmouth.edu

Received 7 December 2016, revised 22 February 2017
Accepted for publication 10 March 2017
Published 22 May 2017

Abstract

Objective. Currently no efficient and reliable technique exists to routinely assess surgical margins during a radical prostatectomy. Electrical impedance spectroscopy (EIS) has been reported as a potential technique to provide surgeons with real-time intraoperative margin assessment. In addition to providing a quantified measure of margin status, a co-registered electrical impedance tomography (EIT) image presented on a surgeon's workstation could add value to the margin assessment process. *Approach.* To investigate this, we conducted a comparative study between EIS and EIT to evaluate the potential these technologies might have for margin assessment. EIS and EIT data was acquired from *ex vivo* human prostates using a multi-electrode endoscopic impedance acquisition probe. *Main results.* EIS and EIT show good predictive performance with a 0.76 and 0.80 area-under-curve (AUC), respectively, when considering discrete frequencies only. A machine learning (ML) algorithm is implemented to combine features, which improves the AUCs of EIS and EIT to 0.84 and 0.85, respectively. Single-

 © 2017 Institute of Physics and Engineering in Medicine Printed in the UK

step EIT takes significantly less time to reconstruct than multi-step EIT, yet provides similarly accurate classification results, making the single-step approach a potential candidate for real-time margin assessment. While the ML-based approach clearly exhibits benefits as compared to the single feature assessment, the decision to use EIS versus EIT is unclear since each approach performs better for different subsets of tissue classifications. *Significance.* The results presented in this paper corroborate our previous studies and present the strongest evidence yet that an intraoperative-capable impedance probe can be used to distinguish benign from malignant prostate tissues. An *in vivo* study with a large cohort will be necessary to definitively determine the preferred approach and to show the clinical effectiveness of using this technology for margin assessment.

Keywords: electrical impedance spectroscopy, electrical impedance tomography, prostate cancer

(Some figures may appear in colour only in the online journal)

1. Introduction

Prostate cancer is currently one of the most common cancers and second most fatal cancer in men in the United States (US). In 2016, approximately 180 890 men were diagnosed with prostate cancer, and 26 120 men were expected to die of the disease (Siegel *et al* 2016). Surgical removal of the prostate through a radical prostatectomy (RP) represents a potential treatment strategy for men with organ-confined prostate cancer. The Center for Disease Control has reported that over 100 000 RPs are performed annually in the US (CDC 2010). To ensure surgical efficacy, it is important to verify that no cancer cells extend beyond the margins of the excised prostate. Cancer found on this margin suggests that additional cancer cells might remain within the peri-prostatic tissue of the pelvic cavity. No clinical protocols are routinely used to intraoperatively assess these surgical margins. Instead, margins are evaluated through pathological assessment of the prostate *following* RP, when it is too late to provide additional surgical intervention. Positive surgical margins (PSMs) are associated with disease recurrence and are often treated with toxic adjuvant therapies. Average PSM rates in contemporary robot-assisted laparoscopic prostatectomy (RALP) procedures range from 6.5% to 32% (Yossepowitch *et al* 2014), and around 80% of the RPs are performed robotically (NCI 2015). Incidence of PSMs decrease disease-free survival rates; 10 years after RP, the disease-free survival rate for patients without PSM is 73–90%, while for patients with PSMs the rate is 49–60% (Orvieto *et al* 2006, Rouanne *et al* 2014). Reducing the number of PSMs will: (1) reduce the morbidity associated with adjuvant and salvage therapies in patients who would have had PSMs, (2) reduce the financial burdens associated with treatment of recurrent cancer on the patient and healthcare providers, and (3) reduce the mortality rate associated with prostate cancer recurrence.

This study explores electrical impedance spectroscopy (EIS) and electrical impedance tomography (EIT) as the basis for a surgical margin assessment (SMA) tool. It has the potential to be a low-cost, radiation free, real-time technique, which could significantly impact clinical outcomes thereby leading to enhanced quality of life for patients following RP. Based on previous findings, EIS has been successfully shown to distinguish between malignant and

benign prostate tissue (Halter *et al* 2007, 2008a, 2008b). Cancerous prostatic tissue has a significantly lower conductivity than benign stroma and glandular prostatic tissues at frequencies ranging from 0.1 to 100 kHz and a permittivity that is significantly higher than all benign tissues at 100 kHz (Halter *et al* 2009). Based on these studies we have been recently developing SMA EIS/EIT probes. Khan *et al* reported preliminary results from this effort where a technique called the composite impedance metric (CIM) was used to establish separation between benign and malignant prostatic tissue that had a predictive accuracy of 90.3% using the support vector machine (SVM) algorithm and a best area-under-curve (AUC) from receiver operator characteristic (ROC) analysis of 0.86 (Khan *et al* 2016). However, there were several limitations to this study that should be addressed. First, the labelling procedure was inexact, probe measurement locations were only known to within a quadrant of a prostatic slice, where the quadrant is roughly 6 times the area of the probe. Second, the resolution of the probed sites for the 9-electrode probe used is limited to a diameter of 7.5 mm. Third, the high frequency phase data used to conduct SVM classification may be affected by the presence of stray capacitance in the system, which is nearly 300 pF at each channel (Khan *et al* 2016).

Other approaches have been investigated for SMA during RP, including several optical-based approaches, e.g. (Yadav *et al* 2009, Gao *et al* 2011), and intraoperative frozen section (IFS) analysis (Fromont *et al* 2003, Von Bodman *et al* 2013). IFS analysis has been the most-studied SMA approach, but its use is still controversial (Von Bodman *et al* 2013), as the IFS procedure adds significant surgical time (20–30 min) and co-registration is challenging.

This report presents an *ex vivo* study of 19 human prostates in which a radially distributed 17-electrode endoscopic probe and Dartmouth's electrical impedance acquisition (EIA) System (figure 1) were used to record impedances. Here we overcome the shortcomings of the previous study (Khan *et al* 2016); (1) probe locations are accurately co-registered to histology, (2) the 17-electrode probe yields higher resolution measurements (the 17-electrode probe provides twice the resolution as the 9-electrode probe used in Khan *et al* (2016)), and (3) a multi-frequency SVM approach is used that is not solely reliant on high frequency reactance/permittivity data. EIS and EIT show good predictive performance with the best AUCs being 0.76 and 0.80, respectively, when considering discrete frequencies, and the SVM improves the AUCs of EIS and EIT to 0.84 and 0.85, respectively (the corresponding sensitivity and specificities are (0.81, 0.73) for EIS and (0.73, 0.90) for EIT, respectively).

The paper is structured as follows. After describing the probe and acquisition system in section 2, the dataset and clinical protocol are described in section 3. Following this, the EIT algorithm is described and data analysis is detailed in terms of features used and the machine learning algorithm leveraged. Benefits and challenges of both techniques and their potential clinical impacts are discussed.

2. Methods

2.1. Data acquisition: Dartmouth electrical impedance acquisition (EIA) system and probe

The Dartmouth EIA system is a broadband (100 Hz–10 MHz) 32-channel data acquisition (DAQ) system with a SNR $>$ 90 dB and possesses high speed capabilities (up to 80 frames/second) (Khan *et al* 2013). The system is flexible and has a modular hardware and software design that allows for performance upgrades such as DAQ frame rate and SNR. The EIA uses National Instruments (NI) hardware and software modules, which offer inherent compatibility over generations of hardware and software revisions.

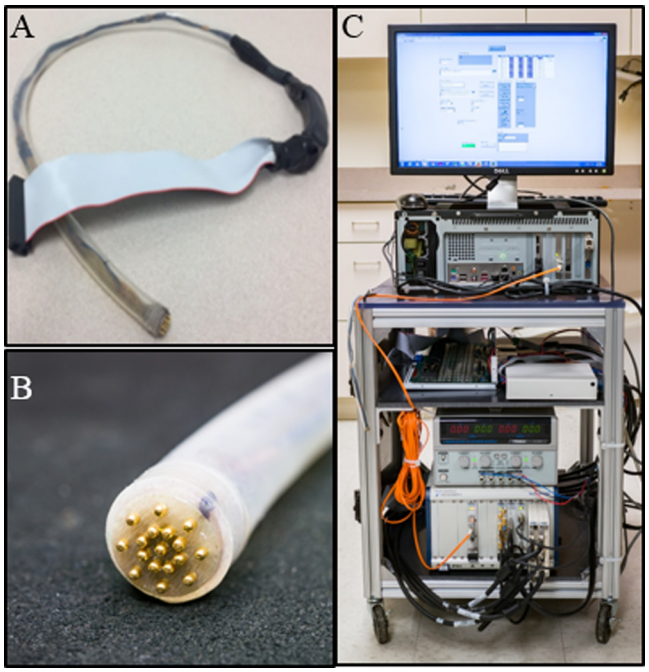

Figure 1. (A) 17-electrode probe showing connector interface to the electrical impedance data acquisition system, (B) the probe surface, and (C) Dartmouth EIA system.

A radially distributed 17-electrode microendoscopic probe is used for data collection (Mahara *et al* 2015); the probe is 11 mm in diameter with 1 mm diameter gold-plated electrodes (205089-4-ND, DigiKey) that protrude 1 mm from the probe face and have rounded hemispherical ends (see figures 1(B) and 2(A)). The probe tip housing is constructed using electrical-grade G-9 type garolite (McMaster Carr, Elmhurst, Illinois), a continuous-woven glass fabric laminated with an epoxy resin. The water absorption of G-9 garolite is 0.69–0.074%, compressive strength is 15 000–35 000 psi, dielectric strength is 370–450 volts/mil, and thermal stability ranges up to 137.8 °C (McMaster-Carr 2014). These characteristics provide for a robust probe design that is strong, nonabsorbent, and capable of undergoing repeated steam sterilization processing (probe exposed to 125 °C for 25 min) as is required prior to intraoperative use.

Multiple four-electrode (tetrapolar) measurement combinations can be used to gauge impedance. We specifically focus on 3 types: (1) All tetrapolar patterns, (2) Outer ring patterns, and (3) Inner ring patterns. Impedance measurements from a total of 14 280 electrode combinations are recorded during each impedance acquisition (All patterns). For outer or inner ring tetrapolar impedance patterns, a small current (<1 mA_{rms} as specified by the IEC 60601-1 standard (IEC 60601-1:2005 2005)) is driven between two electrodes spaced 3 electrodes apart (e.g. 10 and 13 figure 2(B)), and the voltage difference between the pair of adjacent electrodes located between the driving electrodes (e.g. 11 and 12 figure 2(B)) is measured. Using this approach, inner ring impedances were recorded with 8 current drive electrode pairs (6/9, 7/2, 8/3, 9/4, 2/5, 3/6, 4/7, and 5/8) and outer ring impedances were recorded with pairs (14/17, 15/10, 16/11, 17/12, 10/13, 11/14, 12/15, and 13/16). Since these inner and outer

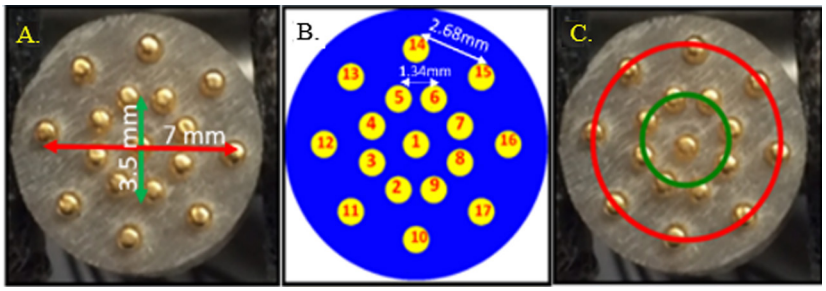

Figure 2. The 17-electrode probe face showing (A) top view of contact surface, (B) electrode numbering scheme, and (C) the inside ring (green) and outside ring (red) of electrodes used for EIS analysis (adapted from Mahara *et al* (2015), © 2017 IEEE. Reprinted, with permission, from IEEE).

patterns are rotationally symmetric, the effects due to unused electrodes (i.e. current shunting) for each measurement pattern should be consistent across all inner and outer measurements, respectively. The reciprocal of each of these drive pairs was also used (i.e. 6/9 and 9/6) to give a total of 16 impedance measurements per ring. A noise filter applied to the data removes patterns whose (1) voltage difference is too small (<50 mV), (2) voltage or current noise power is too large (>2 V and >3/(499 Ω) A for voltage and current, respectively; see Khan *et al* (2016) for description of noise power measurements in this system and note that 499 Ω is the resistor used on the current sense electrode), and/or (3) if the sensed current magnitude is too small (<0.1 mA, in voltage drive mode). These thresholds were empirically determined and were conservatively chosen to keep higher quality measurements.

Prior to making tissue measurements, the probe is placed in a 0.1 S m^{-1} saline bath and impedances are recorded. Using the forward model of EIT (see section 2.3.1) simulated resistances and reactances are calculated. The ratio between the measured and simulated impedances defines a complex, frequency-dependent calibration factor that is used to adjust every tetrapolar impedance measurement. This is a standard approach used to minimize instrumentation errors associated with channel-to-channel variations and electrode imperfections (Wan *et al* 2013).

2.2. Clinical data collection procedure: probing and histology

The probe was used to gauge the electrical properties of 19 *ex vivo* prostates removed during RALP procedures performed by a single surgeon at Dartmouth–Hitchcock Medical Center, which was conducted under an IRB approved protocol and includes data from consenting individuals. Immediately following RALP, the resected prostate was transferred to the Anatomic Pathology Laboratory. The prostate was sectioned into 2–5 mm thick slices and intraprostatic measurements were acquired from the cut tissue surfaces (figure 3) at 11 discrete frequencies (5, 10, 20, 30, 40, 50, 60, 70, 80, 90, 100 kHz). The measurements were performed approximately 30 min post-resection, at which time the prostate cooled to room temperature (~25 °C). The probe was pressed against the cut surface of 3–4 slices per case. Since the applied pressure can impact impedance measurements (González-Correa *et al* 2005), a single individual (AM) performed all EIS measurements while attempting to apply a consistent pressure across all cases. The intraprostatic probed locations included both benign and grossly identifiable cancer regions. Immediately after recording the impedance data, three pins were inserted next

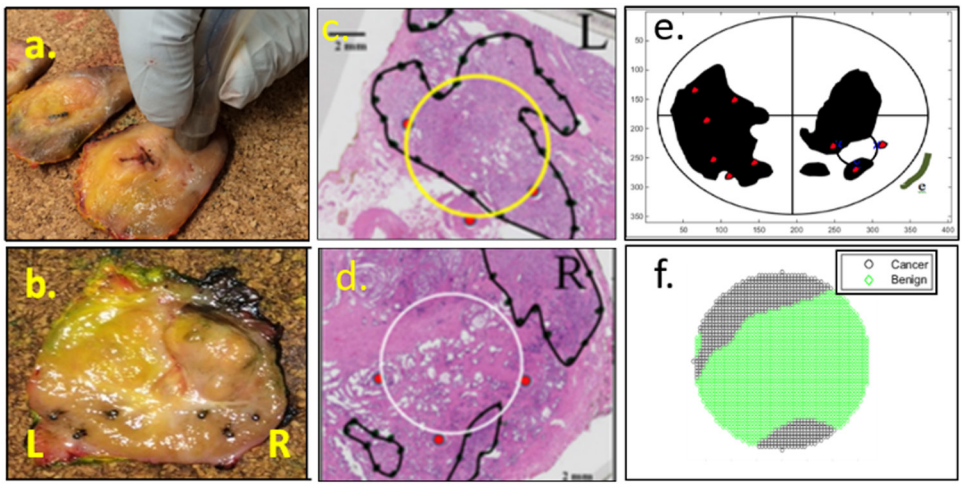

Figure 3. *Ex vivo* data acquisition and labeling procedure. (a) An example of a probed measurement, (b) 3 pins used to localize the probed location, (c) and (d) micrograph (L) and (R) examples showing pin locations in red, (e) cancer islands enclosed in black, and (f) image processing of the probed location is used to determine the percent cancer of the measurement (adapted from Mahara *et al* (2015), © 2017 IEEE. Reprinted, with permission, from IEEE).

to electrode 10, 12, and 16 (figure 2(B)) in order to mark the location and orientation that was probed (figure 3(b)). Specimens were fixed and stained with H&E for microscopic evaluation (figures 3(c) and (d)), maps were created to specify the cancerous regions within the slice and to determine each probed location and orientation (figure 3(e)). Image processing was used to calculate the percent benign and cancer for each probed site (figure 3(f)). The slices are either fully benign (Bn) or have some distribution of prostatic cancer (PCa). The PCa distributions are presented in table 1.

Impedance data were recorded from 135 intraprostatic tissue sites from 19 patients which were divided into 5 groups defined by cancer content (table 1). It has been suggested that the prognosis for men with PSMs <3 mm is statistically better than that of men with PSMs >3 mm (Ochiai *et al* 2008). Given that the area sensed by the probe is 38.5 mm^2 (diameter of 7 mm), a 3 mm diameter (7.1 mm^2) tumor region is equivalent to 18% of the probed area. Thus this 18% cutoff was used to define two of the groups (G2 and G3), which allows for additional clinically relevant analysis of the data.

2.3. Electrical impedance tomography

2.3.1. Forward problem. The forward problem relies on the Laplace equation.

$$\nabla \cdot \sigma \nabla u = 0, \tag{1}$$

to calculate the electric potential, u, over the entire domain, where σ is the conductivity. In order to realistically account for discrete electrodes and obtain accurate boundary electrode voltage data, the complete electrode model (CEM) is used (Somersalo *et al* 1992), which has been found to be the most accurate electrode model (Cheng *et al* 1989). The CEM-based boundary conditions specify the current and contact impedance at each electrode and assume

Table 1. Grouping of *ex vivo* data.

Groups	% Cancer	Cases
1	0%	105
2	1–18%	7
3	19–100%	23
4	1–100%	30
5	100%	12
Total	0–100%	135

that no current flows in or out of the system except through the electrodes. The finite element method (FEM) in 3D with linear basis functions is used to calculate the forward problem.

2.3.2. Inverse problem. The inverse problem aims to recover the conductivity distribution within the domain from the boundary voltage measurements due to different sets of applied currents. At each frequency, the EIS measurements are used as the input to the EIT inverse problem. A Gauss–Newton algorithm employing a Tikhonov regularization scheme is used. This inverse algorithm attempts to minimize the following

$$E(\boldsymbol{\sigma}) = \frac{1}{2}||\mathbf{F}(\boldsymbol{\sigma}) - \mathbf{V}_{\text{Meas}}||_2^2 \; + \frac{\alpha}{2}||\mathbf{L}(\boldsymbol{\sigma} - \boldsymbol{\sigma}_0)||_2^2, \tag{2}$$

with respect to the conductivity, $\boldsymbol{\sigma} \cdot \mathbf{F}(\boldsymbol{\sigma})$ and $\mathbf{V}_{\text{Meas}}$ are concatenated vectors of all the simulated and measured voltage patterns, respectively, α is the Tikhonov factor, $\mathbf{L}$ is a regularization matrix, and $\boldsymbol{\sigma}_0$ is the initial or previous estimate of the conductivity. This is a standard approach to EIT reconstructions that after linearizing the problem results in a iterative algorithm to recover the conductivity, see Lionheart (2004) for a detailed discussion.

We solve the EIT problem in two ways; (1) assuming the conductivity is a constant throughout the whole domain (constant EIT), and (2) assuming that the conductivity varies spatially below the probe site (3D EIT). In the first approach, the regularization term can be ignored because the problem is no longer ill-conditioned when there is only one unknown. The second approach utilizes a technique (Murphy *et al* 2016) that was purposely developed for open-domain probes, such as this SMA device. The technique separates the domain into a local region where we expect sufficient sensitivity to accurately estimate spatially dependent conductivity values and an outer region that is assumed constant (referred to as a mega node (MN)). The local sensitive region is connected to the MN through the regularization matrix, which reduces boundary artifacts. The same parameters that yielded the best reconstructions from Murphy *et al* (2016) are used, i.e. a $20 \times 20 \times 8$ rectilinear grid was used for the inverse dual mesh (Borsic *et al* 2010) where the tolerance for the region of sensitivity was chosen to be 1/400 and the MN constrained Laplace smoothing technique was used with a Tikhonov factor of 1×10^5. The 8 discrete z-values, from the rectilinear grid, correspond to reconstructions at 8 distinct depths, which are 0.2, 0.5, 0.8, 1.1, 1.5, 2.2, 3.2, 4.3 mm. Although some prostate slices were likely thinner than the reconstruction mesh, all reconstructions used this single mesh (extending down to 4.3 mm) for consistency and because slice thickness was not measured.

Only absolute reconstructions were produced in this study, and reconstructions using 1 and 3 steps (iterations) were considered. One would expect that more iterations would provide more accurate reconstructions. However, there is an additional computational cost of using multiple iterations. Thus the EIT results are evaluated in terms of their quality and computational cost.

Table 2. Benign (Bn) to cancer (PCa) comparisons.

Group comparison	% Cancer type		Tissue sites		Ratio (Bn to PCa)
	Bn	PCa	Bn	Ca	
1 versus 2	0%	1–18%	105	7	15.0
1 versus 3	0%	19–100%	105	23	4.6
1 versus 4	0%	1–100%	105	30	3.5
1 versus 5	0%	100%	105	12	8.8

2.4. Data analysis

Benign tissues (Group 1) were compared to cancerous tissues (Groups 2–5) by identifying significant differences and the predictive properties of the impedance features individually and jointly using an SVM. Details of these group comparisons are given in table 2. The predictive measures are the AUC, sensitivity (SN), specificity (SP), positive predictive value (PPV), negative predictive value (NPV), and accuracy (ACCU). The optimal threshold was calculated as the closest point on the ROC curve to (0, 1), i.e. the closest point to 100% sensitivity and 100% specificity.

2.4.1. Features. In this study, EIS, constant EIT, and 3D EIT features are explored. Their descriptions are summarized in table 3 and the feature characteristics are described here. EIS features include the 11 resistances (R), 11 reactances (X), 11 magnitudes ($\sqrt{R^2 + X^2}$), and 11 phases ($\tan^{-1}(X/R)$) of an inner or outer ring impedance pattern corresponding to the 11 frequencies. Samples were considered to be each of the inner or outer patterns (8), standard and reciprocal patterns (2), and all intraprostatic tissue sites (135). Thus the overall size of the EIS feature set for inner and outer patterns was 2160 samples $\times$ 44 features, where $2160 = 8 \cdot 2 \cdot 135$ and $44 = 11 \cdot 4$. The 16 patterns (with reciprocals) were separated into different samples because they represent (physically) different measurements of the prostate tissue and it provided a means to increase the number of samples.

Constant EIT features included the reconstructed conductivity and permittivity values (2) using either inner, outer, or all tetrapolar patterns (3) at the 11 discrete frequencies. 3D EIT features included the average reconstructed conductivity and permittivity values (2) using all the tetrapolar measurements at each of the 8 depths, plus an overall average, at each of the 11 frequencies. The overall feature set size was 135 $\times$ 66 and 135 $\times$ 198, where $66 = 2 \cdot 3 \cdot 11$ and $198 = 2 \cdot (8 + 1) \cdot 11$ for the constant and 3D EIT features, respectively. Samples for the EIT reconstructions corresponded 1-to-1 with the probe sites, as one could not separate reconstructions like the EIS measurements recorded for each pattern.

2.4.1.1. Discrete feature analysis. For each group comparison, significance tests were performed between each group and for each feature the predictive scores were calculated. A two-sample t-test was used to determine significance with a p value of 0.05. A total of 44, 66, and 198 ROC analyses were performed and all performance metrics including AUC, ACCU, SN, SP, PPV, and NPV are computed for the EIS, constant EIT, and 3D EIT feature sets, respectively.

Table 3. Description of features.

Type	Total set size (samples × features)	Sample description	Feature description
EIS (inner or outer)	2160 × 44	From each probe site the 8 patterns, standard or reciprocal	Resistance, reactance, magnitude and phase at each frequency (11)
Constant EIT	135 × 66	Each probe site	Conductivity and permittivity values using inner, outer, and all patterns at each frequency (11)
3D EIT	135 × 198	Each probe site	Conductivity and permittivity values using all patterns at each depth and an overall average (9) at each frequency (11)

2.4.1.2. Multi-feature evaluation: SVM. A binary SVM classifier is used for the group comparisons presented in table 2. Functions from the statistics and machine learning toolbox in MATLAB r2016b are used to implement, train, and test the SVM classifier. For every comparison, we train a SVM model using a leave-one-patient-out (LOPO) approach and a Gaussian kernel function. The LOPO approach is used to ensure that the training is fair, i.e. if data is very consistent on individual patients then this advantage is removed using this training approach. After numerous manual searches for optimal parameters, the kernel scale was set to 5 and the box constraint was set to 1. For the comparisons, the SVM is trained by selecting a randomized subset of Bn datasets equaling the total number of PCa datasets to limit any potential training model biases due to imbalanced datasets (Kotsiantis *et al* 2006). This process is repeated 200 times to minimize effects of variability in results due to randomized datasets. The SVM model outputs predicted labels (classification result) and posterior probabilities (probability that the classifier is correct, (Platt 1999)) from all the random draws; these are used to create ROC curves for each run. An average AUC is calculated across all runs.

An iterative feature extraction algorithm is used to select the optimal subset of features that maximizes the AUC. First, the features that yielded significant differences are sorted in descending order of AUCs from the discrete feature analysis. Next, the SVM classification algorithm is performed using the best feature. Each subsequent feature is tested one at a time where each candidate feature is retained into the optimal set of features if it improves the overall AUC of the SVM. If the AUC of the SVM algorithm decreases then that feature is disregarded. This feature extraction processes iteratively and in a greedy fashion selects the best feature sets that maximizes the AUC of the SVM algorithm. We report results on the final best feature set for each of the group comparisons and approaches.

3. Results

3.1. Discrete feature analysis

Discrete features analyzed include the inner and outer pattern EIS data, constant EIT using 1 and 3 iterations, and 3D EIT using 1 and 3 iterations. As an example, figure 4 shows the outer ring EIS measurements and outer ring constant EIT data using 3 iterations. The data is separated between groups, and an asterisk (∗) denotes when there are significant differences between groups. The boxes represent 25–75% quantiles, the whiskers extend from the

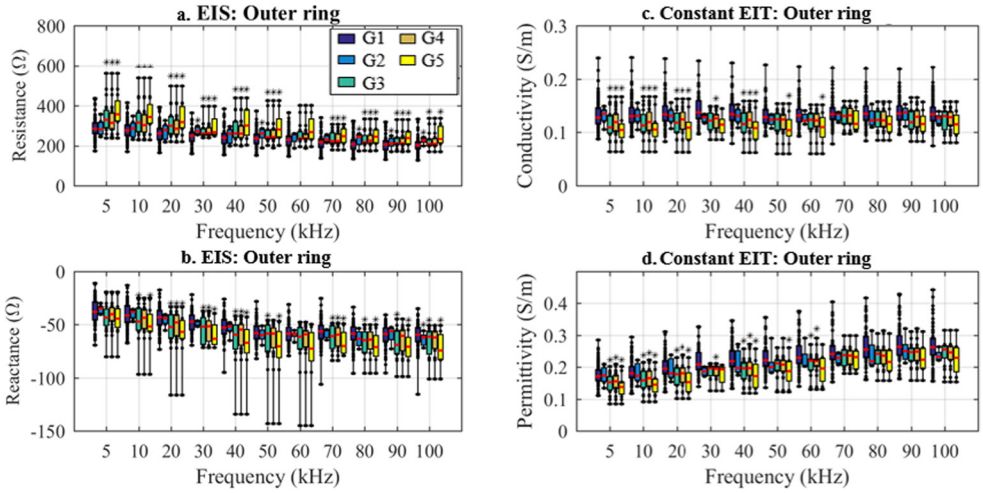

Figure 4. Outer ring EIS impedance ((a) and (b)) and constant EIT conductivity and permittivity data corresponding to all 5 groups and all 11 frequencies. EIS is visualized in terms of the average impedance of the 8 standard patterns from each probe site. The boxes represent 25–75% quantiles, the whiskers extend to the minimum and maximum data point, black dots show all points outside the quantiles, the red line represents the median of the data, and the asterisks (∗) denote when there is a significant difference ($p < 0.05$) between the given group and G1.

minimum to the maximum data points, black dots show all points outside the quantiles, and the red line represents the median of the data. The longer whiskers indicate that there are some apparent outliers, although these data points were not determined to be bad in terms of measurement quality. The impedance and conductivity/permittivity appear related and follow expected trends across frequencies. It is expected that if impedances for cancerous tissues are higher than benign tissues, the conductivities of cancerous tissues would be lower than benign tissues. A similar relationship is observed between the absolute value of the reactance and permittivity. In general, these trends hold as shown in figures 4(a) and (c). No perfect separation exists between any two groups. However, the boxes, representing 25%–75% quantiles, are distinctly separate between G1 and G5 for the three lowest frequencies for the EIS resistance and the constant EIT conductivity and permittivity.

ROC analyses were performed using only features that exhibit significant differences for all four group comparisons. The AUCs for these significantly different features for all EIS and EIT methods are reported in figure 5. The majority of the G1 versus G5 comparison features were significantly different, and yielded the highest AUCs (majority between 0.70–0.85 AUC) among any other group comparisons. This is because G5 (100% PCa) has the highest presence of PCa among any groups, and therefore provides the largest distinction from G1 (Bn) data. The best AUC for the G1 versus G5 comparison was 0.85, which corresponds to permittivity using 3D EIT at a frequency of 90 kHz and depth of 0.5 mm.

On the contrary, only 3 features for outer ring EIS, and 1 feature for inner ring EIS were significantly different for G1 versus G2 and none for any of the EIT based methods. Among the few features that were significantly different, the AUCs were relatively low (close to 0.6). The G2 (<18%) PCa has the least amount of PCa among any PCa groups which we expect to be the most challenging to distinguish from benign prostate. Further, the significant feature

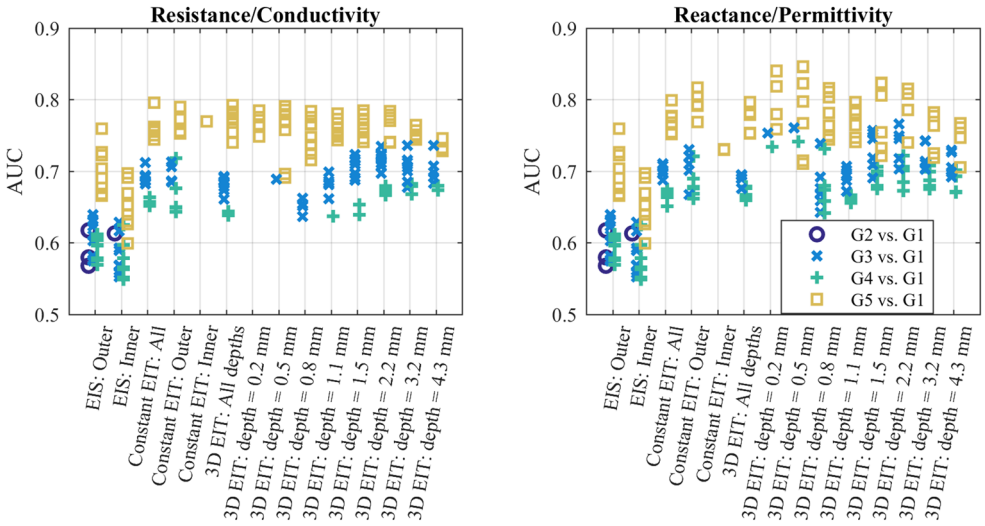

Figure 5. AUC values calculated from performing ROC analysis on features that yielded significant differences from G1 for each of the EIS and EIT methods considered (EIT methods used 3 steps). All frequencies are plotted for each method.

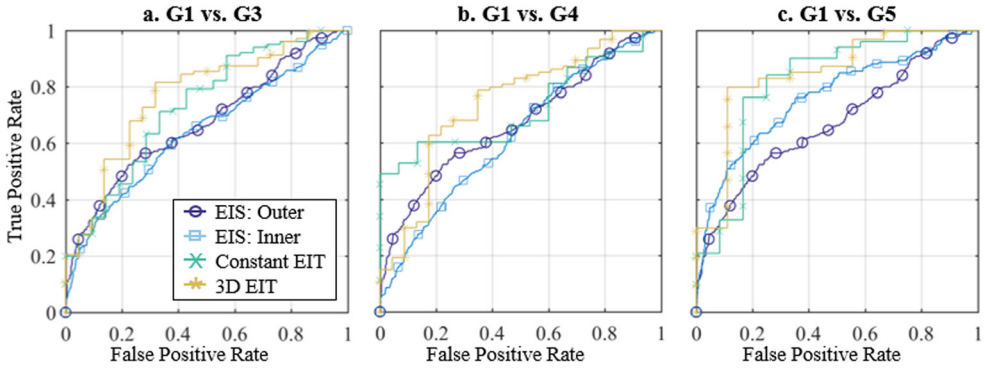

Figure 6. ROC curves of the features with the highest AUCs for the EIS: outer, EIS: inner, constant EIT (3-step), and 3D EIT (3-step). The feature details along with predictive metrics are listed in table 4.

differences and AUC performances for the other two comparisons (G1 versus G3) and (G1 versus G4) were better than G1 versus G2, but worse than G1 versus G5. Formal comparison between G1 and G2 was omitted due to lack of significantly different features and minimal separation in terms of impedance (figure 4).

The features with best AUCs for each of the methods (EIS: outer, EIS: inner, constant EIT, and 3D EIT) are plotted in figure 6 and their predictive properties specified in table 4. The AUCs for EIS outer and EIS inner are less then AUCs for constant EIT and 3D EIT in all three comparisons (G1 versus G3; G1 versus G4; G1 versus G5). This implies that a discrete feature group for EIT is better able to separate Bn from various groupings of PCa than EIS. A striking observation is the very poor positive predictive value (PPV ~0.21–0.45) for all features and group comparisons. This can be primarily attributed to the imbalance between benign

Table 4. Prediction metrics for the best discrete features: sensitivity (SN), specificity (SP), positive predictive value (PPV), negative predictive value (NPV), accuracy (ACCU), and area-under-curve (AUC).

G1 versus G3: method	Freq. (kHz)	Type/depth	SENS	SPEC	PPV	NPV	ACCU	AUC
EIS: outer	20	Resistance	0.56	0.73	0.32	0.88	0.70	0.67
EIS: inner	40	Magnitude	0.60	0.62	0.27	0.88	0.62	0.64
Cons. EIT: Cond., 1-step	40	Outer	0.58	0.81	0.39	0.90	0.77	0.72
Cons. EIT: Perm., 1-step	40	Outer	0.71	0.66	0.31	0.92	0.67	0.74
Cons. EIT: Cond., 3-step	40	Outer	0.58	0.78	0.37	0.90	0.75	0.71
Cons. EIT: Perm., 3-step	40	Outer	0.67	0.71	0.33	0.91	0.70	0.73
3D EIT: conductivity, 1-step	40	1.5 mm	0.76	0.66	0.33	0.93	0.68	0.71
3D EIT: permittivity, 1-step	10	1.5 mm	0.65	0.79	0.41	0.91	0.77	0.76
3D EIT: conductivity, 3-step	90	3.2 mm	0.69	0.74	0.31	0.93	0.74	0.74
3D EIT: permittivity, 3-step	5	2.2 mm	0.68	0.82	0.44	0.92	0.79	0.77
G1 versus G4								
EIS: outer	20	Resistance	0.56	0.73	0.32	0.88	0.70	0.67
EIS: inner	30	Reactance	0.66	0.51	0.27	0.84	0.54	0.62
Cons. EIT: Cond., 1-step	30	Outer	0.73	0.64	0.37	0.89	0.66	0.73
Cons. EIT: Perm., 1-step	30	Outer	1.00	0.53	0.38	1.00	0.63	0.70
Cons. EIT: Cond., 3-step	30	Outer	0.80	0.58	0.35	0.91	0.63	0.72
Cons. EIT: Perm., 3-step	30	Outer	0.87	0.60	0.38	0.94	0.66	0.72
3D EIT: conductivity, 1-step	30	3.2 mm	0.64	0.64	0.31	0.87	0.64	0.68
3D EIT: permittivity, 1-step	10	1.5 mm	0.60	0.79	0.45	0.87	0.75	0.71
3D EIT: conductivity, 3-step	30	3.2 mm	0.64	0.64	0.31	0.87	0.64	0.68
3D EIT: permittivity, 3-step	90	0.5 mm	0.78	0.66	0.36	0.93	0.68	0.74
G1 versus G5								
EIS: outer	40	Magnitude	0.56	0.73	0.32	0.88	0.70	0.67
EIS: inner	40	Resistance	0.75	0.65	0.21	0.96	0.66	0.76
Cons. EIT: Cond., 1-step	10	Outer	0.83	0.81	0.34	0.98	0.81	0.80
Cons. EIT: Perm., 1-step	10	Outer	0.83	0.75	0.29	0.97	0.76	0.82
Cons. EIT: Cond., 3-step	40	Outer	0.82	0.78	0.30	0.97	0.79	0.80
Cons. EIT: Perm., 3-step	40	Outer	0.83	0.76	0.29	0.97	0.77	0.82
3D EIT: conductivity, 1-step	90	0.5 mm	0.78	0.81	0.28	0.97	0.81	0.79
3D EIT: permittivity, 1-step	5	All depths	0.67	0.87	0.38	0.96	0.85	0.80
3D EIT: conductivity, 3-step	40	All depths	0.73	0.82	0.32	0.96	0.81	0.79
3D EIT: permittivity, 3-step	90	0.5 mm	0.89	0.80	0.30	0.99	0.81	0.85

and cancer samples. That is, when there are many more cancer cases than benign, the optimal choice from the ROC analysis is insensitive to the large percent of false positives.

The AUC for inner ring EIS is better than outer ring by 9% for G1 versus G5 comparison, although both are relatively low at 0.76 and 0.67, respectively. However, the outer ring AUC is better than inner ring by 5% and 3% for G1 versus G4 and G1 versus G3, respectively, but the overall AUC performance remain in the mid-60s. Due to the low AUC performance metrics

for EIS based analysis, nothing significant can be concluded from the trends between the inner and outer rings at various groupings. In general, the AUCs are better for EIT results.

For the EIT results, the 1-step constant EIT is nearly the same as the 3-step constant EIT reconstructions, but the 1-step 3D reconstructions are consistently worse than the 3-step 3D reconstructions. Specifically, for the G1 versus G5 comparison, the constant EIT AUCs are identical for 1 step and 3 step estimations for both conductivity and permittivity (i.e. AUCs $= 0.80$ and 0.82, respectively). For 3D EIT reconstructions, the 3-step permittivity estimation is enhanced 5% to 0.85 as compared to same reconstruction using a single step. These trends generally persist for G1 versus G3 and G1 versus G4, although they are not as prominent as that observed for G1 versus G5.

3.2. Multi-feature evaluation

A ROC analysis was performed for an optimal subset of features selected using the greedy, iterative feature extraction algorithm and the SVM binary classification. This analysis uses multi-feature information and can combine useful information from many distinct frequencies. As expected, the AUCs of separation for all comparison are higher than when only using 1 best discrete feature as presented in section 3.1. The ROCs for EIS outer, EIS inner, constant EIT and 3D EIT are presented in figure 7 and table 5.

Although the AUCs for EIT performed better when only 1 best feature set was used compared to EIS, it can be observed that when using a multi-frequency SVM approach, the AUCs for both EIS and EIT based techniques are similar. In fact, the AUC for G1 versus G3 and for G1 versus G4 is higher for both inner and outer EIS methods compared to any corresponding EIT methods. The AUC for G1 versus G5 using EIS methods is also only 1–2% less than AUCs obtained from EIT based methods. Overall, it seems that when using a multi-feature based SVM approach, the EIS based technique has better performance—in terms of AUC—in separating Bn (G1) from presence of PCa $>$ 18% (G3) and PCa $>$ 0% (G4); however EIT has better performance in separating Bn (G1) from presence of 100% PCa (G5). The predictive accuracy of EIT is consistently higher than EIS by 2–3% as well.

3.3. Computational cost of EIT reconstructions and SVM analysis

The computational steps ultimately required for SMA include: (1) DAQ from the EIA system, (2) data extraction, (3) EIT inverse solution (if applicable), and (4) evaluation of trained SVM models. Data extraction and evaluating a trained SVM model requires negligible computational time (after being optimized) ($\ll$1 s). The current DAQ time required to sample an exhaustive pattern set from the 17-electrode probe and the Dartmouth EIA system (Khan *et al* 2015) using 32 averages and a 10 kHz frequency is 1.1 s and the total time required to sample all 11 discrete frequencies from 5 to 100 kHz is 6.99 s. The computational times for the constant and 3D EIT reconstructions assuming 1 and 3 iterations are shown in table 6. These times are reported for a computer with a 2.7 GHz Intel CPU with 16 cores and 94 GB of RAM. The constant EIT with 1 iteration has an essentially negligible computational cost ($\ll$1 s). The 3D EIT technique with 1 iteration for 1 frequency is 2.9 s. If EIT reconstruction at multiple frequencies are necessary, the computation time can be parallelized using multiple cores so the overall time would not be affected. The time required to compute a 3-iteration, single discrete frequency reconstruction for both constant and 3D EIT are significant at ~1.3 and 12.3 min, respectively. At present, these times are

too costly for multi-iteration EIT to be used clinically. However, the multi-iteration 3D EIT can be significantly improved. For instance, if we pre-compute certain data/matrices, use the GPU Jacobian implementation (50 × speedup) from Borsic *et al* (2012), and omit a parabolic-line search step, then given our present mesh and inverse approach we expect a 3-step reconstruction to take approximately 24.8 s—which is ~48× faster than IFS-based assessment (25 s versus 1200 s) and approaches a clinically acceptable time. Regardless, the results from this study do not, at present, imply that additional gains would be provided by performing multiple EIT iterations.

4. Discussion

This study reports the predictive ability of EIS and EIT to distinguish cancerous from benign prostate tissue. The SVM applied to both EIS and EIT data has similar results that illustrate the promise of this technology especially in differentiating between benign and 100% cancerous measurements.

4.1. Limitations of the dataset

While these findings are encouraging, the dataset was small with 3.5 × to 8.8 × as many benign cases as cancerous cases (table 2). One might naturally be concerned with the accuracy of the SVM training and testing given such a small database. To partially mitigate this, we have used best practices (e.g. repeated sampling of the benign dataset to train on balanced datasets) and have used LOPO training to ensure fair data modeling. One can see the effect of balancing the datasets by comparing the NPV and PPV values from the discrete feature (imbalanced—table 4) and multi-feature SVM results (balanced—table 5). That is, the optimal point in the imbalanced sets appear to perform much better in correctly identifying benign cases (NPV ~0.9+) and poorly for cancerous cases (PPV ~0.3), and when the dataset is balanced we see a more realistic/representative results of the data (PPV and NPV ~0.7–0.8).

An additional limitation of the study is that all measurements were recorded from *ex vivo* tissue samples at room temperature. While *in vivo* tissues probed at normal body temperatures will be different in an absolute sense from the *ex vivo* tissues probed here (Haemmerich *et al* 2002), we expect the relationships between the different tissue types (i.e. cancer and benign prostate) to be similar.

4.2. EIT versus EIS

It is compelling to use the EIS data based on its simplicity, but there are two practical reasons that (constant, 1-iteration) EIT may be the preferred method/feature type. First, the conductivity and permittivity reconstructed from EIT are intrinsic properties of the tissue as opposed to probe specific resistance and reactance measurements. Thus the EIT reconstructions can be more easily compared to other studies, e.g. (Halter *et al* 2008b, 2009). As an example, we compare the discrete conductivity at 10 kHz and 100 kHz described here to results from Halter *et al* (2009) in figure 8. The benign and stroma conductivity are consistently larger than cancerous tissue and the general trend of conductivity values are very similar across the two studies. Although the permittivity results provided very good predictive results, we omit this comparison as there is less consistency compared to other studies (Halter *et al* 2008b, 2009) in terms of the benign to cancer relationship and the

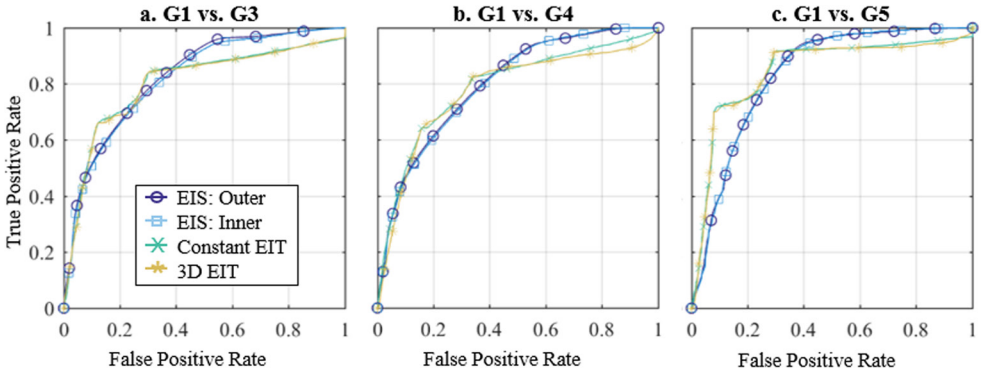

Figure 7. ROC curves of the best multi-feature SVM results for the EIS: outer, EIS: inner, constant EIT, and 3D EIT.

Table 5. Prediction metrics for the multi-feature SVMs: sensitivity (SN), specificity (SP), positive predictive value (PPV), negative predictive value (NPV), accuracy (ACCU), and area-under-curve (AUC).

Comp.	Method	No. features	SENS	SPEC	PPV	NPV	ACCU	AUC
G1 versus G3	EIS: outer	20	0.75	0.73	0.73	0.74	0.74	0.83
	EIS: inner	15	0.74	0.73	0.73	0.74	0.74	0.82
	Constant EIT, 1-step	6	0.84	0.70	0.74	0.82	0.77	0.80
	3D EIT, 1-step	12	0.84	0.70	0.74	0.82	0.77	0.80
	Constant EIT, 3-step	6	0.84	0.70	0.74	0.81	0.77	0.80
	3D EIT, 3-step	8	0.83	0.71	0.74	0.81	0.77	0.80
G1 versus G4	EIS: outer	20	0.73	0.70	0.71	0.72	0.71	0.80
	EIS: inner	19	0.72	0.71	0.71	0.71	0.71	0.80
	Constant EIT, 1-step	1	0.74	0.73	0.73	0.73	0.73	0.78
	3D EIT, 1-step	12	0.70	0.77	0.76	0.72	0.74	0.79
	Constant EIT, 3-step	1	0.71	0.75	0.74	0.72	0.73	0.79
	3D EIT, 3-step	4	0.82	0.66	0.71	0.79	0.74	0.77
G1 versus G5	EIS: outer	18	0.81	0.73	0.75	0.80	0.77	0.84
	EIS: inner	15	0.81	0.72	0.74	0.79	0.76	0.83
	Constant EIT, 1-step	6	0.73	0.90	0.88	0.77	0.81	0.85
	3D EIT, 1-step	6	0.72	0.88	0.86	0.76	0.80	0.84
	Constant EIT, 3-step	5	0.72	0.91	0.88	0.76	0.81	0.85
	3D EIT, 3-step	4	0.72	0.89	0.87	0.76	0.81	0.84

Table 6. Computation time for EIT methods.

Method	Iterations	Time one frequency (s)
Constant EIT	1	8×10^{-4}
3D EIT	1	2.9
Constant EIT	3	79.0
3D EIT	3	737.3 (12.3 min)

permittivity magnitudes. We believe this lack of consistency may be due to resistive-only-load calibration and/or phase changes caused by capacitive coupling through the long, tightly-spaced wires of the probe. The second reason EIT may be preferred is that the 17-electrode probe can produce many measurements (14 280), while the EIS features rely only on the few geometrically identical measurements (16 measurements on the outer or inner ring). Admittedly, one could consider additional non-geometrically identical EIS measurements to produce a more robust EIS/SVM-approach; however, that would likely require a more complex feature selection algorithm and/or SVM model and has not been explored here. Despite these benefits, given the similar results of EIS and EIT and the small sample size, we cannot definitively conclude the best approach. While not explored here, one might also consider combining the EIS and EIT data together to form a more complex classification model. The benefit of this approach might be that the resistance and reactance data associated with EIS can be used to describe different tissue characteristics than the conductivity and permittivity parameters estimated in EIT (Martinsen and Grimnes 2011).

4.3. Single-step versus multi-step EIT

In the presented results the single-step EIT reconstructions appear essentially as good as the multi-step EIT reconstructions. This suggests that the single-step EIT reconstructions are the preferred approach as it yields clinically feasible computational times and does not significantly reduce the quality. However, it is surprising that multiple iterations do not improve the results. This implies that the model cannot better fit the data through multiple iterations. We believe this is either an indication of the limits of the approach based on the frequency-dependent SNR of the probe and system or due to practical issues of the data collection process. First, if the noise in the data is too high, then this could clearly limit the ability to discriminate finer detail that multiple iterations could uncover. Second, during the data collection process there was variability in probe pressure applied and in the prostate slice thickness (2–5 mm). Pressure has been found to potentially produce significant differences in impedance measurements (González-Correa *et al* 2005), and simulations have revealed that impedance measurements can be significantly affected if the prostate slices are thinner than average (2–3 mm). If these factors are significant enough, then they may be removing the potential improvements the multi-step EIT results can yield. Although it was not possible to remove these confounding effects, the positive findings reported here indicate the potential robustness of the EIS/EIT data to practical issues that can arise in data collection.

4.4. Technology promise and comparison

A study that combined laser-induced autofluorescence, white-light remission, and high-frequency impedance spectroscopic measurements reported a highly accurate ability to identify benign and malignant prostate tissue *ex vivo* (Salomon *et al* 2009). Ninety-five tissue samples from 32 patients were stored in liquid nitrogen immediately following a prostatectomy procedure and were later thawed for their experimentation. The statistical analysis of their combined technique demonstrated a differentiation of benign and malignant prostate tissue with a sensitivity of 87.5% and a specificity of 87.3%, and by adding the acquired high frequency impedance data to the statistical analysis, sensitivity and specificity were increased to 93.8% and 92.4%, respectively. Despite the promising results in an *ex vivo* setting, this technology has not been investigated in an *in vivo* setting and many limitations for clinical translation

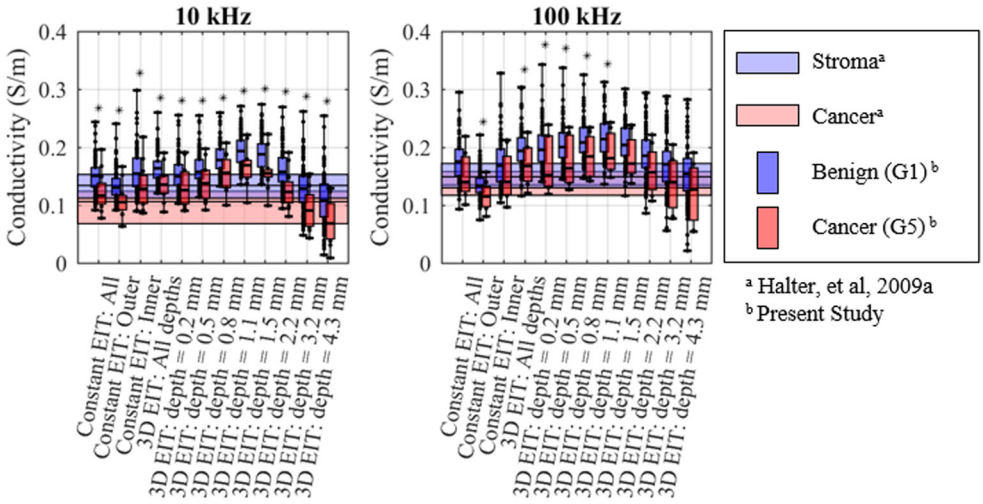

Figure 8. Comparison between the conductivity results using all the methods from the present study (narrow vertical boxes) to the results from Halter *et al* (2009) (wide horizontal boxes). The boxes represent 25–75% quantiles (both studies), the whiskers extend to the minimum and maximum data point, black dots show all points outside the quantiles, the black horizontal line represents the median of the data (both studies), and the asterisks ($*$) denote when there is a significant difference ($p < 0.05$) between the benign and cancerous tissue. Results from Halter *et al* (2009) are significantly different ($p < 0.05$) at both frequencies.

persist, such as—(1) statistical analysis of spectral data was not performed in blinded fashion; (2) it is well established that the freezing then thawing process will significantly impact tissue impedance (Yu *et al* 2004); (3) a limited cancer set was explored ($n = 16$), (4) the pathway for miniaturization of the instrument for use in RALP remains unclear.

Another technology currently being explored for intraoperative pathological characterization of tissue for SMA is the intelligent knife (iKnife). The iKnife uses mass spectrometry to evaluate the plume of smoke emitted as an electrosurgical knife dissects tissue. The plume contains sufficient biological material, enabling the device to discriminate between cancer and benign tissues (Balog *et al* 2013). Many studies have reported the promise of using iKnife and suggest a possibility for potential clinical translation in organs such as stomach, colon, liver, lung, breast, brain (Schäfer *et al* 2009, Balog and Takats 2010, Takats *et al* 2012, Balog *et al* 2013); however, no study has been conducted for prostate. Despite promising results of iKnife in these organ systems, there is a lack of suitability in RALP procedures for several reasons: (1) much of the RALP procedure involves separating the functioning tissue (e.g. nerve, muscle, blood vessels) from the prostate instead of cutting through these structures. These critical structures should not be damaged during the procedure so electrosurgical approaches are not typically recommended near this anatomy; (2) a RALP procedure usually includes carbon dioxide (CO_2) insufflation of the abdominal cavity and the potential interaction effects of CO_2 in context of RALP procedure with other gases used during iKnife mass spectroscopy have not been studied; (3) the current dimension and design of iKnife is not compatible to fit within a laparoscopic da Vinci surgical port.

In comparison to our prior study (Khan *et al* 2016), the clinical parameters are quite similar, but here we have significantly improved registration between impedance measurements,

yielding a more nuanced analysis on accuracy as a function of percent cancer. Overall, the results presented in this paper corroborate our previous studies and present the strongest evidence yet that an intraoperative-capable impedance probe can be used to distinguish benign from malignant prostate tissues.

5. Conclusion

This study has compared EIS and EIT measurements in discrete- and multi-feature approaches on a set of *ex vivo* prostate tissue data. We have found that multi-feature based SVM classification is the preferred approach to distinguish Bn from PCa, which provides significant improvement compared to the best discrete features (up to 16% improvement). Further, the EIS based technique has better performance—in terms of AUC—in separating Bn (G1) from either PCa $>$ 18% (G3) or PCa $>$ 0% (G4); however, EIT has better performance in separating Bn (G1) from presence of 100% PCa (G5) and EIT is at least 2% better in terms of ACCU over all group comparisons. An *in vivo* study with a large cohort will be necessary to definitively determine the preferred approach and to show the clinical effectiveness of the best-technique for margin assessment.

Acknowledgments

This work was supported in part by the National Institutes of Health and National Cancer Institute under Grant 1R01-CA143020-01A1.

References

Balog J and Takats Z 2010 Identification of biological tissues by rapid evaporative ionization mass spectrometry *Anal. Chem.* **80** 7343–50

Balog J *et al* 2013 Intraoperative tissue identification using rapid evaporative ionization mass spectrometry *Sci. Transl. Med.* **5** 194ra93

Borsic A, Attardo E A and Halter R J 2012 Multi-GPU Jacobian accelerated computing for soft-field tomography *Physiol. Meas.* **33** 1703–15

Borsic A, Halter R, Wan Y, Hartov A and Paulsen K D 2010 Electrical impedance tomography reconstruction for three-dimensional imaging of the prostate *Physiol. Meas.* **31** S1–16

CDC 2010 Number of all-listed procedures for discharges from short-stay hospital, by procedure category and sex www.cdc.gov/nchs/data/nhds/4procedures/2010pro4_numberproceduresex.pdf (Accessed: 15 May 2017)

Cheng K S, Isaacson D, Newell J C and Gisser D G 1989 Electrode models for electric current computed tomography *IEEE Trans. Biomed. Eng.* **36** 918–24

Fromont G, Baumert H, Cathelineau X, Rozet F, Validire P and Vallancien G 2003 Intraoperative frozen section analysis during nerve sparing laparoscopic radical prostatectomy: feasibility study *J. Urol.* **170** 1843–6

Gao L, Zhou H, Thrall M J, Li F, Yang Y, Wang Z, Luo P, Wong K K, Palapattu G S and Wong S T C 2011 Label-free high-resolution imaging of prostate glands and cavernous nerves using coherent anti-Stokes Raman scattering microscopy **2** 915–26

González-Correa C A, Brown B H, Smallwood R H, Walker D C and Bardhan K D 2005 Electrical bioimpedance readings increase with higher pressure applied to the measuring probe *Physiol. Meas.* **26** S39–47

Halter R J, Hartov A, Heaney J A, Paulsen K D and Schned A R 2007 Electrical impedance spectroscopy of the human prostate *IEEE Trans. Biomed. Eng.* **54** 1321–7

Halter R J, Hartov A, Paulsen K D, Schned A and Heaney J 2008a Genetic and least squares algorithms for estimating spectral EIS parameters of prostatic tissues *Physiol. Meas.* **29** S111–23
Halter R J, Schned A, Heaney J, Hartov A and Paulsen K D 2009 Electrical properties of prostatic tissues: I. Single frequency admittivity properties *J. Urol.* **182** 1600–7
Halter R J, Schned A, Heaney J, Hartov A, Schutz S and Paulsen K D 2008b Electrical impedance spectroscopy of benign and malignant prostatic tissues *J. Urol.* **179** 1580–6
Haemmerich D, Ozkan O R, Tsai J-Z, Staelin S T, Tungjitkusolmun S, Mahvi D M and Webster J G 2002 Changes in electrical resistivity of swine liver after occlusion and postmortem *Med. Biol. Eng. Comput.* **40** 29
IEC 60601-1 2005 *Medical Electrical Equipment Part 1: General Requirements for Basic Safety and Essential Performance* (Brussels: International Electrotechnical Commission)
Khan S, Borsic A, Manwaring P, Hartov A and Halter R 2013 FPGA based high speed data acquisition system for electrical impedance tomography *Int. Conf. on Electrical Bio-Impedance (ICEBI)* vol 434
Khan S, Mahara A, Hyams E, Schned A and Halter R 2016 Prostate cancer detection using composite impedance metric *IEEE Trans Med. Imaging* **35** 2513–23
Khan S, Manwaring P, Borsic A and Halter R 2015 FPGA-based voltage and current dual drive system for high frame rate electrical impedance tomography *IEEE Trans. Med. Imaging* **34** 888–901
Kotsiantis S, Kanellopoulos D and Pintelas P 2006 Handling imbalanced datasets—a review GESTS *Int. Trans. Comput. Sci. Eng.* **30** 25–36
Lionheart W R B 2004 EIT reconstruction algorithms: pitfalls, challenges and recent developments *Physiol. Meas.* **25** 125–42
Mahara A, Khan S, Murphy E, Schned A, Hyams E and Halter R 2015 3D microendoscopic electrical impedance tomography for margin assessment during robot-assisted laparoscopic prostatectomy *IEEE Trans. Med. Imaging* **34** 1590–601
Martinsen O and Grimnes S 2011 *Bioimpedance and Bioelectricity Basics* (New York: Academic)
McMaster-Carr 2014 G9 Garolite www.mcmaster.com/#garolite/=rix6ok (Accessed: 15 May 2017)
Murphy E, Mahara A and Halter R 2016 A novel regularization technique for microendoscopic electrical impedance tomography *IEEE Trans. Med. Imaging* **35** 1593–603
NCI 2015 Tracking the rise of robotic surgery for prostate cancer www.cancer.gov/about-cancer/treatment/research/rise-robotic-surgery (Accessed: 15 May 2017)
Ochiai A, Sotelo T, Troncoso P, Bhadkamkar V and Babaian R J 2008 Natural history of biochemical progression after radical prostatectomy based on length of a positive margin *Urology* **71** 308–12
Orvieto M A, Alsikafi N F, Shalhav A L, Laven B A, Steinberg G D, Zagaja G P and Brendler C B 2006 Impact of surgical margin status on long-term cancer control after radical prostatectomy *BJU Int.* **98** 1199–203
Platt J C 1999 Probabilistic outputs for support vector machines and comparisons to regular likelihood methods *Advances in Large Margin Classifiers* (Cambridge, MA: MIT Press) pp 61–74
Rouanne M, Rode J, Campeggi A, Allory Y, Vordos D, Hoznek A, Abbou C-C, La Taille A D and Salomon L 2014 Long-term impact of positive surgical margins on biochemical recurrence after radical prostatectomy: ten years of follow-up *Scand. J. Urol.* **48** 131–7
Salomon G *et al* 2009 The feasibility of prostate cancer detection by triple spectroscopy *Eur. Urol.* **55** 376–84
Schäfer K, Dønes J, Albrecht K, Szaniszló T, Balog J, Skoumal R, Katona M, Tóth M, Balogh L and Takáts Z 2009 *In vivo*, *in situ* tissue analysis using rapid evaporative ionization mass spectrometry *Angew. Chem., Int. Ed. Engl.* **48** 8240–2
Siegel R L, Miller K D and Jemal A 2016 *Cancer Stat.* **66** 7–30
Somersalo E, Cheney M and Isaacson D 1992 Existence and uniqueness for electrode models for electric current computed tomography *SIAM J. Appl. Math.* **52** 1023–40
Takats Z, Denes J and Kinross J 2012 Identifying the margin: a new method to distinguish between cancerous and noncancerous tissue during surgery *Future Oncol.* **8** 113–6
Von Bodman C, Brock M, Roghmann F, Byers A, Löppenberg B, Braun K, Pastor J, Sommerer F, Noldus J and Palisaar R J 2013 Intraoperative frozen section of the prostate decreases positive margin rate while ensuring nerve sparing procedure during radical prostatectomy *J. Urol.* **190** 515–20
Wan Y, Borsic A, Heaney J, Seigne J, Schned A, Baker M, Wason S, Hartov A and Halter R 2013 Transrectal electrical impedance tomography of the prostate: spatially coregistered pathological findings for prostate cancer detection *Med. Phys.* **40** 63102

Yadav R, Mukherjee S, Hermen M, Tan G, Maxfield F R, Webb W W and Tewari A K 2009 Multiphoton microscopy of prostate and periprostatic neural tissue: a promising imaging technique for improving nerve-sparing prostatectomy *J. Endourol.* **23** 861–7

Yossepowitch O, Briganti A, Eastham J A, Epstein J, Graefen M, Montironi R and Touijer K 2014 Positive surgical margins after radical prostatectomy: a systematic review and contemporary update *Eur. Urol.* **65** 303–13

Yu T H, Liu J and Zhou Y X 2004 Using electrical impedance detection to evaluate the viability of biomaterials subject to freezing or thermal injury *Anal. Bioanal. Chem.* **378** 1793–800

An Analog Front End ASIC for Cardiac Electrical Impedance Tomography

Arun Rao, *Member, IEEE*, Yueh-Ching Teng, *Student Member, IEEE*, Chris Schaef, *Member, IEEE*, Ethan K. Murphy, Saaid Arshad, Ryan J. Halter, *Member, IEEE*, and Kofi Odame, *Senior Member, IEEE*

***Abstract*—In this paper, an end-to-end CMOS application specific integrated circuit (ASIC) for readout channel in a cardiac electrical impedance tomography system is presented. The ASIC consists of an integrated current driver for current injection, an instrumentation amplifier, variable gain amplifier at the analog front end for voltage readout from electrodes, and an on-chip 10-bit successive approximation register analog to digital converter with serial peripheral interface. The ASIC is fabricated in the CMOS 0.18 μm process with a supply voltage of 3.3 V. Amplitude and phase extraction of the voltages is performed in the digital domain with a matched filter. A fully integrated solution for use in multiple electrode system is demonstrated. The readout chain in the ASIC achieves a minimum signal-to-noise ratio of 71 dB over the frequency range of 500 Hz–700 kHz, while maintaining an average accuracy of 99.7%. Frame rates of 21 frames per second for a 32 electrode system is feasible, and the ASIC has an overall power consumption of 11.8 mW.**

***Index Terms*—ASIC, cardiac monitoring, current driver, electrical impedance tomography, instrumentation amplifier, matched filter, variable gain amplifier.**

I. Introduction

SELF-MANAGEMENT of chronic heart disease is hindered by three critical barriers: (i) the symptoms that patients monitor today are insensitive, non-specific and late indicators of heart failure [1]; (ii) this lack of predictive strength forces management of the condition to be reactive rather than proactive [2], [3]; (iii) single, once-a-day measurements cannot capture the patient's hemodynamic response to the stresses of daily life activities [4], [5], or the diurnal variation in sympathetic activation [6], [7], thus hindering a full understanding of the patient's condition [8], [9].

One possible solution is to use an implanted device for on-demand telemonitoring of pulmonary artery pressure [10]. Unfortunately, this approach is invasive, expensive, and risks infection, bleeding, arterial embolism, prolonged hospitalization, thrombus and cardiogenic shock, among others [11].

Manuscript received December 16, 2017; revised February 19, 2018 and April 5, 2018; accepted April 23, 2018. Date of publication June 12, 2018; date of current version August 15, 2018. This work was supported in part by the U.S. National Science Foundation under Grant 1418497, and in part by the U.S. Department of Defense CDMRP Grants W81XWH-15-1-0572 and W81XWH-15-1-0571. This work was recommended by Associate Editor A. Humeau-Heurtier. *(Corresponding author: Arun Rao.)*

The authors are with the Thayer School of Engineering, Dartmouth College, Hanover, NH 03755 USA (e-mail: arun.rao.th@dartmouth.edu; Yueh-Ching.Teng.TH@dartmouth.edu; christopher.schaef@intel.com; Ethan.K.Murphy@dartmouth.edu; Saaid.H.Arshad.TH@dartmouth.edu; ryan.j.halter@dartmouth.edu; kofi.m.odame@dartmouth.edu).

Color versions of one or more of the figures in this paper are available online at http://ieeexplore.ieee.org.

Digital Object Identifier 10.1109/TBCAS.2018.2834412

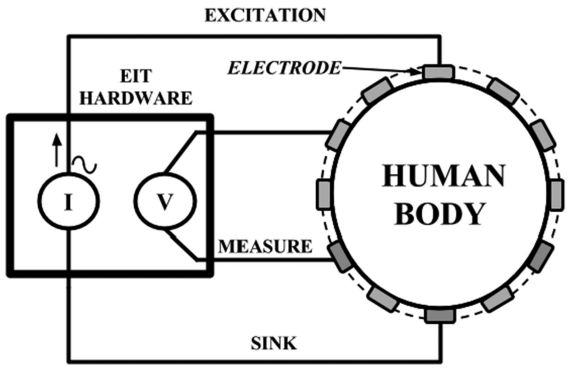

Fig. 1. Block diagram of a typical EIT system. AC current excitation is performed using a pair of electrodes and the voltages induced on the remaining electrodes are measured.

A promising, non-invasive alternative is dynamic electrical impedance tomography (EIT) of the thorax, from which left ventricular volume changes and cardiac output can be extracted. In an EIT system the tissue excitation is performed by injecting alternating current through a pair of electrodes and measuring the boundary voltages induced at the remaining electrodes as shown in Fig. 1. The excitation frequencies can be swept over a pre-determined range depending on the tissue being probed. This idea has been demonstrated previously, including in our own recent work [12] using the EIT Pioneer Set (Swisstom AG, Landquart, Switzerland). The challenge with these systems is that they are large and bulky. They may be appropriate for hospital bedside use, but they are unsuitable for telemonitoring, where physical obtrusiveness and ease of use are critical to ensuring patient adherence [13], [14].

Application specific integrated circuits (ASICs), like the one depicted in Fig. 2, could dramatically miniaturize the cardiac EIT instrumentation system, making its use more feasible in a telemonitoring environment. Unfortunately, the state-of-the-art ASICs for EIT do not meet the performance requirements necessary for cardiac output monitoring. For example, the ASICs described in [15]–[17] do not provide adequate signal-to-noise ratio.

In this paper, we present a novel analog front end ASIC that provides the signal-to-noise ratio, interrogation frequency and power consumption performance needed for a cardiac output monitoring application. Section II presents the system level

1932-4545 © 2018 IEEE. Personal use is permitted, but republication/redistribution requires IEEE permission.
See http://www.ieee.org/publications_standards/publications/rights/index.html for more information.

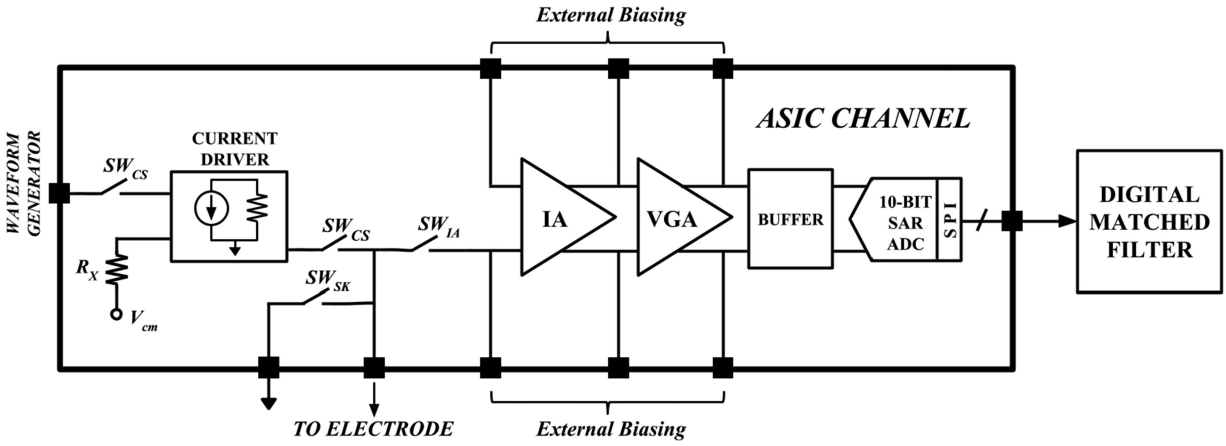

Fig. 2. Block diagram of the cardiac EIT ASIC. The on-chip switches are used to configure the channel in a current-source, current-sink or voltage-read mode. R_X is an on-chip resistor and V_{cm} is the common mode voltage of the current driver. The IA, VGA and the ADC form the voltage readout chain. The digital data from the ADC is sent off-chip using a SPI interface to a digital matched filter for amplitude extraction. Circuit blocks of the ASIC were measured individually with custom built PCBs.

specifications necessary for cardiac monitoring. Section III discusses ASIC building blocks in detail and provides a summary for measured performance. Section IV discusses the system design using the ASIC and provides measured results. Section V summarizes the performance achieved and provides concluding remarks.

II. EIT System Level Specifications

Image reconstruction in dynamic EIT aims to estimate the spatiotemporally-varying electrical properties (conductivity, σ and permittivity, ϵ) within the thorax, provided a set of boundary measurements. These measurements (small-amplitude, imperceptible AC currents that are injected into the thorax, and the resulting voltages that develop on the skin surface), carry information about the internal electrical properties. By solving the inverse problem, it is possible to reconstruct a tomography-like spatial distribution of σ and ϵ.

Over the frequency range 10 Hz to 1 MHz, the conductivity of the blood in the heart is about $\sigma_{\mathrm{h}} = 0.7$ S/m, while that of the background (heart muscle, lungs, fat, bone, etc.) is less than 0.4 S/m [18]. This contrast in electrical properties makes the blood-filled heart visible as a high conductivity region in an EIT image of the thorax. In practice, the frequency of interrogation for cardiac output measurement is at least 20 kHz, in order to avoid the high skin resistivity that would be encountered at lower frequencies [19]. Looking beyond cardiac output measurement, there are some other cardiac EIT applications that might require interrogation frequencies up to 1 MHz. These include bioimpedance spectroscopy for detecting cardiac ischemia [20], measuring fluid index ratio due to edema in congestive heart failure [21], and frequency differencing EIT for anatomic characterization, such as ventricular wall thickness [22]. Also, the entire process of making boundary measurements and constructing an EIT image (a "frame") must be performed at a rate of 14 frames per second (fps) or higher. This way, enough points are captured over the $\sim$1 s cardiac cycle such that heart volume change and cardiac output can be calculated.

To understand the remaining performance requirements of a cardiac EIT system, we made use of a highly detailed digital phantom of the human thorax. The phantom comprises the MRI and CT-based 4D XCAT model [23], mesh generation using distmesh [24] and gmsh [25], a perfusion model [26], ex-vivo tissue values of conductivity and permittivity from multiple frequencies [18], and a 3D finite element (FEM) implementation of the complete electrode [27]. We analyzed the digital phantom assuming a 32 electrode EIT system. As shown in Fig. 3, the phantom produces an image that is qualitatively similar to one constructured from measurements of a human volunteer.

Figure 4(a) shows the boundary voltage amplitudes that were generated by the digital phantom for a typical electrode position, with measurements taken at end diastole and also at end systole. Depending on the anatomy of the subject, the boundary voltages can range in amplitude from tens of millivolts to several hundred millivolts. Interestingly, the voltage measured at end diastole (when the heart is full of blood) is different from that at end systole (just after ejection of blood) by less than 1%. This small change is due to the large amounts of insulating air that are inhaled into the lungs, which confound the relatively smaller signals of blood flow in and out of the heart and cardiac muscle motion.

Since the EIT system must detect the 1% change in voltage amplitude across the systolic cycle in order to extract cardiac output, this would suggest a minimum required signal-to-noise ratio (SNR) of 40 dB. In fact, the EIT image reconstruction problem is poorly conditioned and ill-posed, and demands SNR $>$70 dB for this application. Fig. 4(c) illustrates how the EIT-derived cardiac output would deviate from ground truth if the SNR fell too low.

In summary, an EIT system for cardiac output monitoring must cover a dynamic range from 20 $\mathrm{mV_{pp}}$ to 1 $\mathrm{V_{pp}}$, operate at a frame rate of 14 fps, and maintain an SNR of $>$70 dB. In addition, it must support an interrogation frequency of a few tens of kHz, although frequencies up to 1 MHz would be useful for more generalized cardiac EIT applications. Accuracy and linearity requirements are less stringently defined, especially

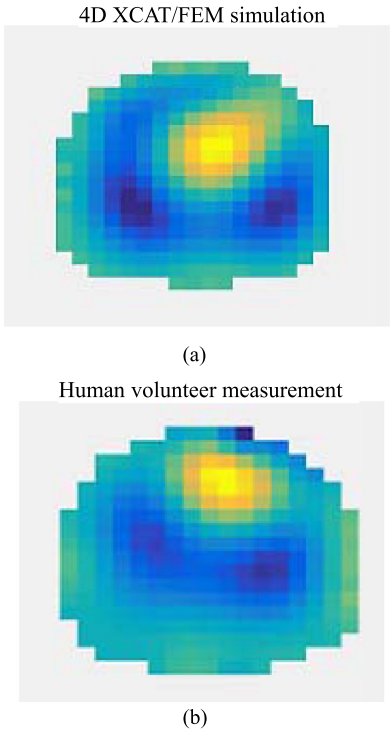

Fig. 3. Cross-sectional conductivity profile of the thorax produced from (a) Digital phantom model; and (b) Bioimpedance boundary voltage measurements of a healthy human subject. The digital phantom model and the in vivo measurements result in qualitatively very similar images, where the heart and lung (from perfusion) are very clearly seen when dynamic EIT imaging is used between end-diastole and end-systole.

with the use of the calibration techniques that we introduced in [28]. Still, it is typical to design for $\geq$99% accuracy and ≤ -40 dB total harmonic distortion [28]–[30].

III. ASIC Design and Description

In this section, we describe the different components that comprise the EIT cardiac output analog front end shown in Fig. 2.

A. Current Driver

System level specifications derived earlier indicate that cardiac monitoring requires an accuracy $\geq$99% and ≤ -40 dB total harmonic distortion. The current driver in the ASIC is capable of generating 1 mA_{pp} sinusoidal current while maintaining total harmonic distortion of $<$1% for frequencies up to 1 MHz. The accuracy of current delivered over this frequency range is $>$99.6%. Accuracy is achieved by designing the current driver with high output impedance, whereas linearity is obtained by using a resistor for voltage to current conversion. The details of the implementation are below.

The current driver for this design is based on the CCII current conveyor [32] shown in Fig. 5. To obtain high linearity, the voltage to current conversion is performed using a 2-stage op-amp in unity gain configuration with a resistor at the terminal X generating current, $I_X = \frac{V_X}{R_X}$ [33]. A class AB buffer at the output of the 2-stage op-amp creates a low impedance node, and

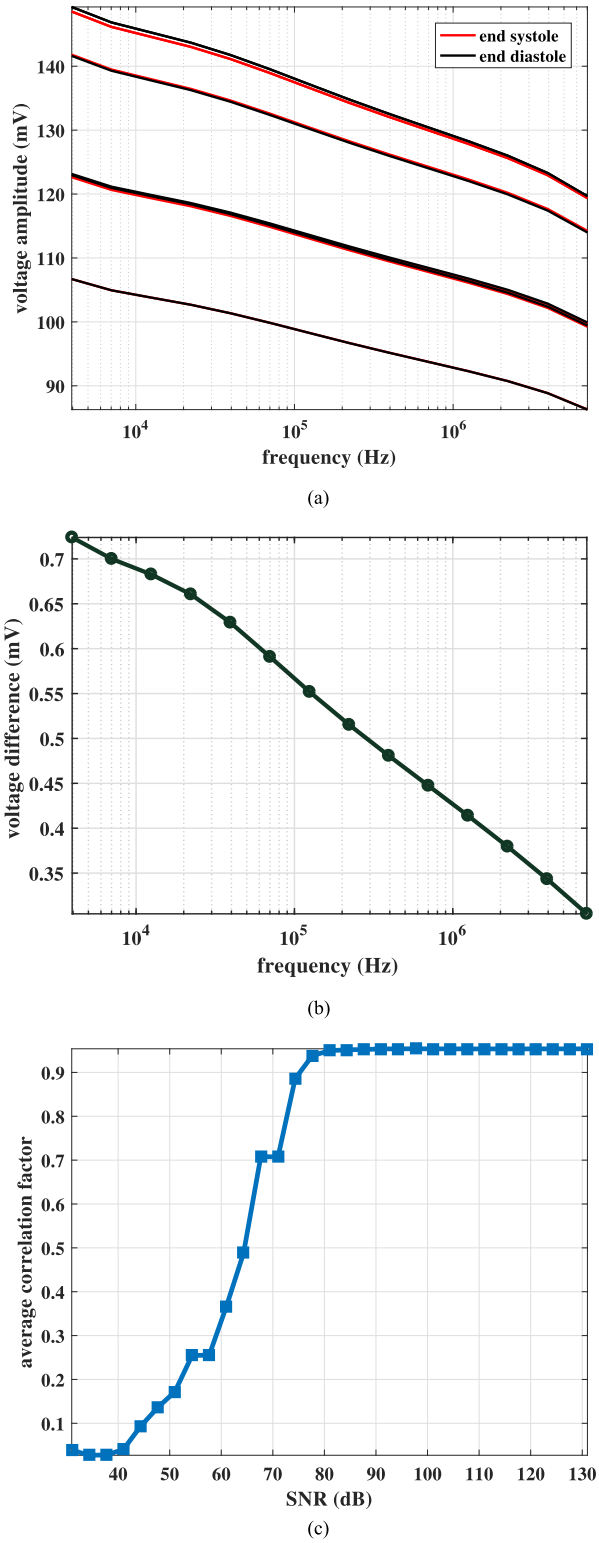

Fig. 4. (a) Boundary voltage amplitude versus frequency plot for some selected electrodes and current source-sink patterns. (b) The voltage difference between end systole and end diastole measured at the same electrode for a representative source-sink pattern from Fig. 4(a). The difference in voltage at these two time points is less than 1 mV, and decreases with frequency. (c) Effect of measurement SNR on accuracy of the extracted heart area [31]. The y-axis is the correlation factor between actual versus EIT-extracted heart area, averaged across the cardiac cycle. For accurate calculation of cardiac output, the correlation factor should ideally be 1. The plot shows that a measurement SNR of at least 75 dB is necessary for sufficiently-high correlation.

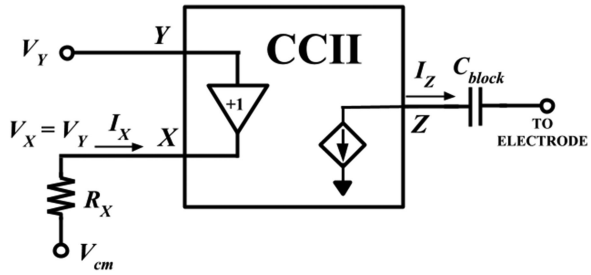

Fig. 5. Block diagram of the current conveyor architecture [32]. Current is generated at terminal X using an on-chip resistor such that $I_X = \frac{V_X}{R_X}$, where $R_X = 500\,\Omega$ and V_X follows the voltage at terminal Y. Current I_X is delivered to terminal Z with a current gain of unity.

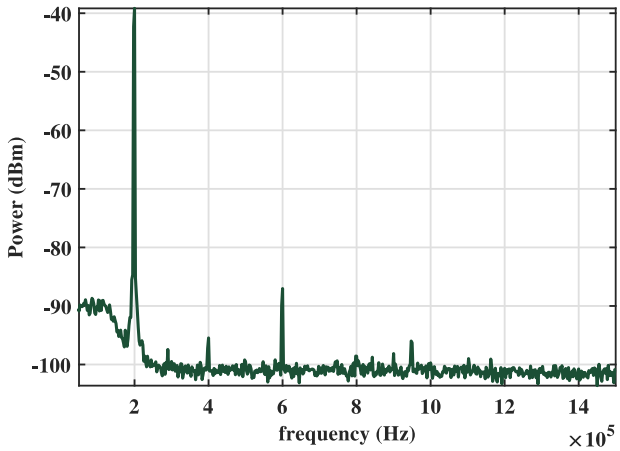

Fig. 6. FFT plot of the current driver delivering 500 μA_{pp} current to a fixed load of 500 Ω. The total harmonic distortion measured is ∼0.5% at an input frequency of 200 kHz.

TABLE I
MEASURED PERFORMANCE OF CURRENT DRIVER

Parameter	Value
Area	0.26 mm^2
Bandwidth	100 Hz - 10 MHz
Output Impedance	101 kΩ @ 1MHz
Max. Output Current	1 mA_{pp}
THD	< 0.1 % @ 50 kHz
Accuracy	99.6 % up to 1 MHz
Power	1.65 mW

the use of indirect compensation technique [34] helps achieve wide-band operation up to 10 MHz. The generated current is mirrored to the output terminal Z through a gain enhanced cascode current structure to provide high output impedance [35]–[37].

Figure 6 shows an example of the current driver's measurement results. When injecting a 200 kHz, 500 μA_{pp} current onto a 500 Ω load, the measured total harmonic distortion is 0.5%. Table I summarizes the other key performance metrics of the current driver.

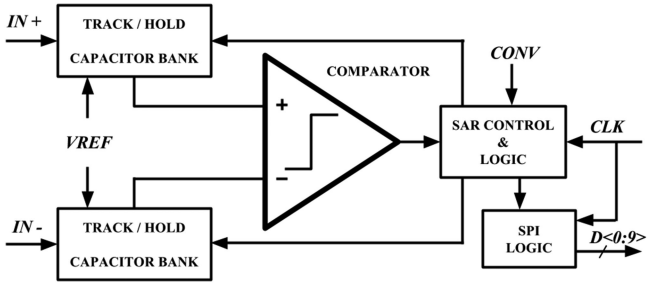

Fig. 7. Block diagram of the differential 10-bit SAR ADC. The maximum sampling rate of the ADC is 250 ksps. Serial data output is achieved by incorporating a SPI interface.

B. 10-b SAR ADC

The ADC samples the voltage readout chain and provides the digital data to an off-chip matched filter to extract the amplitude and phase. A signal-to-noise ratio of 80 dB is desirable to meet the system SNR specifications. Assuming an output-referred noise of IA, VGA chain of 1 mV_{rms} [38], 80 dB SNR can be achieved with a 10 bit ADC and 100 tap matched filter [39].

Next we discuss the sampling rate of the ADC based on the the desired frame rate of 14 fps. The frame rate is calculated by the following formula,

$$\mathrm{FR} = \frac{1}{\mathrm{P_N} \cdot \left(\frac{\mathrm{N_{tap}}}{f_s} + t_s\right)}\ (\mathrm{fps}) \tag{1}$$

where, FR represents the frame rate in frames per second, N_{tap} is the number of taps in the matched filter for amplitude extraction, P_N is the number of current source-sink patterns in a multi-electrode system, f_s is the sampling rate of the ADC and t_s is the settling time after each pattern is switched. With $N_{tap} = 100$, $P_N = 30$ for a 32 electrode system, and ideal settling time of zero, the minimum required sampling speed of the ADC is 42 ksps. In reality, the sampling rate should be higher to account for the settling time during pattern switching to obtain desired precision (see detailed discussion on frame rate in Section IV). The ADC is designed with a maximum sampling rate of 250 ksps.

An SAR ADC architecture was chosen as it exhibits lower power consumption in comparison to other ADC architectures [40]. The block diagram of the ADC designed is shown in Fig. 7. The track and hold comprises of a capacitor bank and CMOS switches controlled by the SAR logic block. An SPI interface was designed to achieve serial data output which simplifies system level design in terms of input/output infrastructure necessary when the ASIC is incorporated in a multiple electrode EIT system. The 10-bit data is available at the SPI interface after 14 clock cycles when the $CONV$ signal is asserted high. The ADC consumes an average current of 77.23 μA with a sampling rate of 250 ksps and input clock frequency of 3.5 MHz. The dynamic characteristics and measured performance parameters of the 10-bit ADC are shown in Table II.

The figure of merit for the ADC is given by (2) [41].

$$\mathrm{FOM_{ADC}} = \frac{\mathrm{P_{avg}}}{f_s \cdot 2^{\mathrm{ENOB}}}\ (\mathrm{J/conv\text{-}step}) \tag{2}$$

TABLE II
MEASURED PERFORMANCE OF 10-BIT SAR ADC

Symbol	Parameter	Value
V_{DD}	Process 0.18 μm	1.8 V
V_{IN}	Differential Input Voltage	0 - 1.2 V
F_s(max)	Sampling Rate	250 ksps
SINAD	Signal to Noise and Distortion	54.98 dB (1 kHz)
ENOB	Effective number of bits	8.84
P_{avg}	Average Power	139 μW
FOM_{ADC}	Figure of Merit	1.25 pJ/conv-step

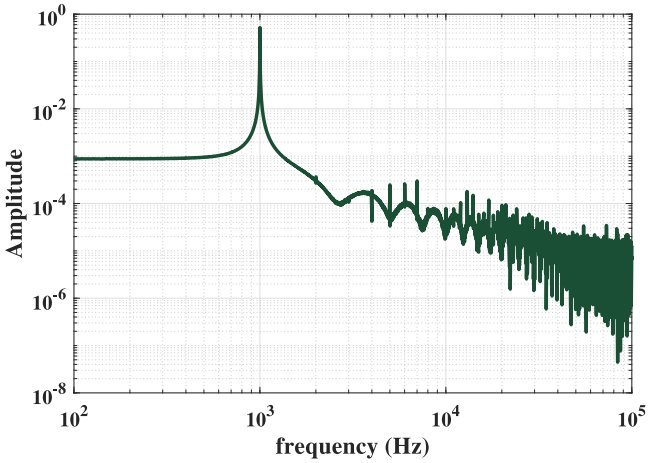

Fig. 8. FFT plot of the ADC for a 1 kHz input signal and sampling rate of 250 ksps.

where, P_{avg} is the average power, f_s is the sampling rate and ENOB represents the effective number of bits for the 10-bit SAR ADC. The ADC achieves an FOM_{ADC} of 1.25 pJ/conv-step.

The FFT plot for a 1 kHz input signal at 250 ksps sampling rate for the ADC is shown in Fig. 8.

C. Voltage Sensing Amplifiers (IA and VGA)

Boundary voltages on electrodes for a few selected current source-sink patterns are shown in Fig. 4(a). The readout chain should amplify these voltages without saturating the channel and provide high linearity (≤ -40 dB) for frequencies up to 1 MHz. The IA is designed with a fixed gain of 3 V/V, as we want to minimize noise, and prevent saturation of the readout chain. The VGA provides three additional gain settings of 1, 3 and 12 V/V. Thus, to amplify the smallest possible voltage (20 mV_{pp}), the readout chain can provide a gain of 36 V/V. The target output-referred noise specification of the IA and VGA chain is 1 mV_{rms}. With a 10-bit ADC and 100 taps in the matched filter, the circuit noise from the voltage sensing amplifiers will provide the required SNR of 80 dB (discussed in the ADC section).

The IA shown in Fig. 9 is a fully differential amplifier based on current conveyors [42]. It has a balanced structure, with high input impedance and linearity. The IA is designed for low noise operation and provides a fixed voltage gain determined by the ratio of two on-chip polysilicon resistors, R_2/R_1. The IA has a common mode rejection ratio (CMRR) over 86 dB, and a measured input-referred noise of 14 $nV_{rms}/\sqrt{Hz}$. The VGA is a fully differential amplifier which has a similar architecture and performance as the IA reported in [38]. Additionally, it has a reconfigurable gain of 0 dB, 9.5 dB and 21.5 dB to fully utilize the input dynamic range of the ADC.

For speed and power constraints, the amplifiers G in Fig. 9 only consists of a few transistors which provide proper level shifting incorporated, for the flipped source follower to increase its dynamic range. It also lowers the output impedance of the source follower, such that the transconductance stage can drive a low value gain resistor R_1 to reduce the overall amplifier noise. The V_{ref} bias voltages are set by on-chip current sources and the implementation of level-shifted source follower concept is similar to our design presented in [38], [43]. The common mode feedback (CMFB) circuit consists of a differential source follower and resistors [44] to control the gate voltage of transistors M_6 and $M_{6'}$.

The magnitude response of cascaded voltage sensing amplifiers which include IA and VGA is shown in Fig. 10. The digitally selectable gains of 9.3, 19 and 30 dB are set by the external control bits. Table III summarizes the measured performance of the IA and VGA. The measured voltage gains deviate less than ± 0.5 dB across the 3dB bandwidth. A total of 18 chips were used for this measurement. In addition the variation in gain across the frequencies of the readout chain can be calibrated out for each channel incorporated into the EIT system.

The ASIC is fabricated in the XFAB 0.18 μm CMOS process with a supply voltage of 3.3 V. The micro-photograph of the ASIC is shown in Fig. 11. The current driver, and the readout channel which contains the IA, VGA and the ADC are clearly indicated.

IV. SYSTEM DESIGN AND RESULTS

The system level block diagram of the ASIC channel is shown in Fig. 12. Necessary bias currents and reference voltages needed for the building blocks in the ASIC are provided by using current source IC's and voltage references. The input to the integrated current driver for voltage-to-current conversion is provided with a waveform generator IC, followed by an anti-aliasing filter with a cut-off frequency of 2 MHz. The output current is varied by changing the amplitude of the sinusoidal input voltage to the current driver. To sense the accurate current injected into the electrode, external sense resistors with switching mechanism is designed on the board. External ADC with anti-aliasing filter is also included as a backup. The output from the on-chip ADC and external ADC's is interfaced to a field programmable gate array (FPGA) using SPI communication protocol. The board is powered with linear dropout regulator (LDO) IC's which provide two voltage levels of 1.8 V and 3.3 V.

A. System Signal-to-Noise Ratio (SNR)

The SNR of the system indicates the noise in the readout signal chain of the EIT system. According to our analysis, the acceptable SNR for accurate cardiac output monitoring should

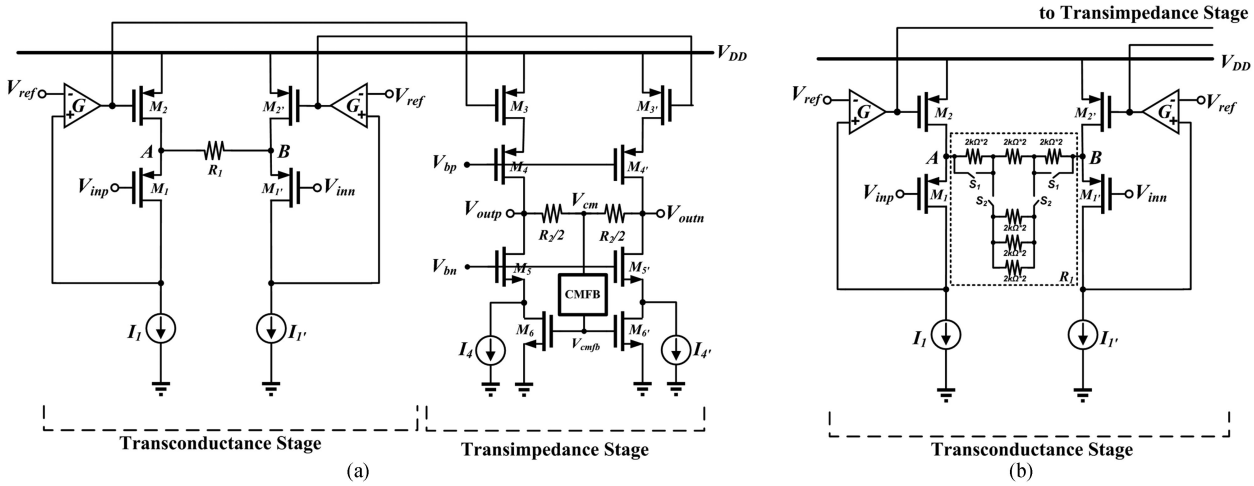

Fig. 9. (a). Simplified schematic of the current conveyor architecture used to implement the IA. The fixed gain is determined by the ratio of on-chip polysilicon resistors $R_1 = 10$ kΩ and $R_2 = 30$ kΩ. (b). The transconductance stage of the VGA is shown, while the transimpedance stage has a similar structure as the IA. Variable gains for the VGA is achieved by the on-chip resistor ladder shown in the figure. Resistor $R_2 = 15$ kΩ in the transimpedance stage is fixed while resistor R_1 in the transconductance stage is variable with values 15 kΩ, 5 kΩ and 2.5 kΩ. Digital control of variable gains is achieved using switches S_1 and S_2.

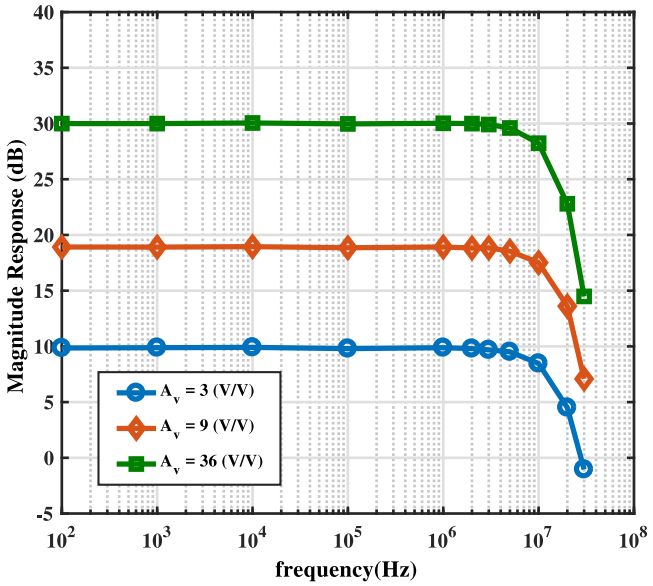

Fig. 10. Measured magnitude response of the readout channel (IA and VGA cascaded). The IA provides a fixed gain of 9.3 dB, whereas the VGA can be programmed to achieve a gain of 0, 9.3 and 21.5 dB with external control bits.

TABLE III
MEASURED IA AND VGA PERFORMANCE SUMMARY

	IA	VGA
V_{DD}	3.3 V	3.3 V
Power	2.07 mW	4.66 mW
Bandwidth	>10 MHz	>10 MHz
Input Impedance (DC)	>1 GΩ	>1 GΩ
Input Noise ($nV_{rms}/\sqrt{Hz}$)	14	80 / 27 / 6.7
Gain (dB)	9.3 (1 kHz)	0 / 9.3 / 21 (1 kHz)
THD (dB) ($V_{out,diff} = 2V$)	-63 (1 kHz)	-70 (1 kHz, A_v = 21 dB)

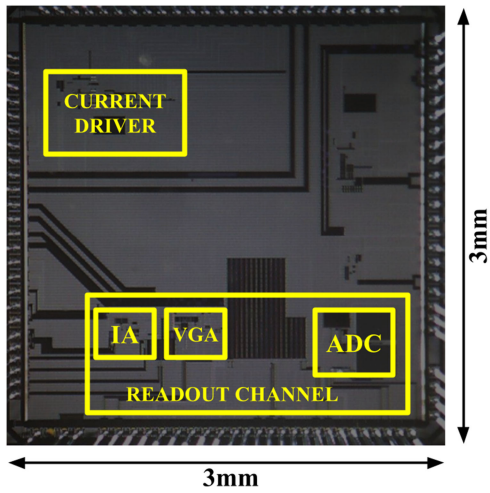

Fig. 11. Chip Micro-photograph. The current driver and the readout channel are shown.

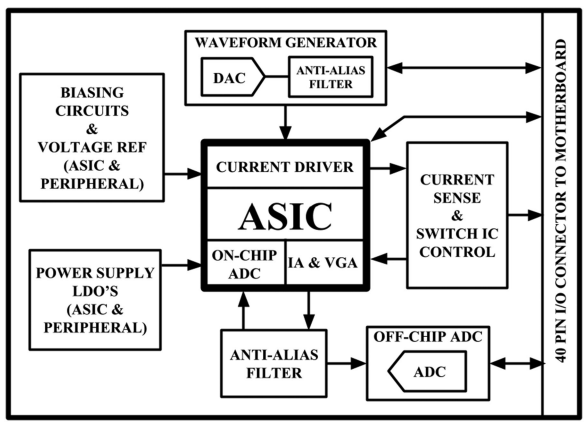

Fig. 12. Block Diagram of the PCB module. The core ASIC is shown with additional circuitry for power supply, biasing, waveform generation, current sensing, switch control, off-chip ADC, and anti-aliasing filters. The 40 pin I/O headers mounts onto a motherboard PCB and contain a large number of ground pins for signal integrity.

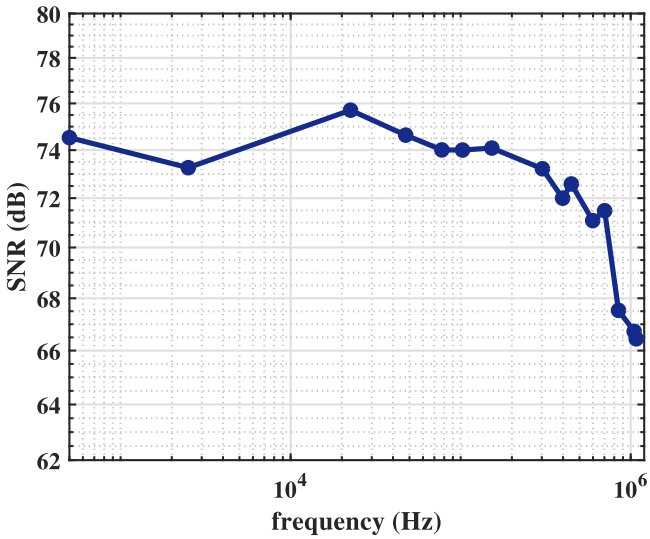

Fig. 13. Signal-to-noise ratio (SNR) at the output of the matched filter that follows the ASIC. SNR was measured using Eq. 3.

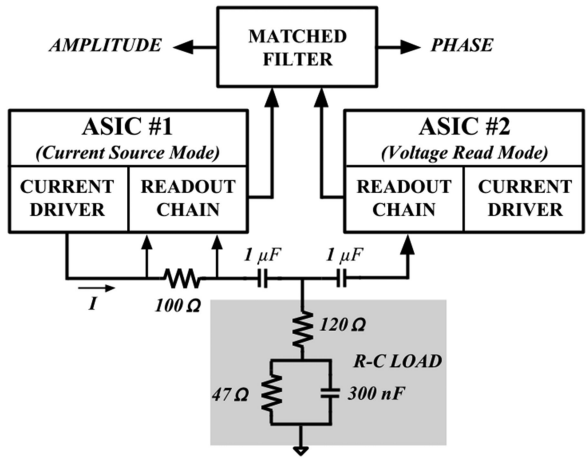

Fig. 14. Setup for obtaining Cole-Cole plot. Representative R-C load is selected via 4D XCAT simulations. Measurement is performed by two channels of the ASIC. Amplitude and phase extraction is performed in the digital domain with a matched filter. Calibration is incorporated to obtain accurate measurements.

be $\geq$70 dB. The SNR formula is given by [28].

$$\text{SNR} = 10 \cdot \log_{10} \cdot \left\{ \frac{\sum_{n=1}^{N} V_n^2}{\sum_{n=1}^{N} (V_n - \overline{V})^2} \right\} \tag{3}$$

where N is the repeated number of SNR measurements, V_n represents the measured SNR value of the signal chain, and $\overline{V}$ represents the mean of all measurements. The ASIC was configured in the voltage readout mode, and the readout channel gain settings chosen such that the ADC input dynamic range was utilized. The ADC sampling rate was set at 250 ksps and the input frequencies swept from 500 Hz to 1 MHz. The digital data from the ADC was sent off-chip and a matched filter used to extract the amplitude. To obtain the SNR of the readout signal chain, $N = 128$, repeated number of measurements were performed. The minimum SNR measured is 71 dB over a frequency range of 500 Hz–700 kHz. At frequencies >700 kHz the input amplitude had to be reduced to prevent distortion and accounts for the drop in SNR value. The measured SNR plot over frequencies of 500 Hz to 1 MHz is shown in Fig. 13.

B. Cole-Cole Plot

An R-C circuit combination is used to model the complex tissue impedance of the thorax. The representative load is chosen from simulations using the 4D XCAT model described earlier, where the voltages induced on the electrodes from select current injection patterns are analyzed across frequencies, (see Fig. 4(a)). The block diagram for the measurement of the representative complex impedance is shown in Fig. 14 which incorporates two ASIC channels. One channel is configured in the current source mode and the accurate current injected in to the R-C load is determined by measuring the voltage across the 100 Ω sense resistor. The second ASIC channel is configured in voltage read mode and measures the voltage induced on the R-C load circuit due to the injected current. In order to obtain high accuracy, a calibration method is adopted where a known value

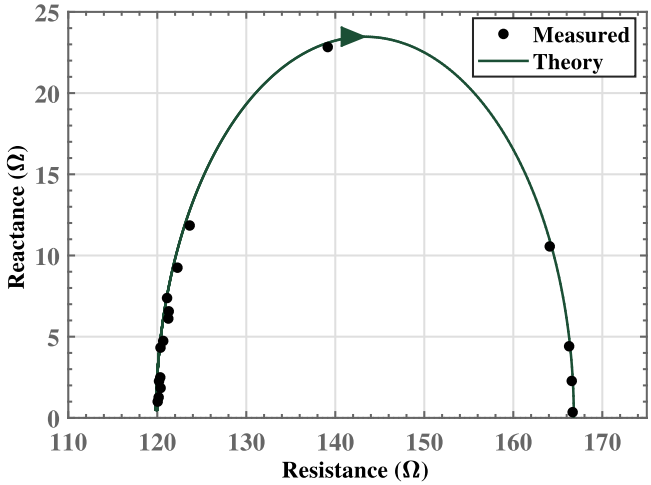

Fig. 15. Cole-Cole plot for a parallel RC load shown in Fig. 14. The measured results are compared with theory for frequencies from 250 Hz–1 MHz.

of current (500 μA) is injected into a fixed resistance (200 Ω). The R-C circuit components, sense resistor and associated parasitics are measured using a LCR meter. To ascertain the exact gain of the readout channel, gain values are incorporated from the measured results of the IA, VGA specifications over frequencies of interest. This data is saved as reference for actual measurement of load and used for calibration. The measured Cole-Cole plot for frequencies of 250 Hz–1 MHz is shown in Fig. 15. An average of 50 measurements are performed for each frequency point and the amplitude and phase are extracted using a matched filter.

Cardiac EIT systems typically have accuracies >99% as it is necessary to measure small impedance changes. The accuracy of the ASIC readout chain is calculated using Eq. 4.

$$\text{Accuracy } (\%) = \left(1 - \frac{\text{V}_{\text{meas}} - \text{V}_{\text{sim}}}{\text{V}_{\text{sim}}}\right) \cdot 100 \tag{4}$$

TABLE IV
PERFORMANCE COMPARISON OF ASIC'S FOR ELECTRICAL IMPEDANCE TOMOGRAPHY

Reference	[15]	[16]	[17]	This Work
Process	0.18 μm CMOS	0.18 μm CMOS	65 nm Mixed CMOS	0.18 μm CMOS
Frequency	up to 90 kHz	10 - 200 kHz	10 - 256 kHz	500 Hz - 700 kHz
Current Injection (peak-peak)	100 - 350 μA	0.1 - 1 mA	0.1 - 1 mA	up to 1 mA
Voltage Gain of Readout Chain (dB)	18 - 40	18 - 60 (6 dB step)	20 - 70 (6 dB step)	9.3, 19, 30
ADC (Sampling Rate)	10-bit (N/A)	10-bit (1 - 200 ksps)	10-bit (1 - 256 ksps)	10-bit (12.5 ksps - 250 ksps)
SNR (dB)	40	56.3[1]	N/A[2]	71[3]
Power (mW)	6.3	1.733	6.69	11.8[4]
FOM (pW/Hz)	700	13.27	N/A	4.75

[1] SNR averaged over measurement index [16].
[2] SNR was not reported. However, the analog matched filter approach used in [17] typically provides an SNR of less than 60 dB.
[3] The minimum achieved SNR is 71 dB over frequency range of 500 Hz - 700 kHz, whereas for the frequency range of 500 Hz - 1 MHz, the minimum achieved SNR is 66.7 dB.
[4] Breakdown of power is as follows. The current driver consumes 1.65 mW, IA and VGA consume 6.73 mW, and the ADC and its driver consume 3.44 mW.

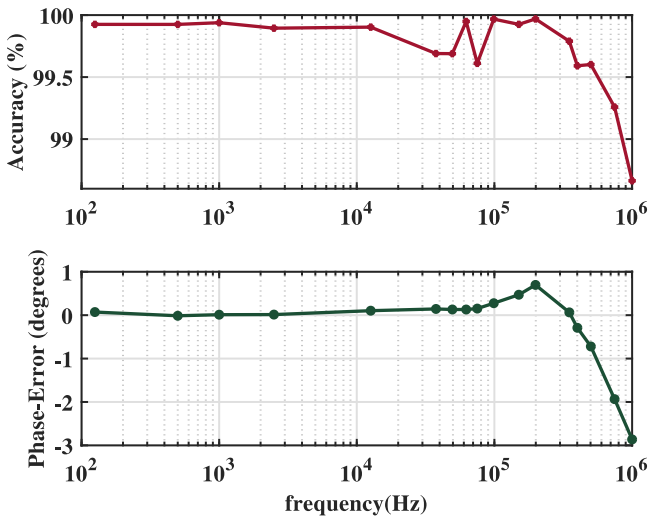

Fig. 16. Accuracy of measured amplitude and phase error over frequencies.

where V_{meas} is the measured voltage and V_{sim} is the voltage obtained from theory. The measured amplitude accuracy and phase error over frequencies is plotted in Fig. 16. An average accuracy of 99.7% is obtained for the measurement of complex impedance amplitude.

C. Frame Rate

To detect the change of heart volume and for accurate cardiac output monitoring the frame rate should exceed 14 fps as shown in our discussion earlier. The frame rate for the system is calculated by (1). It is typical in Swisstom systems and EIDORS modeling [45] to utilize skip patterns for single-ended voltage measurements. In a 32 electrode system using skip patterns, $P_N = 30$. The settling behavior after pattern switching can be studied with the help of the circuit used for measuring the complex impedance shown in Fig. 14. The RC time constant is determined by the DC blocking capacitor (1 μF) and the resistive load (167 Ω). To achieve a 10 bit resolution the voltage at the load requires 7 time constants [46] to settle. N_{tap} is set to 100 and the ADC is sampled at 250 ksps. Frame rates of $\sim$21 fps is feasible with the designed ASIC.

D. Comparison

Table IV summarizes the performance of this work with previously reported literature on EIT ASIC's. A figure of merit for the ASIC channel is defined by (5) [47],

$$\text{FOM} = \frac{\text{Power}}{\text{BW} \cdot 10^{\left(\frac{\text{SNR}}{20}\right)}} \ (\text{W/Hz}) \tag{5}$$

where, Power is the average power consumption per ASIC channel, BW is the bandwidth of the system, and SNR is the minimum signal to noise ratio in decibels over frequency range of 500 Hz–700 kHz. As seen in Table IV the ASIC used for cardiac output measurements in this work is more power efficient than other designs with the lowest FOM of 4.75 pW/Hz. This is achieved by designing an IA and a VGA with wider swing, lower noise and high linearity [38], [43].

V. CONCLUSION

The cardiac EIT system consists of several components such as the analog front-end for signal processing, the digital domain for single point impedance computation, FPGA block for control and communication strategies and reconstruction software to obtain the final image of the thorax. Some of the challenges associated are the signal processing on the ASIC up to 1 MHz, control strategies for electrode switching using FPGA, and robust board design for maintaining signal integrity. This paper measures the performance of the analog chain alone, without it being confounded by other components of the EIT system.

An ASIC with all analog front end components of a cardiac EIT system is fabricated in the CMOS 0.18 μm technology and individual blocks are characterized. The integrated current driver delivers currents up to 1 mA_{pp} while maintaining a THD of $<1\%$. The voltage sensing amplifiers provide gains of 9.3, 19 and 30 dB to process the dynamic range of voltages incident on the electrodes. The readout chain in the ASIC achieves a minimum SNR of 71 dB over frequency range of 500 Hz–700 kHz at the output of the matched filter. An average accuracy of 99.7% is measured by incorporating a representative R-C circuit and calibration scheme. Frame rates of 21 fps are feasible for a 32 electrode system for single ended measurements. The use of power efficient SAR ADC with serial interface for data acquisition enables the ASIC to be used in a multiple electrode EIT system for cardiac output monitoring. The ASIC achieves the desired SNR, frame rate and accuracy specifications with a power consumption of 11.8 mW.

REFERENCES

[1] S. R. Toukhsati, A. Driscoll, and D. L. Hare, "Patient self-management in chronic heart failure establishing concordance between guidelines and practice," *Cardiac Failure Rev.*, vol. 1, no. 2, pp. 128–131, 2015.

[2] A. Hasan and V. Paul, "Telemonitoring in chronic heart failure," *European Heart J.*, vol. 32, no. 12, pp. 1457–1464, Jun. 2011.

[3] P. B. Adamson *et al.*, "Ongoing right ventricular hemodynamics in heart failure: Clinical value of measurements derived from an implantable monitoring system," *J. Amer. College Cardiology*, vol. 41, no. 4, pp. 565–71, Feb. 2003.

[4] A. Sherwood, J. McFetridge, and J. S. Hutcheson, "Ambulatory impedance cardiography: A feasibility study," *J. Appl. Physiol. (Bethesda, Md. : 1985)*, vol. 85, no. 6, pp. 2365–2369, Dec. 1998.

[5] A. D. Goedhart, N. Kupper, G. Willemsen, D. I. Boomsma, and E. J. de Geus, "Temporal stability of ambulatory stroke volume and cardiac output measured by impedance cardiography," *Biol. Psychology*, vol. 72, no. 1, pp. 110–117, Apr. 2006.

[6] F. Lechin, B. van der Dijs, and A. E. Lechin, "Autonomic nervous system assessment throughout the wake-sleep cycle and stress," *Psychosomatic Med.*, vol. 66, no. 6, pp. 974–976, Nov. 2004.

[7] A. P. J. van Eekelen, J. H. Houtveen, and G. A. Kerkhof, "Circadian variation in base rate measures of cardiac autonomic activity," *Eur. J. Appl. Physiol.*, vol. 93, no. 1–2, pp. 39–46, Oct. 2004.

[8] M. Metra, "Use of cardiopulmonary exercise testing with hemodynamic monitoring in the prognostic assessment of ambulatory patients with chronic heart failure," *J. Amer. College Cardiology*, vol. 33, no. 4, pp. 943–50, Mar. 1999.

[9] G. Cybulski, *Ambulatory Impedance Cardiography : The Systems and Their Applications*. Berlin, Germany: Springer, 2010.

[10] J. T. Heywood *et al.*, "Impact of practice-based management of pulmonary artery pressures in 2000 patients implanted with the CardioMEMS sensor," *Circulation*, vol. 135, no. 16, pp. 1509–1517, Apr. 2017.

[11] W. T. Abraham *et al.*, "Wireless pulmonary artery haemodynamic monitoring in chronic heart failure: A randomised controlled trial," *Lancet*, vol. 377, no. 9766, pp. 658–666, Feb. 2011.

[12] E. K. Murphy, S. H. Arshad, and R. J. Halter, "Cardio-respiratory gated electrical impedance tomography for monitoring stroke-volume," in *Proc. 18th Int. Conf. Biomed. Appl. Electric. Impedance Tomography*, Jun. 2017, p. 22.

[13] B. K. Hensel, G. Demiris, and K. L. Courtney, "Defining obtrusiveness in home telehealth technologies: A conceptual framework," *J. Amer. Med. Informat. Assoc.*, vol. 13, no. 4, pp. 428–431, Jul. 2006.

[14] J. H. M. Bergmann and A. H. McGregor, "Body-worn sensor design: What do patients and clinicians want?" *Ann. Biomed. Eng.*, vol. 39, no. 9, pp. 2299–2312, Sep. 2011.

[15] L. Yan, J. Bae, S. Lee, T. Roh, K. Song, and H. J. Yoo, "A 3.9 mW 25-electrode reconfigured sensor for wearable cardiac monitoring system," *IEEE J. Solid-State Circuits*, vol. 46, no. 1, pp. 353–364, Jan. 2011.

[16] S. Hong, J. Lee, J. Bae, and H. J. Yoo, "A 10.4 mW electrical impedance tomography SoC for portable real-time lung ventilation monitoring system," *IEEE J. Solid-State Circuits*, vol. 50, no. 11, pp. 2501–2512, Nov. 2015.

[17] M. Kim *et al.*, "A 1.4-mΩ sensitivity 94-dB dynamic-range electrical impedance tomography SoC and 48-channel hub-SoC for 3-D lung ventilation monitoring system," *IEEE J. Solid-State Circuits*, vol. 52, no. 11, pp. 2829–2842, Nov. 2017.

[18] D. Andreuccetti, R. Fossi, and C. Petrucci, "An internet resource for the calculation of the dielectric properties of body tissues in the frequency range 10 Hz–100 GHz," 1997.

[19] E. T. McAdams, J. Jossinet, A. Lackermeier, and F. Risacher, "Factors affecting electrode-gel-skin interface impedance in electrical impedance tomography," *Med. Biol. Eng. Comput.*, vol. 34, no. 6, pp. 397–408, Nov. 1996.

[20] M. M. Gebhard, E. Gersing, C. J. Brockhoff, P. A. Schnabel, and H. J. Bretschneider, "Impedance spectroscopy: A method for surveillance of ischemia tolerance of the heart," *Thoracic Cardiovascular Surgeon*, vol. 35, no. 1, pp. 26–32, Feb. 1987.

[21] B. C.-H. Kwan *et al.*, "Bioimpedance spectroscopy for the detection of fluid overload in Chinese peritoneal dialysis patients," *J. Int. Soc. Peritoneal Dialysis*, vol. 34, no. 4, pp. 409–16, Jun. 2014.

[22] A. Adler and A. Boyle, "Electrical impedance tomography: Tissue properties to image measures," *IEEE Trans. Biomed. Eng.*, vol. 64, no. 11, pp. 2494–2504, Nov. 2017.

[23] W. P. Segars, G. Sturgeon, S. Mendonca, J. Grimes, and B. M. W. Tsui, "4D XCAT phantom for multimodality imaging research," *Med. Phys.*, vol. 37, no. 9, pp. 4902–4915, Aug. 2010.

[24] P.-O. Persson and G. Strang, "A simple mesh generator in MATLAB," *SIAM Rev.*, vol. 46, no. 2, pp. 329–345, Jan. 2004.

[25] C. Geuzaine and J.-F. Remacle, "Gmsh: A 3-D finite element mesh generator with built-in pre- and post-processing facilities," *Int. J. Numer. Methods Eng.*, vol. 79, no. 11, pp. 1309–1331, Sep. 2009.

[26] F. Braun *et al.*, "Aortic blood pressure measured via EIT: investigation of different measurement settings," *Physiological Meas.*, vol. 36, no. 6, pp. 1147–1159, Jun. 2015.

[27] A. Borsic, A. Hartov, K. D. Paulsen, and P. Manwaring, "3D electric impedance tomography reconstruction on multi-core computing platforms," in *Proc. IEEE 30th Annu. Int. Conf. Eng. Med. Biol. Soc.*, Aug. 2008, pp. 1175–1177.

[28] R. J. Halter, A. Hartov, and K. D. Paulsen, "A broadband high-frequency electrical impedance tomography system for breast imaging," *IEEE Trans. Biomed. Eng.*, vol. 55, no. 2, pp. 650–659, Feb. 2008.

[29] R. Cook, G. Saulnier, D. Gisser, J. Goble, J. Newell, and D. Isaacson, "ACT3: A high-speed, high-precision electrical impedance tomograph," *IEEE Trans. Biomed. Eng.*, vol. 41, no. 8, pp. 713–722, Aug. 1994.

[30] A. Hartov *et al.*, "A multichannel continuously selectable multifrequency electrical impedance spectroscopy measurement system," *IEEE Trans. Biomed. Eng.*, vol. 47, no. 1, pp. 49–58, Jan. 2000.

[31] E. K. Murphy, R. J. Halter, and K. Odame, "Simulation study for the design of an EIT system for cardiac output monitoring," in *Proc. 41st Annu. Northeast Biomed. Eng. Conf.*, Apr. 2015, pp. 1–2.

[32] A. Sedra and K. Smith, "A second-generation current conveyor and its applications," *IEEE Trans. Circuit Theory*, vol. CT-17, no. 1, pp. 132–134, Feb. 1970.

[33] I. Jivet and B. Dragoi, "On-electrode autonomous current generator for multi-frequency EIT," *Physiological Meas.*, vol. 29, no. 6, pp. S193–S201, Jun. 2008.

[34] V. Saxena and R. Baker, "Indirect feedback compensation of CMOS Op-Amps," in *Proc. IEEE Workshop Microelectron. Electron Devices*, 2006, pp. 3–4.

[35] A. Sedra, G. Roberts, and F. Gohh, "The current conveyor: History, progress and new results," *IEEE Proc. G Circuits, Devices Syst.*, vol. 137, no. 2, pp. 78–87, Apr. 1990.

[36] E. Sackinger and W. Guggenbuhl, "A high-swing, high-impedance MOS cascode circuit," *IEEE J. Solid-State Circuits*, vol. 25, no. 1, pp. 289–298, Feb. 1990.

[37] A. Zeki and H. Kuntman, "Accurate and high output impedance current mirror suitable for CMOS current output stages," *Electron. Lett.*, vol. 33, no. 12, pp. 1042–1043, Jun. 1997.

[38] Y.-C. Teng and K. M. Odame, "A 10 MHz 85 dB dynamic range instrumentation amplifier for electrical impedance tomography," *in Proc. IEEE Biomed. Circuits Syst. Conf.*, Oct. 2014, pp. 632–635.

[39] E. K. Murphy, M. Takhti, J. Skinner, R. J. Halter, and K. Odame, "Signal-to-noise ratio analysis of a phase-sensitive voltmeter for electrical impedance tomography," *IEEE Trans. Biomed. Circuits Syst.*, vol. 11, no. 2, pp. 360–369, Apr. 2017.

[40] N. Verma and a. P. Chandrakasan, "An ultra low power ADC for wireless micro-sensor applications," *Electr. Eng. Comput. Sci.*, vol. Master, pp. 143–147, 2005.

[41] R. H. Walden, "Analog-to-digital converter survey and analysis," *IEEE J. Sel. Areas Commun.*, vol. 17, no. 4, pp. 539–550, Apr. 1999.
[42] B. Wilson, "Universal conveyor instrumentation amplifier," *Electron. Lett.*, vol. 25, no. 7, pp. 470–471, 1989.
[43] Y.-C. Teng, M. Takhti, and K. M. Odame, "A power adaptive variable gain instrumentation amplifier for electrical impedance tomography," in *Proc. IEEE Biomed. Circuits Syst. Conf.*, Oct. 2015, pp. 1–4.
[44] B. Razavi, *Design of Analog CMOS Integrated Circuits*. New York, NY, USA: McGraw-Hill, 2003.
[45] "EIDORS : Electrical Impedance Tomography and Diffuse Optical Tomography Reconstruction Software," [Online]. Available: http://eidors3d.sourceforge.net/
[46] T. Corrigan, "AN-1024 APPLICATION NOTE : How to Calculate the Settling Time and Sampling Rate of a Multiplexer." [Online]. Available: http://www.analog.com/media/en/technical-documentation/application-notes/AN-1024.pdf
[47] S.-Y. Peng *et al.*, "A power-efficient reconfigurable OTA-C filter for low-frequency biomedical applications," *IEEE Trans. Circuits Syst. I, Reg. Papers*, vol. 65, no. 2, pp. 543–555, Feb. 2018.

Arun Rao (M'16) received the B.E degree from Bangalore University, Bengaluru, India, and the M.S. degree in electrical engineering from Utah State University, Logan, UT, USA. He is currently working toward the Ph.D with the Thayer School of Engineering, Dartmouth College, Hanover, NH, USA. He is interested in small form factor hardware system design and novel circuits for biomedical instrumentation and image sensors.

Yueh-Ching Teng (S'17) received M.Sc degree in electrical and computer engineering from Ohio State University, Columbus, OH, USA, in 2011. He is currently working toward the Ph.D. degree with Thayer School of Engineering, Dartmouth, Hanover, NH, USA. From 2011 to 2012, he was a Research Assistant Engineer with the ElectroScience Laboratory where he worked on analog/mixed-signal circuit designs for RFID applications. In 2017, he was an analog design intern at Texas Instruments, Manchester, USA. His current research interests are in the field of read-out amplifier design for biomedical applications, sensor interface, and power management circuits.

Christopher Schaef (M'16) received the B.S and M.S. degrees in industrial engineering from Helmut-Schmidt University, Hamburg, Germany, in 2010 and 2011, respectively and the Ph.D. degree from Dartmouth College, Hanover, NH, USA, 2016. He is currently a Power Delivery Researcher with the Circuits Research Laboratory, Intel Corporation, Santa Clara, CA, USA. His research interests are in integrated power management, energy harvesting, and hybrid dc-dc converters.

Ethan Murphy received the B.S and M.S degree from Worcester Polytechnic Institute, Worcester, MA, USA, in 2002 and Ph.D degree in all mathematics from Colorado State University, Fort Collins, CO, USA, in 2007. Prior coming to Dartmouth in 2014, he worked in industry and academic positions. He is currently a Research Scientist with the Thayer School of Engineering, Dartmouth College, Hanover, NH, USA. His interests are in inverse problems, specifically electrical impedance tomography, medical imaging, data fusion, and error analysis.

Saaid Arshad received the AB degree in engineering sciences from Dartmouth College, Hanover, NH, USA, in 2014. He is currently working toward the Ph. D. degree with the Thayer School of Engineering, Dartmouth College, Hanover, NH, USA, under Assistant Professor of Engineering Ryan J. Halter. He is interested in applications of electrical impedance tomography to cardiovascular physiology, image processing, and medical imaging.

Ryan J. Halter (M'05) is an Assistant Professor of Engineering with the Thayer School of Engineering, Dartmouth College, Hanover, NH, USA. His research interests are in biomedical instrumentation, medical imaging, electrical impedance tomography and spectroscopy, tissue bioimpedance, cancer detection technologies, traumatic brain injury, medical robotics, and image guidance.

Kofi Odame (S'06–M'08–SM'15) is an Associate Professor of electrical engineering with the Thayer School of Engineering Dartmouth College, Hanover, NH, USA. His primary interest is in analog integrated circuits for nonlinear signal processing. This work has applications in low-power electronics for implantable and wearable biomedical devices, as well as in autonomous sensor systems.

Physiological Measurement

IPEM Institute of Physics and Engineering in Medicine

PAPER

Fused-data transrectal EIT for prostate cancer imaging

To cite this article: Ethan K Murphy *et al* 2018 *Physiol. Meas.* **39** 054005

View the article online for updates and enhancements.

Related content

- Anatomically accurate hard priors for transrectal electrical impedance tomography (TREIT) of the prostate
H Syed, A Borsic, A Hartov et al.
- Sensitivity study of an ultrasound coupled TREIT system for prostate imaging
Y Wan, R Halter, A Borsic et al.
- Electrical impedance tomography reconstruction for 3D imaging of the prostate
A Borsic, R Halter, Y Wan et al.

This content was downloaded from IP address 129.170.195.196 on 21/08/2018 at 15:10

IOP Publishing Physiol. Meas. 39 (2018) 054005 (13pp) https://doi.org/10.1088/1361-6579/aabf22

Physiological Measurement

IPEM Institute of Physics and Engineering in Medicine

PAPER

Fused-data transrectal EIT for prostate cancer imaging

Ethan K Murphy[1], Xiaotian Wu[1] and Ryan J Halter[1,2]

[1] Thayer School of Engineering, Dartmouth College, Hanover, NH 03755, United States of America
[2] Geisel School of Medicine, Dartmouth College, Hanover, NH 03755, United States of America

E-mail: Ethan.K.Murphy@dartmouth.edu

RECEIVED
15 December 2017

REVISED
6 April 2018

ACCEPTED FOR PUBLICATION
18 April 2018

PUBLISHED
24 May 2018

Keywords: electrical impedance tomography, measurement sensitivity, data fusion, prostate cancer

Abstract

Objective: Prostate cancer is a significant problem affecting 1 in 7 men. Unfortunately, the diagnostic gold-standard of ultrasound-guided biopsy misses 10%–30% of all cancers. The objective of this study was to develop an electrical impedance tomography (EIT) approach that has the potential to image the entire prostate using multiple impedance measurements recorded between electrodes integrated onto an end-fired transrectal ultrasound (TRUS) device and a biopsy probe (BP). *Approach*: Simulations and sensitivity analyses were used to investigate the best combination of electrodes, and measured tank experiments were used to evaluate a fused-data transrectal EIT (fd-TREIT) and BP approach. *Main results*: Simulations and sensitivity analysis revealed that (1) TREIT measurements are not sufficiently sensitive to image the whole prostate, (2) the combination of TREIT + BP measurements increases the sensitive region of TREIT-only measurements by 12×, and (3) the fusion of multiple TREIT + BP measurements collected during a routine or customized 12-core biopsy procedure can cover up to 76.1% or 94.1% of a nominal 50 cm^3 prostate, respectively. Three measured tank experiments of the fd-TREIT + BP approach successfully and accurately recovered the positions of 2–3 metal or plastic inclusions. *Significance*: The measured tank experiments represent important steps in the development of an algorithm that can combine EIT from multiple locations and from multiple probes—data that could be collected during a routine TRUS-guided 12-core biopsy. Overall, this result is a step towards a clinically deployable impedance imaging approach to scanning the entire prostate, which could significantly help to improve prostate cancer diagnosis.

1. Introduction

Prostate cancer is a significant problem for men. One of every seven men will be diagnosed with the disease, and in 2016 over 180 000 newly diagnosed cases were reported in the US (Siegel *et al* 2016). Detecting prostate cancer non-invasively is clinically challenging. Prostate-specific antigen (PSA)-based screening has a high sensitivity, but low specificity due to numerous benign processes elevating PSA levels in the blood (Walsh 2007). Men with elevated levels of PSA routinely undergo an image-guided biopsy procedure for more accurate diagnosis (Shariat and Roehrborn 2008). During these procedures, transrectal ultrasound (TRUS) is used to visualize the prostate and a series of 6–20 biopsy cores are typically extracted from standard locations within the prostate (TRUS alone is not sufficiently sensitive and specific for targeted biopsy (Harvey *et al* 2012)). Unfortunately, TRUS-guided biopsies miss 10%–30% of all cancers (Walsh 2007); these low detection rates stem largely from the small volume of tissue sampled during these biopsy procedures (typically <1% of the prostate volume) (Harnden *et al* 2008).

Our overall goal is to improve the accuracy of prostate cancer diagnosis using transrectal electrical impedance tomography (TREIT) so that cancers of clinical significance can be identified earlier through targeted biopsy. Numerous *ex vivo* studies have found that electrical impedance can be used to differentiate cancerous from benign prostate tissue (Lee *et al* 1999, Halter *et al* 2007, Salomon *et al* 2009). Furthermore, TREIT has been described as a potential adjunct to TRUS (Wan *et al* 2010, Syed *et al* 2012), and one study considered the fusion of TREIT and a biopsy probe (BP) electrode (though the development was very preliminary) (Wan *et al* 2012). The early work in TREIT-based imaging systems relied on the use of a *side-fired* TRUS probe which provided 3D ultrasound images of the prostate. While having the 3D prostate image was useful for mesh generation in EIT, this

© 2018 Institute of Physics and Engineering in Medicine

geometry was not compatible with routine clinical biopsy procedures in which an *end-fired* TRUS probe is the standard-of-care; the side-fired TRUS probe required men to be in a more exposed and uncomfortable lithotomy position as opposed to a lateral position used for an end-fired probe. In addition to being more commonly used, end-fired probes also yield significantly higher rates of cancer detection (Ching *et al* 2009). Here we explore how TREIT might be coupled to an *end-fired TRUS probe* and optimized for imaging during prostate biopsy procedures.

The challenge in transitioning to an end-fired probe is that the surface area available for electrodes is significantly less than that available on a side-fired device. As a result, fewer or smaller electrodes must be used and the maximum electrode spacing will be reduced; this reduced spacing directly impacts the depth of sensitivity (e.g. section 2.5.2 of (Loke 2013)). Comparing the region of sensitivity between the two geometries reveals that the side-fired probe is sensitive to 21× more volume of a nominal prostate (50 cm^3) than an end-fired probe (12.6% compared to 0.6%). Here we show that coupling electrodes on the TRUS probe with distant electrodes embedded on a BP placed within the prostate increases the region of sensitivity to 94.6% and 7.2% for the side- and end-fired probes, respectively. While sensitivity for the coupled approach using the end-fired geometry is still too small, we hypothesize that fusing EIT data recorded from multiple states (i.e. BP positions) will provide sufficient sensitivity for imaging the entire prostate with a standard-of-care end-fired TRUS probe. For the remainder of this manuscript, TRUS and TREIT will refer to the end-fired geometry unless explicitly defined to be referencing a side-fired probe.

This study presents a simulated experiment, sensitivity analysis, and three measured tank experiments to (1) illustrate why it is necessary and advantageous to combine BP with TREIT data and (2) demonstrate *for the first time* that recording TREIT + BP impedance data from multiple locations in a saline filled tank can be successfully fused to produce accurate reconstructions of conductivity. Through the simulated experiment, we show that the end-fired TREIT probe by itself can accurately detect a 2 mm metal inclusion (without noise) out to a maximum distance of only 12–13 mm from the probe face. While combining TRUS + BP measurements together increased the sensitive region of TRUS-only measurements by 12×, this volume is still insufficient to image the entire prostate. To overcome this, we have developed a fused-data (fd) approach to couple multiple TREIT + BP measurements together.

Three saline tank experiments were conducted to validate specific aspects of the fd-TREIT + BP approach. Specifically, 2–3 metal and plastic inclusions were submerged in the tank and multiple impedance measurements were recorded from the TREIT + BP device when it was (1) rotated at a fixed radius around a set of inclusions, (2) randomly translated around the inclusions in a single x/y-plane, and (3) randomly translated in four x/y-planes about the inclusions. Electromagnetic (EM) tracking was used to record the TRUS-probe state (position and orientation) for the latter two experiments. These three experiments were each important validation steps towards a generalized fusion of 3D state data for EIT and were used to establish that (1) fd-EIT is feasible (rotation experiment), (2) fd-EIT using EM tracking is feasible (single z-plane experiment), and (3) fd-EIT using EM tracking can produce accurate 3D reconstructions (four z-plane experiment). Reconstructions were successful in all three experiments, yielding average position errors of 1.27, 2.49, and 2.56 mm, respectively. The fd-TREIT + BP algorithm was investigated through exploration of (1) the size of the reconstructed region of interest (ROI) over which the conductivity distribution was allowed to vary, (2) the voxel sizes of the reconstruction mesh, and (3) the data used in the reconstruction algorithm.

Here we demonstrate the potential improvements that can be realized in EIT when multiple probes are combined to image a volume of interest. In particular, this work demonstrates the feasibility of fusing data extracted from an end-fired TRUS-based prostate biopsy procedure. Tank experiments specifically suggest that by combining end-fired TREIT electrodes with four electrodes embedded on a BP and sampling from multiple positions (as would be done in a multi-core prostate biopsy procedure), one can produce spatially accurate images able to identify inclusions ~2× beyond the sensitivity region of the TREIT probe alone. A final contribution is the description of the open-domain fusion algorithm which can be considered for other applications with similar constraints.

The paper is structured as follows. Section 2 describes the forward and inverse EIT problems, instrument tracking, the experiments conducted, and the measurement system, parameters and metrics used for analysis. Section 3 describes the results of the simulated experiment, sensitivity and measurement analysis, and three measured tank experiments. Section 4 discusses the likely approaches to overcome the sensitivity of the current algorithm to parameter values, and describes steps towards clinical evaluation of the method.

2. Methods

2.1. Forward problem

The forward problem relies on solving the Laplace equation, $\nabla \cdot \sigma \nabla u = 0$, over an open domain, where σ is the conductivity and u is the electric potential. The complete electrode model (CEM) is used to realistically

account for discrete electrodes (Somersalo *et al* 1992). The forward problem calculates the electric potential distribution throughout the domain and voltages on the electrodes assuming the conductivity distribution and applied currents on the electrodes are known. The CEM boundary conditions specify no current flows in or out of the domain except through the electrodes. The open domain is modeled by expanding the modeled domain sufficiently so that effectively no current is flowing near the boundaries representing open portions of the domain. The solution to the forward problem is calculated in 3D using the finite element method (FEM) with linear basis functions.

2.2. Inverse methods

The inverse method considered here is the standard Gauss–Newton algorithm employing a Laplace-smoothing Tikhonov regularization scheme. At a given state, standard EIT data, which we refer to as a frame of data, is collected on the TREIT array and BP electrodes (TREIT + BP). Here we considered fused-data EIT which combines frames from multiple states of the TREIT + BP data. Similar to the approach in Murphy *et al* (2017a), the aim is to minimize the following objective function:

$$E(\boldsymbol{\delta\sigma}) = \sum_{n=1}^{N_S} \|\boldsymbol{J_n}\boldsymbol{\delta\sigma} - \boldsymbol{\Delta v_n}\|_2^2 + \lambda \|\boldsymbol{L}(\boldsymbol{\sigma}_0 + \boldsymbol{\delta\sigma})\|_2^2, \tag{1}$$

where N_S is the number of states of data fused together, $\mathbf{J}_n$ is the Jacobian corresponding to the nth state, $\boldsymbol{\Delta v_n}$ is the voltage differences of the nth state, λ is the Tikhonov factor, $\mathbf{L}$ is the regularization matrix, σ_0 is the initial guess of the conductivity distribution, and $\boldsymbol{\delta\sigma}$ is the perturbation we aim to solve for at each iteration. Note each $\mathbf{J_n}$ and $\boldsymbol{\Delta v_n}$ are size $N_P \times N_C$ and $N_P \times 1$, respectively, where N_P is the number of measurement patterns and N_C are the number of coarse inverse voxels. One can rewrite (1) equivalently as

$$E(\boldsymbol{\delta\sigma}) = \|\boldsymbol{J_{FD}}\boldsymbol{\delta\sigma} - \boldsymbol{\Delta v_{FD}}\|_2^2 + \lambda \|\boldsymbol{L}(\boldsymbol{\sigma}_0 + \boldsymbol{\delta\sigma})\|_2^2, \tag{2}$$

where $\boldsymbol{J_{FD}}$ and $\boldsymbol{\Delta v_{FD}}$ are concatenated matrices and vectors from all the states. This formulation allows one to use the standard updating formula:

$$\boldsymbol{\delta\widetilde{\sigma}} = \left(\boldsymbol{J_{FD}^T J_{FD}} + \lambda \boldsymbol{L}^T\boldsymbol{L}\right)^{-1}\left(\boldsymbol{J_{FD}^T \Delta v_{FD}} - \boldsymbol{\lambda L}^T\boldsymbol{L\sigma}_0\right). \tag{3}$$

Only difference images are considered in this study. Thus $\boldsymbol{\Delta v_{FD}}$ is the difference between a test measurement and a reference measurement of homogeneous conductivity.

Our inverse implementation uses the dual-mesh method (Borsic *et al* 2010), which allows one to solve the Jacobian on a fine mesh while estimating the conductivity on a much coarser inverse mesh. This approach yields an electric potential with high accuracy throughout the domain and enables a convenient approach to fuse data from different states. For difference imaging, assuming a homogeneous conductivity, the coarse Jacobian for any state is calculated by the following: (1) a fine Jacobian, $\mathbf{J}_{F,0}$, is computed on the fine mesh in a untransformed state (e.g. State 1, figure 1); (2) a single coarse mesh is chosen (red, uniform grid in figure 1); (3) the fine mesh (FEM mesh) is transformed to a specific measured state (e.g. State 2 or 3, figure 1) and a coarse-to-fine matrix is constructed, $\mathbf{P}_n$; and (4) the coarse Jacobian of the nth state is then computed by $\boldsymbol{J}_n = \mathbf{J}_{F,0}\mathbf{P}_n$. Note that $\mathbf{P}_n$ is size $N_F \times N_C$, where N_F and N_C are the number of fine (FEM) and coarse voxels, respectively, and that the ith column of $\mathbf{P}_n$ is zeros except for 1's at rows corresponding to associated fine nodes of the ith coarse voxel. For example, the cyan fine nodes highlighted in figure 1, which are different for each of the three states, are associated to the fixed coarse voxel (blue box). The computational cost is primarily due to the untransformed fine Jacobian, which is solved using the formulation derived in Geselowitz (1971). Thus, for difference imaging where $\mathbf{J}_{F,0}$ could be computed previously, the computational time is very minimal for all coarse Jacobians.

The open domain is modeled in the inverse problem via a mega-node, which has been used in Syed *et al* (2012) and Murphy *et al* (2016). In practical terms, the coarse mesh that we define encompasses a region in the domain, a reconstructed ROI, where we expect sufficient sensitivity to resolve spatially varying conductivity. Outside of this region a single conductivity value is reconstructed, and this is referred to as a mega-node.

2.3. Instrument tracking

In order to specify the TRUS probe location and orientation within our imaging domain (i.e. the different states in figure 1), EM tracking was used to localize the TRUS/TREIT probe. An Aurora V2 EM tracking system (Northern Digital Inc., Ontario, Canada) was used to track a 1 × 5 mm six degree-of-freedom sensor attached directly to the TRUS probe via heat shrink (see figure 2(D)) and a second similar sensor embedded in a 85 mm long pointing stylus. The EM-tracked stylus pointed to five known locations on the TRUS probe to register the probe in EM-space. The BP was affixed to the TRUS probe and the stylus pointed to the electrodes on the BP for registration. The stylus was also used to determine the location of the inclusions by pointing to the surface of the inclusions and then subtracting the respective radii. All tracking data in the form of Cartesian 3D coordinates

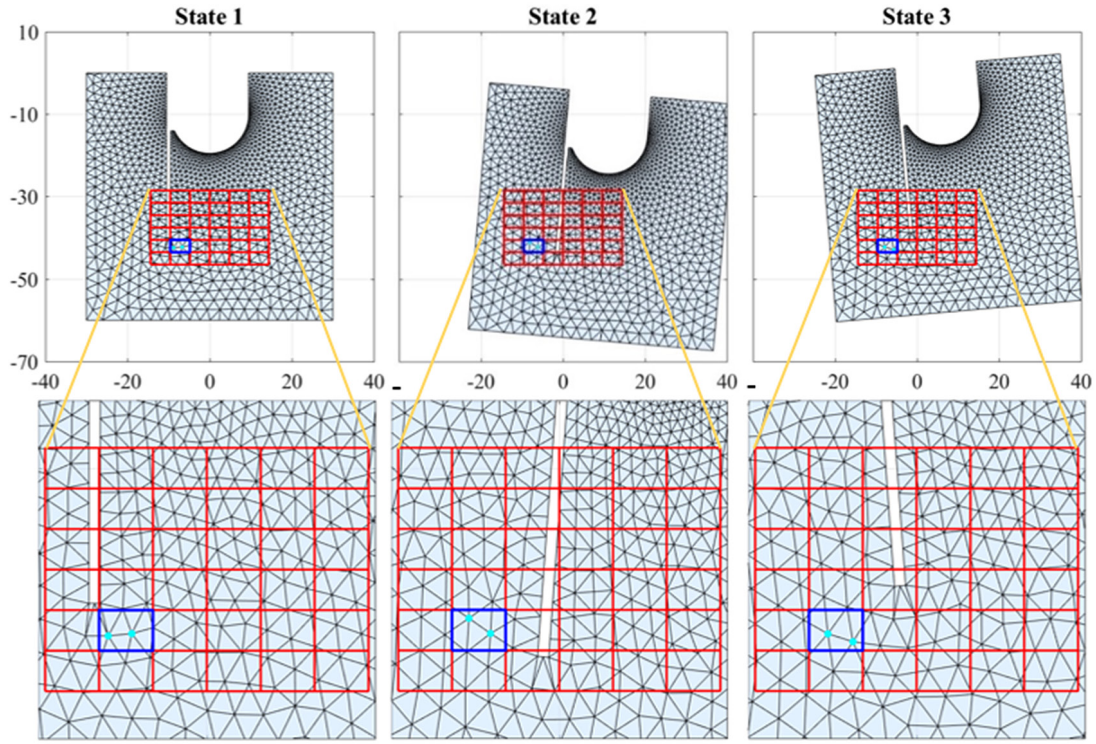

Figure 1. 2D illustration of coarse-to-fine fusing process, which involves a fixed coarse mesh (red uniform grid) and a fine FEM mesh that is translated and rotated to the state of each measurement. A coarse voxel is highlighted in blue and associated fine FEM nodes are highlighted as cyan nodes for each state. The TRUS probe and biopsy needle are cut-out of the domain because they represent boundaries in terms of electrode modeling.

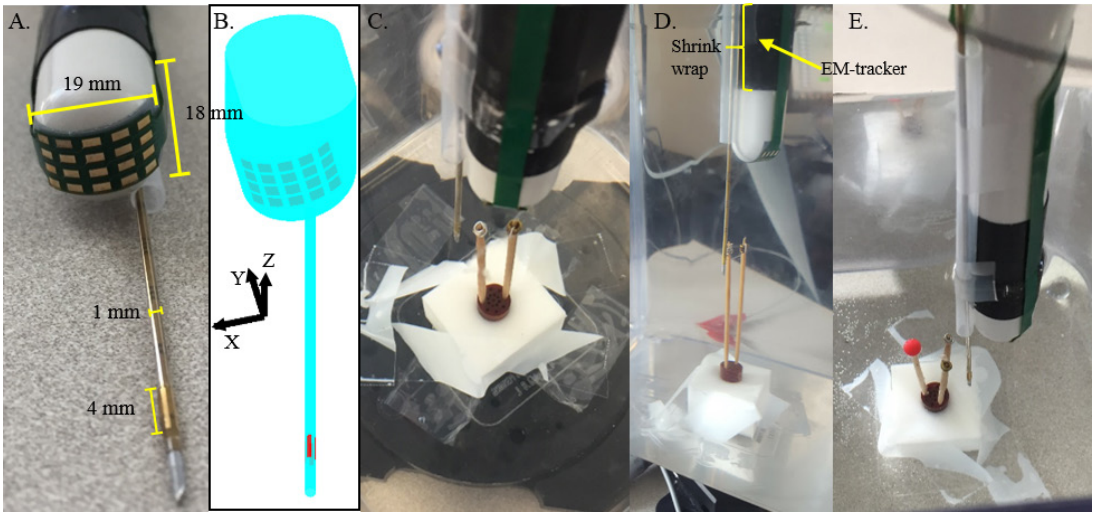

Figure 2. The TRUS and BPs (A) compared to its modeled counterpart (B), and photographs from the rotation experiment with two metal inclusions (C), the 1 *z*-plane, *x*/*y*-translation experiment also with two metal inclusions (D), and the four *z*-plane, *x*/*y*-translation experiment and three inclusions (one plastic and two metal) (E).

(translation) and quaternions (orientation) was acquired via serial communication with the Aurora system in MATLAB. A planar phantom consisting of a checkerboard pattern with 25.4 mm squares was used to evaluate the EM tracking system accuracy. The stylus was tracked while pivoting (20 times) at each corner from a chosen set of grid corners. This yielded average distances of 25.725 mm between adjacent sides with a standard deviation of 0.55 mm (n = 209). At least two EM measurements were used to determine each inclusion position, which implies position accuracy within $0.39 = 0.55/\sqrt{2}$ mm (assuming error within ± 1 SD and the error is unbiased and normally distributed). The errors in BP and TRUS registration should be smaller due to averaging over four and five points, respectively.

Table 1. Details of Experiments.

Experiment	BP used	No. of states/frames	Inclusions	Diameters
Simulated inclusions	No	1	1 metal	2 mm
Measured rotations	Yes	18	2 metal	3 mm
Measured 1 Z-plane, x/y-translations	Yes	25	2 metal	3 mm
Measured 4 Z-plane, x/y-translations	Yes	60 (15-per slice)	2 metal, 1 plastic	3 and 5 mm

2.4. Experiment and modeling details

All experiments were based on the dimensions of a Phillips C9-EC TRUS probe and all tank experiments incorporated a BP (figure 2(A)). Twenty gold-plated electrodes (size 1.5 mm $\times$ 2.0 mm) configured in a 4 $\times$ 5 grid were printed on a 1 mil polyamide substrate and secured with a pressure sensitive adhesive over the active element of the TRUS probe; the electrode array is sonolucent to provide multi-modal imaging with both TRUS and TREIT (Wan *et al* 2012). Four gold-plated electrodes (size 4 mm $\times$ 0.6 mm) were similarly printed on 1 mil thick polyamide substrate and secured around the BP (Everitt *et al* 2018). A 3D FEM mesh that matched the probe and electrode dimensions, which had roughly 500k nodes and 3M elements, (figure 2(B)) was produced using gmsh (Geuzaine and Remacle 2009). To model the open domain, the mesh was extended 80 mm in the x- and y-directions from the probe face and 20 mm behind and 70 mm in front of the tip of the TRUS probe; along the z-direction (see figure 2(B) for axes orientations). The remainder of this section details the experiments conducted and the modeling choices made for the coarse meshes.

2.4.1. Experiment descriptions

The BP is held fixed relative to the TRUS probe for all measured tank experiments with the BP electrodes always 37 mm in front of the probe face. There was one simulation experiment and three measured tank experiments. The tank experiments (figures 2(C)–(E)) include rotations, x/y-translations in a single plane, and x/y-translations at four different depths (or z-planes) of the TRUS probe. Table 1 details the experimental parameters.

2.4.1.1.Simulation experiment

Simulations were performed to provide an estimated depth of sensitivity that the TRUS probe can achieve without the presence of the BP electrodes. Simulated data was produced corresponding to a single metal inclusion with 2 mm diameter placed 3–20 mm from the TRUS probe in 1 mm steps at angles spanning from $-45°$ to 45° degrees with respect to the TRUS probe axis.

2.4.1.2.Measured rotation experiment

The TREIT + BP system was held fixed and the saline tank (positioned on a rotation stage) was rotated in 20° increments. This yielded 18 frames of TREIT + BP data for reconstruction. The inclusions were centered about the rotation axis and were separated by 12 mm. The TRUS probe was also centered on the rotation axis with the BP offset 11 mm from the rotation axis and in the same direction; the BP electrodes were located 37 mm in front of the TRUS probe face. The metal inclusions were tightly wound copper wire of 3 mm diameter, and were placed on ~2 mm diameter wooden posts that were soaked in saline overnight to minimize their effect on measurements.

2.4.1.3.Measured 1 Z-plane, x/y-translation experiment

Twenty-five frames of TREIT + BP data were recorded from random translations of the TRUS probe at a fixed depth within the saline tank. Two 3 mm diameter metal inclusions spaced 10 mm apart were used for this experiment (see figures 2(D) and 6(B)). The states (position and orientation) of the TRUS probe were recorded with the EM tracker.

2.4.1.4.Measured 4 Z-plane, x/y-translation

Sixty frames of EIT data were recorded from random translations of the TRUS probe at four different depths or z-planes (15 frames per z-plane) (see figures 2(E) and 6(C)). There were three inclusions; two 3 mm diameter metal inclusions and a 5 mm diameter plastic bead. The three inclusions were placed in different x/y-locations and at different depths (z). The true locations were determined via the pointing stylus using the EM tracker.

2.4.2. Coarse mesh descriptions

Two types of coarse meshes were considered: (1) a cylindrical-based mesh that fans out from the TRUS probe face in the simulation experiment, and (2) a Cartesian-based mesh within a cylinder representing the ROI about the inclusions in the three measurement experiments.

2.4.2.1.Simulation experiment's coarse mesh

The cylindrical coordinates extended from the probe face (a radius of 8 mm from an origin chosen within the TRUS probe) to 32 mm, angles $\pm 60°$ from the axis of the TRUS probe (z-axis in figure 2(B)), and the cylinder height is in the y-axis (see figure 2(B)). There are a total of 1401 voxels centered at 10, 20, and seven equally spaced points in the radial, angular, and y-axis directions, respectively, and a single mega-node modeled the remaining domain.

2.4.2.2.Measurement experiments' coarse mesh

The coarse meshes for the measured tank experiments were all Cartesian based in a cylindrical ROI centered on the mean of the inclusions. It was important to explore how large of an ROI can be used, since the aim is to image the entire prostate. To investigate this, reconstructions were performed by varying (1) the voxel sizes from $1.5 \times 1.5 \times 2.7$ mm to $3.0 \times 3.0 \times 2.7$ mm in 0.5 mm steps, and (2) the radius of the ROI's from 5 to 20 mm in variable step sizes (~2–3 mm). This resulted in coarse meshes ranging from 209 to 4712 voxels.

2.5. Sensitivity and measurement analysis

The region of sensitivity and the effective number of independent measurements were investigated to characterize the impact of probe geometry and individual measurement patterns. Regions of sensitivity recorded from multiple states were grouped to evaluate how accurately the electrical properties can be estimated throughout an entire prostate. Here, measurement patterns are specified as IIVV groupings for each impedance measurement where II represents the current injection electrode pair (I1,I2) and VV represents the differential voltage sensing pair of electrodes (V1,V2).

2.5.1. Regions of sensitivity

The regions in which measurements were deemed to have sufficient sensitivity for imaging were analyzed for the previously used side-fired TRUS probe (Syed *et al* 2012) and the end-fired TRUS and BP probes for different sets of IIVV patterns. The region of sensitivity was determined by collecting all coarse mesh voxels whose maximum relative sensitivity (given by the Jacobian) were greater than a specified tolerance, e.g. the relative sensitivity of the ith coarse voxel, $(\mathbf{j}_{\boldsymbol{Rel}})_{\boldsymbol{i}}$, is defined as

$$(\mathbf{j}_{\boldsymbol{Rel}})_{\boldsymbol{i}} = \left(\max_{1 \leqslant m \leqslant N_P} |\boldsymbol{j}_{\boldsymbol{m,i}}| \right) / \left(\max_{1 \leqslant i \leqslant N_C} \left[\max_{1 \leqslant m \leqslant N_P} |\boldsymbol{j}_{\boldsymbol{m,i}}| \right] \right), \tag{4}$$

where $\boldsymbol{j}_{\boldsymbol{m,i}}$ is the (m, i)th component of the Jacobian matrix, $\mathbf{J}$. A tolerance of 1/500 was used; this tolerance has previously been demonstrated to provide a good estimate of the region of sensitivity (Murphy *et al* 2016). If fused-data is considered, then the maximum calculation in (4) represents the highest sensitivity over all the patterns and all the considered states for each coarse node. A nominal prostate with volume 50 cm^3 (assumed spherical), and placed 0.5 cm away from the probe to account for the rectal wall, was used to quantify how much of the prostate was encompassed by the region of sensitivity.

2.5.2. Imaging the entire prostate using 12-core biopsy data

The region of sensitivity about the BP electrodes on the end-fired BP analysis was used to determine the percentage of the prostatic volume that could be imaged by fusing together data recorded during a 12-core biopsy procedure of a nominal 50 cm^3 prostate; this analysis assumes that TREIT + BP data can be recorded at one or two depths by simply translating the BP during needle insertion or removal. Three methods were used to determine BP locations: (1) standard probe sites determined from diagrams in Numao *et al* (2008) and Baumann *et al* (2012), (2) two optimal depths per core assuming BP needle trajectories from a standard 12-core biopsy, (3) two optimal depths per core with optimal BP needle trajectories that are within T_D degrees of the standard. The optimization method utilized Matlab's genetic algorithm (*ga*), which is a heuristic optimization method that can quickly find near-optimal solutions.

2.5.3. Number of independent measurements

The effective number of independent measurements was investigated using Picard's condition (Hansen 1998). Assuming the Jacobian is decomposed into its singular value decomposition, $\mathbf{J} = \mathbf{USV}^T$, the Picard condition determines the effective number of singular values by finding where the singular values (diagonal of $\mathbf{S}$) drops to the level of noise (determined via the Fourier coefficients $|\boldsymbol{u}_{\boldsymbol{n}} \cdot \boldsymbol{v}_{\boldsymbol{FD}}|$, where $\boldsymbol{u}_{\boldsymbol{n}}$ is the nth columns of $\mathbf{U}$). Two examples of singular value curves and Fourier coefficients are given in section 3.2 (figure 5(A)) to illustrate the process. The effective the number of singular values is essentially the number of independent measurements.

Table 2. Reconstruction parameters.

Experiment	Patterns per frame/state	Max. patterns used in reconstructions	Tik. factor	Threshold tolerance
Simulated inclusions	29 070	29 070	1×10^1	0.75
Measured rotations	64	1152	1×10^3	0.8
Measured 1 Z-plane, x/y-translations	107	2675	1×10^5	0.7
Measured 4 Z-plane, x/y-translations	19	1140	1×10^3	0.8 metal, −0.8 plastic

2.6. Measurement system, additional parameters, and metrics

Impedance data was recorded using a custom designed EIT system (Khan *et al* 2015). All data was sampled at 10 kHz. Data was recorded on exhaustive, non-flip, non-bipolar IIVV sets of 22 electrodes (18 from TRUS probe and four from the BP), which totaled 43 890 (($C_4(22)$ 4-electrode combinations) × (six IIVV electrode orderings per combination) = 43 890 patterns). Here flip patterns, e.g. for an IIVV = [1 2 3 4], refer to [1 2 4 3], [2 1 3 4], and [2 1 4 3]. In the tank experiments only data that had patterns with 2-TRUS and 2-BP electrodes were used, which numbered 3672. The number of patterns used for image reconstructions were further reduced using a highly restrictive filter that removed any 'bad' patterns, which were determined from homogeneous saline measurements recorded on the day of the experiment. These bad patterns were defined as those that (1) exceeded a noise threshold based on the noise filter described in Murphy *et al* (2017b), (2) reported impedances more than 10% greater than or less than a scalar-best fit to simulated data (patterns where $(\gamma \boldsymbol{v}_{Meas} - \boldsymbol{v}_{Sim})/\boldsymbol{v}_{Sim} > 10\%$, where γ is a scalar that minimizes the impedance differences), (3) had a (log-base 10) coefficient of variation (CoV) that was more than 0.08 away from a log-linear fit, and (4) that had a best fit slope (impedance per sample) that was over 0.03. The CoV constraint was heuristically chosen and was developed to remove measurements that had a CoV that was too high (small voltages likely corrupted by noise) or too low (possibly saturated measurements with unrealistically small standard deviations). The last requirement aimed at removing patterns that experienced a drift, which has intermittently been observed in some measurement patterns in our system. After the overall noise filtering there were 64, 107, and 19 patterns at each BP location for the rotation, 1 z-plane, x/y-translation, and 4 z-plane, x/y-translation experiments, respectively. The average standard deviations from these good patterns for these three experiments were 0.135 mV, 0.134 mV, and 0.096 mV, respectively. In all experiments the saline was 0.1 S m^{-1}, and in all measured reconstructions a saline calibration step was performed after noise filtering (Soni *et al* 2003).

The remaining parameters used in the reconstructions (Tikhonov factor) and data analysis (threshold tolerance) are shown in table 2. Note that the simulated experiment assumed 20 TRUS electrodes, did not use BP electrodes, and the 29 070 patterns represents the full set of exhaustive, non-flip, non-bipolar IIVV patterns for 20 electrodes, i.e. ($C_4(20)$ 4-electrode combinations) × (six IIVV electrode orderings per combination). The threshold tolerance multiplied by the absolute maximum of each reconstruction was used to determine if a coarse voxel was declared a reconstructed conductor or insulator. Both the Tikhonov factor and threshold tolerance were heuristically determined.

The metrics used to evaluate the reconstructions were (1) the center of mass of the reconstructed conductivities exceeding a specified tolerance, and (2) the mean position error of the connected conductive or insulative regions. In the second metric, the position error was averaged over the position error of each reconstructed conductive or insulative region by calculating the minimum distance to the true position of the metal inclusions or plastic bead, respectively.

3. Results

This section presents the results for (1) the single-inclusion simulation experiment, (2) the sensitivity and measurement analysis of the TRUS and BP electrode measurements, and (3) the three saline tank experiments.

3.1. Single-inclusion simulation TREIT experiment (TRUS electrodes only)

The first experiment involved only the TRUS electrodes and simulated imaging of a metal inclusion that was positioned at varied distances and angles from the probe face (figure 3(A)). These simulations revealed that the maximum accurate distance that a single metal inclusion could be recovered, defined as a mean position error of less than 2 mm, is 12–13 mm away from the probe face (figure 3(B)) with no added noise. Given that the rectal wall is approximately 5 mm thick and that a prostate may be 50 mm in maximum dimension, this experiment implies that TREIT only data may be insufficient to image the whole prostate.

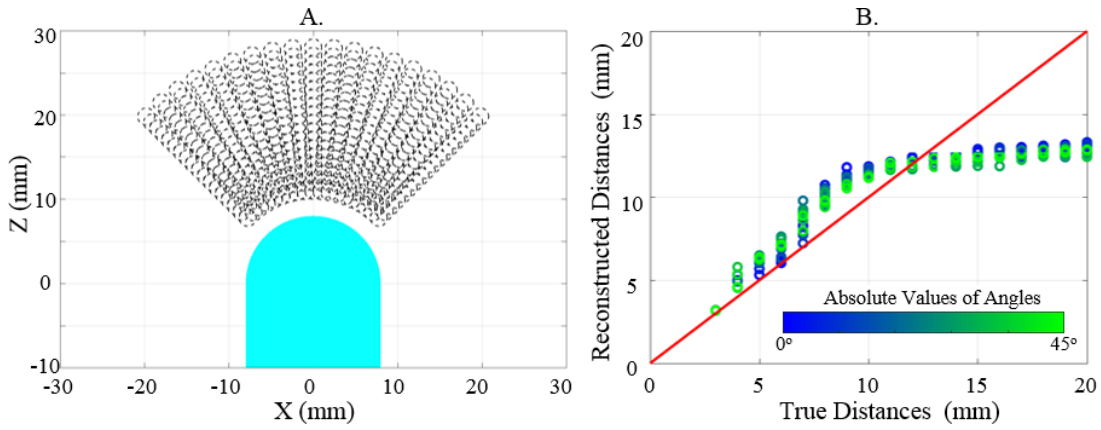

Figure 3. (A) Location of the true simulated inclusions, and (B) a plot comparing the reconstructed and true inclusion distances. This simulated experiment revealed a 12–13 mm maximum depth sensitivity without noise.

3.2. Sensitivity and measurement analysis

3.2.1. Region of sensitivity

Ideally, TREIT will have sufficient sensitivity within all regions encompassing the prostate, which we model as a 50 cm^3 sphere for this analysis. The larger side-fired TREIT probe has significantly more sensitivity than the end-fired geometry (12.6% versus 0.6%, respectively; compare figures 4(A) and (C)). Incorporating BP patterns significantly increases the volume of sensitivity; the side-fired probe increases to 94.6% (compared to 12.6%) and the end-fired probe increases to 7.2% and 1.8% (compared to 0.6%) assuming either two TRUS and two BP electrode patterns or BP-only patterns, respectively. This analysis reveals how much more challenging the EIT problem is for the end-fired geometry as compared to the side-fired probe and that the two TRUS and two BP patterns provide significantly more sensitivity than the TRUS-only or BP-only patterns of the end-fired geometry. Overall, this suggests that data fusion using impedances recorded from multiple BP locations is needed to have sufficient sensitivity throughout the entire prostate. Although the three tank experiments were not explicitly designed to reconstruct over an entire prostate, these experiments provide examples for visualizing the effective region of sensitivity available through fusion of all measurements into a single Jacobian (figures 4(F)–(H)). The overall percent coverage of a nominal 50 cm^3 prostate from these three experiments (table 3) is 33.2%, 55.4%, and 91.4% for the rotation, one Z-plane, and four Z-plane experiments, respectively. Thus we see that with multiple (x, y, z)-translations of the BP one can nearly cover the entire prostate, achieving a similar coverage to the side-fired TRUS probe with BP electrodes at a single position (91.4% compared to 94.6%).

3.2.2. Imaging the entire prostate using 12-core biopsy data

A 3.6 cm^3 spherical region of sensitivity exists about each measurement site (e.g. figure 4(D)). Fusion of EIT measurements from standard 12-core BP sites resulted in 45.0% coverage of the prostate. Two optimal depths assuming standard trajectories from a 12-core biopsy resulted in 76.1% coverage of the prostate. Two optimal depths and optimal trajectories that were within 5 and 10 degrees from a standard 12-core biopsy resulted in 88.0% and 94.1% coverage of the prostate, respectively.

3.2.3. Number of independent measurements

Based on Picard's condition (figure 5(A)) and the four z-plane experimental data, the average number of effective singular values over the 60 data frames was roughly seven and four for all two TRUS & two BP patterns (3672) and for only those patterns actually used (19), respectively (figure 5(B)); this finding was similar for all reconstruction ROIs and pixel sizes considered. The primary reason there are so few independent measurements per data frame is that the ROI is centered on the average inclusion position, which is outside the region of sensitivity near to the face of the end-fired TRUS probe. This analysis illustrates another way in which the small size of the end-fired TRUS probe and its corresponding small region of sensitivity contribute to the challenging nature of the problem. Furthermore, despite using only 19 measurements at each probed location for reconstruction, this analysis shows that this represents a reduction of only three effective independent measurements per data frame as compared to the maximum possible when using all two TRUS and two BP patterns. This suggests that even though the number of patterns remaining after noise filtering is small for the three experiments (64, 107, and 19; table 2, column 2), these patterns are likely sufficient for estimating the conductivity in the ROIs.

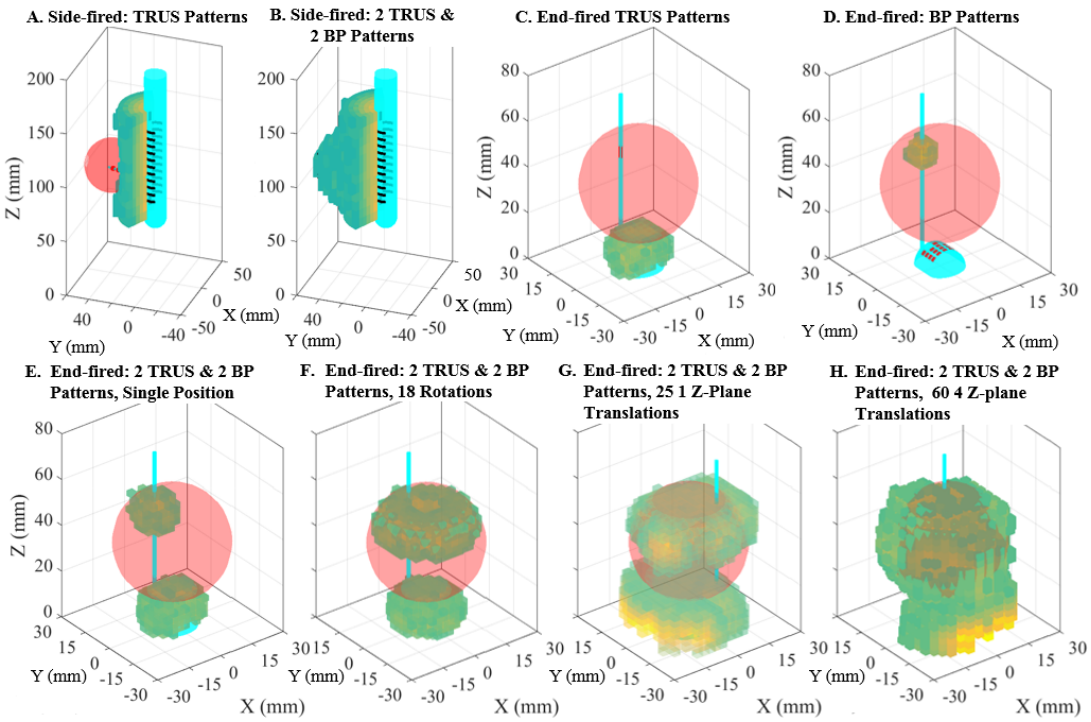

Figure 4. Illustration of the regions of sensitivity for the previously studied side-fired TRUS probe assuming (A) TRUS-only patterns and (B) two TRUS and two BP patterns, and the end-fired probe assuming (C) TRUS patterns only, (D) BP patterns only, (E) patterns with two TRUS and two BP patterns, and overall sensitivity from fusing two TRUS and two BP patterns corresponding to the (F) rotation, (G) one *Z*-plane, and (H) four *Z*-plane experiments.

Table 3. Volume of sensitivity regions and percent volume assuming a 50 cm^3 prostate.

Probe	Measurements	Volume near TRUS (cm^3)	Volume near BP (cm^3)	Total volume (cm^3)	Total percent volume (%)
Side-fired	TRUS patterns	6.3	NA	6.3	12.6
Side-fired	2 TRUS/2 BP	47.3	NA	47.3	94.6
End-fired	TRUS patterns	0.3	0.0	0.3	0.6
End-fired	BP patterns	0.0	0.9	0.9	1.8
End-fired	2 TRUS/2 BP	0.6	3.0	3.6	7.2
End-fired	1 TRUS/3 BP	0.0	1.5	1.5	3.0
End-fired	3 TRUS/1 BP	0.4	0.0	0.4	0.8
End-fired	2 TRUS/2 BP fused: rotation exp.	0.7	15.9	16.6	33.2
End-fired	2 TRUS/2 BP fused: 1 *Z*-plane exp.	3.0	24.7	27.7	55.4
End-fired	2 TRUS/2 BP fused: 4 *Z*-plane exp.	NA	45.7	45.7	91.4

3.3. Saline tank experiments

The average position error for the rotations in a single *z*-plane with 2 metal inclusions (figure 6), *x*/*y*-translations in a single *z*-plane with 2 metal inclusions (figure 7(A)), and *x*/*y*-translations in four *z*-planes with 2 metal and 1 plastic inclusions (figure 7(B)) are shown as a function of the ROI radius for the four resolutions considered. The best reconstructions in terms of average position error are listed in table 4 and shown in figure 9 in three views for each of the three experiments. Figure 9 also shows the positions of the BP electrode measurements (black dots), reconstructed conductors (yellow blocks) and insulators (blue blocks), true conductors (red spheres) and insulators (pink spheres), and ROIs (green cylinders).

For the rotation experiment, the two inclusions can only be resolved when the reconstruction ROI radius ranges from 5.2 to 6.4 mm. For larger ROI radii, the two inclusions merge into a single, centrally located elevated region of conductivity. Based on the sensitivity study in section 3.2, this could be due to the small sensitivity in the center of the ROI (i.e. the central portion of the annular sensitivity volume of figure 4(F)).

In addition to reconstructing images with impedance data collected from all BP locations in the translation experiments, we also (figures 9(B) and (C)) reconstructed images using subsets of data recorded when the BP was positioned within a limited radius; this enabled us to evaluate how the position of the BP influences the accuracy of the reconstructed inclusions (multiple curves in figures 7(A) and (B)). Figure 8 illustrates the number of BP

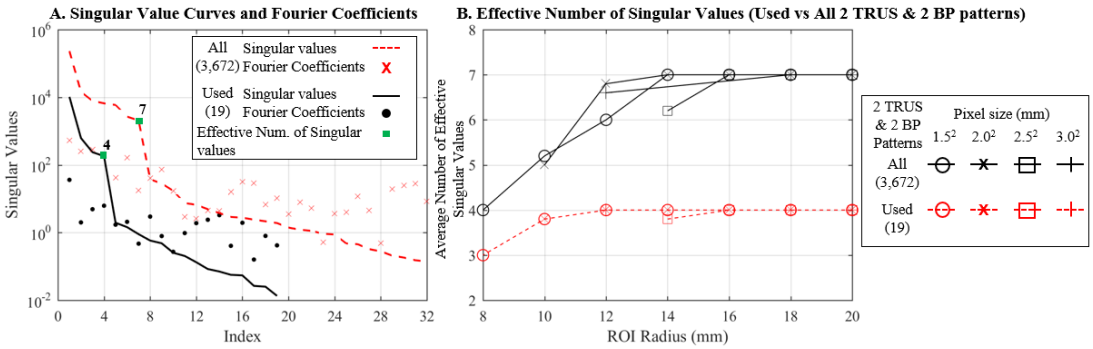

Figure 5. (A) Two examples of using Picard's condition to determine the number of effective singular values (i.e. there are four and seven singular values above the noise level of the Fourier coefficients), and (B) the average number of effective singular values for the used and all two TRUS and two BP patterns across all the pixel sizes and ROIs considered. (A) Only shows the first 32 singular values of the 3672 singular values assuming all two TRUS & two BP patterns, because all pertinent information for Picard's condition analysis is contained in this zoomed-in window.

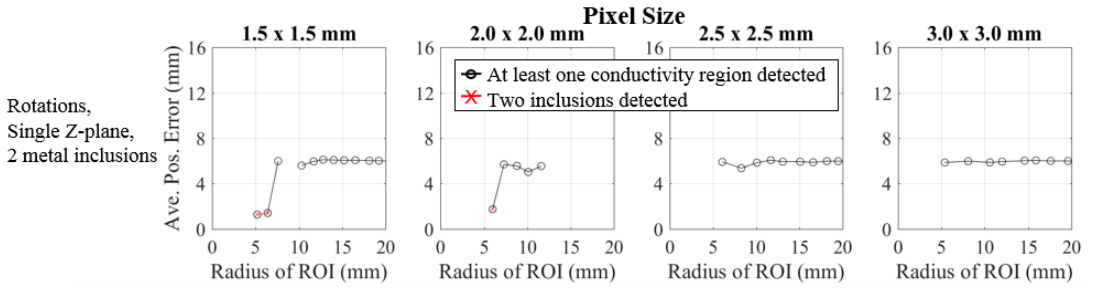

Figure 6. Average position error for the measured rotation experiment with two metal inclusions. The four plots show results for coarse voxels with size 1.5 × 1.5 mm to 3.0 × 3.0 mm in 0.5 mm steps.

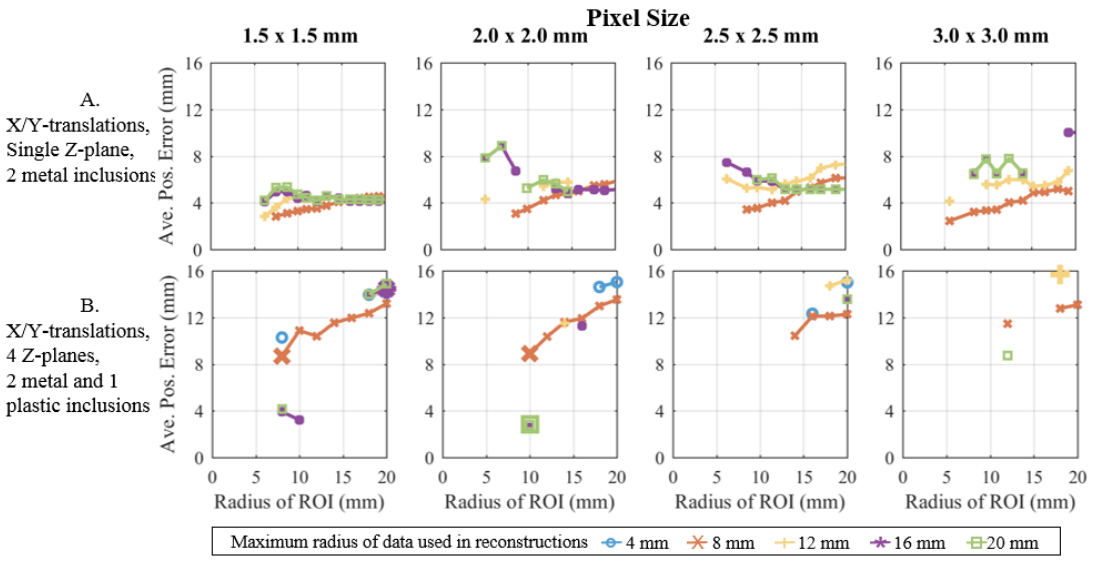

Figure 7. Average position error for the saline tank experiments assuming (A). 1 *z*-plane, *x*/*y*-translations with two planar, metal inclusions, and (B) four *z*-plane, *x*/*y*-translations with two metal and one plastic inclusions. The columns show results for coarse voxels with size 1.5 × 1.5 mm to 3.0 × 3.0 mm in 0.5 mm steps. Each curve corresponds to reconstructions that used EIT data in which BPs (*x*/*y*) radial position was less than a specified maximum tolerance (defined in legend). Results are only shown in (A) if two conductors were detected, and in (B) if at least one insulator and one conductor were detected. Further, in (B) markers are enlarged if the correct number of targets were found (two conductors and one insulator).

probe locations that are within selected maximum radii. The single *z*-plane *x*/*y*-translation experiment showed the best robustness to varying ROI radii and voxel size; all parameter settings yielded similar average position errors. However, similar to the rotation experiments, the position errors were slightly better both qualitatively and quantitatively when the ROI extended just beyond the inclusions.

Table 4. Best quantitative results.

Experiment	Voxel size (mm)	Max. radius of data	ROI radius (mm)	Ave. pos. error (mm)
Rotations	1.5 × 1.5	11 mm (fixed)	5.2	1.27
1 *Z*-plane, *x*/*y*-translations	3.0 × 3.0	8 mm	5.6	2.49
4 *Z*-planes, *x*/*y*-translations	2.0 × 2.0	16 mm	10	2.56

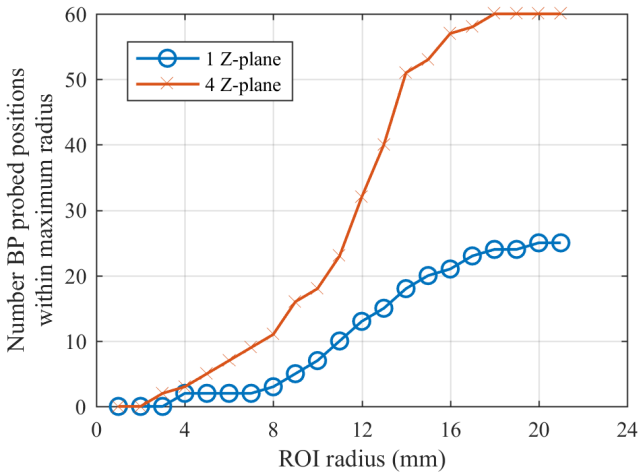

Figure 8. Number of data points within the ROI of each given radius. These curves illustrate how many frames of data were used in figures 7(A) and (B).

The four *z*-plane, *x*/*y*-translation experiment was similar to the rotation experiment in that there was a small ROI radius range (8–10 mm) that resulted in small average position errors. The metal inclusions were positioned at 7.3 and 6.6 mm and the plastic inclusion at 9.6 mm from the center of the imaging domain. In all three experiments it appears that an ROI radius extending to just beyond the inclusions produces the best results.

4. Discussion

Fusing data recorded from TRUS- and BP-based electrodes positioned at multiple sites within a domain (i.e. fd-TREIT + BP) provides enhanced EIT sensitivity as compared to TRUS-based imaging alone and aligns with the routine clinical scenario of sampling multiple cores during end-fired TRUS-guided prostate biopsy procedures. Sensitivity analysis revealed that 76.1% or 94.1% of a nominal 50 cm^3 prostate could be covered with fd-TREIT + BP using data recorded during a routine or custom 12-core biopsy, respectively. Given that the typical human prostate ranges from 15 to 30 cm^3 (Walsh 2007), this fused-data EIT approach has the potential to image nearly the full prostatic volume even in cases in which the prostate is larger in size (e.g. >50 cm^3) due to benign prostatic hyperplasia or adenocarcinoma (Uzzo *et al* 1995). Two significant steps that are being pursued in current research are (1) how to design the approach to be more robust to parameter selection (i.e. ROI and voxel size), and (2) how to image the entire prostate or an ROI within the prostate (e.g. through the use of a BP with additional electrodes along its length). We note that during the TRUS-guided biopsy procedure images such as figures 4(F) and (G) could be constructed in real time to help guide probing locations and ensure full- or nearly full coverage of the prostate.

A significant limitation of this approach is that the accuracy of the reconstruction is largely dependent on the ROI over which electrical properties are estimated. The results presented here suggest that the reconstruction ROI should encompass a volume that extends to just beyond the inclusions; however, the inclusion, or tumor, location will not typically be known in the clinical setting. One approach to improve the current method is to employ a sensitivity-based coarse mesh similar to those developed in a 2D closed domain EIT scenario (Saulnier *et al* 2001) and in open-domain applications (Loke 2013, Murphy *et al* 2016). In some clinical cases (e.g. MR-TRUS fusion), the tumor location may be known *a priori* (Siddiqui *et al* 2015); in these situations, the TREIT ROI could be specified based on the tumor locations identified in MR images registered to the ultrasound image space. Additionally, incorporating the prostate boundary and/or tumor locations/boundary using hard prior (Syed *et al* 2012) or soft-prior (Murphy *et al* 2017c) techniques may further improve the robustness of the method.

A second limitation of the study was that the number of BP locations sampled was larger than typically collected during a 12-core biopsy, i.e. 18, 25, and 60 for rotation, one *z*-plane, and four *z*-plane, respectively. While the 60 measurements far exceed the standard 12-core limit, if multiple samples are recorded as the biopsy needle

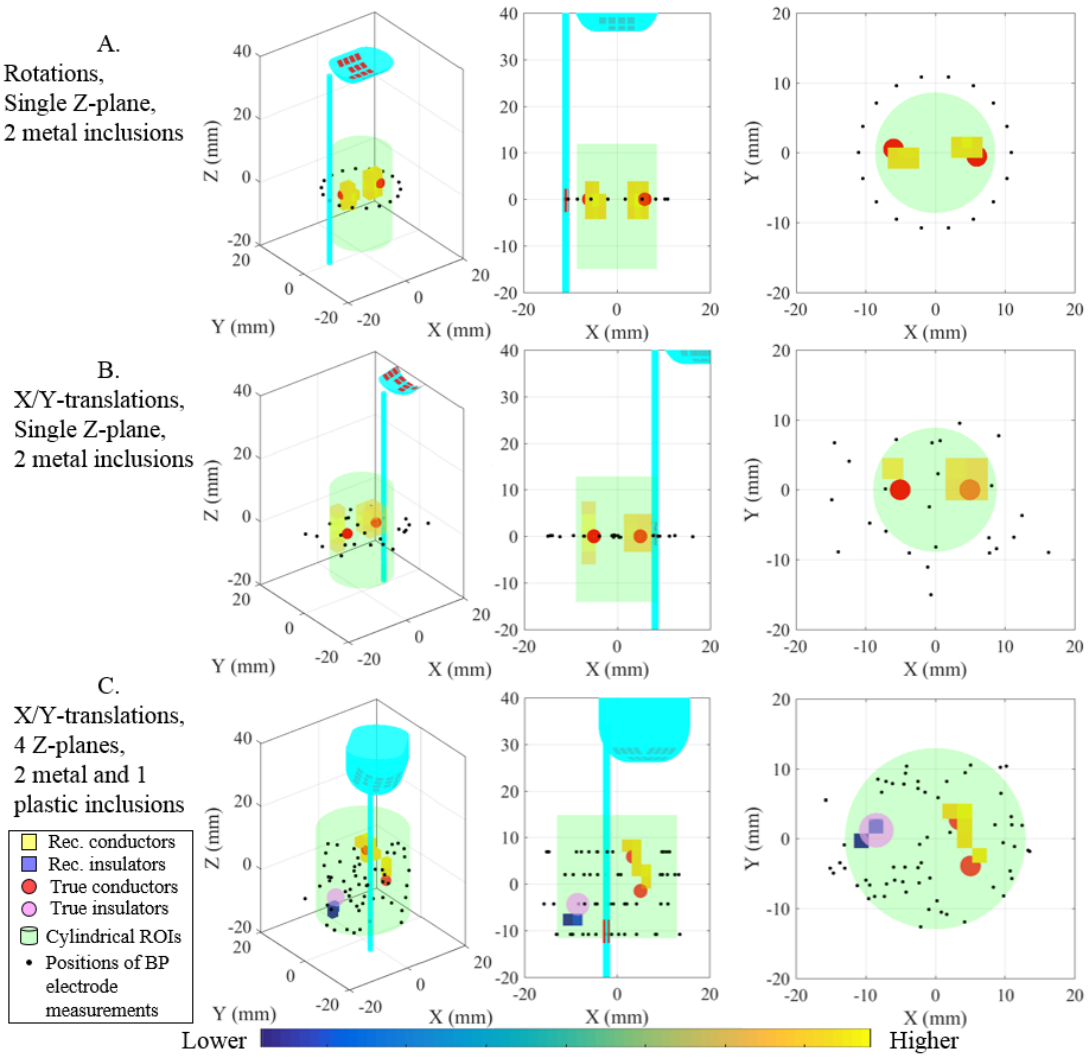

Figure 9. Three views of reconstructions that yielded minimum average position errors in the three saline tank experiments: (A) rotations in a single *z*-plane with two metal inclusions, (B) *x*/*y*-translations in a single *z*-plane with two planar, metal inclusions, and (C) *x*/*y*-translations in four *z*-planes with two metal and one plastic inclusions.

is advanced, or if additional electrodes are embedded along the shaft of the biopsy needle, multiple *z*-plane data can be recorded from a single biopsy location. For example, if four *z*-planes are sampled as the biopsy needle is inserted, only 15 cores would need to be extracted to sample at 60 total locations. We are currently exploring the potential of recording at multiple depths during a single core extraction and of embedding additional electrodes along the length of the biopsy needle.

We have demonstrated that we can accurately track our imaging system, record impedances from multiple locations, and fuse all data together to reconstruct a single estimate of the 3D conductivity distribution within a ROI. All experiments were conducted in a homogenous saline bath with high-contrast inclusions. A logical next step would be to image gelatin phantoms and *ex vivo* prostates in order to explore the efficacy of this technology in a more clinically relevant scenario.

5. Conclusions

Simulations and sensitivity studies reveal that (1) TREIT measurements recorded from an end-fired probe are not sufficiently sensitive to image the whole prostate and that (2) the combination of TREIT + BP measurements recorded from multiple location can essentially cover an entire nominal 50 cm^3 prostate. Three measured tank experiments of the fd-TREIT + BP approach successfully and accurately recovered the positions of two to three metal or plastic inclusions. The measured tank experiments represent important steps in the development of an EIT reconstruction algorithm that can combine impedance data recorded from multiple locations and from multiple probes. Importantly, the current method has the potential to image a majority of a prostate (76.1%) during a routine TRUS-guided 12-core biopsy procedure. Ongoing prostate phantom work is aiming to further refine the approach for an *ex vivo* imaging study.

Acknowledgments

This work was supported in part by the Department of Defense Congressionally Directed Medical Research Program under Grant W81XWH-15-1-0102.

ORCID iDs

Ethan K Murphy https://orcid.org/0000-0002-4635-3384

References

Baumann M, Mozer P, Daanen V and Troccaz J 2012 Prostate biopsy tracking with deformation estimation *Med. Image Anal.* **16** 562–76

Borsic A, Halter R, Wan Y, Hartov A and Paulsen K D 2010 Electrical impedance tomography reconstruction for three-dimensional imaging of the prostate *Physiol. Meas.* **31** S1–16

Ching C B, Moussa A S, Li J, Lane B R, Zippe C and Jones J S 2009 Does transrectal ultrasound probe configuration really matter? end fire versus side fire probe prostate cancer detection rates *J. Urol.* **181** 2077–83

Everitt A, Manwaring P and Halter R J 2018 A real-time 4-bit imaging electrical impedance sensing biopsy needle for prostate cancer detection *Proc. SPIE* **10578** 1–10

Geselowitz D B 1971 An application of electrocardiographic lead theory to impedance plethysmography *IEEE Trans. Biomed. Eng.* **18** 38–41

Geuzaine C and Remacle J F 2009 Gmsh: a 3D finite element mesh generator with built-in pre- and post-processing facilities *Int. J. Numer. Methods Eng.* **79** 1309–31

Halter R J, Hartov A, Heaney J A, Paulsen K D and Schned A R 2007 Electrical impedance spectroscopy of the human prostate *IEEE Trans. Biomed. Eng.* **54** 1321–7

Hansen P C 1998 *Rank-Deficient and Discrete Ill-Posed Problems* (Philadelphia, PA: Society for Industrial and Applied Mathematics) (http://epubs.siam.org/doi/book/10.1137/1.9780898719697).

Harnden P, Naylor B, Shelley M D, Clements H, Coles B and Mason M D 2008 The clinical management of patients with a small volume of prostatic cancer on biopsy: What are the risks of progression? a systematic review and meta-analysis *Cancer* **112** 971–81

Harvey C J, Pilcher J, Richenberg J, Patel U and Frauscher F 2012 Applications of transrectal ultrasound in prostate cancer *Br. J. Radiol.* **85** S3–17

Khan S, Manwaring P, Borsic A and Halter R 2015 FPGA-based voltage and current dual drive system for high frame rate electrical impedance tomography *IEEE Trans. Med. Imaging* **34** 888–901

Lee B R, Roberts W W, Smith D G, Ko H W, Epstein J I, Lecksell K and Partin A W 1999 Bioimpedance: Novel use of a minimally invasive technique for cancer localization in the intact prostate *Prostate* **39** 213–8

Loke M H 2013 Tutorial: 2D and 3D electrical imaging surveys *Geotomo Software Malaysia Technical Report* 127 (http://seisweb.oma.be/bibadmin/uploads/pdf/COURSENOTES.pdf)

Murphy E K, Mahara A and Halter R J 2017a Absolute reconstructions using rotational electrical impedance tomography for breast cancer imaging *IEEE Trans. Med. Imaging* **36** 892–903

Murphy E K, Mahara A, Khan S, Hyams E S, Schned A R, Pettus J and Halter R J 2017b Comparative study of separation between *ex vivo* prostatic malignant and benign tissue using electrical impedance spectroscopy and electrical impedance tomography *Physiol. Meas.* **38** 1242–61

Murphy E, Mahara A and Halter R 2016 A novel regularization technique for microendoscopic electrical impedance tomography *IEEE Trans. Med. Imaging* **35** 1593–603

Murphy E K, Mahara A, Wu X and Halter R J 2017c Phantom experiments using soft-prior regularization EIT for breast cancer imaging *Physiol. Meas.* **38** 1262–77

Numao N, Kawakami S, Yonese J, Koga F, Saito K, Fujii Y, Ishikawa Y, Fukui I and Kihara K 2008 Three-dimensional 26-core biopsy-based patient selection criteria for nerve-sparing radical prostatectomy *Int. J. Urol.* **15** 1061–6

Salomon G *et al* 2009 The feasibility of prostate cancer detection by triple spectroscopy *Eur. Urol.* **55** 376–84

Saulnier G J, Blue R S, Newell J C, Isaacson D and Edic P M 2001 Electrical impedance tomography *IEEE Signal Process. Mag.* **18** 31–43

Shariat S F and Roehrborn C G 2008 Using biopsy to detect prostate cancer *Rev. Urol.* **10** 262–80 (PMID:19145270)

Siddiqui M M *et al* 2015 Comparison of MR/ultrasound fusion-guided biopsy with ultrasound-guided biopsy for the diagnosis of prostate cancer *JAMA* **313** 390–7

Siegel R L, Miller K D and Jemal A 2016 Cancer statistics *CA Cancer J. Clin.* **66** 7–30

Somersalo E, Cheney M and Isaacson D 1992 Existence and uniqueness for electrode models for electric current computed tomography *SIAM J. Appl. Math.* **52** 1023–40

Soni N K, Dehghani H, Hartov A and Paulsen K D 2003 A novel data calibration scheme for electrical impedance tomography *Physiol. Meas.* **24** 421–35

Syed H, Borsic A, Hartov A and Halter R J 2012 Anatomically accurate hard priors for transrectal electrical impedance tomography (TREIT) of the prostate *Physiol. Meas.* **33** 719–38

Uzzo R G, Wei J T, Waldbaum R S, Perlmutter A P, Byrne J C and Vaughan D 1995 The influence of prostate size on cancer detection *Urology* **46** 831–6

Walsh P 2007 *Campbell's Urology* (Philadelphia, PA: Saunders)

Wan Y, Borsic A, Hartov A and Halter R 2012 Incorporating a biopsy needle as an electrode in transrectal electrical impedance imaging *Proc. Annual Int. Conf. IEEE Engineering in Medicine and Biology Society EMBS* pp 6220–3

Wan Y, Halter R, Borsic A, Manwaring P, Hartov A and Paulsen K 2010 Sensitivity study of an ultrasound coupled transrectal electrical impedance tomography system for prostate imaging *Physiol. Meas.* **31** S17–29

IOP Publishing Physiol. Meas. 40 (2019) 034005 (11pp) https://doi.org/10.1088/1361-6579/ab0c3c

Physiological Measurement

IPEM Institute of Physics and Engineering in Medicine

CrossMark

RECEIVED
29 November 2018

REVISED
26 February 2019

ACCEPTED FOR PUBLICATION
4 March 2019

PUBLISHED
29 March 2019

PAPER

Current-conveyor-based wide-band current driver for electrical impedance tomography

A J Rao, E K Murphy, M Shahghasemi and K M Odame

Thayer School of Engineering, Dartmouth College, Hanover, NH, United States of America

E-mail: arun.j.rao.th@dartmouth.edu

Keywords: bio-impedance, integrated current driver, current conveyor, wide-band, electrical impedance tomography

Abstract

Objective: In this paper a wide-band integrated current driver for electrical impedance tomography (EIT) is presented. The application is primarily for prostate and breast cancer detection which require the tissue to be interrogated at frequencies up to 10 MHz while achieving low harmonic distortion and high accuracy. *Approach*: The current driver is based on current conveyor architecture and can deliver 1.2 mA of peak to peak ac current between frequencies of 100 Hz–10 MHz. It is fabricated in CMOS 0.18 μm technology with a power supply of 3.3 V, and occupies a core area of 0.26 mm^2. *Main results*: The measured harmonic distortion for a peak current of 1.2 mA is $<$0.1% for frequencies less than 100 kHz, and increases to 0.68% at 10 MHz. The measured output impedance of the current driver is 101 kΩ at 1 MHz and 19.5 kΩ at 10 MHz. *Significance*: The circuit is suitable for high frequency active electrode applications.

1. Introduction

Bio-impedance varies widely between cancerous and benign tissues and exhibits frequency-dependent characteristics which have been used for differentiating various kinds of cancer (Saulnier *et al* 2001). Electrical impedance tomography (EIT) is an imaging modality that incorporates the bio-impedances of various parts of the measured tissue to provide a spatial mapping of the organ being probed. By injecting a sinusoidal current into the tissue at the source electrode and measuring the voltages induced at the remaining electrodes, impedance of tissue is obtained, as shown in figure 1. One of the key advantages of an EIT system is its relatively smaller size and inexpensive cost compared to other imaging techniques such as magnetic resonance imaging (MRI) or computerized tomography (CT). Importantly, EIT is also non-ionizing.

A major challenge of EIT is that it requires an accurate, high-output impedance current driver to deliver a pure sinusoidal signal to the tissue being interrogated. The EIT current driver has traditionally been implemented as a Howland current source with discrete components (Tucker *et al* 2013). This implementation unfortunately introduces a significant amount of parasitic capacitance, which limits the bandwidth of the EIT system. To achieve higher frequencies of operation, the current driver must be implemented in an integrated circuit (IC), as part of an active electrode system, whereby the electronics are physically close to the electrodes and parasitic capacitance is minimized. Several promising IC current drivers have recently been proposed (Yan *et al* 2011, Constantinou *et al* 2014, 2015, Hong *et al* 2015, Kim *et al* 2017, Wu *et al* 2018). Unfortunately, none of the solutions reported in the literature have measured operation beyond the 1 MHz range, where electrical impedance interrogation of intracellular physiology could provide increased contrast between benign and cancerous tissue (Jossinet 1998, Halter *et al* 2008). Also, none of the previous implementations are designed to drive a DC blocking capacitor, which is necessary for patient safety in EIT measurements (Lionheart *et al* 2001, McEwan *et al* 2007).

In this paper, a wide-band, current-conveyor-based, integrated CMOS current driver is introduced. Compensation for high-speed operation at the transconductance stage is achieved using the indirect compensation technique (Saxena 2007) which enables operation up to 10 MHz. Also, current-mode circuits (Wilson 1990) at the output stage further aid in the wide-band operation of the designed current driver. Finally, a DC servo-loop circuit at the output branch maintains reliable operation of the current driver in the presence of a DC blocking capacitor at the current injection electrode.

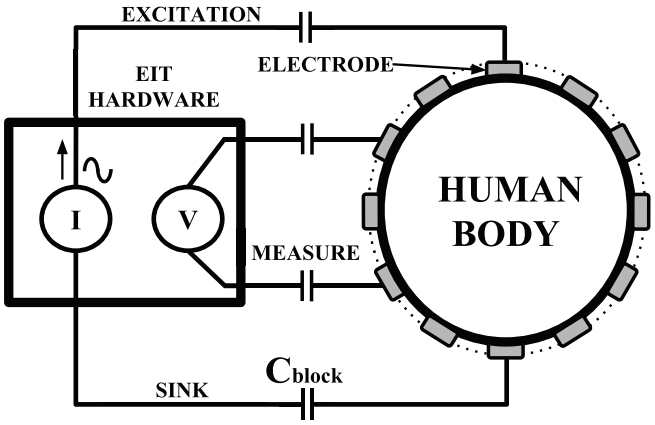

Figure 1. Block diagram of a typical EIT system. AC current excitation is performed using a pair of electrodes and the voltages induced on the remaining electrodes are measured.

2. Overview

Our proposed current driver for this design is based on the CCII current conveyor (Sedra and Smith 1970) shown in figure 2. The input to the current driver is the voltage, V_Y. This is buffered to V_X, which generates a current $I_X = \frac{V_X}{R_X}$ through the load resistor R_X. The current I_X is mirrored to the output of the current-controlled current source, and $I_Z = I_X$ flows through a DC-blocking capacitor, C_{block}, to an electrode and into the tissue. Our current driver architecture (figure 3) is based on the work presented in Jivet and Dragoi (2008). We modified the original architecture to make it suitable for high frequency EIT applications. In particular, we designed the two-stage operational amplifier (op-amp) of figure 3 with indirect compensation around a class AB control circuit, to enable current interrogation frequencies up to 10 MHz. Also, we implemented a DC-biasing servo loop at the output of the current driver; this ensures proper operation of the current driver in the presence of a 1 μF DC-blocking capacitor that is necessary for patient safety.

3. Circuit design and analysis

Details of the circuit implementation are presented in this section.

3.1. V-I conversion

Figure 4 shows the circuit diagram of the two-stage op-amp with indirect compensation technique used for the voltage to current conversion in the current driver. A RHP pole zero appears in the transfer function of a conventional two-stage op-amp compensated using a compensation capacitor C_c. This problem has been well-studied (Baker 2010) and various compensation techniques exist to cancel the RHP zero or move it into the LHP to improve stability. However, the nulling resistor technique for compensation is process dependent and the use of a transistor in triode region of operation can cause issues with large signal behavior (Baker 2010). Also, the value of compensation capacitor selected limits the speed of the circuit when high frequency of operation is desired.

In the indirect compensation technique, the compensation capacitor is not directly connected to the op-amp output. Instead, pole-splitting is achieved indirectly using a common gate transistor, M_{cg}, feeding the current from the output back to the first stage. Input transistors M_2, M_3, with current mirror loads M_4, M_5 and cascoded tail transistors M_0, M_1 form the input stage of the two stage op-amp. The gain of the input stage is given by $A_{v1} = g_{m2}(r_{o3}||r_{o5})$, where $g_{m2} = g_{m3} = G_{M1}$ are the transconductances of the input differential pair and r_{o3}, r_{o5} are the output impedances of transistors M_3, M_5 respectively. The branch comprising of transistors M_6, M_8, M_9, and M_{cg} form the indirect compensation branch in the circuit along with the compensation capacitor C_c. The gate of the common gate transistor M_{cg} is tied to the common mode voltage of the circuit. The currents in the input differential pair transistors and the indirect feedback branch are kept equal to achieve $G_{m1} = g_{m,cg}$. The output branch which provides the second stage gain is provided by transistors M_{10} and M_{13} which is the current source load. The gain is given by, $A_{v2} = g_{m10}(r_{o10}||r_{o13})$, where g_{m10} is the transconductance of transistor M_{10} and r_{o10}, r_{o13} are the output impedances of transistors M_{10}, M_{13} respectively. The bias voltages v_{cn1} and v_{cn2} are provided using a wide swing cascode current mirror (Carusone *et al* 2012) (not shown). Class AB output buffer stage is formed by transistors M_{11}, M_{12}, M_{14}, and M_{15}. When voltage, v_1, at the gate of transistor M_{10} increases, M_{15} turns on and M_{14} turns off, as the gates of M_{11} and M_{12} move towards GND. Similarly, M_{14} sources all the current

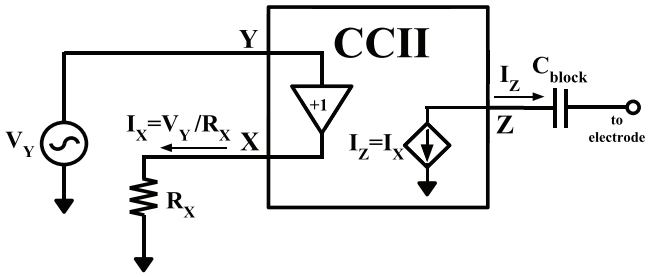

Figure 2. Block diagram of the current conveyor architecture (Sedra and Smith 1970). Current is generated at terminal X using an on-chip resistor such that $I_X = \frac{V_X}{R_X}$, and V_X follows the voltage at terminal Y. Current I_X is delivered to terminal Z with a current gain of unity.

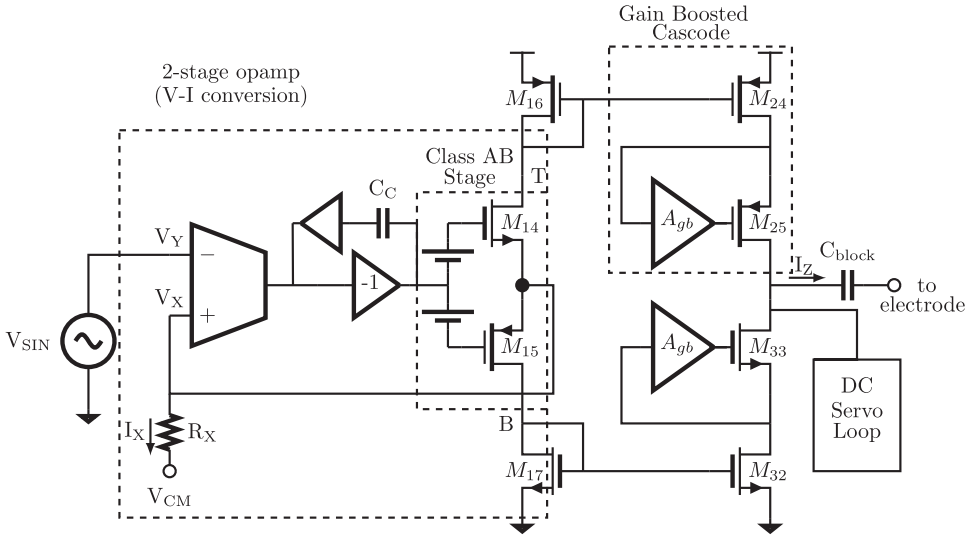

Figure 3. The architecture of the current driver. (a) The voltage to current conversion is performed using a two-stage op-amp with indirect feedback compensation. (b) Class AB output stage at the output of the op-amp is necessary for generating the sinusoidal current at terminal X using a resistor R_X. (c) Current is mirrored to the high output impedance terminal Z with a gain enhanced current mirror forming the output stage.

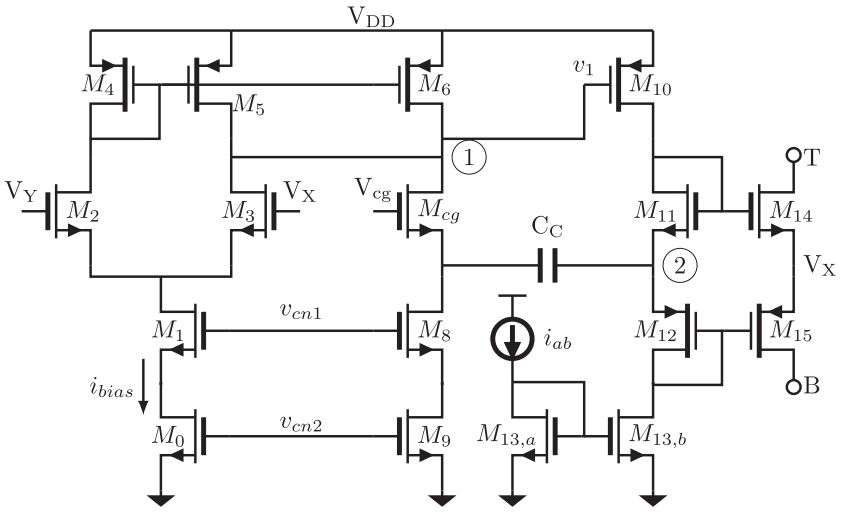

Figure 4. Two-stage op-amp with indirect compensation followed by a class AB output stage. (a) The current from the output node 2 is indirectly fed to node 1 using the common gate transistor M_{cg}. This forms the indirect feedback compensation technique. (b) Transistors $M_{11}, M_{12}, M_{14}, M_{15}$ form the class AB output stage to source and sink currents into node X. Gate voltages, v_{cn1} and v_{cn2} are set by gate biasing circuits (not shown).

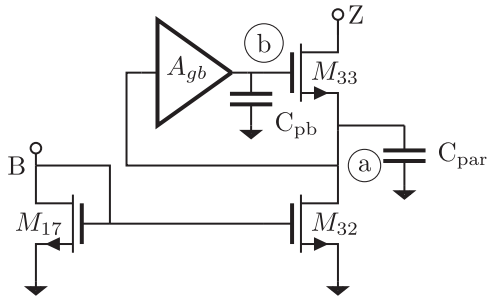

Figure 5. The gain boosted cascode structure with the amplifier A_{gb} providing an overall output impedance of $Ag_{m2}r_{o2}r_{o1}$ at node Z.

when v_1 decreases, which implies a class AB operation. The current source i_{ab} provides the necessary DC current bias for the class AB output branch.

Compared to conventional frequency compensation techniques, the indirect compensation technique uses smaller capacitors (Saxena 2007). The reduced footprint allows multiple current drivers to be integrated onto a single chip; this avoids the parasitic capacitance that would be experienced by a single, multiplexed current source (Saulnier *et al* 2001).

3.2. Gain boosted cascode output stage

The high output impedance necessary for the current driver is achieved by using the structure shown in figure 5. The gain boosting amplifier in figure 5 should have high unity gain frequency and exhibit single pole behavior to ensure stability. To achieve this we implement the amplifier as a common source amplifier with a current source load (transistors $M_{26} - M_{31}$ of figure 6). Gain boosting is similarly implemented for the PMOS half of the output branch, using transistors $M_{18} - M_{23}$. The low frequency small signal gain of the PMOS and NMOS gain boosting amplifiers is given by the following equations (Zeki and Kuntman 1997):

$$A_{gb,P} = g_{m21}(r_{o21} \| r_{o23}) \tag{1}$$

$$A_{gb,N} = g_{m29}(r_{o29} \| r_{o31}) \tag{2}$$

where g_{m21}, g_{m29} are the transconductances of transistors M_{21}, M_{29} respectively and r_{o21}, r_{o23}, r_{o29}, r_{o31} are the output impedances of transistors $M_{21}, M_{23}, M_{29}, M_{31}$ respectively. From equations (1) and (2), the overall output impedance at node Z is given as

$$Z_{out} = (g_{m25}r_{o25}r_{o24}g_{m21}(r_{o21} \| r_{o23})) \parallel (g_{m33}r_{o33}r_{o32}g_{m29}(r_{o29} \| r_{o31})) . \tag{3}$$

3.3. Output DC servo-loop

In EIT applications, a DC blocking capacitor at the output of the current driver ensures that no DC current flows into the human tissue (Lionheart *et al* 2001). This results in an equivalent structure at the output stage of the current driver as shown in figure 7. Mismatch in the DC values of i_{pmos} and i_{nmos} will cause the output node Z to rail to either V_{DD} or GND. To avoid this, and to maintain a suitable DC bias voltage at node Z, we use the servo-loop circuit shown in figure 8. Here the output branch of the current driver is shown where an operational transconductance amplifier (OTA) sets the output voltage to V_{CM}, which is typically at 1.65 V. The OTA is implemented as a current mirror OTA with input transistors sized to minimize the capacitive loading at node Z. The high output impedance of the OTA along with the capacitor C_{EXT}, external to the ASIC, forms a low-pass circuit. In the designed circuit M_{FB} is 1/30 times the width of transistor M_{32}, while the length remains the same. Its loading effect at the drain of transistor M_{32} is negligible. The designed servo-loop circuit sets the output branch at a reliable operating voltage such that the cascode transistors in the output branch have sufficient headroom for reliable operation.

4. Measured results

The current driver was fabricated in XFAB 0.18 μm XH018 CMOS process with supply voltage of 3.3 V. Design, layout and simulation was performed using Virtuoso Cadence. The resistor R_X of figure 3 was implemented as a 500 Ω resistor, integrated on the ASIC. Two additional current driver test structures were also designed and included in the chip for complete measurement. The current driver core area with test structures is approximately 0.26 mm^2 as shown in figure 9.

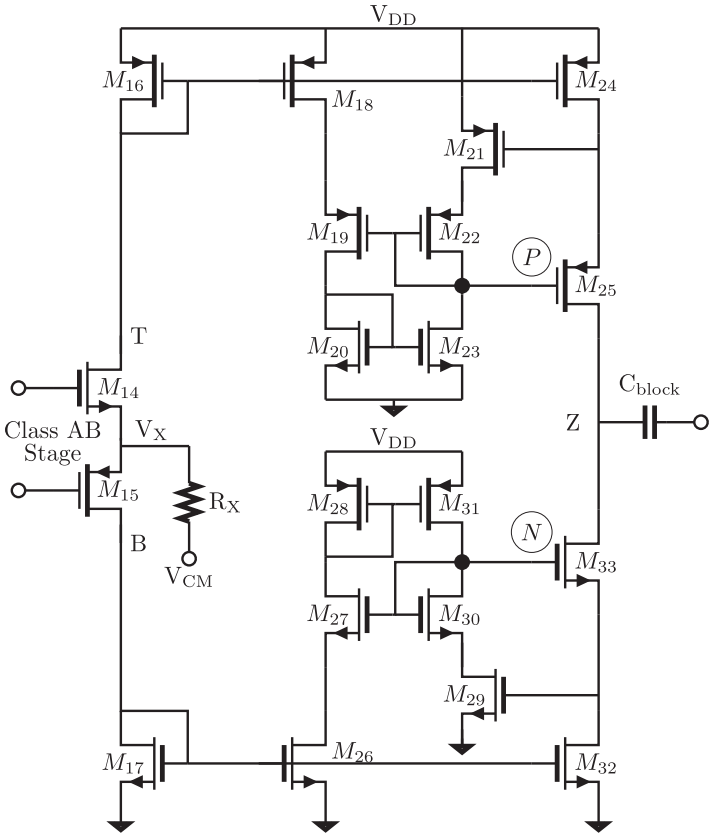

Figure 6. Mirroring of current generated at node X to output node Z using a gain boosted cascode structure. The auxiliary amplifiers for the gain boosted cascode structure have a single pole nature to enable high-frequency operation.

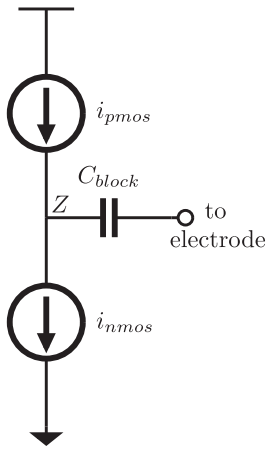

Figure 7. With a DC blocking capacitor C_{block}, the voltage at node Z can rail to either V_{DD} or GND and cause unreliable operation.

4.1. Harmonic distortion

The input signals to the current driver was generated using a Kiethley Instruments 3300 waveform generator capable of generating sinusoidal signals greater than 10 MHz with negligible distortion contributing to the measurements. A 600 mV peak to peak voltage at the input terminal Y generates the maximum current of 1.2 mA at terminal Z. The output voltage at the load was monitored using a Rigol 1104-Z oscilloscope. Figure 10 shows the measured THD values against frequencies. Current values of 1 mA, and 1.2 mA are chosen to show the performance of the current driver with a 500 Ω load. The current driver achieves a THD of less than 0.7% harmonic distortion at 10 MHz while delivering a current of 1.2 mA to the load.

4.2. Noise

A Stanford Research Systems SRS 785 spectrum analyzer was used for noise measurements of the current driver. Due to limitations of the equipment, noise was measured up to 100 kHz. Figure 11 shows a comparison of

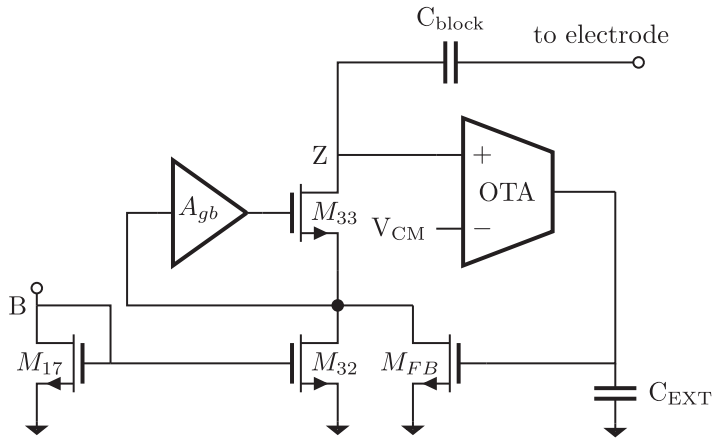

Figure 8. Structure designed to keep the current driver in the proper operating regime. The OTA at the output stage sets the output voltage to the common mode reference voltage V_{CM}, which ensures that all the transistors in the output branch of the current source structure are in saturation thus enabling reliable operation.

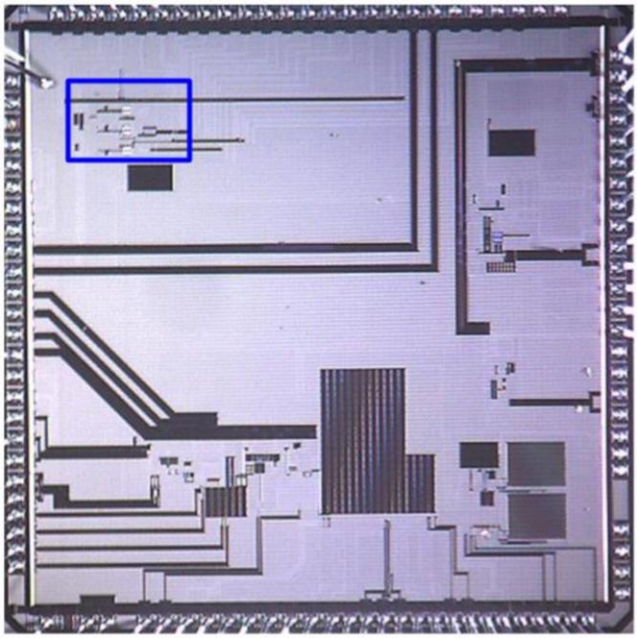

Figure 9. Chip micro photograph. The current driver with test structures are indicated by the blue rectangle.

measured noise with respect to Cadence simulations.The total integrated noise at the output was approximately 658 μV determined by simulation.

4.3. Output impedance

The measurement of the output impedance of the current driver was performed as described in Cook *et al* (1994). The test configuration uses a Linear Technology LT1806 wide bandwidth precision op-amp as a negative feedback amplifier. To obtain accurate measurements, we used calibration and feedback resistors with tolerance of 0.1%. The associated parasitics of the board were measured using a Instek 821 precision LCR meter. The measured board parasitics, along with the output pad capacitance of the chip (terminal Z), were incorporated into the calculation of the output impedance. An average of 2500 points for a single frequency point measurement was used to obtain reliable measurement data. Figure 12 shows the output impedance versus frequency for the current driver. The output impedance is 101 kΩ at 1 MHz, and 19.5 kΩ at 10 MHz.

4.4. Cole–Cole plots and accuracy

The suitability of the designed current driver for complex impedance measurements up to 10 MHz was verified with the setup shown in figure 13. An R-C circuit combination was used to model the complex tissue impedance of the breast (Halter *et al* 2008). A peak-to-peak input voltage of 500 mV was fed from the signal generator such

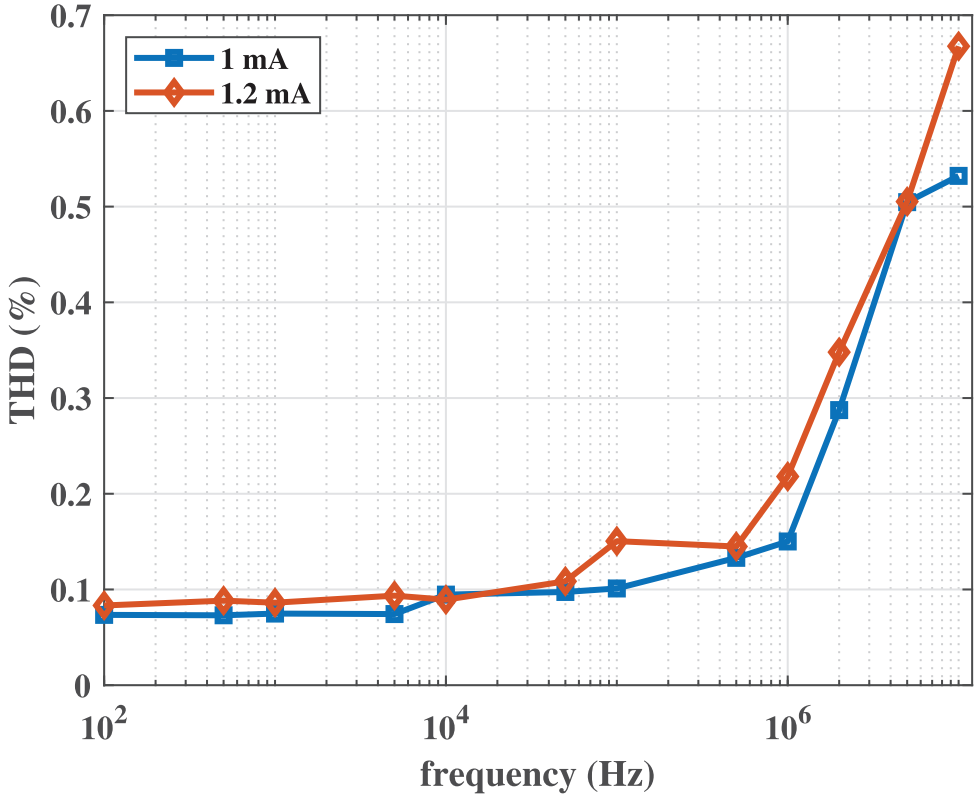

Figure 10. Measured THD versus frequency for current levels 1 mA and 1.2 mA. The worst harmonic distortion measured for the current driver is approximately 0.7%.

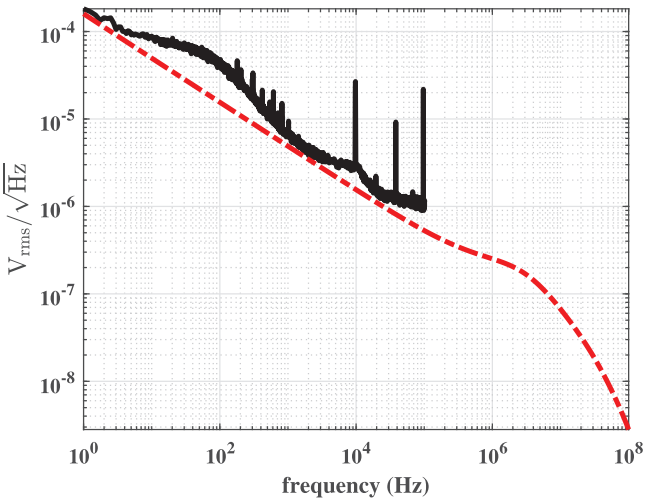

Figure 11. Plot showing the simulated (dashed curve) versus measured (solid curve) results of the noise at the output of the current driver. Higher frequency noise measurements could not be performed due to equipment limitations.

that 1 mA_{pp} of current was injected into the load. A 100 Ω sense resistor with 0.1% tolerance was included at the output to measure the accurate current from the current driver. The voltage across the sense resistor was captured by the data acquisition system. A digital matched filter in MATLAB was then used to extract the amplitude and phase of the complex load. The value of the passive components used in the setup was measured using an LCR meter and incorporated into the accuracy calculations. An average of 50 measurements was performed for each frequency point to obtain accurate results. The measured Cole–Cole plot for the complex impedance setup is shown in figure 14.

4.5. Saline tank measurements

To illustrate the functioning of the current driver in a full EIT system, saline tank experiments were performed to obtain impedance images. The architecture of the 16-electrode EIT system is shown in figure 15. An ASIC

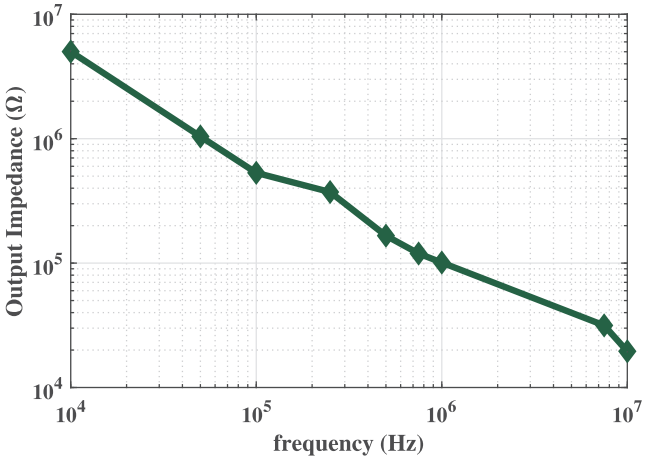

Figure 12. Output impedance versus frequency for the current driver. The measured output impedance is 101 kΩ at 1 MHz, and 19.5 kΩ at 10 MHz.

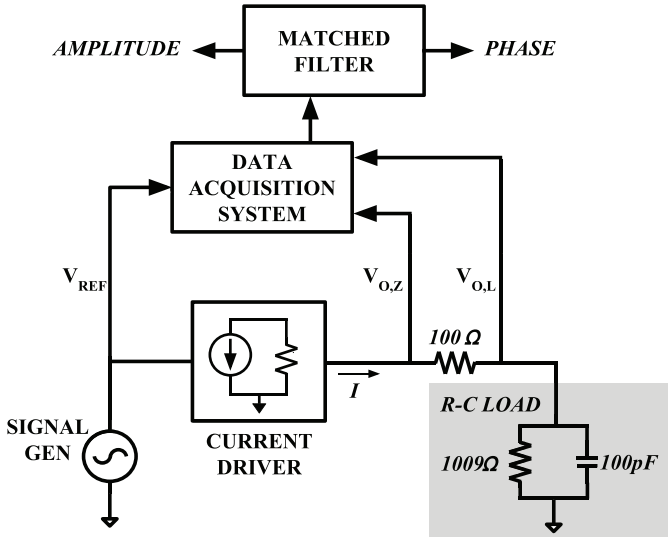

Figure 13. Setup for current driver testing. Input signal is fed by a signal generator and the voltage across the sense resistor is captured by the data acquisition system. Amplitude and phase extraction is performed in the digital domain with a matched filter.

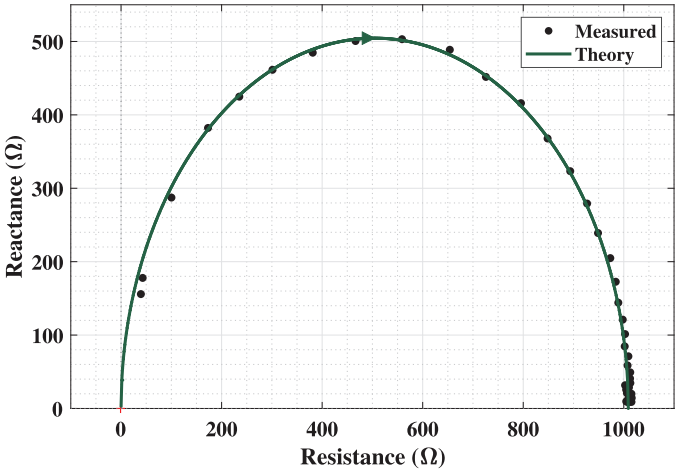

Figure 14. Cole–Cole plot for a parallel R-C load shown in figure 13 to model the complex tissue impedance.

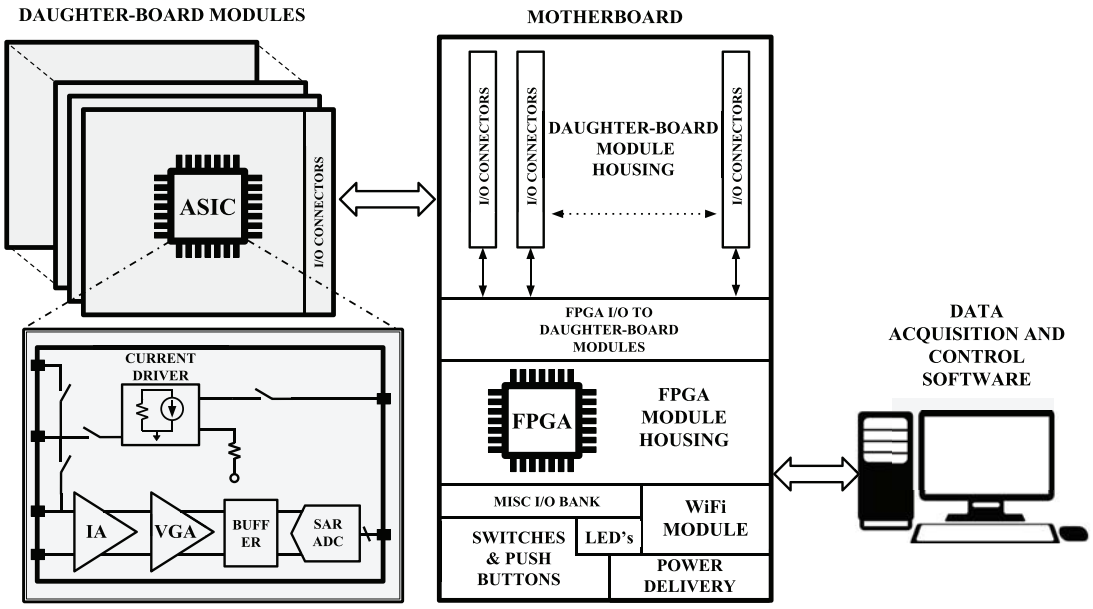

Figure 15. Architecture of the EIT system. An ASIC which includes the current driver, IA, VGA, and ADC, implements the core EIT functionality and is included on the daughter-board module with required voltage references, current biases and switch configuration IC's. The daughter-boards are mounted on the motherboard with I/O connectors. The FPGA on the motherboard is responsible for control, data acquisition, and communication. The data from the FPGA is sent to the MATLAB software on the computer to form impedance matrices and re-construct images.

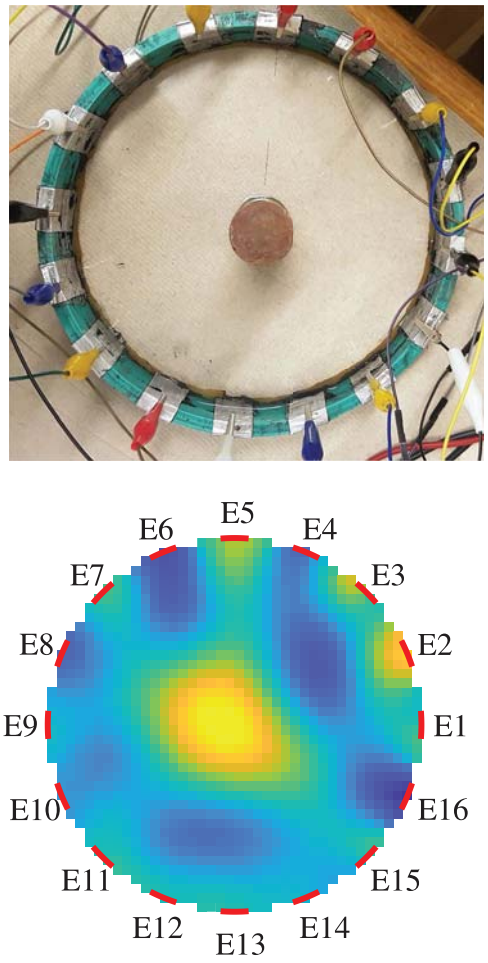

Figure 16. Saline tank setup and reconstructed image. (a) Brass rod of 1.3 cm diameter placed at the center of the saline tank with water depth of 1.27 cm and conductivity 1000 μS cm^{-1}. (b) Reconstructed image for the saline tank setup.

Table 1. Measured performance and comparison.

Parameter	Yan *et al* (2011)	Constantinou *et al* (2015)	Hong *et al* (2015)	Kim *et al* (2017)	Wu *et al* (2018)	This work
Architecture	Differential current generator	Negative feedback	Differential current generator	Differential current generator	Negative feedback	Current conveyor II
Bandwidth	90 kHz	⩽1 MHz	⩽200 kHz	256 kHz	500 kHz	**100 Hz–10 MHz**
Output impedance	>560 kΩ @ 90 kHz	360 **k**Ω @1 MHz	—	—	**1.12 MΩ @ 500 kHz**	101 kΩ @ 1 MHz, 19.5 kΩ @ 10 MHz
Maximum output current (peak-peak)	350 μA	1 mA	1 mA	1 mA	**6 mA**	1.2 mA
THD (current) (frequency)	0.81% (250 μA) (Unknown)	<0.1% (1 mA) (50 kHz)	<0.1% @ 0.1 mA (Unknown)	<0.47% (1 mA) (128 kHz)	<0.18% (6 mA) (500 kHz)	**<0.14%** (**1.2 mA**) (**500 kHz**) **<0.7%** (**1.2 mA**) (**10 MHz**)

was designed with circuits such as the current driver, instrumentation amplifier (IA), variable gain amplifier (VGA), analog-to-digital converter (ADC) and switches which implement majority of the EIT functionality. Daughter-board modules include the ASIC with voltage references, biasing, switching mechanisms, power and serial interfaces. A motherboard houses the daughter-board modules along with an FPGA carrier board, and peripheral components. The FPGA controls the various SPI interfaces and acquires the digital data in parallel from all the channels on the daughter-board modules. Digital matched filter was implemented on the FPGA fabric to extract the in-phase and quadrature component of voltages to reduce the data throughput from the hardware. Computed data was sent to the MATLAB software on a computer to generate impedance matrix and obtain reconstructed images. Difference imaging was performed with a standard Gauss–Newton algorithm using Laplace-smoothing Tikhonov regularization.

An 8.5 cm diameter tank was filled with a saline solution of conductivity 1000 μS cm^{-1} which is in the range of value reported for different breast tissues (Jossinet and Schmitt 1999). The tank was fitted with conductive polymer plugs in contact with alligator clip electrodes attached to the tank. The spacing between electrodes was 3.25 cm. An initial experiment consisted of filling the tank with saline to a height of 1.27 cm to form a baseline measurement. Subsequent experiments were performed with a brass rod of diameter 1.3 cm placed at the center of the saline tank. Two hundred and forty current source-sink patterns were used to obtain data from the designed 16-electrode EIT system. The image obtained from the saline tank experiment using reconstruction algorithms (Murphy *et al* 2017) is shown in figure 16.

5. Discussion

The reduction in the output impedance can be attributed to the placement of the output port of the current driver in the ASIC. Adjacent pads increase the capacitive coupling, and degrade the high frequency measurements. The estimated parasitic capacitance of the ASIC pads is ∼3.5 pF and this value is consistent with the measured results (at lower frequencies). A future iteration of the ASIC will isolate the adjacent pads to obtain improved measurement of the output impedance.

The impedance values for cancer (CA), mammary gland (MA) and fibroadenoma (FA) tissues for breast, at 1 MHz are 139, 69, and 17.4 Ω respectively (Jossinet 1996, Murphy *et al* 2017). Similarly for prostate, impedance values for cancerous (CP), and glandular (GI) tissues at 10 MHz are 145 and 118 Ω respectively (Halter *et al* 2008, Wan *et al* 2010). Thus, the output impedance of the current driver of 101 kΩ at 1 MHz and 19.5 kΩ at 10 MHz represents an error of less than 0.01% which is well within the accuracy requirement of EIT systems (Halter *et al* 2008, Rao *et al* 2018).

The current driver achieves wide-band operation up to 10 MHz, necessary for EIT prostate and breast cancer detection. The THD values achieved are an improvement from previously reported integrated designs. The use of indirect feedback compensation enables wide-band operation with a small compensation capacitor. This is especially helpful when integrating multiple EIT channels on a single ASIC. On-chip bandgap references for biasing would improve the integration of the current driver in building multiple channel EIT systems. Table 1 shows a comparison with previously reported current drivers. None of the current driver implementations reported in the comparison table have measured operation up to the 10 MHz range, where electrical impedance interrogation of intracellular physiology could provide increased contrast between benign and cancerous tissue. A DC blocking capacitor is essential when interfacing with tissue for patient safety and is not included in these implementations. The current driver design presented in this paper has an architecture which addresses these issues

6. Conclusion

A CMOS wide-band current driver based on current conveyor architecture is presented. High linearity is achieved by the use of a resistor for current generation in the V-I conversion phase, whereas high accuracy is obtained by the use of a gain boosted cascode structure for high output impedance. The design was fabricated in the 0.18 μm process and can deliver 1.2 mA of current up to frequencies of 10 MHz. The above performance is achieved while maintaining harmonic distortion of less than 1% essential for EIT imaging (Rao *et al* 2018). A servo-loop circuit is designed for the output branch of the current driver to account for the DC blocking capacitor when injecting current into the human tissue. The current driver specifications have been measured using custom built PCBs and its performance characterized with a complex load impedance up to 10 MHz. A 16-electrode EIT system which incorporates the current driver was used to measure a saline tank setup and an image is obtained. The circuit is intended for use in active electrodes and EIT applications which require high frequency of operation to detect cancerous tissues.

Acknowledgments

This work was supported in part by the US National Science Foundation, under Grant No. 1418497, US Department of Defense CDMRP Grant Nos. W81XWH-15-1-0572 and W81XWH-15-1-0571.

ORCID iDs

A J Rao https://orcid.org/0000-0002-8769-2606
E K Murphy https://orcid.org/0000-0002-4635-3384

References

Baker R J 2010 *Circuit Design, Layout and Simulation* 3rd edn (New York: Wiley-IEEE Press)
Carusone T C, Johns D, Martin K W K W and Johns D 2012 *Analog Integrated Circuit Design* (New York: Wiley)
Constantinou L, Bayford R and Demosthenous A 2015 A wideband low-distortion CMOS current driver for tissue impedance analysis *IEEE Trans. Circuits Syst.* II **62** 154–8
Constantinou L, Triantis I F, Bayford R and Demosthenous A 2014 High-power CMOS current driver with accurate transconductance for electrical impedance tomography *IEEE Trans. Biomed. Circuits Syst.* **8** 575–83
Cook R, Saulnier G, Gisser D, Goble J, Newell J and Isaacson D 1994 ACT3: a high-speed, high-precision electrical impedance tomograph *IEEE Trans. Biomed. Eng.* **41** 713–22
Halter R J, Hartov A and Paulsen K D 2008 A broadband high-frequency electrical impedance tomography system for breast imaging *IEEE Trans. Biomed. Eng.* **55** 650–9
Halter R J, Hartov A, Paulsen K D, Schned A and Heaney J 2008 Genetic and least squares algorithms for estimating spectral EIS parameters of prostatic tissues *Physiol. Meas.* **29** S111–23
Hong S, Lee J, Bae J and Yoo H J 2015 A 10.4 mw electrical impedance tomography soc for portable real-time lung ventilation monitoring system *IEEE J. Solid-State Circuits* **50** 2501–12
Jivet I and Dragoi B 2008 On-electrode autonomous current generator for multi-frequency EIT *Physiol. Meas.* **29** S193–201
Jossinet J 1996 Variability of impedivity in normal and pathological breast tissue *Med. Biol. Eng. Comput.* **34** 346–50
Jossinet J 1998 The impedivity of freshly excised human breast tissue *Physiol. Meas.* **19** 61–75
Jossinet J and Schmitt M 1999 A review of parameters for the bioelectrical characterization of breast tissue *Ann. New York Acad. Sci.* **873** 30–41
Kim M *et al* 2017 A 1.4 mΩ-sensitivity 94 dB dynamic-range electrical impedance tomography SoC and 48-channel hub-SoC for 3D lung ventilation monitoring system *IEEE J. Solid-State Circuits* **52** 2829–42
Lionheart W R B, Kaipio J and McLeod C N 2001 Generalized optimal current patterns and electrical safety in EIT *Physiol. Meas.* **22** 85–90
McEwan A, Cusick G and Holder D S 2007 A review of errors in multi-frequency EIT instrumentation *Physiol. Meas.* **28** S197–215
Murphy E K, Mahara A and Halter R J 2017 Absolute reconstructions using rotational electrical impedance tomography for breast cancer imaging *IEEE Trans. Med. Imaging* **36** 892–903
Rao A, Teng Y C, Schaef C, Murphy E K, Arshad S, Halter R J and Odame K 2018 An analog front end ASIC for cardiac electrical impedance tomography *IEEE Trans. Biomed. Circuits Syst.* **12** 729–38
Saulnier G, Blue R, Newell J, Isaacson D and Edic P 2001 Electrical impedance tomography *IEEE Signal Process. Mag.* **18** 31–43
Saxena V 2007 Indirect feedback compensation technique for multi-stage operational amplifiers *PhD Thesis* Boise State University
Sedra A and Smith K 1970 A second-generation current conveyor and its applications *IEEE Trans. Circuit Theory* **17** 132–4
Tucker A S, Fox R M and Sadleir R J 2013 Biocompatible, high precision, wideband, improved Howland current source with lead-lag compensation *IEEE Trans. Biomed. Circuits Syst.* **7** 63–70
Wan Y, Halter R, Borsic A, Manwaring P, Hartov A and Paulsen K 2010 Sensitivity study of an ultrasound coupled transrectal electrical impedance tomography system for prostate imaging *Physiol. Meas.* **31** S17–29
Wilson B 1990 Recent developments in current conveyors and current-mode circuits *IEE Proc. Circuits Devices Syst.* 137 63
Wu Y, Jiang D, Bardill A, de Gelidi S, Bayford R and Demosthenous A 2018 A high frame rate wearable EIT system using active electrode asics for lung respiration and heart rate monitoring *IEEE Trans. Circuits Syst.* I **65** 3810–20
Yan L, Bae J, Lee S, Roh T, Song K and Yoo H J 2011 A 3.9 mW 25-electrode reconfigured sensor for wearable cardiac monitoring system *IEEE J. Solid-State Circuits* **46** 353–64
Zeki A and Kuntman H 1997 Accurate and high output impedance current mirror suitable for CMOS current output stages *Electron. Lett.* **33** 1042

Physiological Measurement

IPEM Institute of Physics and Engineering in Medicine

PAPER

Noise-robust bioimpedance approach for cardiac output measurement

Recent citations

- Focus on Recent Advances in Electrical Impedance Tomography
Richard Bayford and Nick Polydorides

To cite this article: Ethan K Murphy *et al* 2019 *Physiol. Meas.* **40** 074004

View the article online for updates and enhancements.

AAS | IOP Astronomy ebooks

Part of your publishing universe and your first choice for astronomy, astrophysics, solar physics and planetary science ebooks.

iopscience.org/books/aas

This content was downloaded from IP address 129.170.69.35 on 06/12/2019 at 17:38

IOP Publishing Physiol. Meas. 40 (2019) 074004 (12pp) https://doi.org/10.1088/1361-6579/ab0d45

Physiological Measurement

IPEM Institute of Physics and Engineering in Medicine

PAPER

Noise-robust bioimpedance approach for cardiac output measurement

Ethan K Murphy[1], Justice Amoh[1], Saaid H Arshad[1], Ryan J Halter[1,2] and Kofi Odame[1]

[1] Thayer School of Engineering, Dartmouth College, Hanover, NH 03755, United States of America
[2] Geisel School of Medicine, Dartmouth College, Hanover, NH 03755, United States of America

E-mail: ethan.k.murphy@dartmouth.edu

RECEIVED
14 December 2018

REVISED
28 February 2019

ACCEPTED FOR PUBLICATION
6 March 2019

PUBLISHED
26 July 2019

Keywords: electrical impedance tomography, deep neural network, cardiac monitoring, noise modeling

Abstract

Objective: Congestive heart failure is a problem affecting millions of Americans. A continuous, non-invasive, telemonitoring device that can accurately monitor cardiac metrics could greatly help this population, *reducing unnecessary hospitalizations and cost*. *Approach*: Machine learning (ML) algorithms trained on electrical-impedance tomography (EIT) data are presented for portable cardiac monitoring. The approach was validated on a simulated thorax and a measured tank experiment. A highly detailed 4D chest model (finite element method mesh and conductivity profiles) was developed utilizing the 4D XCAT phantom to provide realistic data. The ML algorithms were trained using databases that assumed the presence of poorly contacting electrodes without any assumptions of knowing which electrodes would be bad in the experiment. The trained ML algorithms were compared to EIT evaluated with and without removing bad electrodes. *Main results*: A regression support vector machine and a deep neural network (DNN) were found to be the most accurate and robust to poorly contacting electrodes while not needing to know which electrodes were in poor contact in the simulated and measured experiments, respectively. *Significance*: Although the ML algorithms are not always better than EIT (with bad electrodes removed), the comparable results without needing *a priori* knowledge of which electrodes are bad is seen as a very promising feature. An evaluation of computational costs showed that the DNN required comparable computational power to the other methods while requiring less memory, which could make the DNNs an attractive algorithm for a low-power, portable system. This work represents an important validation of the method using measured data, and model development, which is needed to apply this method on real clinical data. Additionally, the developed 4D simulated thorax model could be an important tool within the EIT community.

1. Introduction

Congestive heart failure (CHF) currently affects an estimated 5.8 million Americans, making it one of the most common reasons why those aged 65 and over are hospitalized (Hal *et al* 2012). Adverse cardiac events account for more than one million hospitalizations per year in the United States (Butler *et al* 2010, Purcell *et al* 2014). With a growing proportion of the population living with some form of heart failure, the ability to pro-actively and accurately monitor cardiovascular health is crucial. Telemonitoring is becoming increasingly important to proactively address this growing need (Chaudhry *et al* 2010, Hasan and Paul 2011, Purcell *et al* 2014). The primary metric of interest is cardiac output (CO) (Alhashemi *et al* 2011, Marik 2013). CO is the product of heart-rate (HR) and stroke volume (SV), where stroke volume is the difference between the maximum and minimum left ventricular (LV) volume. A promising technology to non-invasively and continuously monitor CO is electrical impedance tomography (EIT). EIT uses multiple bioimpedance measurements recorded from electrodes placed around the chest, and, generally, uses physics-based approaches to recover the conductivity, which has been shown to correlate well with SV in several studies (Vonk-Noordegraaf *et al* 2000, Fagerberg *et al* 2009, Pikkemaat *et al* 2014). We have been developing a wearable EIT system for continuous monitoring of CO

© 2019 Institute of Physics and Engineering in Medicine

with low power constraints and potential smart-phone compatibility (Arshad *et al* 2015, Takhti *et al* 2016, Rao *et al* 2018).

Although EIT appears more promising than commercial electrical bioimpedance systems based on the sophisticated modeling of EIT, there remain significant concerns of error due to several sources: here we focus on one of the primary sources of errors in wearable systems, electrode contact issues, i.e. 'bad' electrodes. There have been a number of studies that have attempted to address this problem by (1) compensating for bad electrodes by simultaneously solving for both internal conductivity and the electrode contact impedances (Heikkinen *et al* 2002, Boverman *et al* 2009, Demidenko *et al* 2011), (2) automatically detecting bad electrodes and simply removing them (Asfaw and Adle 2005, Jeon *et al* 2017), or (3) automatically detecting bad electrodes and adjusting their measurements in some way to mitigate their effect (Hartinger *et al* 2009, Mamatjan *et al* 2013, Zhang *et al* 2017). It was concluded in Heikkinen *et al* (2002) that the simultaneous reconstruction of conductivity and contact impedance was not practical in situations without a homogeneous (or known) measured reference frame. In Hartinger *et al* (2009) bad electrodes are compensated by increasing the measurement variance of respective measurements, in Mamatjan *et al* (2013) a similar approach was used but the data was also 'cleaned' with a projection technique, and in Zhang *et al* (2017) a Grey model based on a time-series of data was used to estimate data from bad electrodes. Simply removing measurements corresponding to bad electrodes appears to be a very practical solution that results in good reconstructions. The main challenge is in reliably determining which electrodes are bad. This becomes increasingly challenging as more electrodes are bad, e.g. the work in Hartinger *et al* (2009) could only reliably detect up to two bad electrodes.

In this paper, we introduce a new bioimpedance-based method powered by machine learning (ML) for measuring cardiac output (and left ventricular (LV) volume in general) that is robust to the presence of faulty electrodes. Our approach uses the same measurement data as EIT and is similar to a lung EIT approach (Zifan and Liatsis 2012). However, instead of initially using the data to reconstruct an EIT image, from which LV volume is calculated, our novel method inputs the data to a noise-robust ML regression model, which directly extracts LV volume information. The noise robustness and simplicity of the approach could significantly reduce the overall computational requirements making this approach attractive for a CO monitoring device that requires robustness and low-power operation in a non-clinical setting. Three ML algorithms are considered; a regression support vector machine (rSVM), a regression decision tree (rDT), and a more sophisticated deep neural network (DNN). The ML models are compared to EIT (with and without bad electrodes removed) on a simulated chest phantom (figure 1(A)) and a measured saline tank experiment (figure 1(B)). The simulated thorax model built upon a sophisticated 4D thorax model (Segars *et al* 2010) could be a useful tool within the EIT community. The rSVM and DNN outperform EIT (with bad electrodes removed) for up to four and six electrodes partially removed, respectively, on simulated data, and the DNN approach provided similar results to EIT (with bad electrodes removed) with three electrodes partially removed. A major advantage of the ML approach is that it provides better or comparable results without requiring knowledge of which electrodes are bad.

This paper continues with the description of (1) traditional EIT, (2) parameter selection and the linear regression model for EIT, (3) the simulated thorax model, (4) the experiments, and (5) the ML algorithms and (testing and training) databases. Results of both experiments are then discussed along with a comparison on the number of floating point operations (FLOPS) and memory needed for the EIT and ML approaches. Future development needed for this approach to work successfully on clinical data are discussed, and conclusions are summarized.

2. Methods

2.1. Traditional EIT

2.1.1. *Forward problem*

The forward problem relies on solving the generalized Laplace equation,

$$\nabla \cdot \sigma \nabla u = 0, \tag{1}$$

over the entire domain, where σ is the conductivity and u is the electric potential. The complete electrode model (CEM) is used to realistically account for discrete electrodes (Somersalo *et al* 1992). The forward problem calculates the electric potential distribution throughout the domain and voltages on the electrodes assuming the conductivity and applied currents on the electrodes are known. The CEM boundary conditions additionally specify each electrode's contact impedance and assume that current only flows in or out of the system through the electrodes. The solution to the forward problem is calculated in 3D using the finite element method (FEM) with linear basis elements (Borsic *et al* 2008).

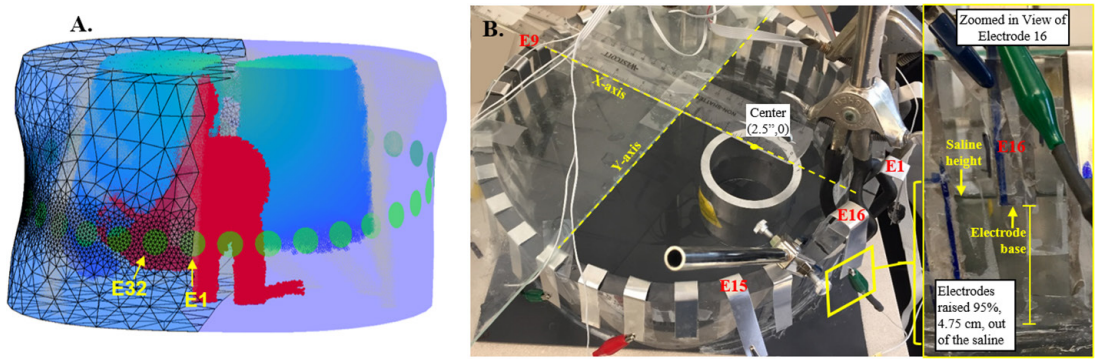

Figure 1. (A) FEM mesh produced from 4D XCAT. A coarse surface mesh (left side) is produced in distmesh with encoded electrodes, and a fine 3D mesh produced in gmsh, wherein heart, lung, aorta, and ribs are visualized. (B) The saline tank experiment with 16 electrodes connected to an EIT system (on a 32 electrode tank). Clamps were used to hold the electrodes partially out of the saline, simulating partially contacting electrodes.

2.1.2. Inverse methods

A standard Gauss–Newton algorithm is employed using Laplace-smoothing Tikhonov regularization producing 2D images of data from the single ring of electrodes (see figure 1(A)) via 3D modeling of the forward problem, i.e. standard 2.5D reconstructions. The aim is to minimize the following objective function:

$$\arg\min_{\delta\sigma} \|\mathbf{J}\delta\sigma - (\mathbf{v}_{Test} - \mathbf{v}_{Ref})\|^2 + \alpha\|\mathbf{L}\delta\sigma\|^2, \tag{2}$$

where $\delta\sigma$ is a perturbation from some estimated or known conductivity, $\mathbf{J}$ is the Jacobian, α is the Tikhonov parameter, $\mathbf{L}$ is the regularization matrix, and $\mathbf{v}_{Test}$ and $\mathbf{v}_{Ref}$ are the test and reference voltages, respectively. Here only difference images are considered. This problem can be solved directly via the following formula:

$$\delta\sigma = \left(\mathbf{J}^T\mathbf{J} + \alpha\mathbf{L}^T\mathbf{L}\right)^{-1}\mathbf{J}^T(\boldsymbol{\Delta}\mathbf{v}), \tag{3}$$

where $\mathbf{v}_{Test} - \mathbf{v}_{Ref} = \boldsymbol{\Delta}\mathbf{v}$. This solution, i.e. a single-step linearized Tikhonov regularized solution, has widespread use in the medical industrial and geophysical EIT community (Holder 2005).

2.2. Parameter selection and linear regression for EIT

In the experiments, linear regression is applied to the reconstructed heart areas or inclusion diameters from thresholded EIT images and the true values. A two-step optimization strategy was performed to find the best Tikhonov and threshold values. Specifically, we searched over a set of possible Tikhonov parameters ranging from 1×10^{-3} to 1×10^{4}, where for each value a 1D minimization procedure was performed on the RMS error of the linear regression resulting from the threshold value. At each threshold the heart area was determined by calculating the area, A_{rec}, of all the voxels above the threshold. The reconstructed inclusion diameter (for the tank experiment) was defined as the diameter of the circle that yielded the reconstructed area, i.e. $d_{rec} = 2\sqrt{A_{rec}/\pi}$.

2.3. Simulated thorax

The model for simulated thorax data is based on the 4D XCAT model, which is a highly detailed extended cardiac-torso model that is based on visible human anatomical data, 4D cardiac-gated multi-slice CT data, 3D MRI data, and 4D respiratory-gated multi-slice CT data (Segars *et al* 2010). Non-uniform rational basis splines are used to model individual anatomical tissues/organs that are 4D. Multiple parameters within the model can be adjusted. In this study, a single cardiac cycle of 11 frames is considered with a fixed chest size (that is, assuming a breath-hold). At any time frame, the XCAT model provides the FEM model with the exterior of the domain and interior labels so that accurate conductivity distributions can be produced. The exterior boundary of the domain is approximated using a combined Fourier series and radial-basis-functions (RBF), i.e. it extends a common Fourier series for 2D-chest approximations (Murphy and Mueller 2009, Boyle *et al* 2012) into 3D. The boundary model is given by

$$r_S(\theta, z) = r_0 + \sum_{j=1}^{9}\left[exp\left(-\frac{(z - z_{c,j})^2}{\sigma_z^2}\right)\sum_{n=1}^{8}\left(a_{j,n}\cos(n\theta) + b_{j,n}\sin(n\theta)\right)\right], \tag{4}$$

where there are nine linearly spaced RBF centers from the bottom to top of the chest. The weights $(a_{j,n}, b_{j,n})_{j,n=1}^{9,8}$ can be solved using a straight forward linear least squares implementation given a sufficient number of boundary points. Furthermore, the electrodes (assumed equally spaced) are encoded in the mesh via construction of

Table 1. Measurement frame description for 16-electrode saline tank and 32-electrode simulated thorax experiments.

Approach	Experiment	Skip patterns	Voltage type	Frame size
EIT	Simulated thorax	1–7	Differential	6496 × 1
EIT	Measured tank	1–7	Differential	1456 × 1
rSVM/rDT	Simulated thorax	1–7	Single-ended	6496 × 1
rSVM/rDT	Measured tank	1–7	Single-ended	1456 × 1
DNN	Simulated thorax	1–7	Single-ended	224 × 32
DNN	Measured tank	1–7	Single-ended	112 × 16

an initial coarse 2D surface mesh using distmesh (see left side of figure 1(A), Persson and Strang (2004)). The coarse 2D surface mesh is then input to Gmsh (Geuzaine and Remacle 2009) to construct the full 3D mesh of approximately 360k nodes and 1.9M elements. A slightly less dense mesh is used for the Jacobian calculation for EIT reconstructions so that no inverse crime is committed (Lionheart 2004). No internal structures were explicitly defined within the 3D mesh. Mesh element quality was maximized by constructing the mesh from an optimized surface triangulation via distmesh, by tuning h-parameters of the electrode and background nodes, and by Gmsh's optimization algorithm. This resulted in a mean and minimum mean ratio (a mesh element quality metric (Liu and Joe 1994) computed using (Burkardt 2019)) of 0.84 and 0.018 across all XCAT meshes, respectively.

The initial conductivity model is produced by relabeling the voxels of the 3D image of the XCAT model to the corresponding conductivity values based on literature Andreuccetti *et al* (2017) at 50 kHz of the heart tissue, blood, lung, bone, cartilage, air, tissue, skin, and background tissue, and then interpolating onto the nodes of the FEM mesh (see figure 1(A)). The conductivity distribution is then improved by incorporating a blood perfusion model (based on Braun *et al* (2015)), where the lung conductivity is given by the following equation:

$$\sigma_i(t) = \sigma_L \left[1 + \Delta\sigma_{LMAX} \cdot P_L \left(t - \frac{d_{PV_i}}{PWV}\right)\right] \tag{5}$$

and σ_L is the nominal lung conductivity, $\Delta\sigma_{LMAX}$ is a factor used to control the maximum increase in conductivity, P_L is the pulmonary arterial distension, d_{PV_i} is the distance from each point in a given lung to its pulmonary valve, and PWV is the pulse wave velocity of the blood through the lung. We choose a nominal conductivity of 0.09 S m^{-1} (σ_L), allow for a maximum conductivity increase of 10%, and take the pulse wave velocity to be 1.5 m s^{-1} based on Braun *et al* (2015). The blood volume entering the pulmonary artery given by the XCAT model is used as a surrogate for P_L.

2.4. Description of experiments and test data

2.4.1. Simulated thorax experiment

The simulated experiment used the model described in section 2.3 assuming (1) 32 electrodes equally spaced in a horizontal plane centered at the heart height and (2) 11 heart frames of data that cover a portion of the cardiac cycle where the LV volume ranged from 52 ml to 119 ml. The simulated experimental data (*test data*) included 660 frames where 1–6 electrodes were partially occluded (50%–95% in 5% steps, i.e. ten possibilities) for each of the 11 heart frames. The partially contacting electrodes were $\{1\}$, $\{1, 2\}$, $\{1, 2, 32\}$, $\{1, 2, 31, 32\}$, $\{1, 2, 3, 31, 32\}$, and $\{1, 2, 3, 30, 31, 32\}$. These electrodes were chosen because they are the closest to the heart region and therefore are most sensitive to changes within this region; consequently, contact variability for these electrodes specifically will have a significant impact on how accurately cardiac activity can be recovered. For each set of partially contacting electrodes, all electrodes within the set were occluded by the same percent. Single-ended measurements were simulated assuming skip (injection) patterns of one through seven, which results in 224 injection patterns on the 32 electrodes. This matrix (32 × 224) of single-ended voltages (differenced by a reference set of single-ended voltages) was used as input to the ML algorithms. The EIT reconstructions were based on the same data, converted to voltage differences, with bipolar measurements removed, which resulted in data of size 6496 × 1; see table 1. Bipolar measurements are removed because heuristically these measurements are the most effected by partially contacting electrodes.

2.4.2. Saline tank phantom experiment

Impedance data was recorded from a cylindrical, saline-filled tank with 28 cm diameter, 5 cm depth, 16 electrodes each with widths of 1.2 cm and heights of 5 cm (figure 1(B)). The background conductivity was 0.1 S m^{-1}, and there were six metal inclusions used (considered one at a time) with diameters ranging from 1.5" to 4" in 0.5" steps and centered at (2.5", 0). Impedance data was recorded using a custom designed EIT system (Kahn *et al* 2015) at 10 kHz. Measurements for partially contacting electrodes were achieved by lifting the electrodes 60%, 70%, 80%, 90%, and 95% out of the saline. For each percent occlusion considered, electrodes 1, 2, and 16 were

Table 2. Regression SVM (rSVM) and regression decision tree (rDT) parameters.

ML Type	Experiment	Basis/transform function	Num. of support vectors/children
rSVM	Simulated thorax	Linear (scale = 68.55)	3798
rSVM	Measured tank	Linear (scale = 0.44)	1608
rDT	Simulated thorax	Identity	41
rDT	Measured tank	Identity	2731

all removed the same percent out of the tank. These particular electrodes were chosen using similar rationale as in the simulated thorax experiment, i.e. they are expected to result in the most challenging scenario of electrode contact issues. Single-ended measurements are recorded assuming skip (injection) patterns of one through seven, which resulted in 112 injection patterns on the 16 electrode tank. This matrix (16×112) of single-ended voltages (differenced by a reference set of single-ended voltages) was used as input to the ML algorithms. The EIT reconstructions were based on the same data, converted to voltage differences, and similarly to the simulated thorax experiment bipolar measurements were removed, which resulted in data of size 1456×1 (table 1).

2.5. Machine learning algorithms

Three ML algorithms were evaluated in this study. Two standard ML algorithms, a rSVM and a rDT, and the third a deep neural network specifically designed to be robust to noise.

2.5.1. Regression SVM and regression decision tree

The rSVM and rDT algorithms were implemented directly from Matlab's Machine Learning Toolbox. In both the XCAT and tank experiments the training was performed in the same manner. First, simulated voltage data was stretched into vectors of length 6720×1 and 1456×1 for the XCAT and tank experiments, where bipolar measurements were removed. Differencing was performed assuming the smallest heart frame and homogeneous frame with no errors in the XCAT and tank experiments, respectively. The large databases were then randomly down-selected to 10 000 samples in both experiments. Training was performed several times to ensure that this resulted in negligible changes. The number of variables was reduced to 104 and 464 using principal component analysis (PCA) for the XCAT and tank experiment, respectively. This reduction was chosen based on numerical considerations and because 104 and 464 are the number of independent measurements expected. According to the PCA, the variation explained by the first 104 and 464 variables was greater than 99.999% for this number of variables. The coefficients from the PCA were used to map the testing datasets to the PCA subspaces. The rSVM and rDT algorithms were then trained using Matlab's built-in hyper-parameter optimization algorithm. Listing of the basis/transform functions and number of support vectors/children are given in table 2 for the rSVM and rDT, respectively.

2.5.2. Deep neural network

Deep neural networks (DNN) are highly expressive models that have proven effective for a variety of data analysis and pattern recognition tasks. Through a series of hierarchical non-linear transformations, neural networks are able to extract salient task-specific features from raw input data. Convolutional neural networks, in particular, are designed to capture spatially local and global patterns in multidimensional inputs, and are thus used in image and video processing tasks. In this work, we implement DNNs featuring convolutional layers to learn salient features from unprocessed impedance measurements which are suitable for predicting the expected cardiac output.

The input data to the DNNs are 2D matrices of single-ended voltages (figure 2(A)), in the format: (number of electrodes) × (number of current injection patterns). Calculating correlations across rows (current patterns as variables) and across columns (electrodes as variables) revealed the (generally local) correlations present in the matrix form of the data (figures 2(B) and (C), respectively). Hence, a 2D convolutional neural network is a practical choice for capturing the spatial interdependencies in the data.

A pre-processing step is required to accommodate the symmetric nature of the measurements. In the experimental setup, since electrodes are arranged in a circle, the first and last electrodes are adjacent to each other. However, those same electrodes are far apart in a simple 2D input matrix representation. To address this, the first N_W rows of the input matrix are repeated at its end to provide the network with this wraparound information. This pre-processing step was observed to improve network performance.

The architecture of the neural network used was identified using a hyper-parameter optimization toolkit. Using a tree of Parzen estimators (TPE) (Bergstra *et al* 2011), the optimization toolkit determined optimal number of layers as well as corresponding optimal number of hidden units. The hyper-parameter search process involved the training of over 50 different models to find the configuration. Unlike the network architecture, the optimal number of wraparound rows ($N_W = 4$) was identified in a heuristic manual search manner.

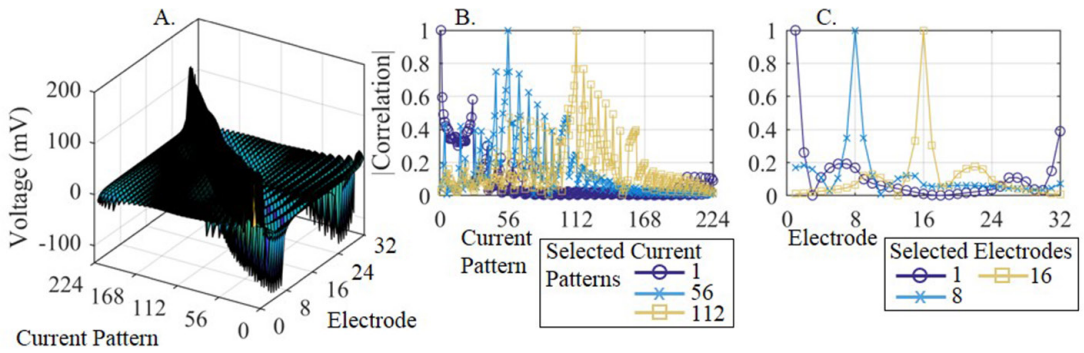

Figure 2. Example matrix of simulated single-ended voltages from the simulated thorax model (A) and corresponding absolute correlations of selected current patterns across electrodes (B) and selected electrodes across current patterns (C), which reveals the 'spatial' correlations in the singled-ended 'images'.

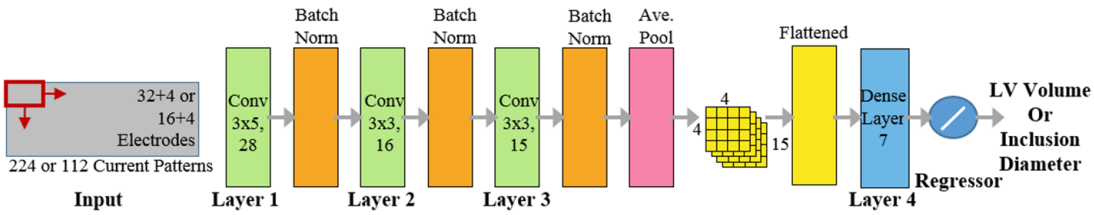

Figure 3. Architecture of the network: five layer DNN with three convolutional layers, a dense 4th layer, and a final regression layer that predicts the LV volume or inclusion diameter (depending on the experiment) from an input matrix of single-ended voltages (differenced by a reference frame).

The resulting network architecture (figure 3) featured five layers in all. Layers 1–3 are convolutional layers of size 28, 16, 15, respectively. The 2D convolutional kernel sizes were $(3, 5)$ for the first and $(3, 3)$ for the second and third. The corresponding kernel strides were $(2, 3)$ for the first two layers and $(1, 3)$ for the third layer. The output sizes of the convolutional layers are $(18, 75)$, $(9, 25)$ and $(9, 9)$, respectively. All convolutional layer activations were rectified linear units (ReLU), preceded by mini-batch normalization. An average pooling layer downsamples the output of layer three into a $4 \times 4 \times 15$ matrix. This is then flattened into a 240×1 vector, and fed to a seven-unit dense layer. The output layer is a single linear regressor node for predicting heart volume. In all, there are 8600 parameters in the neural network.

The DNN was implemented in Python using the Tensorflow deep learning library, with the Keras wrapper. Training was performed with the Adam optimization algorithm for stochastic gradient descent, with a batch size of 32 for 80 epochs, completing in 10 min on a computer with an Nvidia GTX 1080 Ti GPU, a 3.8 GHz Core i5 CPU and 64 GB of RAM.

2.5.3. Simulated thorax databases

The simulated thorax database was designed assuming the bad electrodes were unknown. The databases include many samples of simulated non-idealities, where each sampled error is simulated over all 11 heart frames. The non-idealities include percentages of electrodes being occluded and a rotation of the electrode plane from horizontal (horizontal is assumed ideal). The percent occlusions varied from 50% to 95% in 5% steps, and the electrode plane was rotated through the heart center along the left-right axis by randomly selected angles from the set ($\pm 0.7, \pm 0.5$, and ± 0.3 degrees). The training database consisted of 77 000 samples, which had 11 samples with no error (i.e. 11 heart frames with no error) and 7000 sets of 11 heart frames with random sampled errors. For each random sample of errors, five electrodes were chosen where it was uniformly chosen between good contact and partial contact and a random electrode plane rotation was chosen. For partially contacting electrodes the percent occluded was randomly selected among the 50%–95% options. A different mesh was used for each electrode plane rotation and the only training data that used the same mesh as in testing was from the 11 samples with no occluded electrodes, i.e. good data. The test set used to evaluate the ML algorithms is the simulated XCAT data, described in section 2.4.1.

2.5.4. Saline tank phantom databases

The saline tank database assumes no knowledge of which electrodes have partial contact. Thus random sets of electrodes (1–5 bad electrodes per sample) were picked to have partial contact of random amounts (5%–95% in 5% steps). The total database consisted of 84 000 samples, in which there were six conductivity distributions and

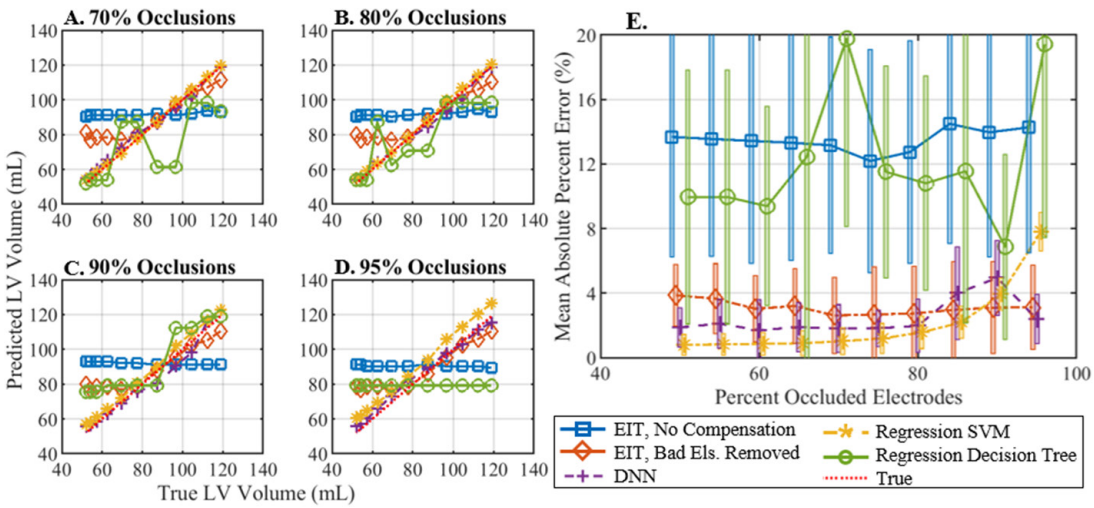

Figure 4. Predicted LV volume for each of the methods considered (EIT with no compensation, EIT with bad electrodes removed, DNN, and rSVM and rDT models) on the simulated thorax example where electrodes 1, 2, and 32 were (A) 70%, (B) 80%, (C) 90%, and (D) 95% occluded. (E) Mean errors with ± 1 standard deviations of the predicted LV volume from each method assuming electrodes 1, 2, and 32 were partially occluded.

4000 random samples with one bad electrode, 3000 random samples for two and three bad electrodes each, and 2000 random samples for four and five bad electrodes each. The test set used to evaluate the ML algorithms is the measured tank data, described in section 2.4.2.

2.6. Additional parameters

Optimal Tikhonov parameters were found to be ten in the simulated thorax experiment and one and ten for the tank experiment when using all electrodes and when electrodes 1, 2, and 16 were removed, respectively. The mesh used for simulations and the Jacobian calculation in the saline tank experiment was ~30k nodes and ~150k elements and was constructed using Netgen (Schöberl 1997).

3. Results

3.1. 4D XCAT simulated thorax

The predicted LV volumes, assuming 70%, 80%, 90%, and 95% occlusions of electrodes 1, 2, and 32, are shown for all five methods (figures 4(A)–(D)), i.e. EIT without compensation, EIT with bad electrodes removed, the DNN, rSVM, and rDT. The EIT approach with no electrode compensation has the largest errors followed closely by the rDT. These two methods do not track the LV volume well. The average relative errors and ± 1 standard deviations across percent occluded (figure 4(E)) show that the rSVM approach appears best for up to 85% occluded. The rectangles depicting standard deviations reveal there is significant overlap of the distributions. The only cases that have statistically significant separation, according to a two-sample T-test ($p < 0.01$), are rSVM from EIT with bad electrodes removed at 50% and rSVM from the other two good approaches at 95%. The upward trends of DNN and rSVM are expected as percent occlusion increases because of the resulting measurement noise. However, it is surprising that the 95% occlusion results in a smaller error for the DNN.

All methods were evaluated assuming all sets of bad electrodes (figure 5). One can clearly see that EIT with no compensation and the rDT are very sensitive to partial occlusions, where EIT with no compensation essentially fails after one electrode is partially occluded and the rDT fails after three electrodes are partially occluded. The other methods perform quite well over all the scenarios, except DNN with six partial contacting electrodes. Specifically, DNN and rSVM perform nearly identically for up to four electrodes bad (averaging 1.95% and 2.08%, respectively), and EIT with bad electrodes removed and rSVM yield consistent error across all combinations of electrodes (average 5.40% and 2.30%, respectively). It is expected that the ML results will degrade as the number of bad electrodes increases (especially when there are more bad electrodes than in the training data, i.e. greater than five). This expectation is consistent for the DNN and rDT results, but it is incorrect for rSVM, which performs exceptionally well with five and six bad electrodes. Overall, the rSVM appears to be the best approach in this simulated experiment as it does not require knowledge of bad electrodes and works well up to six partial occluding electrodes. Illustrations of the loss curves on the training and testing sets over 80 epochs reveal good convergence while indicating the network is not overfitting the training database (figure 6(A)).

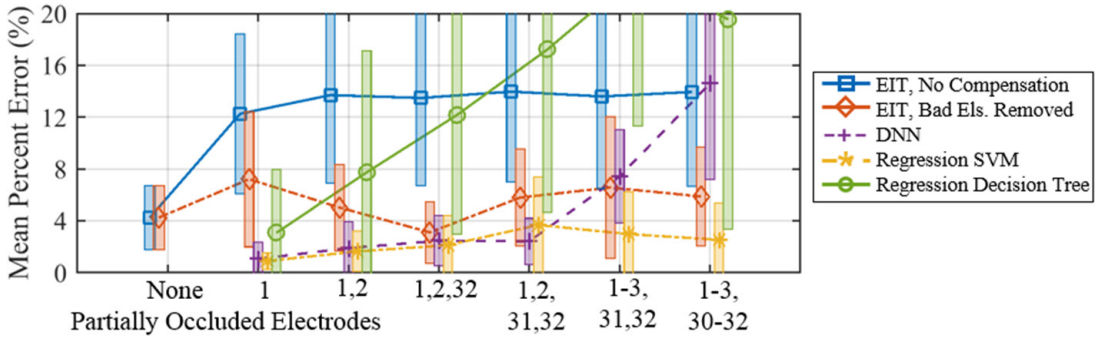

Figure 5. Overall mean percent errors with ±1 standard deviations across each set of partially occluded electrodes (0–6 bad electrodes) using EIT with no compensation, EIT with bad electrodes removed, DNN, and rSVM and rDT models for the simulated thorax example.

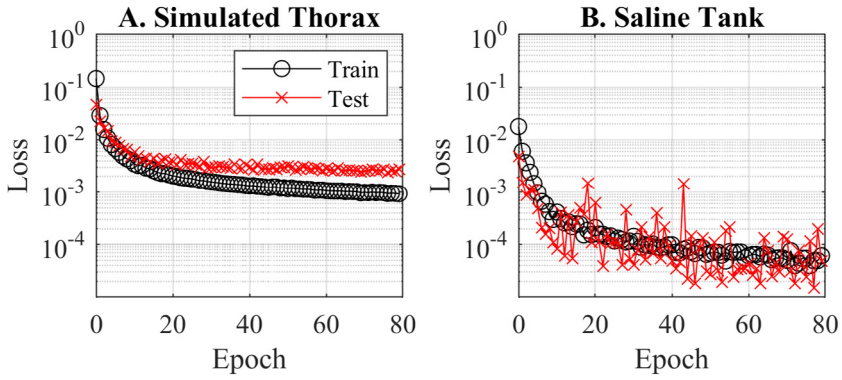

Figure 6. Logistic loss curves of the training and testing databases (assuming unknown bad electrodes) for (A) the simulated thorax and (B) saline tank.

3.2. Saline tank phantom

EIT reconstructions for the no compensation approach (figure 7) reveal that the reconstructions are qualitatively very sensitive to the partially contacting electrodes with artifacts worsening with increasing percent occlusion. In contrast, when the bad electrodes are removed, the EIT reconstructions qualitatively appear quite robust to partially contacting electrodes (last row of figure 7 which shows 95% occlusion). The ML algorithms do not produce images, so there are no qualitative images to present.

The predicted inclusion diameters, assuming 70%, 80%, 90%, and 95% occlusions of electrodes 1, 2, and 16, are shown for all methods, except the rDT (figures 8(A)–(D)). The rDT predicted a three inch diameter inclusion for nearly all cases (∼35% error) clearly indicating it did not successfully work here. EIT with no compensation performs poorly, rSVM significantly degrades in quality starting at 90% occluded electrodes, and the remaining two approaches perform well on all cases and are very close to the diagonal. To more clearly show the difference in accuracy, the mean absolute percent error and ±1 standard deviations across all experiments are displayed for each approach and percent occlusion (figure 8(E)). The two approaches (EIT bad electrodes removed and DNN) have very similar accuracies (statistically no significant difference). Both have a very slight upward trend as percent occlusion increases that surprisingly decreases at 95% occluded. While EIT with bad electrodes removed is a commonly used approach, the similar accuracy to the DNN approach on measured data strongly validates the hypothesis that DNN algorithms can practically work on measured data when trained on simulated data. A similar check on the loss curves for this experiment shows good convergence while indicating the network is not overfitting the training database (figure 6(B)).

3.3. Computational cost

We measured the computational cost in terms of memory storage required and the number of FLOPs, which we use as a surrogate measure for speed. The results are summarized in table 3. The difference in the number of FLOPs between the EIT approaches is due to the reduced number of measurements associated with removal of bad electrode data. The required memory is the same for the EIT approaches because both, in general, require storage of the complete Jacobian, which accounts for the vast majority of memory. A major cost in terms of FLOPs and memory required for the rSVM and rDT algorithms is the PCA-preprocessing step (shown in the table). The values for rSVM and rDT include the PCA component. One can see that a trained rDT has negligible

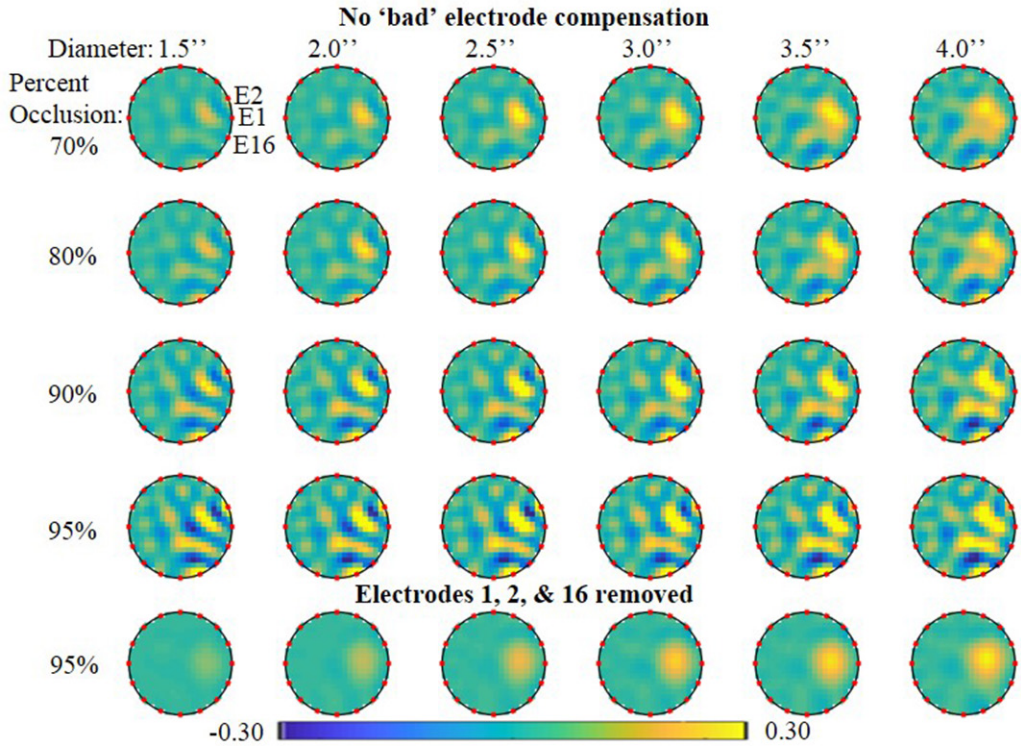

Figure 7. EIT reconstructions for measured difference data with electrodes 1, 2, and 16 occluded 70%, 80%, 90% and 95% in the first four rows assuming no bad electrode compensation. The final row depicts EIT reconstructions with 95% occlusions with bad electrodes removed. Qualitatively, 95% occlusions with bad electrodes removed look nearly the same reconstructions using all good data (not shown).

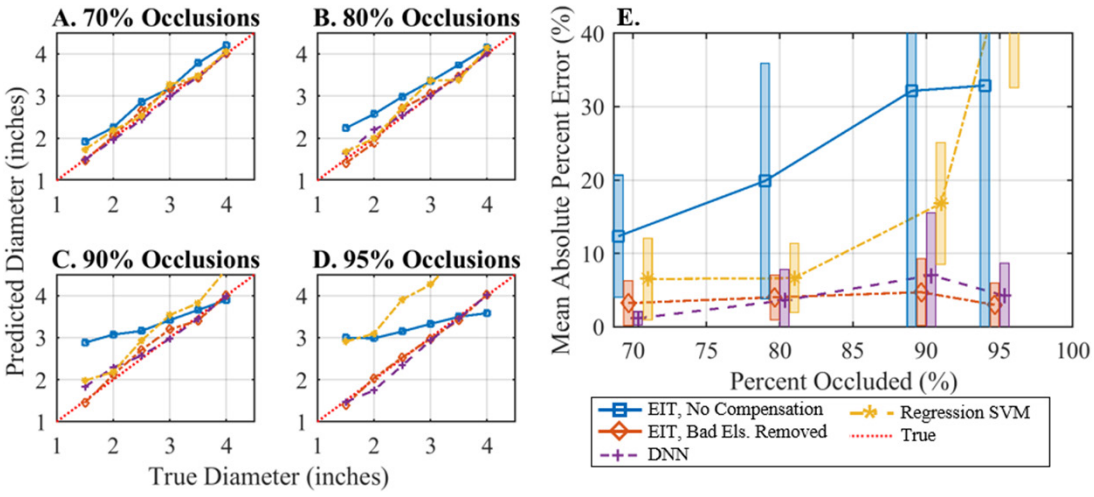

Figure 8. Reconstructed diameters from the tank experiment using EIT with no compensation, EIT with bad electrodes removed, DNN, and rSVM with electrodes 1, 2, and 16 occluded (A) 70%, (B) 80%, (C) 90%, or (D) 95%. (E) Mean absolute percent error with ± 1 standard deviations of the four methods over the six metal inclusions with three repeated measurements per inclusion.

computational or memory costs. The DNN memory costs are the least among methods, but their required FLOPs are similar to the other methods (2nd lowest and highest in the XCAT and tank, respectively). Overall, on a current desktop computer these are all reasonable and fast calculations, but for the envisioned use of this technology in a portable, low-power system the comparable computational and lower memory requirements of the DNNs may make it a more attractive method.

4. Discussion

This study highlights a proof-of-concept demonstration of how a ML-approach (designed to be robust to poorly contacting electrodes) can be used to predict cardiac metrics through an imageless approach in a

Table 3. Computational cost of the different methods.

	FLOPs (×1000)		Memory required (MB)	
Method	XCAT	Tank	XCAT	Tank
EIT no compensation	3846	920	15.38	3.68
EIT three bad Els. removed	2589	366	15.38	3.68
PCA-preprocessing	6243	304	25.00	1.22
rSVM	9775	642	39.10	2.57
rDT	6246	304	25.35	1.23
DNN	3259	940	0.34	0.29

simulated thorax and a measured saline tank experiment, and provides details of a 4D thorax model that can be used to produce richly detailed simulations. This method is robust up to six and three bad electrodes in simulated and measured experiments, respectively, and should be of interest to others in the EIT community for related applications, as current EIT approaches can only handle up to two poorly contacting electrodes (Hartinger *et al* 2009). For instance, quantitative outcomes in lung-EIT applications could be considered. The DNN approach is seen as most promising as given its success in the more challenging measured tank experiment. Although these results are promising, the thorax experiment is only simulated and does not necessary imply this exact approach will work as well with patient data.

Approaches that may be needed to expand this approach to patient data are (1) further development of the perfusion model of the thorax simulation, (2) incorporating patient-specific information into the training of the DNN databases, and (3) incorporating more information into the DNN for LV volume prediction. Patient-specific information could include height and weight (or chest dimensions) and could potentially include heart size and LV volume recorded during controlled data collection (where at-home LV prediction would be the purpose of the device). Additionally, as surface or near surface conductivities strongly effect the overall measurements, a small database of simulated voltages from a sampling of skin and subcutaneous fat thicknesses can be used to select the best skin and fat thicknesses for the given patient. Lastly in terms of expanding the information provided to the DNN, a promising approach could be to give the DNN not the difference between two frames of data but a time-window of impedance data (e.g. 30 s), which is very similar to the approach used in Zifan and Liatsis (2012). The DNN can then automatically perform differencing of the data while being robust to bad electrodes—*thus reducing the restrictions on data filtering that is commonly needed in EIT applications*.

Other real-time methods could have been considered such as Calderón's method or the D-bar method (Muller *et al* 2017), the GREIT method (Adler *et al* 2009), or Gauss–Newton approaches with alternative regularization schemes. However, the computational cost of each method are similar (in the context of difference imaging), i.e. GREIT and Gauss–Newton approaches are $O(N_m N_{px})$, whereas Calderón's and D-bar are $O(N_{px}M^2)$ and $O(N_{px}M^2 \log(M))$ (Muller *et al* 2017), respectively, where N_m is the number of measurements, N_{px} is the number of pixels in the output image, and M is the number of points along an axis in the complex plane. One would expect M^2 to be on the same order as N_m. In the experience of the authors, GREIT and Gauss–Newton approaches are expected to have similar robustness to noise and Calderón's method (similar processing used in D-bar) has significant problems with partially contacting electrodes. Thus a full comparison of the robustness of multiple EIT reconstruction methods to partially contacting electrodes was deemed outside the scope of this study, i.e. evaluating the utility of ML algorithms in these scenarios.

5. Conclusion

A new imageless electrical impedance tomography, robust to poorly contacting electrodes, trained ML algorithm is described for portable cardiac output monitoring. EIT and ML approaches are evaluated on simulated and measured experiments. The ML algorithms generally perform comparably with the standard EIT approach to handling bad electrodes (removing them), but with the very strong advantage (ML) of not needing to know which electrodes are bad. This is a potential, significant advantage of the ML algorithms. In terms of ML algorithms, the rSVM was best in the simulated experiment, whereas the DNN was best in the measured tank experiment. Analysis of the computational cost shows that the DNN may be attractive as a method for the envisioned low-power, portable system because of its comparable computational and lower memory requirements. Overall, this work represents an important step in validation of the method using measured data, and model development, which is needed to apply this method to real clinical data.

Acknowledgment

This work was supported in part by the U.S. National Science Foundation, under Grant No. 1418497, the National Institutes of Health under Grant No. 5R01CA143020, and US DoD CDMRP Grant No. W81XWH-15-1-0571.

ORCID iDs

Ethan K Murphy https://orcid.org/0000-0002-4635-3384
Saaid H Arshad https://orcid.org/0000-0001-6506-357X

References

Adler A *et al* 2009 GREIT: a unified approach to 2D linear EIT reconstruction of lung images *Physiol. Meas.* **30** S35–55
Alhashemi J A, Cecconi M and Hofer C K 2011 Cardiac output monitoring: an integrative perspective *Crit. Care* **15** 214
Andreuccetti D, Fossi R and Petrucc C 2017 An Internet resource for the calculation of the dielectric properties of body tissues in the frequency range 10 Hz–100 GHz *IFAC-CNR* http://niremf.ifac.cnr.it/tissprop/htmlclie/htmlclie.php (Accessed: 20 November 2017)
Arshad S H, Kunzika J S, Murphy E K, Odame K and Halter R J 2015 Towards a smart phone-based cardiac monitoring device using electrical impedance tomography *IEEE BioCAS Conf. Proc. (22–24 October 2015)* (https://doi.org/10.1109/BioCAS.2015.7348452)
Asfaw Y and Adle A 2005 Automatic detection of detached and erroneous electrodes in electrical impedance tomography *Physiol. Meas.* **26** S175–83
Bergstra J S, Bardenet R, Bengio Y and Kégl B 2011 Algorithms for hyper-parameter optimization *Advances in Neural Information Processing Systems* pp 2546–54
Borsic A, Hartov A, Paulsen K D and Manwaring P 2008 3D electric impedance tomography reconstruction on multi-core computing platforms *Proc. Annu. Int. Conf. of the IEEE Engineering in Medicine and Biology Society* pp 1175–7
Boverman G, Isaacson D, Saulnier G J and Newell J C 2009 Methods for compensating for variable electrode contact in EIT *IEEE Trans. Biomed. Eng.* **56** 2762–72
Boyle A, Adler A and Lionheart W 2012 Shape deformation in two-dimensional electrical impedance tomography *IEEE Trans. Med. Imaging* **31** 2185–93
Braun F *et al* 2015 Aortic blood pressure measured via EIT: investigation of different measurement settings *Physiol. Meas.* **36** 1147–59
Burkardt J 2019 TET_MESH_QUALITY interactive program for tet mesh quality https://people.sc.fsu.edu/~jburkardt/m_src/tet_mesh_quality/tet_mesh_quality.html (Accessed: 12 February 2019)
Butler J, Chirovsky D, Phatak H, McNeil A and Cody R 2010 Renal function, health outcomes, and resource utilization in acute heart failure: a systematic review *Circ. Heart Fail.* **3** 726–45
Chaudhry S, Mattera J, Curtis J, Spertus J A and Herrin J 2010 Telemonitoring in patients with heart failure *New Engl. J. Med.* **363** 2301–9
Demidenko E, Borsic A, Hartov A, Wan Y and Halter R 2011 Statistical estimation of EIT electrode contact impedance using magic Toeplitz matrix *IEEE Trans. Bio-med. Eng.* **58** 2194–201
Fagerberg A, Stenqvist O and Aneman A 2009 Electrical impedance tomography applied to assess matching of pulmonary ventilation and perfusion in a porcine experimental model *Crit. Care* **13** R34
Geuzaine C and Remacle J F 2009 Gmsh: a 3D finite element mesh generator with built-in pre- and post-processing facilities *Int. J. Numer. Methods Eng.* **79** 1309–31
Hal M J, Levant S and DeFrances C J 2012 Hospitalization for congestive heart failure: United States, 2000–2010. NCHS data brief www.ncbi.nlm.nih.gov/pubmed/23102190
Hartinger A E, Guardo R, Adler A and Gagnon H 2009 Real-time management of faulty electrodes in electrical impedance tomography *IEEE Trans. Biomed. Eng.* **56** 369–77
Hasan A and Paul V 2011 Telemonitoring in chronic heart failure *Eur. Heart J.* **32** 1457–64
Heikkinen L M, Vilhunen T, West R M and Vauhkonen M 2002 Simultaneous reconstruction of electrode contact impedances and internal electrical properties: II. Laboratory experiments *Meas. Sci. Technol.* **13** 1855–61
Holder D 2005 *Electrical Impedance Tomography* (Bristol: Institute of Physics Publishing) (https://doi.org/10.1186/1475-925X-4-27)
Jeon M H, Khambampati A K, Kim B S, Kang S I and Kim K Y 2017 Image reconstruction in EIT with unreliable electrode data using random sample consensus method *Meas. Sci. Technol.* **28**
Kahn S, Manwaring P, Borsic A and Hlater R J 2015 FPGA-based voltage and current dual drive system for high frame rate electrical impedance tomography *IEEE Trans. Med. Imaging* **34** 888–901
Lionheart W R B 2004 EIT reconstruction algorithms: pitfalls, challenges and recent developments *Phys. Meas.* **25** 125–42
Liu A and Joe B 1994 Relationship between tetrahedron shape measures *Bit* **34** 268–87
Mamatjan Y, Gaggero P, Muller B, Grychtol B and Adler A 2013 Compensating electrode errors due to electrode detachment in electrical *Canadian Medical and Biological Engineering Society p* 36
Marik P E 2013 Noninvasive cardiac output monitors: a state-of the-art review *J. Cardiothoracic Vascular Anesthesia* **27** 121–34
Muller P A, Mueller J L and Mellenthin M M 2017 Real-time implementation of Calderns method on subject-specific domains *IEEE Trans. Med. Imaging* **36** 1868–75
Murphy E K and Mueller J L 2009 Effect of domain shape modeling and measurement errors on the 2D D-bar method for EIT *IEEE Trans. Med. Imaging* **28** 1576–84
Persson P-O and Strang G 2004 A simple mesh generator in MATLAB *SIAM Rev.* **46** 329–45
Pikkemaat R, Lundin S, Stenqvist O, Hilgers R-D and Leonhardt S 2014 Recent advances in and limitations of cardiac output monitoring by means of electrical impedance tomography *Anesthesia Analgesia* **119** 76–83
Purcell R, McInnes S and Halcomb E J 2014 Telemonitoring can assist in managing cardiovascular disease in primary care: a systematic review of systematic reviews *BMC Family Pract.* **15** 43
Rao A, Teng Y, Schaef C, Murphy E, Arshad S, Halter R and Odame K 2018 An analog front end ASIC for cardiac electrical impedance tomography *IEEE Trans. Biomed. Circuits Syst.* **12** 729–38
Schöberl J 1997 NETGEN an advancing front 2D/3D-mesh generator based on abstract rules *Comput. Vis. Sci.* **1** 41–52

Segars W P, Sturgeon G, Mendonca S, Grimes J and Tsui B M W 2010 4D XCAT phantom for multimodality imaging research *Med. Phys.* **37** 4902

Somersalo E, Cheney M and Isaacson D 1992 Existence and uniqueness for electrode models for electric current computed tomography *SIAM J. Appl. Math.* **52** 1023–40

Takhti M, Teng Y C and Odame K 2016 A high frequency read-out channel for bio-impedance measurement *Proc. IEEE Int. Symp. on Circuits and Systems* pp 1514–7

Vonk-Noordegraaf A, Marcus J T, Bronzwaer J G F, Postmus P E, Faes T J C and de Vries P 2000 Determination of stroke volume by means of electrical impedance tomography Determination of stroke volume by means of electrical impedance tomography *Physiol. Meas.* **21** 285–93

Zhang G, Dai M, Yang L, Li W, Li H, Xu C, Shi X, Dong X and Fu F 2017 Fast detection and data compensation for electrodes disconnection in long-term monitoring of dynamic brain electrical impedance tomography *Biomed. Eng. Online* **16** 1–23

Zifan A and Liatsis P 2012 Lungprints: an alternative view in multiple-stream time-series analysis of bioimpedance signals *19th Int. Conf. on Systems, Signals and Image Processing* pp 236–9

Phantom Studies of Fused-data TREIT using only Biopsy-probe electrodes

Ethan K. Murphy, Xiaotian Wu, Alicia Everitt, and Ryan J. Halter

***Abstract*—This study further develops fused-data transrectal electrical impedance tomography (fd-TREIT) for prostate cancer imaging by improving method robustness while evaluating the approach on challenging phantoms constrained to a clinical-like setup. The new approach incorporates 8 electrodes (in 2 rows) on a biopsy probe (BP) and 12 electrodes on the face of a transrectal ultrasound (TRUS) probe and includes a biopsy gun, instrument tracking, 3D-printed holder and guide, and the EIT hardware and software. The approach was evaluated via simulation, a series of prostate gel phantoms, and an ex vivo bovine sample. The simulation experiment surprisingly found that using only biopsy-probe measurements, i.e. omitting TRUS-probe measurements, significantly improves robustness to noise. This led to simpler modeling and consequently significant decreases in computational times (~13x speed-up, yielding reconstructions times of ~27 minutes). The gel phantom experiments resulted in reconstructions with area under the curve (AUC) values from receiver operator characteristic (ROC) curves of > 0.85 for 4 out of the 5 tests, and when incorporating inclusion boundaries resulted in absolute reconstructions yielding 1.9% and 12.2% average absolute percent errors for 3 consistent tests and all 5 tests, respectively. Furthermore, the ex vivo bovine test revealed qualitatively that the fd-TREIT approach can largely discriminate a complex adipose and muscle interface in a realistic setting using data from only 9 biopsy probe measurements. The algorithms developed here on these challenging phantoms suggest strong promise for this technology to aid in imaging during routine 12-core prostate biopsies.**

***Index Terms*— Data fusion, electrical impedance tomography, electrical impedance myography, inverse problem, bioimpedance.**

I. Introduction

Prostate cancer is a significant problem for men, affecting 1 in 7 while being the 2nd leading cause of cancer death for men [1].

In addition to challenges in accurately detecting prostate cancer, there is currently no clinical test or imaging modality able to accurately discriminate between aggressive and indolent prostate cancer [2]. The standard diagnosis for prostate cancer is a 12-core transrectal ultrasound (TRUS)-guided biopsy, which samples across the whole prostate – but can additionally sample lesions detected from multi-parametric magnetic resonance imaging (mpMRI). The gold-standard, TRUS-guided biopsies, miss 10%–30% of all cancers [3]. These low detection rates largely are a result of the small volume of tissue sampled during the biopsy procedures (typically <1% of the prostate volume) [4]. If imaging could be done around the biopsy probe (BP) during the biopsy procedure, then significantly more tissue could be effectively sampled – *potentially significantly reducing the number of missed cancers*. Further, if this imaging is sensitive to cancer grades, then accurate grading could be known prior to a potential surgical intervention, which could help reduce overtreatment in care for prostate cancer.

Numerous studies have found significant ($p<0.001$) electrical property contrast between benign and malignant prostate tissues ([5]–[8]) and more importantly significant electrical property differences between high- and low-grade cancer ([9]). The impedance grade discrimination capabilities were significantly better than standard of care TRUS-guided biopsy procedures, and similar to that reported for MRI-based alternatives (the most promising techniques) [10]–[13]. From these studies and leveraging electrical impedance tomography (EIT), a technique called transrectal EIT (TREIT) has been established ([14]); this study continues its development. EIT aims to reconstruct 3D conductivity (and permittivity) distributions from sets of voltages measured from injected current patterns on electrodes that lie on the boundary of the domain. In the TREIT application with BP there are electrodes that are placed around the BP and TRUS probe. In particular this study further developed fused data TREIT (fd-TREIT) from [15] by 1) adding a second row of 4 electrodes (8 total on the BP), 2) incorporating the biopsy gun using a 12-core protocol, and 3) utilizing a sensitivity-based method to determine the imaging region (overcoming a significant problem from [15]). Three sets of experiments were run: 1) simulation tests evaluating robustness to noise, 2) gel prostate phantoms testing realistic conductivity contrasts, and 3) an ex vivo bovine test providing a challenging complex adipose/muscle interface to image. The simulation experiment surprisingly found that using only measurements from the BP significantly reduced sensitivity to noise, which has the bonus effect of simplifying the modeling and significantly speeding up computational times. The gel phantom experiments resulted

Copyright (c) 2010 IEEE. Personal use of this material is permitted. However, permission to use this material for any other purposes must be obtained from the IEEE by sending a request to pubs-permissions@ieee.org.

This work was supported in part by the U.S. National Institutes of Health under Grant 1R01CA143020–01A1 and DoD Congressionally Directed Medical Research Program under Grant W81XWH-15-1-0102.

*E. K. Murphy and A. C. Everitt are with the Thayer School of Engineering, Dartmouth College, Hanover, NH 03755, USA (email: ethan.k.murphy@dartmouth.edu).

X. Wu is with the Gordon Center for Medical Imaging at Massachusetts General Hospital and Harvard Medical School, Boston, MA 02114 USA (e-mail: xwu23@mgh.harvard.edu).R. J. Halter is affiliated with the Thayer School of Engineering and Geisel School of Medicine at Dartmouth College, Hanover, NH 03755 USA (e-mail: ryan.halter@dartmouth.edu).

in reconstructions with area under the curve (AUC) values from receiver operator characteristic (ROC) analysis of > 0.85 for 4 out of the 5 tests, and when incorporating inclusion boundaries into the inverse problem resulted in absolute reconstructions (after a scalar fit across the tests) yielding 1.9% and 12.2% average absolute percent errors for 3 consistent tests and all 5 tests, respectively. This shows very impressive accuracy, while still revealing that approaches to account for noise/artifacts need to be addressed. Lastly, the ex vivo bovine test revealed that qualitatively the fd-TREIT approach can largely discriminate adipose and muscle tissue; quantitatively the AUC was 0.69.

The paper is structured as follows: Section II describes the fd-TREIT system, the forward and inverse EIT problems, data collection, registration and segmentation details, and the experiments. Section III describes the results of the simulation study, gel and ex vivo bovine phantoms, computational times, and registration errors. Section IV discusses the impact of these results and approaches to further improve them.

II. Methods

A. *Fused-data TREIT System*

The TREIT system consists of 1) a 20 electrode array wrapped around the face of the Phillips C9-EC TRUS probe (Fig. 1D) and 8 electrodes wrapped around an 18 gauge BP (Remington Medical NAC-1820 ULTRA Biopsy Needle) (Fig. 1C) which then connects to our custom EIT system ([16]), 2) a TRUS probe (Fig. 1A-B) with a Pro-Mag Ultra biopsy instrument (gun) mounted on its side, and 3) an Aurora V2 EM tracking system (Northern Digital Inc., Ontario, Canada, Fig. 1A) with 1 x 5 mm six degree-of-freedom EM trackers (Fig. 1A-B). The TRUS-electrodes are sonolucent and all electrodes are gold-plated on a flexible polyamide substrate. Further details of the BP electrodes are given in [17]. A needle guide (Fig. 1B) is attached to the end of the TRUS probe, ensuring consistent firing directions, which has an EM tracker encased within it. The TRUS-probe holder, needle guide, and BP mounting bracket (Fig. 1E) were produced using a Form 2 Formlabs 3D printer.

The TRUS probe was registered to EM-space by recording the location of 5 known points on the TRUS probe (magenta dots in Fig. 1B&D) using a registered EM-tracked pointer (Fig. 1A). The BP electrodes were registered by pointing to each electrode in each row to estimate the row center locations. Since the BP was in a fixed position relative to the TRUS probe, a tracker for the BP was unnecessary. All tracking data, i.e. tracker states, in the form of Cartesian 3D coordinates (translation) and quaternions (orientation) were acquired via serial communication with the Aurora system in MATLAB. The effective position accuracy of the EM tracker has a standard deviation of 0.39 mm ([15]). The errors in BP and TRUS registration should be smaller due to averaging over 4 and 5 points, respectively.

Voltage Measurements. The EIT system records frames of voltage data from the TRUS and BP electrodes at each biopsy-core state. We refer to each measurement as an IIVV pattern where II represents the current injection electrode pair (I1,I2) and VV represents the differential voltage sensing pair of electrodes (V1,V2). Subsets of BP-only patterns and BP+TRUS patterns are investigated. The subsets were chosen to be patterns that heuristically should provide good signal. The BP-only patterns consisted of 1) the four patterns of top-only and bottom-only patterns (n=8) and 2) patterns with the source and sink electrodes on different rows and the voltage difference electrodes also on different rows (n=584). The TRUS+BP patterns included all BP-only patterns and included patterns where the sink and source current electrodes consisted of one on the BP and one on the TRUS and similarly for the voltage difference electrodes (n=3760). Since our current EIT system only has 20 channels, these patterns used only 12 of the 20 TRUS electrodes (see Fig. 1D) and all 8 BP electrodes. A noise filter was used (see [15]) to remove noisy patterns. The average standard deviations from these good patterns for the experiments were 0.51, 0.29, 0.22, and 0.20 mV for 10, 20, 40, and 80 kHz, respectively, corresponding to an average injected current of ~0.6 mA across all frequencies.

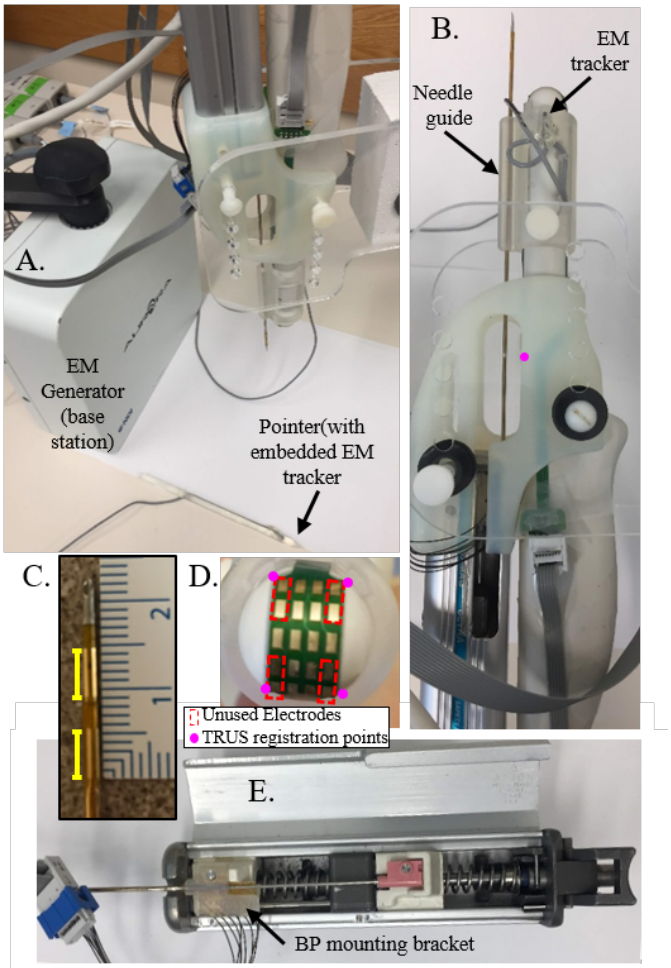

Fig. 1. A. The Phillips C9-EC transrectal ultrasound probe in holder and stand with attached biopsy gun and EM generator and pointer, B. side view of the needle guide and tracker, C. BP electrodes, D. TRUS electrodes, and E. the opened biopsy gun showing mounting assembly.

B. *EIT Image Reconstruction*

1) *Forward Problem*

The forward problem computes the electric potential within the domain and the electrode voltages on the boundary given a specified injected current on boundary electrodes. The

complete electrode model (CEM) is used [18], based on a 3D finite element method (FEM) implementation [19]. The CEM realistically accounts for the contact impedance and shunting of electrodes. The US/EIT geometry is an open domain geometry, which is accurately modeled by expanding the modeled domain so that effectively no current flows near the open boundaries. 3D FEM meshes were constructed in Gmsh ([20]) that modeled 1) the TRUS electrodes and BP electrodes (Fig. 2A, 1.0M nodes, 6.1M elements) and 2) the BP-electrodes only (Fig. 2B-C, 225k nodes, and 1M elements).

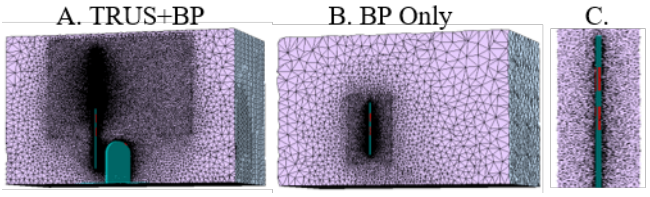

Fig. 2. A. TRUS+BP and BP-only meshes, which have high density of nodes near electrodes. C shows a zoom-in of the BP electrodes.

2) Inverse Problem

The inverse problem is solved with a Gauss-Newton algorithm that fuses data from N_S states and employs Laplace-smoothing Tikhonov regularization (initially described in [21]). After a linearization step ([22]) the error to be minimized, $E(\delta\boldsymbol{\sigma})$, is

$$\boldsymbol{E(\delta\sigma)} = \sum_{n=1}^{N_S} \|\mathbf{J}_n\boldsymbol{\delta\sigma} - \Delta\boldsymbol{v}_n\|_2^2 + \lambda\|\mathbf{L}(\boldsymbol{\sigma}_0 + \boldsymbol{\delta\sigma})\|_2^2, \quad (1)$$

where $\boldsymbol{\delta\sigma}$ is the conductivity update, $\boldsymbol{\sigma}_0$ is an initial estimate, $\mathbf{J}_n$ is the Jacobian corresponding to the nth state, $\Delta\boldsymbol{v}_n$ is the voltage difference (between measured and simulated) of the nth state, $\mathbf{L}$ is the regularization matrix, and λ is the Tikhonov regularization factor. The Jacobian $\mathbf{J}_n$ is size $N_P \times N_{rN}$, where N_P is the number of measurement patterns and N_{rN} is the number of reconstruction nodes. The least squares solution to (1) is

$$\boldsymbol{\delta\tilde{\sigma}} = (\mathbf{J}_{FD}^T\mathbf{J}_{FD} + \lambda\mathbf{L}^T\mathbf{L})^{-1}(\mathbf{J}_{FD}^T\Delta\boldsymbol{v}_{FD} - \lambda\mathbf{L}^T\mathbf{L}\boldsymbol{\sigma}_0). \quad (2)$$

where $\mathbf{J}_{FD}$ and $\Delta\boldsymbol{v}_{FD}$ are concatenated matrices and vectors from all the states. The updated estimate of the conductivity is $\tilde{\boldsymbol{\sigma}}_1 = \boldsymbol{\sigma}_0 + \beta\boldsymbol{\delta\tilde{\sigma}}$, where β is chosen using a parabolic line-search algorithm [23]. The process is iterated to obtain an absolute reconstruction of the conductivity distribution.

Dual Mesh. The algorithm performs 3D reconstructions utilizing the dual-mesh method [23], which allows one to solve the Jacobian on a FEM mesh while estimating the conductivity on a different *reconstruction* mesh. This permits the measurements from each state to be associated to one fixed region for reconstruction. The mapping for each state n is defined by a matrix $\mathbf{P}_n$ of size $N_{fN}\times N_{rN}$ where N_{fN} is the number of nodes in the FEM mesh. The mapping is constructed in three steps. The first step is to calculate the following

$$(\mathbf{P}_n)_{i,j} = \begin{cases} \frac{1}{\|X_i^{fN} - X_j^{rN}\|}, & \text{if } i = arg\min_{k=1\ldots N_{fN}} \|X_k^{fN} - X_j^{rN}\| \\ 0 & \text{otherwise.} \end{cases} \quad (3)$$

which is a matrix that assigns the closest FEM node to each reconstruction node, weighted by the inverse distance (the closer the distance the higher the weight). Secondly, we scale each row that has associated reconstruction nodes to sum to one. Third, any unassociated FEM nodes are associated to the closest reconstruction node. This particular mapping strategy was very helpful in combining reconstruction meshes with FEM meshes with highly variable node density. The mapping is illustrated in a 2D example with high density near the needle at two states (Fig. 3A-D). The primary case of multiple reconstruction nodes (magenta) associated with a FEM node (black) is shown in Fig. 3E, whereas the alternative where a FEM node was unassociated is shown in Fig. 3F.

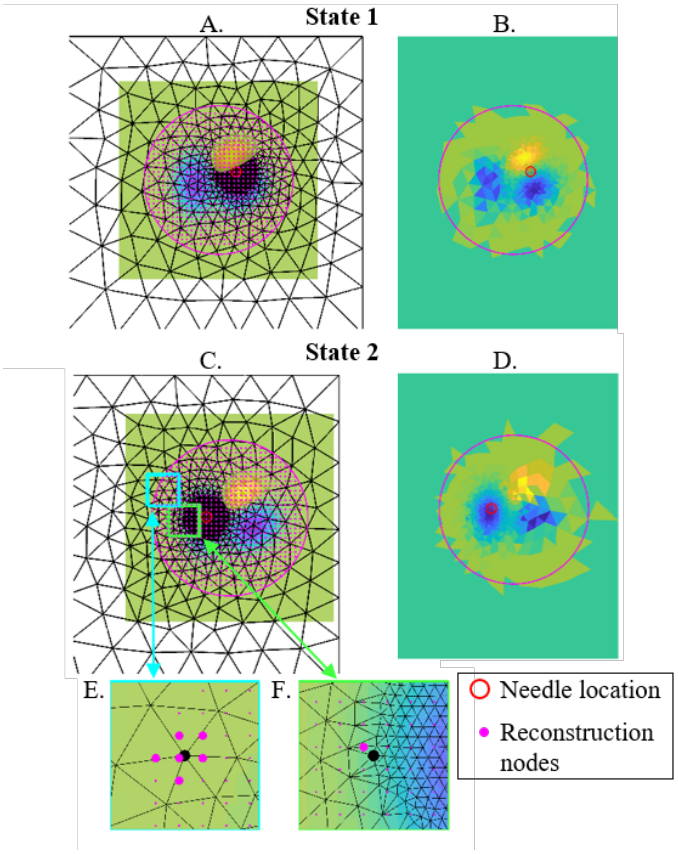

Fig. 3. Illustration of FEM mesh, reconstruction grid (magenta circle and dots), and true conductivity distribution (three Gaussians) at two states (A and C) and the resulting discrete conductivity mapped from reconstruction grid to the FEM mesh (B and D). The FEM mesh has high density near the needle (red circle), which yields an accurate mapping in this high sensitivity region around the needle. Zoomed in views shows multiple reconstruction nodes (magenta) associated with a FEM node (black) (E) and a case where a FEM node was unassociated and therefore mapped to the closest reconstruction node (F). The mapping of the mega-node yields a constant conductivity outside the reconstruction region.

Open Domain. The open domain/local regions of sensitivity are modeled with the aid of a mega-node (MN), which consists of all FEM nodes outside of a prescribed region of interest (ROI), see Fig 4. This ROI includes the region that heuristically has sufficient sensitivity to produce spatially varying

conductivity images and a transition zone to allow for transition to the MN without affecting the inner conductivity values. We use a sensitivity-based technique described in [24] to form a joint ROI from each individual state. That is, for a given state form a ROI by finding all nodes that have a sensitivity, defined by,

$$s_j = \max_{i=1\ldots N_P} \left| (\mathbf{J}_0)_{ij} / \left(\mathbf{v}_{sim}(\sigma_0)\right)_i \right| \quad (4)$$

which is over a tolerance S_0. In (4) $\mathbf{J}_0$ is an untransformed Jacobian, $\mathbf{v}_{sim}(\sigma_0)$ is the simulated voltages, and the vale s_j can be interpreted as the maximum boundary voltage percent change caused by a perturbation from the jth reconstruction node. The convex hull of all the individual ROIs is used as the full ROI. This is illustrated in a 3-state example (Fig. 4) for S_0 = 1/1000 where the red region represents the ROI from a single state and the blue region shows the combined ROI. The TRUS and needle are cyan and the prostate is shown in green.

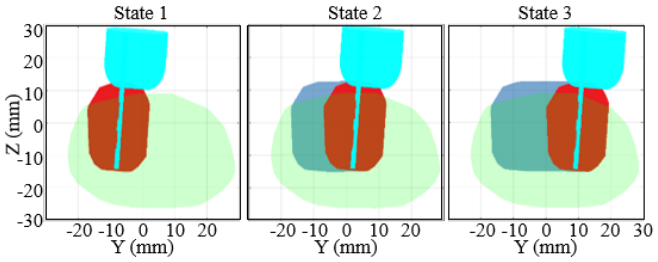

Fig. 4. Illustration of a 3-state example of the fd-TREIT ROI (blue region) that results by combining the sensitivity-based ROI from each state (red region) via a convex hull. The sensitivity tolerance used was S_0 = 1/1000, the TRUS and needle are cyan, and the prostate is shown in green.

Soft-prior regularization. The soft-prior regularization is encoded within a Laplace smoothing regularization approach as was done in [25]. The Laplace regularization essentially connects adjacent nodes (Fig. 5), and the soft-prior information is encoded by removing connections that cross the boundaries. For example in Fig. 5, the prostate and tumor boundaries are encoded within a 2D reconstruction mesh (red dots are nodes, black line segments are connections). Specifically, this study encodes the main boundary (gel prostate or ex vivo bovine) into the regularization, referred to as B-SR (Boundary-Soft-prior Regularization), or encodes both the boundary and inclusions (for gel prostate experiments), referred to as I+B-SR (see Fig. 5). A background/saline and prostate mega-node are used to model the conductivity outside the region of sensitivity (green region). Although not illustrated, the mega-nodes are connected via the Laplace smoothing to boundary nodes of the ROI.

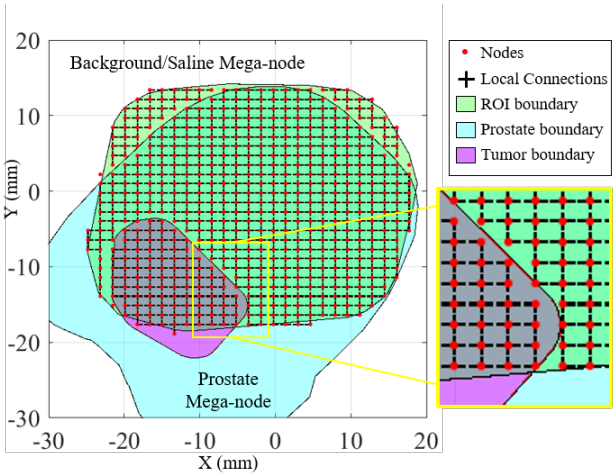

Fig. 5. 2D illustration of Laplace smoothing regularization and soft-priors encoding of a tumor (magenta) and prostate (cyan).

C. Data Collection, Registration, and Segmentation

The experiments were performed in a saline-filled tank where the gel phantom or ex vivo bovine was held fixed between two plastic rigs with thin thread (see Fig. 6A). For each state the TREIT probe, which was held at a fixed height with a stand, was slid to a chosen location wherein the biopsy gun was fired sending the BP into the sample. At this time 1) 3 frames of EIT data, 2) an US image, and 3) EM-tracker data was recorded. This process was performed 12 and 9 times for the gel and ex vivo bovine phantoms, respectively.

After this data was recorded, EM-registration and validation data was then collected. The registration data were 16 points. On the top rig, the stylet was placed into 8 holes (used for thread, see Fig. 6A), and the stylet was placed at 8 equally spaced points on the bottom rig (an angle to place the stylet in the hole was not possible). Additionally, 16 validation points were recorded at the intersection of each thread, which coincides with the top surface of the sample.

Finally the rig was removed from the large tank, placed into a small tank, and imaged with a Phillips 3T MRI (Fig. 6B). The MR image was then segmented yielding the 1) top and bottom rig holes, 2) sample boundary, and 3) (if applicable) inclusion boundaries via a custom Matlab GUI (Fig. 6B-C).

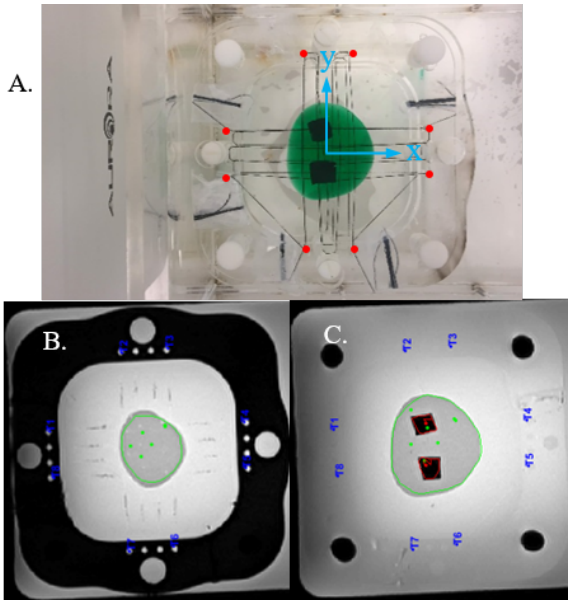

Fig. 6. Illustration of rig (A), top-rig registration points (red dots), and inverse (problem) frame (light blue) for a gel prostate phantom with corresponding MR image (B-C) showing the segmented prostate (green lines) and tumor boundaries (red lines) and the top-rig registration points (blue).

We chose to perform the reconstructions in a frame, referred to as the inverse frame (IF), that was centered on the sample (calculated as the mean of the 16 registration rig points) with x and y axes aligned with the vertical and horizontal registration points from Fig. 2A and the z-axis coming out of the page. Points in the EM frame, $\boldsymbol{p}_{EM}$, are converted to the inverse frame by the following

$$\mathbf{p}_{IF} = \mathbf{R}_{EM}^{IF}(\mathbf{p}_{EM} - \mathbf{c}_{EM}) \quad (1)$$

where $\mathbf{R}_{EM}^{IF}$ is a rotation matrix from the EM to IF frame and $\mathbf{c}_{EM}$ is the center in the EM frame. Then the MR-registration points are aligned with the EM-registration points in the IF frame by aligning frames and matching centers. The frame alignment is performed by finding orthonormal vectors defining x-, and y-, and z-axes as in Fig. 6A for rig points in the IF frame, and MR frame and constructing the following rotation matrix

$$\mathbf{R}_{\boldsymbol{MR}}^{\boldsymbol{IF}} = [\mathbf{u}_{x,IF} \quad \mathbf{u}_{y,IF} \quad \mathbf{u}_{z,IF}][\mathbf{u}_{x,MR} \quad \mathbf{u}_{y,MR} \quad \mathbf{u}_{z,MR}]^T \quad (2)$$

which converts from the MR frame to the natural basis and then to the IF frame. At this point two metrics are calculated: 1) average difference between MR and EM rig points in the IF frame, and 2) average error between the EM-top sample points and MR-sample boundary surface.

Mesh Transformations. Based on the TRUS/mesh registration a mesh-to-TRUS mapping is constructed, $\mathbf{T}_{msh}^{TRUS}$, which is a 4x4 matrix that includes a rotation matrix and translation vector, assuming homogeneous points are applied to the mapping. Further the TRUS tracker yields a transformation from the TRUS-tracker to the EM frame, $\mathbf{T}_{TRUS}^{EM}$. Thus to transform the mesh points, $\mathbf{p}_{msh}$, to the IF frame the following steps are performed

$$\mathbf{p}_{IF} = \mathbf{R}_{EM}^{IF}(\mathbf{D}\mathbf{T}_{TRUS}^{EM}\mathbf{T}_{msh}^{TRUS}[\mathbf{p}_{msh}^{T} \quad 1]^T - \mathbf{c}_{EM}) \quad (1)$$

where $\mathbf{D}$ is a matrix that converts from homogeneous (4xn) to standard points (3xn).

D. Experiments

Three sets of experiments were performed that used simulation, gel phantoms, and ex vivo bovine phantoms to evaluate the approach and determine its feasibility.

1) Simulation Study: The simulation study was used to evaluate the sensitivity of the choice of ROI size and the choice of IIVV patterns due to variability and bias in the prostate position and variability in the voltage measurements. The parameters of the study are listed in Table I. For each error type and modeling choice 50 random samples were drawn and 5-step absolute reconstructions were calculated assuming the scenario of the first gel prostate experiment (see Table II, there are two inclusions) using the B-SR approach. The metrics used are position error, radius error, background standard deviation, and number of reconstructed inclusions. The inclusions were detected as pixels greater than 0.7 of the maximum and connected regions were separated as different reconstructed inclusions. The background was determined to be pixels that were < 0.5 of the maximum. The radius of each inclusion was calculated as the radius that results from a sphere with equal volume to the reconstructed inclusion.

Table I. Simulation Study Parameters

Model Approach	Values
ROI tolerances	1/50, 1/100, 1/250, 1/500, 1/1000, Whole prostate
IIVV patterns	BP-only or BP+TRUS
Error Type	Standard Deviations
Bias registration position	0.5 to 3.0 in 0.5 mm steps
Noise in state position	0.5 to 3.0 in 0.5 mm steps
Variability in voltage	0.2, 0.5, 1.0, 2.5, 5, 10%

2) Gel Prostate Phantom Study: This study included five gelatin prostates (Table II) each with two inclusions of various separation distances, volumes, and conductivities. The conductivities were obtained by using test cells of the gels (4 cm long block with cross-sectional side of 2 cm x 2 cm) that were measured using an impedance analyzer (HP4284A).

The gelatin prostates (Fig. 6A) were constructed using a silicone prostate mold, saline of a specified conductivity, and 10% gelatin (Sigma Aldrich, gel strength 300). The inclusions were made prior to the prostate using the same saline/gelatin ratio but with different saline conductivity and with an addition of 1-5% graphite powder. The inclusions were suspended in the prostate mold with a thin thread. The prostate liquid-gelatin was added after cooling to approximately 30° C to minimize melting of the inclusions. Although the conductivity values are different from expected prostate tissues, the contrast for test 1 (26%) and 4 (22%) are similar, i.e. there is a 11% and 26% contrast between cancerous tissue and glandular or stromal tissue, respectively [26].

The 12-core biopsy TREIT experiments were performed for each prostate. As the inclusions were visible, biopsy locations were chosen to ensure the inclusions and surrounding areas

were sampled. Anecdotally, the sampled locations were near best-case locations. Five-step absolute reconstructions were performed using both B-SR and I+B-SR approaches. B-SR and I+B-SR images were analyzed qualitatively and quantitatively. The B-SR results were quantified by analyzing ROC curves using three choices of thresholds; 1) optimal for each test (nearest 2-norm point to 100% sensitivity and 100% specificity, 2) best specificity with 100% sensitivity, and 3) a heuristic best threshold across all tests. This analysis assumes the inclusion pixels essentially correspond to a tumor, which should result in a positive test. The I+B-SR results were analyzed quantitatively by investigating average values of the inclusion, benign prostate region, and the contrast (inclusion-to-benign contrast).

Table II. Phantom Study Parameters

Test	1	2	3	4	5
Inc. Sep. (cm)	1.87	1.70	1.66	2.21	1.83
Inc. Vol. (cm^3)	1.1, 1.1	0.8, 0.9	1.4, 1.2	1.0, 1.1	1.3, 1.0
Prost. Vol. (cm^3)	45.2	48.9	47.8	44.8	48.8
Inc. Cond. (S/m)	0.40	0.38	0.41	0.34	0.59
Prost. Cond. (S/m)	0.32	0.23	0.28	0.28	0.27
Inc. Cond ratio	1.26	1.65	1.49	1.22	2.17

3) Ex vivo Bovine Phantom Study: The experiment involved a 9-core biopsy TREIT experiment on a sample of ex vivo bovine tissue (never frozen) with a large adipose section crossing diagonally through the ROI (Fig. 7). The biopsy sites coincided with the centers of the grids formed by the threads holding the tissue sample. The sample was ~3 cm thick, which resulted in all 8 electrodes falling within the tissue after firing. Only five-step, absolute B-SR reconstructions were performed. Results were analyzed similar to the B-SR gel prostate experiments. Quantitative thresholds were chosen as follows 1) optimal, 2) best specificity with 100% sensitivity, and 3) a heuristic-threshold qualitatively chosen based on contour plots. The sensitivity and specificity were calculated relating adipose tissue to a positive test, i.e. to the inclusion/tumor from the gel prostate experiments.

Fig. 7. Photo of the ex vivo bovine sample. The white is adipose tissue, pink is the muscle, and the 9 squares created by the crossing thread were used as the approximate BP insertion sites.

E. Additional Parameters

In all experiments the saline was approximately 0.1 S/m, and in all measured reconstructions a saline calibration step was performed after noise filtering ([27]). A Tikhonov value of 1×10^5 was heuristically determined through visual evaluation of reconstructions. All reconstructions only used the real-part of the data, producing conductivity-only images.

III. Results

A. Simulation Study

Selected results of the simulation study (Fig. 8) show box and whisker plots from the 50 samples (25-75% quantiles) of the position error and number of reconstructed inclusions (should be 2) due to position bias and variability errors using BP-only and TRUS and BP measurement patterns and ROI tolerances from 1/50 to 1/1000 and also the whole prostate. All simulation results are given in S.I Fig. 1. The most striking observation is that TRUS+BP patterns result in overall higher errors and a wider spread in the number of reconstructed inclusions. Implying that BP-only patterns are substantially more robust to noise.

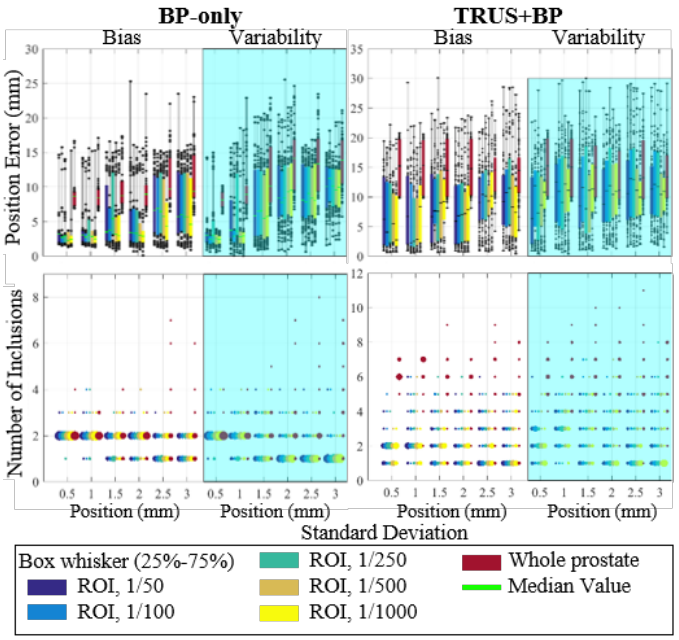

Fig. 8. Box and whisker plots (25-75% quantiles) corresponding to 50 reconstructions of the position error and number of reconstructed inclusion (should be 2) due to position bias and variability errors using BP-only and TRUS+BP measurement patterns and ROI tolerances from 1/50 to 1/1000 and also the whole prostate. The significantly larger noise using TRUS+BP patterns imply BP-only patterns are substantially more robust to noise – i.e. *the preferred patterns to use*.

One can see that choosing the ROI as the whole prostate (red box in Fig. 7) results in higher errors compared to other ROI tolerances. However, the choice of the best ROI tolerance is less clear. In numerous cases an ROI tolerance of 1/1000 looks best (either lowest error or near lowest with smallest variations), but it is not always the best. Additionally, the change of the ROI appears to mainly have a small effect. Based on these simulation results the remaining reconstructions are performed using the BP-only patterns and the ROI tolerances are analyzed further.

B. Gel Prostate Phantom Experiments

In order to determine a best ROI to use on the measured phantom experiments, 5-step absolute reconstructions were performed using B-SR approach with ROI tolerances of 1/50 to 1/1000 and AUCs were calculated (Fig. 9). Results are similar to the simulation results, in that there is no clear-cut best. Technically, 1/1000 is the maximum with an average AUC of

0.855 over the five gel samples, but 1/250 and 1/500 result in very close values of 0.847 and 0.849, respectively. Therefore, we considered these results to be roughly equivalent and present ROI tolerance results corresponding to 1/500, as these qualitatively appeared best.

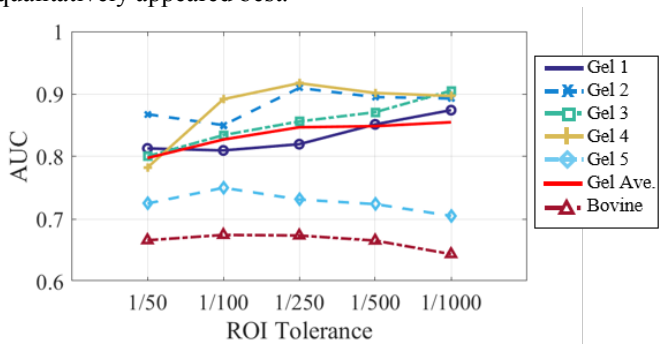

Fig. 9. Area under the ROC curves (AUC) for each gel test, the average gel test AUCs, and bovine test versus the ROI tolerances considered.

Three slices of absolute reconstructions using BP-only electrodes and an ROI tolerance of 1/500 for B-SR (Fig. 10) and I+B-SR (Fig. 11) for gel tests 3-5 illustrate the quality of the reconstructions at 40 kHz. Reconstructions of all gel tests using B-SR and I+B-SR with slices covering the whole prostate are shown in S.II (Figs 2-3). The two inclusions appear merged in tests 3 and 5 using B-SR (Fig. 10) likely due to the inclusions' separation distance, when the inclusions were further separated (test 4) the two inclusions are roughly differentiated (via the optimal threshold). Quantitative analysis of the B-SR reconstructions (Table III) reveal 1) impressive AUCs for tests 1-4 (> 0.85), 2) relatively low specificity (max of 59%) when sensitivity is fixed at 100%, and 3) comparable heuristic tolerance results except for test 4. The heuristic tolerance uses a fixed threshold, which is the average optimal tolerance for tests 1, 2, 3 & 5 and equal to 0.86 of the maximum from the reconstruction.

In the planned application to cancer detection, the sensitivity gives the percent of cancer detected correctly, which should be 100% so no cancer would remain after a surgery. Thus from Table III the results declare 62%, 41%, 49%, 52%, and 95% of the benign tissue cancerous – clearly significant portions of the benign regions.

The ROIs covered 66%, 58%, 56%, 58%, and 67% of the prostate volume for the 5 prostate tests, respectively, which have total prostate volumes (Table II) similar to real prostates. Although ideally 100% of the prostate is imaged, this approach (fd-TREIT with sensitivity-based ROI) covers a substantial portion of the prostate andis much larger than the tissue volume sampled at present (< 1% prostate volume).

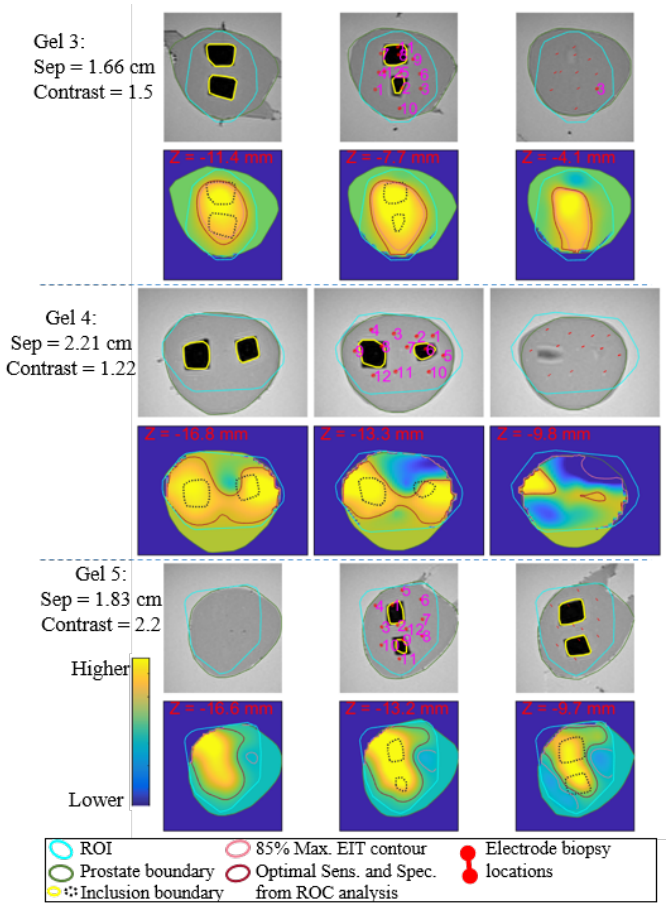

Fig. 10. Absolute reconstructions (5-step) using B-SR with an ROI of 1/500 (cyan) for gel tests 3-5 at 40 kHz. The prostate (green) and inclusions (yellow or black) are clearly seen in the MR images (top row of each test) with overlaid biopsy positions and the EIT images (bottom rows) show contours of 85% max and optimal (ROC curve).

Table III. Phantom and Ex vivo Bovine ROC Results, showing sensitivity (sens.) and specificity (spec.) for several approaches.

Test	1	2	3	4	5	Bovine
AUC	0.85	0.90	0.87	0.90	0.72	0.67
Opt. Sens.	0.77	0.87	0.80	0.88	0.67	0.59
Opt. Spec.	0.78	0.78	0.77	0.79	0.72	0.67
Opt. Tol. Frac.	0.87	0.85	0.86	0.98	0.65	0.33
Best Spec. with 100% Sens.	0.38	0.59	0.51	0.48	0.05	0.10
Heuristic Sens.	0.86	0.87	0.84	1.00	0.56	0.29
Heuristic Spec.	0.67	0.77	0.73	0.08	0.80	0.93

The I+B-SR results assume that the inclusion boundary is known. Consequently, the reconstructions in Fig. 11 should ideally have uniform yellow (high conductivity) within the inclusions and uniform blue/blue-green in the benign region. Gels 3 & 4 mostly follow this expectation, except for a small blue artifact towards the top of Gel 3 and a blue artifact at the top right of 4. These are likely related to small errors in the segmentation of the prostate or state of the biopsy electrodes. The uniformity assumption in Gel 5 reveals a large error. This could be a combination of two likely issues; state 5 top center biopsy appeared to have electrodes on the prostate boundary. As the exact location is not known we removed the state from

the reconstruction, and states 1 and 2 appear to have just grazed the tumor. In effect, the location of the states appear that they would have trouble differentiating the boundary of the inclusions and this (sensitivity to sample locations) is a current limitation of the method.

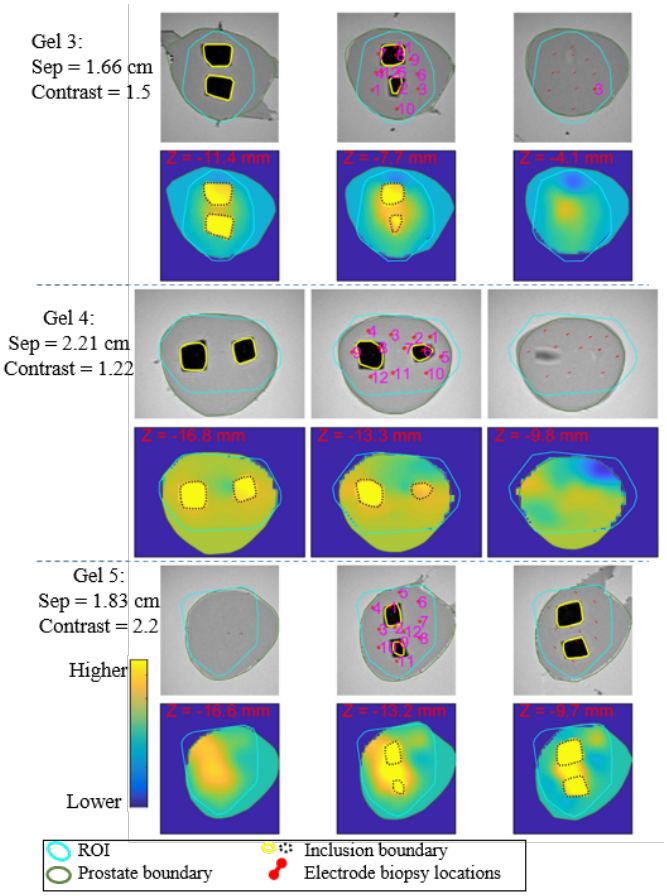

Fig. 11. Absolute reconstructions (5-step) using I+B-SR with an ROI of 1/500 (cyan) for gel tests 3-5 at 40 kHz. The prostate (green) and inclusions (yellow or black) are clearly seen in the MR images (top row of each test) with overlaid biopsy positions and the EIT images (bottom rows).

Quantitatively, Fig. 12A shows the average values in the prostate (omitting inclusion) and inclusion values corresponding to the I+B-SR EIT reconstructions and the test cell measurements for all five gel tests across the frequencies 10, 20, 40, 80 kHz from left to right. There was some unintentional variability with the prostate gelatin conductivity. Thus contrasts (Fig. 12B) were used to more clearly illustrate the quality of the reconstructions. Important to note, a single scalar factor (1.11) was applied to the EIT contrast ratio across all tests to produce Fig. 12B. The value chosen provided an overall best fit for tests 1, 3, and 4. The average absolute percent errors in contrast were 10.0% and 19.9% for tests 1,3,4 and tests 1-5, respectively, without the scaling factor, and were 1.9% and 12.2% for tests 1,3,4 and tests 1-5, respectively, with the scaling factor.

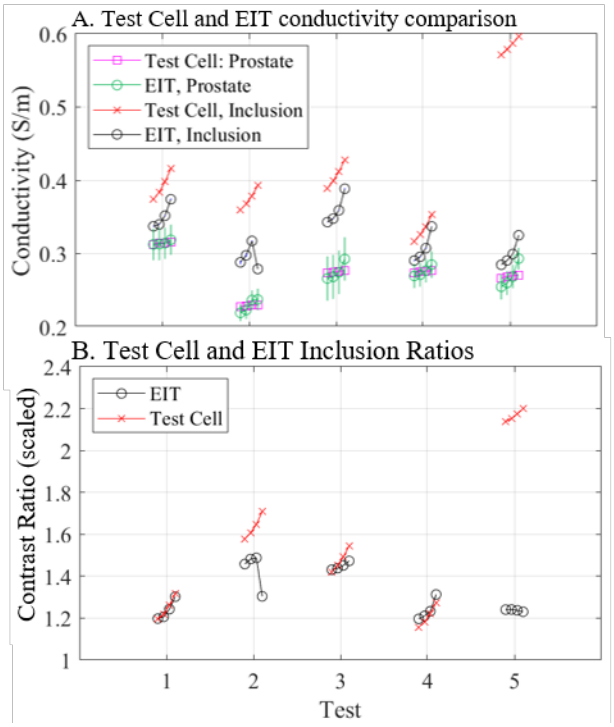

Fig. 12. A. Test cell and average EIT conductivity values for the (benign) prostate and inclusions for all five gel experiments where the 4 points for each test are results at 10, 20, 40, and 80 kHz, and B. scaled contrast (inclusion-to-prostate) ratios. A scaling factor of 1.11 was used, which was calculated as a best-fit for tests 1, 3, and 4.

C. Ex Vivo Bovine Experiment

Four slices from the X/Y-, X/Z-, and Y/Z-planes of the absolute reconstruction using BP-only electrodes and an ROI of 1/500 for B-SR (Fig. 13) reveal the quality of the ex vivo bovine results. A heuristically chosen threshold yields a contour that roughly separates large portions of adipose and muscle tissue. Quantitatively, the AUCs from all ROI tolerances (Fig. 9) reveal a low sensitivity to the ROI choice, and Table III summarizes the AUC (0.67), sensitivity and specificity values for ROI tolerance of 1/500. The adipose tissue was equated with a positive test. The interface between the adipose and muscle tissue is complex and given that the EIT had no information as to its delineation, this reconstruction is seen as a very good EIT reconstruction.

D. Computational Cost/Time

The mesh sizes and computational times show that using the BP-only mesh allows for accurate modeling with 10x less nodes, yielding ~10x speed-up in the forward solution, and 13x speed-up in the overall inverse problem calculation (assuming 5-steps, 12 states and an ROI tolerance of 1/500). These computations utilized 1) Thayer's Linux servers, which have 40, 2.4 GHz processors with 256 GB of RAM total, 2) an optimized EIT toolbox [19], and 3) parfor in Matlab to run the forward and Jacobian calculations in parallel.

Table IV. Computational Times

Mesh	BP-only	TRUS+BP
Number nodes	225k	1M
Number elements	1.2M	6.2M
Forward calculation	55 sec	9.2 min
5-step abs. recon, 12 states	27.6 min	~6 hours

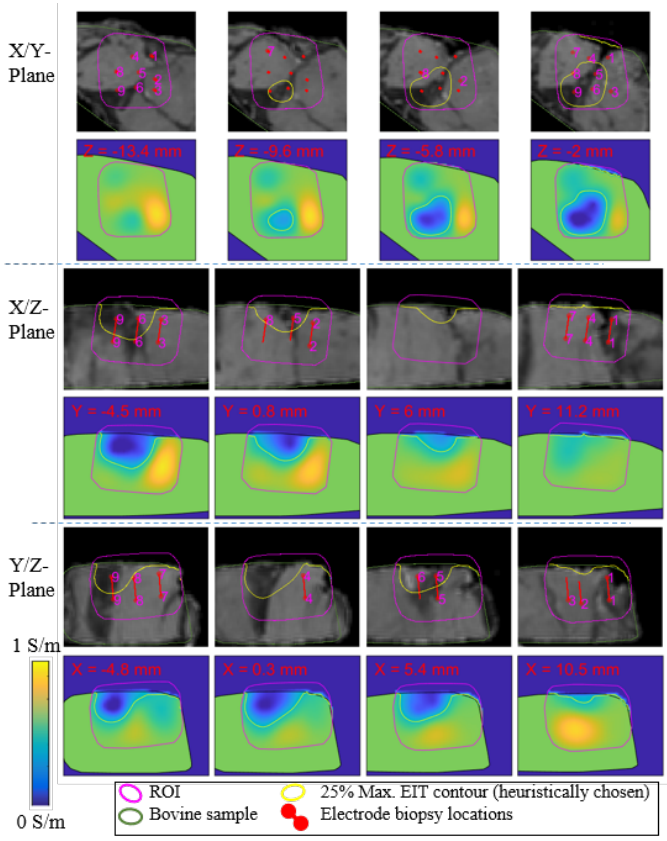

Fig. 13. Absolute reconstruction (5-step) using B-SR with an ROI of 1/500 (magenta) for the ex vivo bovine experiment. The bovine sample (green) and muscle/adipose tissue are clearly seen in the MR images (top row of each plane slices) with overlaid biopsy positions and EIT images (bottom rows) show a contour of 25% of the maximum – heuristically chosen to be best show the muscle/adipose boundary.

E. EM/MR Registration Errors

The registration errors are shown by the average distances between the MR and EM for the 8 top rig points and the between the sample (gel prostate or ex vivo bovine) and the thread intersection points (Table V). Both show very good agreement. Errors ranged from 0.70 to 1.51 mm with averages of ~1 mm for both distance types.

Table V. Registration Average Distance Errors (mm)

Test	MR and EM top rig	Surface to EM
Gel 1	0.93	0.78
Gel 2	0.67	0.70
Gel 3	0.86	0.90
Gel 4	1.51	1.16
Gel 5	0.98	0.96
Ex vivo Bovine	1.22	1.73

IV. Discussion

In terms of EIT reconstructions, this study shows very impressive results, reconstructing small-contrast inclusions in gel prostates and roughly identifying a complex adipose/muscle interface in an ex vivo bovine sample using absolute reconstruction in this fd-TREIT method with B+SR approach. Despite the errors that are involved (tracking errors, numerical approximations in the fusion/inverse process, possible off-axis biopsy needle trajectories) the approach appears quite robust to all of these factors. Accurate boundary extraction using the B+SR is limited, but roughly expected given the moderate resolution of EIT. However, if B-SR is only used to detect tumors, then the gel phantom results show good promise. It is possible that more accurate inclusion boundaries could be achieved by using alternative regularization techniques such as L1 or total variation [28], [29].

The I+B-SR results show very accurate average contrast ratio errors (1.9% when excluding problem cases and 12.2% over all tests) over the small set of gel tests. If similar results using this approach can be attained on real prostates (given suspicious lesion information from mpMRI) then this approach could have significant impact on clinical care. Despite these good results, the confounding artifacts are present in some of the images (e.g. gel 2 in Fig. 12 and gel 5 in Fig. 11). These artifacts appear to be likely caused by inaccuracies in the prostate segmentation or the modeled location of the biopsy electrodes. In ongoing research, we are using a segmentation approach utilizing a commercial software (Mimics [30]) and investigating if the needle trajectory can be improved by information extracted from the ultrasound images.

Beyond investigating different regularization approaches and methods of reducing modeling errors, the other likely approaches to improve results are 1) speeding up the computational process, and 2) adding more electrodes to the BP. The latter approach is mainly straightforward to implement, but requires careful circuit design. More electrodes on the BP would likely increase the volume of the region of sensitivity (towards our goal of 100% coverage of the prostate), and it could increase the flexibility of the measurements. For example, in the current 8-electrode setup if the electrodes are too close to the boundary they are removed entirely. With more electrodes there would likely be more remaining electrodes in these cases, which would allow us to retain row separated patterns where currently we are just removing all the data from that state.

The computational process is two-fold. First there is pulling together all the data (EM, EIT, MR) segmenting and performing steps such as the ROI construction and calculating mappings from reconstruction nodes to FEM nodes for all states. The second is the actual computation of the inverse problem, which is ~27 minutes (Table IV). If reconstructions could be produced in near real-time, then there could be feedback in percent prostate covered or quality of the reconstruction. Part of this speed-up can be achieved through off-line steps and streamlining our approach, but improving the computational time of the inverse problem remains challenging - and is part of ongoing investigations.

V. Conclusions

This study further developed the fd-TREIT approach, tested this approach on challenging phantoms, and now appears ready for ex vivo evaluation of the technique on prostate tissue. Important results include the determination that BP-only measurements result in improved robustness – resulting in simpler modeling and consequently significant decreases in computational times. Additionally, the sensitivity-based ROI resulted in a robust method of determining the region to image. Specifically, the gel phantom experiments showed impressive AUCs (> 0.85 for 4 out of the 5 tests) and when incorporating inclusion boundaries resulted in absolute reconstructions yielding 1.9% and 12.2% in average absolute percent errors for 3 consistent tests and all 5 tests, respectively. Further, the ex vivo bovine test revealed that qualitatively the fd-TREIT approach can largely discriminate a complex adipose and muscle interface in a realistic setting using data from only 9 biopsy probe measurements. Overall, the methods developed here and impressive phantom results suggest a strong promise for this technology to aid in imaging during routine 12-core prostate biopsies.

Acknowledgements

This work was supported in part by DoD CDMRP Grant W81XWH-15-1-0571.

References

[1] R. L. Siegel, K. D. Miller, and A. Jemal, "Cancer statistics," *CA Cancer J Clin*, vol. 66, no. 1, pp. 7–30, 2016.

[2] J. W. Anast, G. L. Andriole, T. A. Bismar, Y. Yan, and P. A. Humphrey, "Relating biopsy and clinical variables to radical prostatectomy findings: Can insignificant and advanced prostate cancer be predicted in a screening population?," *Urology*, vol. 64, no. 3, pp. 544–550, 2004.

[3] P. Walsh, Ed., *Campbell's Urology*, 9th ed. Philadelphia: Saunders, 2007.

[4] P. Harnden, B. Naylor, M. D. Shelley, H. Clements, B. Coles, and M. D. Mason, "The clinical management of patients with a small volume of prostatic cancer on biopsy: What are the risks of progression? A systematic review and meta-analysis," *Cancer*, vol. 112, no. 5, pp. 971–981, 2008.

[5] R. J. Halter, A. Hartov, J. a. Heaney, K. D. Paulsen, and A. R. Schned, "Electrical impedance spectroscopy of the human prostate," *IEEE Trans. Biomed. Eng.*, vol. 54, no. 7, pp. 1321–1327, 2007.

[6] R. J. Halter *et al.*, "The correlation of in vivo and ex vivo tissue dielectric properties to validate electromagnetic breast imaging: initial clinical experience.," *Physiol. Meas.*, vol. 30, no. 6, pp. S121–S136, 2009.

[7] G. Salomon *et al.*, "The Feasibility of Prostate Cancer Detection by Triple Spectroscopy," *Eur. Urol.*, vol. 55, no. 2, pp. 376–384, 2009.

[8] E. K. Murphy *et al.*, "Comparative Study of Separation between Ex-Vivo Prostatic Malignant and Benign Tissue using Electrical Impedance Spectroscopy and Electrical Impedance Tomography," *Physiol. Meas.*, vol. 38, pp. 1242–1261, 2017.

[9] R. J. Halter, A. R. Schned, J. A. Heaney, and A. Hartov, "Passive bioelectrical properties for assessing high- and low-grade prostate adenocarcinoma," *Prostate*, vol. 71, no. 16, pp. 1759–1767, 2011.

[10] K. L. Zakian *et al.*, "Correlation of proton MR spectroscopic imaging with gleason score based on step-section pathologic analysis after radical prostatectomy.," *Radiology*, vol. 234, no. 3, pp. 804–814, 2005.

[11] N. M. deSouza *et al.*, "Diffusion-weighted magnetic resonance imaging: a potential non-invasive marker of tumour aggressiveness in localized prostate cancer," *Clin. Radiol.*, vol. 63, no. 7, pp. 774–782, 2008.

[12] H. Hricak, P. L. Choyke, S. C. Eberhardt, S. A. Leibel, and P. T. Scardino, "Imaging prostate cancer: A multidisciplinary perspective," *Radiology*, vol. 243, no. 1, pp. 28–53, 2007.

[13] M. De Rooij, E. H. J. Hamoen, J. J. Fütterer, J. O. Barentsz, and M. M. Rovers, "Accuracy of multiparametric MRI for prostate cancer detection: A meta-analysis," *Am. J. Roentgenol.*, vol. 202, no. 2, pp. 343–351, 2014.

[14] A. Borsic, R. Halter, Y. Wan, A. Hartov, and K. D. Paulsen, "Sensitivity study of a 3D electric impedance tomography prostate probe," *Physiol. Meas.*, vol. 30, pp. S1–S18, 2009.

[15] E. K. Murphy, X. Wu, and R. J. Halter, "Fused-data transrectal EIT for prostate cancer imaging," *Physiol. Meas.*, vol. 39, no. 5, p. 054005, May 2018.

[16] S. Khan, P. Manwaring, A. Borsic, and R. Halter, "FPGA-Based Voltage and Current Dual Drive System for High Frame Rate Electrical Impedance Tomography," *IEEE Trans. Med. Imaging*, vol. 34, no. 4, pp. 888–901, 2015.

[17] A. Everitt, R. J. Halter, and P. Manwaring, "A real-time 4-bit imaging electrical impedance sensing biopsy needle for prostate cancer detection," in *Medical Imaging 2018: Biomedical Applications in Molecular, Structural, and Functional Imaging*, 2018, vol. 10578, no. March, p. 45.

[18] E. Somersalo, M. Cheney, and D. Isaacson, "Existence and Uniqueness for Electrode Models for Electric Current Computed Tomography," *SIAM J. Appl. Math.*, vol. 52, no. 4, pp. 1023–1040, 1992.

[19] A. Borsic, A. Hartov, K. D. Paulsen, and P. Manwaring, "3D electric impedance tomography reconstruction on multi-core computing platforms," *Conf. Proc. Int. Conf. IEEE Eng. Med. Biol. Soc.*, vol. 2008, no. 1557–170X (Print), pp. 1175–1177, 2008.

[20] T. Lee, M. Leok, and N. H. McClamroch, "Geometric numerical integration for complex dynamics of tethered spacecraft," *Proc. 2011 Am. Control Conf.*, no. May, pp. 1885–1891, 2011.

[21] E. K. Murphy, A. Mahara, and R. J. Halter, "Absolute Reconstructions Using Rotational Electrical Impedance Tomography for Breast Cancer Imaging," *IEEE Trans. Med. Imaging*, vol. 36, no. 4, pp. 892–903, 2017.

[22] W. R. B. Lionheart, "EIT reconstruction algorithms: pitfalls, challenges and recent developments," *Physiol. Meas.*, vol. 25, no. 1, pp. 125–142, 2004.

[23] A. Borsic, R. Halter, Y. Wan, A. Hartov, and K. D. Paulsen, "Electrical impedance tomography reconstruction for three-dimensional imaging of the prostate," *Physiol. Meas.*, vol. 31, no. 8, pp. S1–S16, 2010.

[24] E. Murphy, A. Mahara, and R. Halter, "A Novel Regularization Technique for Microendoscopic Electrical Impedance Tomography," *IEEE Trans. Med. Imaging*, vol. 35, no. 7, pp. 1593–1603, 2016.

[25] E. K. Murphy, A. Mahara, X. Wu, and R. J. Halter, "Phantom Experiments using Soft-Prior Regularization EIT for Breast Cancer Imaging," *Physiol. Meas.*, vol. 38, pp. 1262–1277, 2017.

[26] R. J. Halter, A. Schned, J. Heaney, A. Hartov, and K. D. Paulsen, "Electrical Properties of Prostatic Tissues: I. Single Frequency Admittivity Properties," *J. Urol.*, vol. 182, no. 4 SUPPL., pp. 1600–1607, 2009.

[27] N. K. Soni, H. Dehghani, A. Hartov, and K. D. Paulsen, "A novel data calibration scheme for electrical impedance tomography.," *Physiol. Meas.*, vol. 24, no. 2, pp. 421–435, 2003.

[28] A. Borsic, B. M. Graham, A. Adler, and W. R. B. Lionheart, "In vivo impedance imaging with total variation regularization," *IEEE Trans. Med. Imaging*, vol. 29, no. 1, pp. 44–54, 2010.

[29] A. Borsic and A. Adler, "A primal–dual interior-point framework for using the L1 or L2 norm on the data and regularization terms of inverse problems," *Inverse Probl.*, vol. 28, no. 9, p. 095011, 2012.

[30] "3D Medical Image Processing Software | Materialise Mimics." [Online]. Available: http://www.materialise.com/en/medical/software/mimics. [Accessed: 04-May-2017].

A 1 MHz Miniaturized Electrical Impedance Tomography System for Prostate Imaging

Arun Rao, *Student Member, IEEE,* Ethan K Murphy, *Member, IEEE,* Ryan J Halter, *Senior Member, IEEE,* and Kofi M Odame, *Senior Member, IEEE*

***Abstract*—An ASIC for a high frequency electrical impedance tomography (EIT) imaging system for prostate cancer screening is presented. The ASIC enables a small form-factor architecture, which ensures high signal-to-noise ratio (SNR) at MHz frequencies. The ASIC was designed in a standard CMOS 0.18-μm technology. A prototype miniaturized EIT system was built and it was evaluated using a model transrectal probe immersed into a saline tank with a metal inclusion phantom that simulated a prostate cancer lesion. The system maintained an SNR of between 66 dB and 76 dB over the frequency range of 500 Hz to 1 MHz. Also, it produced reconstructed EIT images that depicted the presence of the small metal inclusion "lesion".**

***Index Terms*—Electrical impedance tomography, EIT, application specific integrated circuit, ASIC, biomedical instrumentation, imaging, hardware system design, prostate imaging.**

I. Introduction

Standard prostate cancer screening is poor at gauging disease extent and aggressiveness. This often leads to overtreatment and unnecessary radical prostatectomy [1]. To improve prostate cancer screening, we and others have proposed transrectal electrical impedance tomography [2]. Transrectal EIT, or TREIT, is an imaging technique that distinguishes cancerous from benign tissue by identifying anomalies in the electrical properties of the prostate.

The challenge is that the best contrasts in TREIT are only observed for high-frequency ($\geq$ 100 kHz) impedance signatures [3]. Our recent TREIT system operates at these frequencies, but it is physically large; using it in an in-vivo clinical setting would require long cables to transmit analog signals between the probe and the instrumentation electronics [4]. And for high frequency analog signals, long cables are prone to channel cross talk and parasitic impedances, which severely degrade image quality [5].

If the EIT instrumentation analog front end (AFE) were built as an application specific integrated circuit (ASIC) and incorporated into the TREIT probe, it would eliminate the long analog cable connections. However, no ASIC-based system to date has met the technical specifications necessary for TREIT imaging. In this paper, we derive the performance requirements of a TREIT ASIC. We present a pathfinder ASIC for achieving these specifications, and we evaluate its performance in a prototype TREIT imaging system.

II. Transrectal Electrical Impedance Tomography

We have designed and constructed a flexible sonolucent electrode array to interface with an end-fired transrectal ultrasound (TRUS) probe and a multi-electrode biopsy needle, able to simultaneously sense electrical signals and extract tissue cores (see Fig. 1). During biopsy, the electrodes are used to inject low amplitude sinusoidal currents into the tissue, and then used to read the resulting boundary voltages that develop on the surface of the tissue. The voltage difference between a pair of electrodes due to a particular current source/sink configuration is known as an IIVV pattern. In Fig. 2 for instance, IIVV pattern 1-15-16-14 is the voltage difference between electrodes E16 and E14 when current is injected into E1 and sunk by E15. Hundreds of these IIVV patterns are collected and used to reconstruct a single tomography-like map of conductivity and permittivity of prostatic tissue.

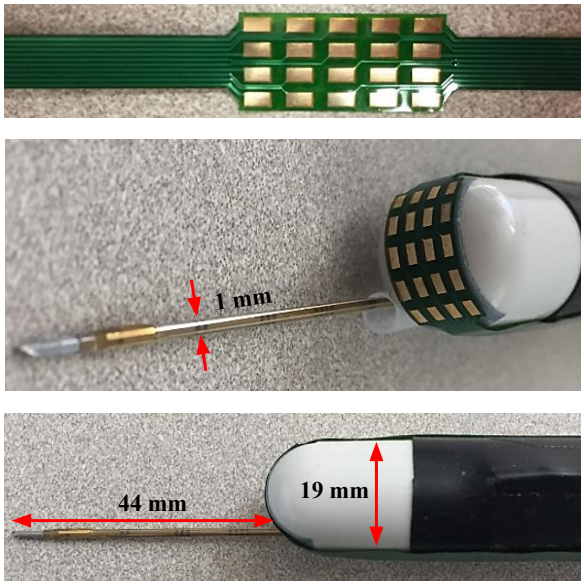

Fig. 1. Proposed TREIT probe for prostate electrical impedance tomography imaging. It comprises a flexible sonolucent PCB with a 4x5 grid array of electrodes (top) wrapped around an end-fired transrectal ultrasound probe with a biopsy needle (center and bottom).

III. EIT Specifications to Detect Cancer

A. Operating Frequency

As we showed in previous work with ex vivo samples, the admittivity properties of the prostate are higher in malignant than in benign tissue [3]. Also, the difference in admittivity values is most pronounced for frequencies above 100 kHz (Fig. 3). To make use of this high contrast region, we require that the ASIC current driver and voltage readout chain operate up to at least 1 MHz.

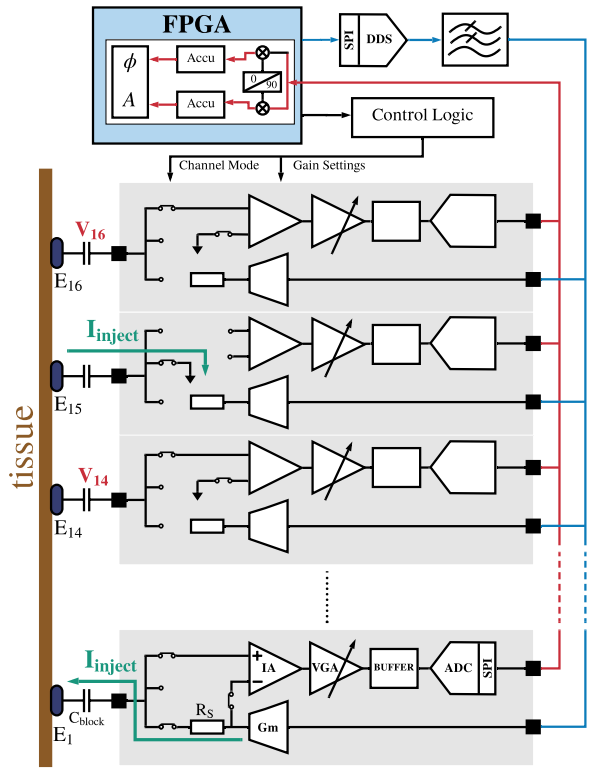

Fig. 2. Block diagram of a the designed 16-electrode EIT system. AC current excitation is performed using a pair of electrodes (1 and 15) and the voltages induced on the remaining electrodes are measured. DC isolation between the patient and instrumentation is achieved using capacitor, C_{block}.

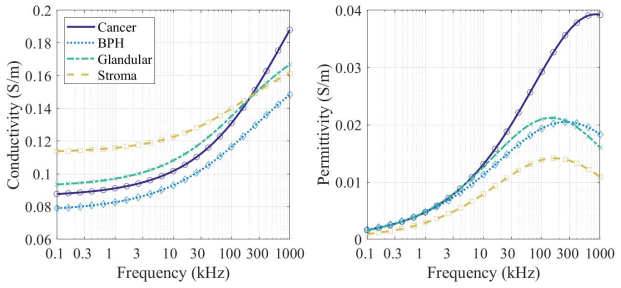

Fig. 3. The conductivity and permittivity of prostate tissue from 100 Hz to 1 MHz. Aca, BPH, GI, and Str represent prostate adenocarcinoma, benign prostatic hyperplasia, nonhyperplastic glandular tissue, and stroma respectively. Cancerous tissues exhibit significantly lower conductivity, whereas the admittivity between cancerous and surrounding tissues increase with higher frequency of operation [3].

B. Signal-to-Noise Ratio

For the TREIT image to be clinically useful, the IIVV patterns must be measured with adequate signal-to-noise ratio (SNR). In particular, the SNR of the amplitude and phase of boundary voltage measurements (like V_{14} and V_{16} in Fig. 2) must be sufficiently high.

We estimated the minimum required SNR by simulating a 3D finite element method (FEM) model of the prostate and an end-fired 20 electrode TREIT probe [6](see Fig. 4). To detect a 5 mm cancerous lesion that is 4 mm away from the TREIT probe, the SNR of the difference in IIVV patterns between this and a normal, 'reference' prostate must be at least 10 dB. That is,

$$\mathrm{SNR}_{\Delta_{vv}} = 10\log_{10}\left(\frac{\overline{V_c}^2}{\sigma_{vv}^2} - \frac{\overline{V_{ref}}^2}{\sigma_{vv}^2}\right) \geq 10\mathrm{dB}, \qquad (1)$$

where V_c is the IIVV pattern for the prostate with the lesion, and V_{ref} is the same IIVV pattern for a reference healthy prostate. The overbars denote the mean of these voltages, taken over several repeated measurements in a real-world, noisy environment. Also, σ_{vv} is their standard deviation.

We used the FEM model to generate an exhaustive set of (noise-free) IIVV patterns from 100 Hz to 1 MHz, with and without a lesion. For each pattern, we set $\mathrm{SNR}_{\Delta_{vv}} = 10$ dB and solved Eqn. 1 for σ_{vv}. From this, we derived the minimum allowable SNR for boundary voltage measurements. Figure 5 shows that this SNR is 65-90 dB for the phase component and approximately 80 dB for the amplitude component. If the electrodes are on the biopsy needle (versus on the TREIT probe), then the single-ended voltage SNR requirements can be relaxed to 55-73 dB.

C. Input voltage range

Generally for an M-electrode EIT system, we need at least M*(M-3)/2 IIVV measurements with the prescribed level of signal-to-noise ratio in order to reconstruct a useful image. However, depending on the tissue properties, current injection pattern and current injection amplitude, the system could encounter some boundary voltages that are too small to be practicably measured with the required level of SNR. We can discard these low-amplitude measurements, as long as there are enough other remaining measurements for image reconstruction. From our FEM simulations, we found that discarding boundary voltages smaller than 30 mV still leaves us with several hundred IIVV patterns – enough to perform

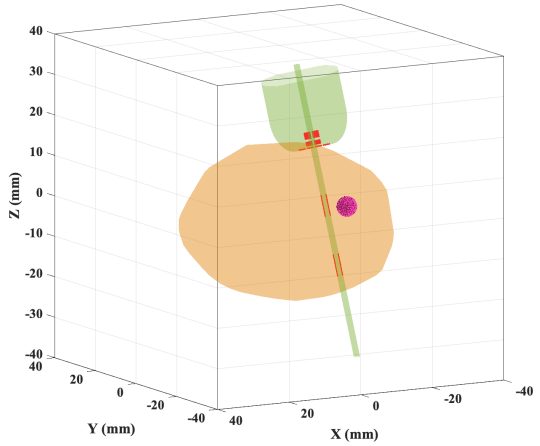

Fig. 4. Simulation setup for determining the SNR requirements of amplitude and phase for boundary voltage measurements. Prostate (orange), transrectal ultrasound (TRUS) and biopsy needle (green), and tumor (magenta).

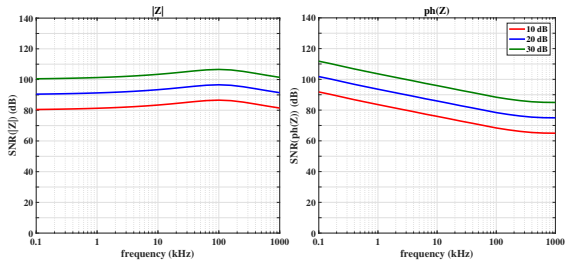

Fig. 5. SNR requirement for boundary voltage measurements for prostate imaging determined using FEM simulations and setup shown in Fig. 4.

image reconstruction in a 20 electrode system. Also, given the maximum safe current injection limits [7], the largest expected amplitude for the boundary voltage is 1 V. So, the EIT system is required to handle boundary voltages with an amplitude dynamic range of 30 mV to 1 V.

D. Other Considerations

For patient comfort, and to minimize motion artifact, the TREIT frame rate should be at least 10 frames per second (FPS). This means that the system must measure all of the required IIVV patterns, and complete the image reconstruction algorithm, in 100 ms or less.

Accuracy and linearity requirements are less stringently defined, especially with the use of our calibration techniques (See Appendix A). Still, it is typical to design for $\geq$ 99% accuracy and ≤ -40 dB total harmonic distortion [8], [9], [10].

IV. Analog Front-End ASIC

We designed an instrumentation analog front end ASIC to meet the above system-level specifications. Figure 6 shows the schematic of one channel of our custom IC, while the chip micro-graph of the ASIC, fabricated in the X-Fab 0.18-μm CMOS process, is shown in Fig. 7. It is a modified, 4-channel version of our previously-introduced EIT analog front end circuitry [11], [12], [13]. To reduce cross-talk between the channels, layout was optimized between analog and digital circuit blocks. Analog input-output pads were isolated to reduce coupling capacitance and improve high frequency behavior (see Fig. 8). To prevent digital noise from interfering with the current injection and voltage readout chain, the sensitive analog components and noisy digital blocks were placed in separate deep n-wells.

A. Current Driver

We used the current conveyor (CCII)-based current driver shown in Fig. 9 to inject sinusoidal currents of up to 1 mA_{pp} into the tissue under study. The current driver's input voltage, V_Y, is produced by an off-chip direct digital synthesis (DDS) block and is buffered to V_X, which generates a current $I_X = \frac{V_X}{R_X}$ through resistor R_X. The CCII mirrors this current to the output, $I_Z = I_X$, driving it through a DC-blocking capacitor, C_{block} and into the tissue. C_{block} protects the patient from excessive DC currents, without the physical bulk of a transformer. Since the resistor R_X provides a linear voltage-to-current conversion, the output current exhibits a relatively low THD of 0.15% for a 1 MHz, 1 mA_{pp} output. Also, the current driver has a gain-boosted cascode output stage [14], [15] which provides an output impedance of 0.1 MOhms at 1 MHz.

B. Readout Chain

When current is injected into the tissue, the readout chain of Fig. 6 is used to amplify, sample and digitize the sinusoidal voltage that develops on the tissue surface. Each voltage reading involves multiple samples (or "taps"), from which the FPGA-implemented digital matched filter extracts the sinusoidal voltage's amplitude and phase. To ensure successful EIT image reconstruction, the extracted amplitude and phase must be measured with an SNR of at least 65 dB. To achieve this, we considered the readout chain's thermal noise, quantization noise and number of taps per measurement, which all factor into the SNR via [16],

$$\mathrm{SNR_A} = 10 \cdot \log_{10} \cdot \left[\frac{\mathrm{A}^2(\frac{\mathrm{N_{tap}}}{2})}{\frac{\mathrm{V_{FS}}}{12 \cdot 2^{\mathrm{B}}} + \sigma_{\mathrm{n}}^2} \right] \quad (2)$$

where A is the maximum expected voltage amplitude, and N_{tap} is the number of taps (or samples) in the matched filter. Also, $\frac{V_{FS}}{12 \cdot 2^B}$ is the quantization noise power, where B is the ADC resolution and σ_n is the variance of the thermal noise referred to the ADC input.

The instrumentation amplifier produces the majority of the thermal noise, on the order of 1 mV_{rms}. Meanwhile, the ADC resolution is ideally 8-10 bits to maximize power efficiency [11], [17], [18]. This gives the required number of taps per voltage measurement as,

$$\mathrm{N_{tap}} = \frac{2 \cdot 10^{\frac{\mathrm{SNR_A}}{10}}}{\mathrm{A}^2} \cdot \left(\frac{\mathrm{V_{FS}}}{12 \cdot 2^{\mathrm{B}}} + \sigma_{\mathrm{n}}^2 \right) \quad (3)$$

To meet the 10 fps frame rate, the voltage measurements must be taken for all possible current injection patterns ($\frac{16*15}{2} = 120$ patterns for a 16 electrode system) in less than 0.1 seconds. Since we need 100 taps per measurement to meet the SNR specification, this translates to an ADC sample rate of at least $\frac{100*120}{0.1} = 120,000$ samples per second. We designed the ADC for 250 kSa/s to allow for settling time between current injection patterns. To process signals higher than 125 kHz, we used the undersampling technique described below. The measured SNR across frequencies and the readout chain details are shown in Fig. 10.

C. Undersampling

Undersampling refers to sampling a signal at a rate lower than the Nyquist sample rate. This causes aliasing, a generally undesirable phenomenon because high frequency content can get superimposed onto low frequency content. In the case of undersampling an EIT boundary voltage, the effect of aliasing is simply to downconvert a high frequency sinusoid

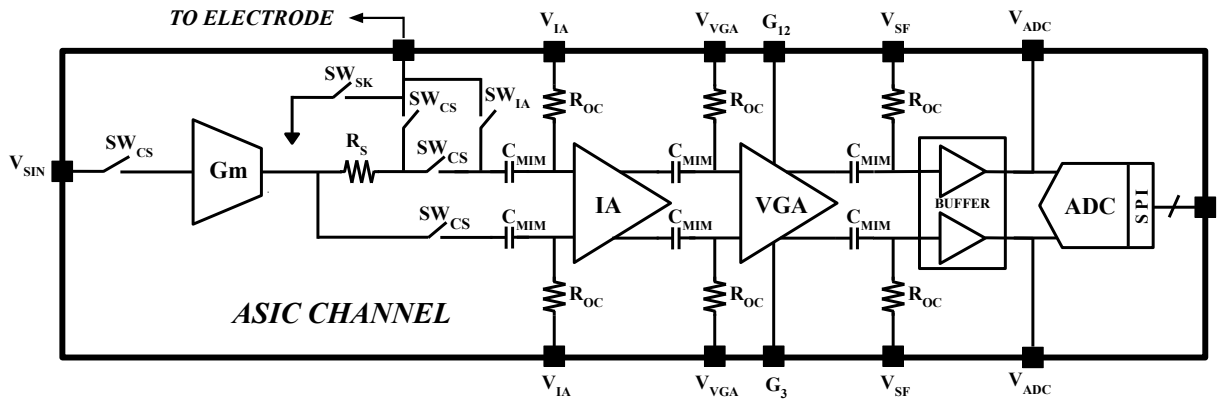

Fig. 6. Details of one channel of the 4-channel EIT instrumentation AFE ASIC. The on-chip switches are used to configure the channel in a current-source, current-sink or voltage-read mode. On-chip capacitors decouple each stage and resistors implemented as off-state transistors are used for input biasing. The IA, VGA, buffer and the ADC form the voltage readout chain. The digital data from the ADC is sent off-chip using a SPI interface to compute amplitude and phase with a matched filter on a FPGA. The performance of the 4-channel ASIC was measured using a custom built PCB.

to a lower frequency. There is no low frequency content to interact with and distort the aliased signal. And, importantly for image reconstruction, aliasing preserves the original phase and amplitude of the boundary voltage.

For the undersampling technique to work well in practice, two constraints must be met. First, the sampling frequency and the input signal frequency must be coprime. This avoids the potential for repeated sampling of the same point (e.g. if a 1000 kHz signal were sampled at 100 samples/second, it is possible that only the zero crossings of the signal would be sampled). The second constraint is that there must be a whole number of samples in one period of the aliased signal. This enables a proper matched filter implementation following the ADC, thus maximizing the SNR of the readout chain.

Considering the two constraints above, there is significant overhead in designing an undersampling scheme for any arbitrary interrogation frequency. Instead, our approach is to choose a fixed set of interrogation frequencies that fall within the frequency range of interest and that satisfy the two undersampling constraints via,

$$f_{in} = \frac{(N_{tap} \cdot K \pm 1) \cdot f_S}{N_{tap}} \quad (4)$$

where $N_{tap} = 100$ is the number of samples (i.e. matched filter taps) and $f_S \leq 250$ kHz is the ADC sample rate.

For example, for $f_S = 100$ ksps, $N_{tap} = 100$, and $K = 10$, we have $f_{in} = 1001$ kHz. This gives an aliased signal of 1 kHz, for which we obtain 100 samples in one full period of 1 ms. The frequency domain representation for this example is shown in Fig. 11.

V. Measurement Results

We evaluated the performance of our ASIC-based multi-frequency EIT system with the modular test setup shown

Fig. 7. Chip Micro-photograph. 4 channels are integrated into a single ASIC. Various blocks are shown.

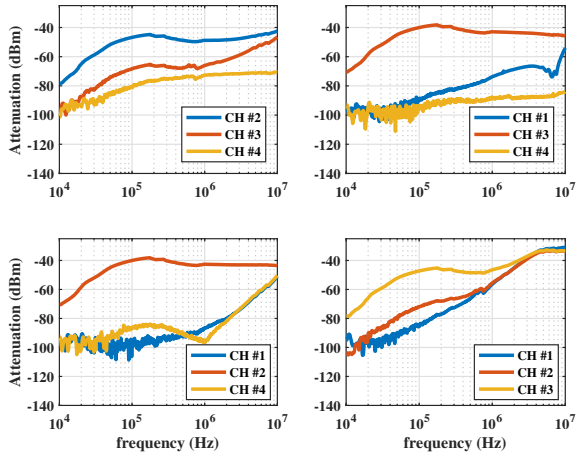

Fig. 8. Channel cross-talk for all channels on the 4-channel ASIC. Each channel is driven with a sinusoid (power of 0 dBm) and the fundamental magnitude appearing at the output of the VGA (with channel gain of 3 V/V) on the remaining channels measured with respect to the driven channel. A spectrum analyzer with a tracking generator is used for this measurement, for frequency range of 10 kHz to 10 MHz.

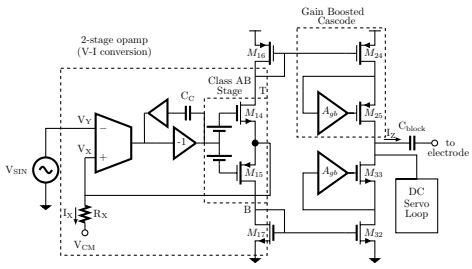

(a)

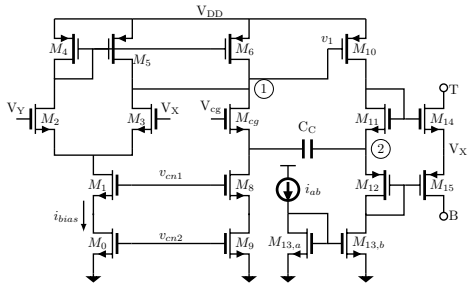

(b)

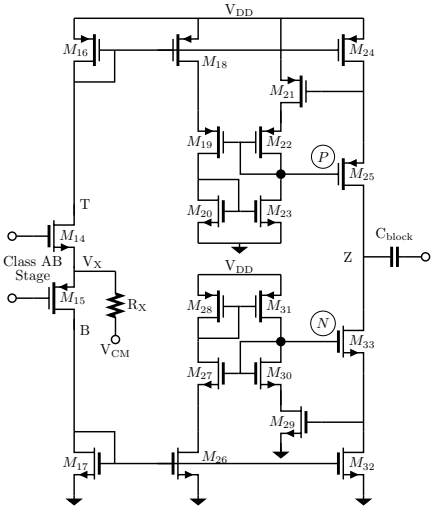

(c)

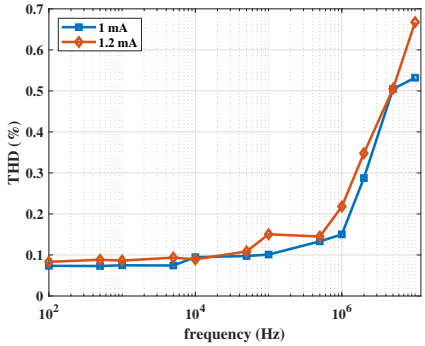

(d)

Fig. 9. (a) Current conveyor II (CCII) based wide-band current driver [12]. (b) The V-I is performed at the 2-stage opamp with class AB output stage and a resistor. (c) The high output impedance is achieved using a gain enhanced cascode structure. (d) Plot of total harmonic distortion for the current driver across frequencies for 2 current levels.

in Figs. 12 and 13. It is a 20-channel system, comprising 5 daughterboards (each housing a 4-channel instrumentation ASIC), an Adafruit Feather HUZZAH (Adafruit Industries, New York, NY) for wireless data transmission and an Artix-7 FPGA evaluation board (Xilinx Inc., San Jose, CA) for system

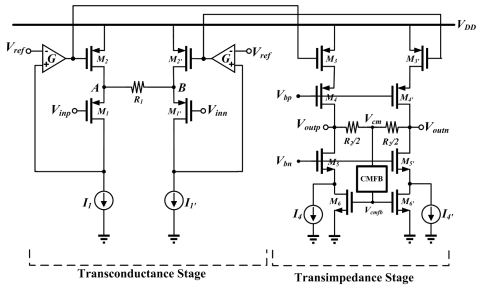

(a)

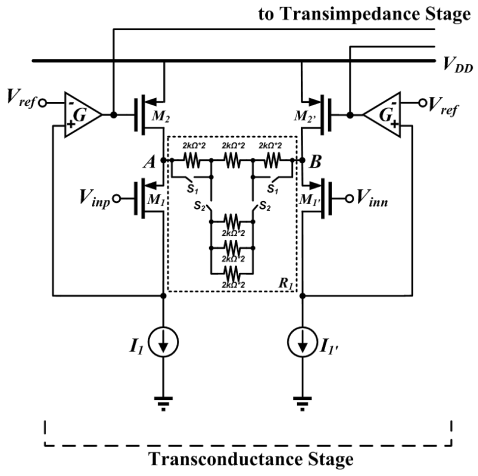

(b)

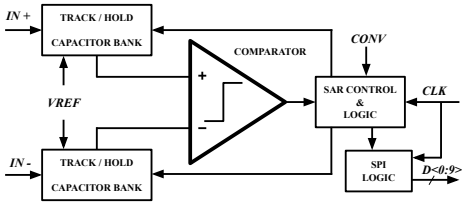

(c)

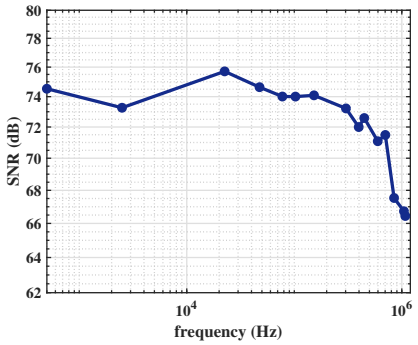

(d)

Fig. 10. (a), (b) Schematic of the IA and VGA [13]. (c) Block diagram of the on-chip 10-bit SAR ADC. (d) SNR plot across frequencies for the readout chain.

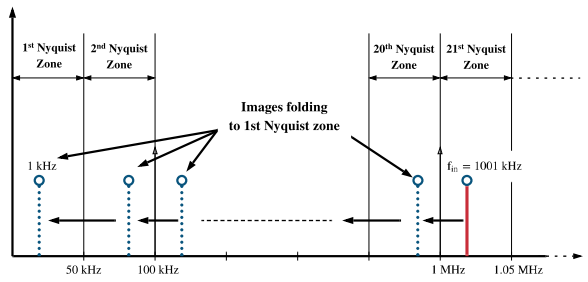

Fig. 11. Frequency domain representation for interrogation frequency of 1001 kHz and 100 ksps sampling rate. The aliased frequency is folded back to the 1st Nyquist zone representing a 1 kHz signal. 100 samples are obtained in a single waveform period of the aliased frequency.

control and match-filter amplitude/phase extraction. A single motherboard provides power and I/O slots to host all of the above components. This modular approach facilitates testing and debugging. For example, one of the daughter boards was sacrificed and used to monitor the FPGA's communication and control signals, leaving 16 fully-functional channels for image reconstruction experiments. Following this proof of concept system, we will build future versions on a single PCB for a hand-held form factor.

In addition to an instrumentation ASIC, each daughter board (see Fig. 14) contains one AD9834 sinusoidal waveform generator chip (Analog Devices Inc., Norwood, MA) to provide input to the ASIC's current drivers. The waveform generator's output frequency and amplitude are set by the FPGA via SPI. The FPGA also uses SPI to communicate with the instrumentation ASICs: to set the channels' readout gain, operation mode (current sink, current source or voltage readout) and to collect the digitized voltages. In turn, initial setup information (number of electrodes, vector of injection frequencies, etc.) is downloaded to the FPGA from a workstation computer via UART.

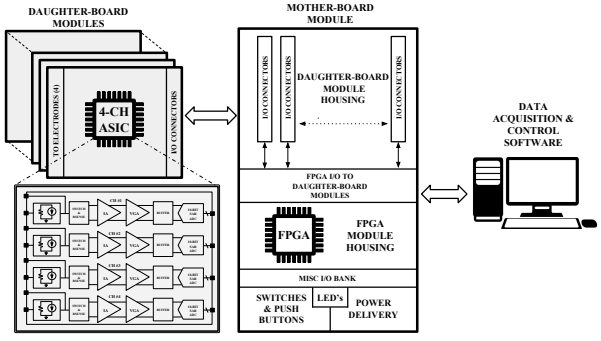

Fig. 12. Architecture of the 16-electrode channel EIT system. The custom built 4-channel ASIC implements the core EIT functionality and is included on a daughter-board module with required power, voltage references, current biases and switch IC's. A motherboard houses the daughter-board module and FPGA carrier board. The Artix-7 FPGA on the mother-board is responsible for control, data acquisition, and computations. The data from the FPGA is sent to the MATLAB software on the computer to form impedance matrices and re-construct images.

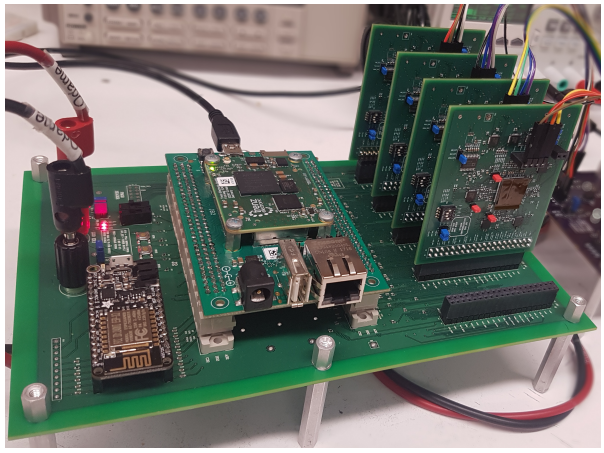

Fig. 13. 16-electrode EIT system for prostate imaging.

A. *Saline Tank Measurements*

To validate the functioning of the EIT system, we performed impedance imaging experiments of a saline tank. An 8.5 cm diameter tank was filled to a height of 1.27 cm with a saline solution of conductivity 1000 μS/cm. The tank was fitted with conductive electrodes in contact with alligator clips attached to the tank. The spacing between each electrode was 3.25 cm. In an initial experiment, we took baseline measurements with only saline solution in the tank. Subsequent experiments involved a brass rod inclusion of diameter 1.3 cm placed inside the tank of saline solution: for one experiment, the rod was placed at the center of the tank; in another experiment, the rod was placed close to the edge, near electrode 16. The

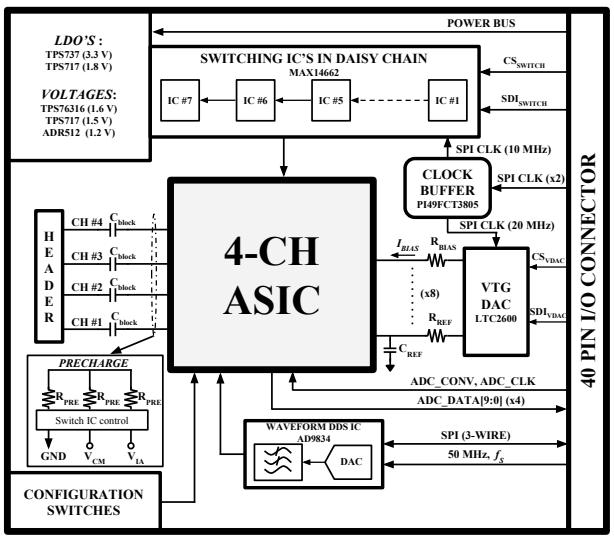

Fig. 14. Daughter-board module block diagram. The module includes the 4-channel ASIC which provides majority of the EIT functionality. Peripheral IC's generate voltage references, bias currents, sinusoidal stimulus for the ASIC and switching mechanisms for channel configuration. Several SPI interfaces are implemented to communicate with the IC's and the ASIC. Pre-charge circuits reduce settling time at the output of each channel. The channel outputs are connected to headers, using a DC blocking capacitor C_{block}. Power is supplied to each module from the I/O connectors. A large number of GND pins are included in the connectors to ensure proper ground connection with the motherboard.

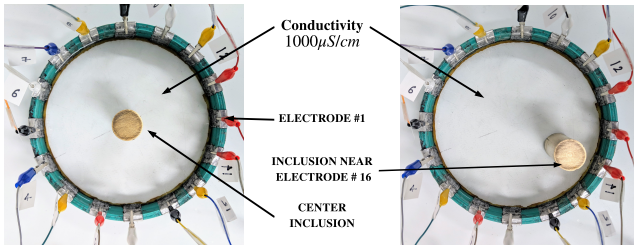

Fig. 15. Saline tank experiment setup with a 16-electrode EIT system. The conductivity of the solution was set to 1000 $\mu S/cm$. Brass rod inclusion at the center of the saline tank and inclusion placed close to electrode # 16.

experimental setups with center and off-center inclusion is shown in Fig. 15. For each experiment, data was acquired for 6 frequencies from 1 kHz to 1 MHz with 240 current source/sink patterns per frequency and a current injection amplitude of 550 μA. We processed the data with our in-house reconstruction algorithm [19] to generate the impedance images shown in Figs. 16 and 17.

B. Transrectal Probe Experiment

To simulate the TREIT application, we tested our system with the probe and tank setup shown in Fig. 18. The probe was a 3D-printed model of a Phillips C9 TRUS probe (Koninklijke Philips N.V., Amsterdam, Netherlands), around which was wrapped a flexible printed circuit board of 20 gold-plated electrodes. The probe was immersed in a saline tank solution of conductivity 1100 μS/cm. A tightly wound copper wire inclusion of diameter approximately 2 mm was placed at a distance of $\leq$ 1 mm from the probe tip (Fig. 19). This metal inclusion was used to model a prostate cancer lesion. 16 of the probe electrodes were connected to our EIT system 0.1 inch connectors. Data was acquired for 6 frequencies from 1 kHz to 1 MHz with 240 current source/sink patterns per frequency and a current injection amplitude of 235 μA. As the reconstructed images in Fig. 20 show, our EIT system was able to detect the metal inclusion (yellow blocks in the 3D images) across the various test frequencies.

VI. Discussion

The performance specifications for our ASIC and overall EIT system are listed in Table I. In the context of transrectal electrical impedance tomography for enhancing prostate cancer diagnosis, the primary target specifications for an EIT analog front end are: 1 kHz to 1 MHz interrogation frequency range; 65-90 dB SNR (probe tip electrodes) or 55-73 dB SNR (biopsy needle electrodes); 16 to 20 electrode channels; 10 FPS data acquisition rate; hand-held form factor.

As Table II shows, existing EIT analog front ends that meet the measurement requirements were based on commercial-off-the-shelf (COTS) discrete components [4], [20]. So, with more than a dozen channels, these AFEs are too large to fit the hand-held form factor of a TREIT probe. This is crucial, because large instrumentation must be placed far from the patient, neccessitating long cables for transmitting analog signals between the electrodes and the rest of the EIT system. At high frequencies, this arrangement would severely degrade the system's SNR performance. ASIC-based AFEs address the problem of form factor, and can enable the high frequency interrogation required in a prostate imaging application. Table II shows that our solution outperforms other ASIC-based AFEs in terms of high SNR at high frequencies. Our solution meets all the specifications for prostate imaging with the biopsy needle, while falling a little short for use with probe electrodes. Nevertheless, our experimental results suggest that, even for the more stringent probe electrodes application, our EIT system is able to detect small inclusions in a saline solution. An improved ADC with ENOB $\geq$ 10 would produce even better performance. The frame rate of the system depends primarily on the ADC's sample rate and the amount

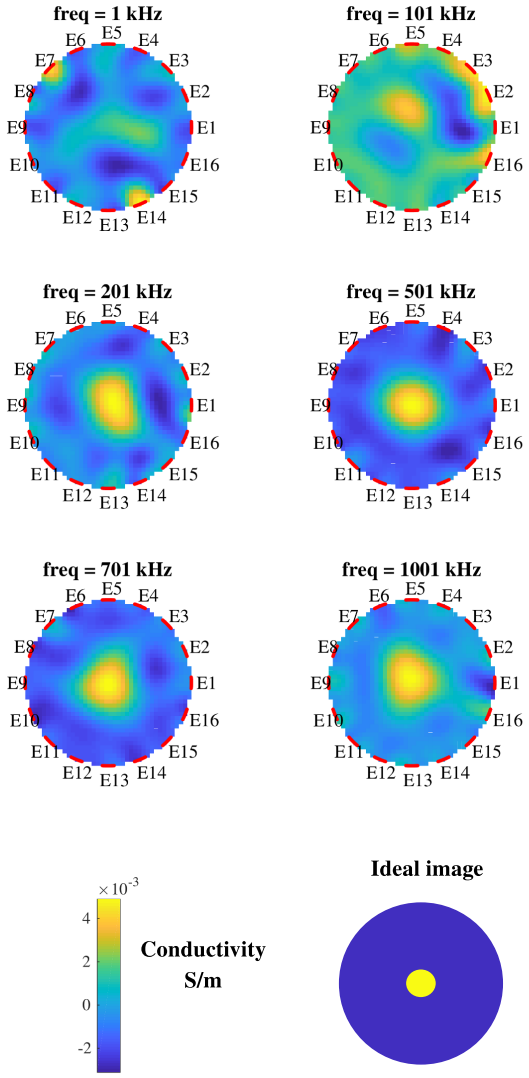

Fig. 16. Images obtained for the center inclusion with an ideal image to the left. Data for 1 kHz could not be obtained due to issues with hardware setup. It is included here as the images were obtained from the same dataset.

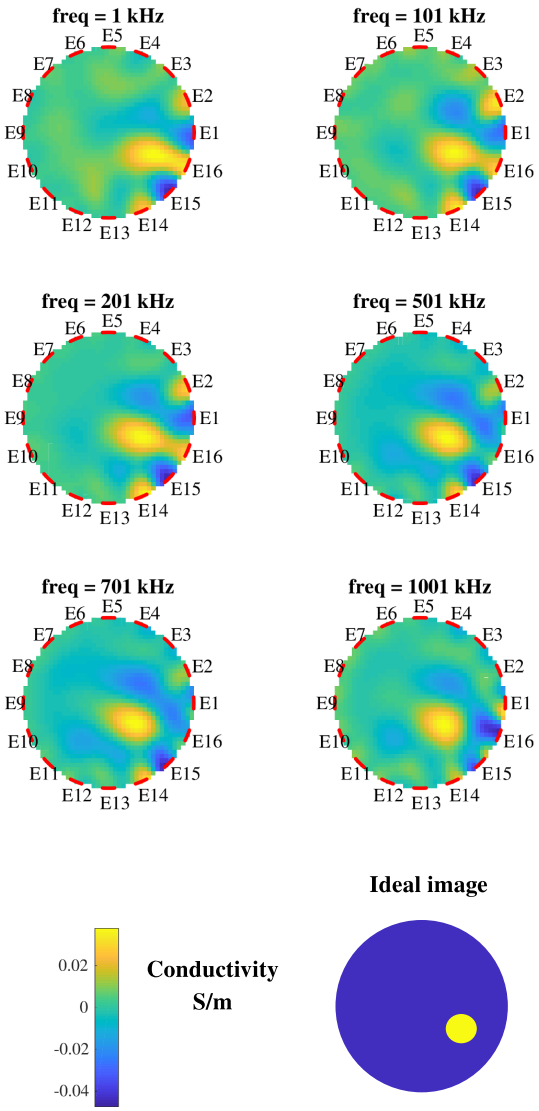

Fig. 17. Images obtained for the off-center inclusion with an ideal image to the left. All images obtained for the same dataset are shown.

of settling time needed between measurements. Our current driver exhibited poor phase margin, due to the proximity of the servo-loop pole to a dominant pole associated with the C_{block} capacitor and the current driver's output impedance. This caused slow settling and the target frame rate was not achieved. The solution to this problem is to increase the frequency of the servo-loop pole; we have verified this solution in simulation and will implement it in future iterations of the chip.

VII. Conclusion

We derived the detailed system level specifications necessary for transrectal electrical impedance tomography. A 4-channel ASIC was designed and fabricated in the CMOS 0.18-μm technology for high frequency EIT. It integrates a novel current driver for current injection, instrumentation amplifier

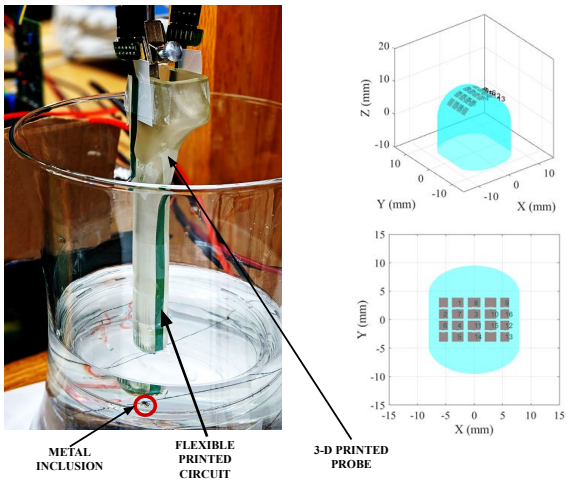

Fig. 18. TRUS setup with the electrode array on a flexible printed circuit, immersed in a saline tank solution.The 16 electrode positions used for our EIT measurements are shown in the bottom-right figure.

to interface with the tissue, VGA to provide variable gain and an ADC with SPI interface for digitization. The readout chain operates between 500 Hz - 1 MHz with an SNR range of 66 dB - 76 dB. The ASIC is integrated into a prototype modular 16-electrode EIT system consisting of daughter-boards, motherboard, FPGA and custom software framework. Saline tank experiments and transrectal probe setups were used to obtain reconstructed images of inclusions in a saline tank solution. The pathfinder EIT system in this paper demonstrates the feasibility of EIT for obtaining high contrast images for prostate imaging.

Appendix A
Calibration

The designed EIT system is prone to various sources of systematic errors, particularly for the ASIC channel. Potential sources of errors are listed below and a pictorial representation is shown in Fig. 21.

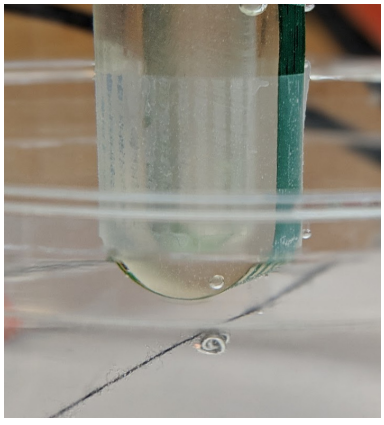

Fig. 19. Probe setup with a zoomed in section of the inclusion and separation from electrode array.

- *AD9834 IC output :* The AD9834 IC provides the sinusoidal input for the current drivers on the ASIC for each daughter-board module. The differences in the output voltage amplitudes from the AD9834 IC across the modules need to be accounted for during calibration.
- *On-chip resistors :* Each ASIC channel includes 2 on-chip resistors: R_X for generating the current to be injected into the tissue, and R_S for sensing the current (see Figs. 9 and 6). Due to process variations during fabrication the resistor values vary. This causes variation in both the injected current and the voltage induced across the sense resistor. Variation in the resistor values should be included in the measurements.
- *Channel gain :* The readout chain consists of the IA with a fixed gain of 3 V/V, and VGA with variable gains of of 1, 3 and 12 V/V. Due to process variations there is a channel-to-channel variation in gain which affects the voltage measurements.

1) Voltage-read mode: A calibration scheme is proposed for the EIT system which includes all the above sources of errors. First, the measurement errors in the voltage-read mode is calculated and accounts for the channel variation due to IA and VGA gain. The circuit to calculate the gain

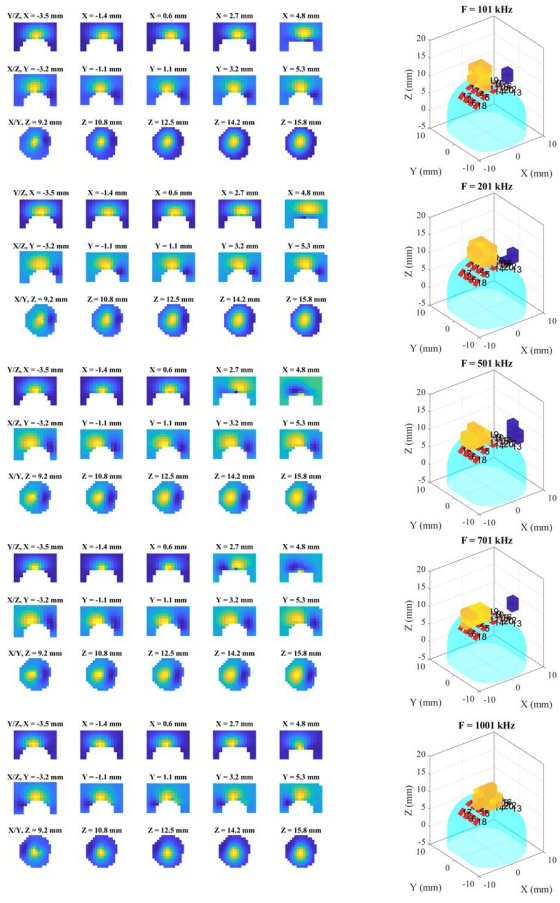

Fig. 20. Images obtained across frequencies for the 16-electrode TRUS setup in the saline tank shown in Fig. 18. The yellow blocks in the reconstructed 3D images are conductivity regions that are within 70 % of the maximum measured conductivity. That is, they represent the metal inclusion.

TABLE I
EIT SYSTEM SPECIFICATIONS

Application		Prostate Imaging
ASIC		
Process		XFAB 0.18-μm CMOS
Supply Voltage	Analog	3.3 V
	Digital	1.8 V
Current Driver	Frequency	100 Hz - 10 MHz
	Amplitude	up to 1.2 mA
	Output Impedance	101 kΩ@ 1 MHz 19 kΩ@ 10 MHz
	THD	$<$ 1% @ 10 MHz
Read-out Chain	Gain	IA : 9.3 dB VGA : 0, 9.3, 21 dB
	Input Noise	IA : 14 nV/$\sqrt{\text{Hz}}$ VGA : 80, 27, 6.7 nV/$\sqrt{\text{Hz}}$
SAR ADC	ENOB	8.84 bits
	Sampling Rate	250 ksps (max)
Power (per channel)		11.4 mW
EIT System		
Electrodes		16
Scan Patterns		Programmable
THD (readout chain)		0.2% @ 1 MHz
Frequency		1 kHz - 1 MHz
SNR		66-76 dB
Digital Interfaces		SPI, UART

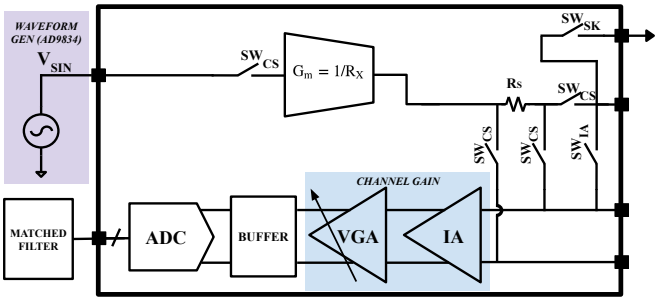

Fig. 21. Sources of measurement errors in the EIT system.

calibration coefficient of each channel is shown in Fig. 22. All the channels of the EIT system are configured in the voltage-read mode and connected to a sinusoidal voltage source with known amplitude, A. Ideally the voltage at the output of each channel is,

$$V_O = A \cdot G \tag{5}$$

where G is the gain of the readout chain for all channels in the EIT system. However, due to the variations in channel gain, the value of V_O varies across channels. A calibration coefficient, α_G is defined which accounts for the gain variation

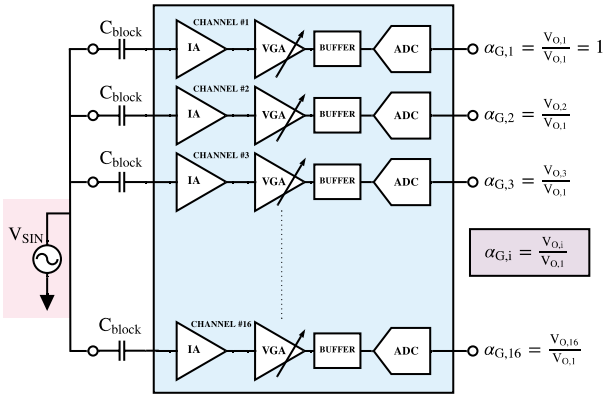

Fig. 22. Circuit to determine the calibration coefficient of the channel gain. All channels of the EIT system are configured in the voltage-read mode and input with a known voltage with amplitude A. With channel # 1 as the reference, and gain, G of the readout channels, the calibration coefficient, α_G is calculated for all channels.

with channel # 1 as the reference. The calibration coefficient is given as,

$$\alpha_{G,i} = \frac{V_{O,i}}{V_{O,1}} \ , \tag{6}$$

where i represents the channel number in the EIT system. The procedure for obtaining the coefficient, α_G, is repeated for all possible gain combinations of the readout chain across the desired frequencies.

2) Current-source mode: The circuit in Fig. 23 determines the calibration coefficients for the channel configured in the current-source mode. The sources of error in this configuration are the output voltage amplitude differences from the AD9834 IC, on-chip resistor variations, and channel gain.

The on-chip resistor, R_X generates the sinusoidal current in the V-I conversion stage of the current driver. The current output from the current driver is,

$$I_Z = \frac{\alpha_{SIN} \cdot V_{SIN}}{\alpha_X \cdot R_X} \ , \tag{7}$$

where, I_Z is the output from the current driver, V_{SIN} is the output voltage amplitude from the waveform generator IC, α_{SIN} is the corresponding calibration coefficient, and α_X is the calibration coefficient of the on-chip resistor, R_X. The voltage at the load is given as,

$$V_L = \frac{\alpha_{SIN} \cdot V_{SIN}}{\alpha_X \cdot R_X} \cdot R_L \tag{8}$$

where R_L, is the load resistance measured accurately with an LCR meter. The voltage, V_L, is measured using an oscilloscope and includes the calibration coefficients α_{SIN} and α_X. Voltage at the output of the readout chain, V_O includes the calibration coefficients, α_G, α_{SIN} and α_X and is given as,

$$V_O = \frac{\alpha_{SIN} \cdot V_{SIN}}{\alpha_X \cdot R_X} \cdot \alpha_S \cdot R_S \cdot \alpha_G \cdot G \ , \tag{9}$$

where, α_S is the unknown calibration coefficient per channel to be determined, R_S is the sense resistor, α_G is the gain coefficient per channel determined by configuring all channels in voltage readout mode (Equation. 6), and G is the selected gain of the voltage readout channel. By measuring voltages V_L, and V_O, the effect of calibration coefficients α_{SIN} and α_X is accounted for. Using equation 8 and 9,

$$\alpha_S = \frac{V_O \cdot R_L}{V_L \cdot R_S \cdot \alpha_G \cdot G} \tag{10}$$

Calibration matrices are computed with channel # 1 as the reference. The calculations are shown for one channel configured as the current-source and the above procedure is repeated for all channels and desired frequencies at which the EIT system will operate. Details of the entire calibration procedure is illustrated in the flowchart of Fig. 24.

ACKNOWLEDGMENT

This work was supported in part by the U.S. National Science Foundation, under Grant No. 1418497, U.S. Department

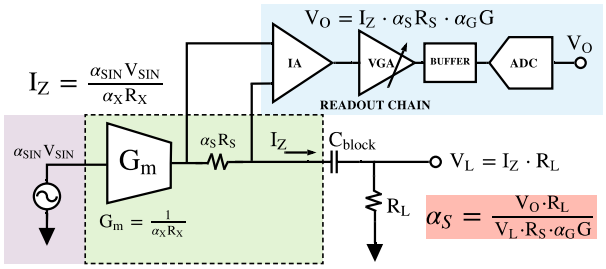

Fig. 23. Calibration circuit for a channel in the EIT system in the current-source mode. Variations due to AD9834 output, on-chip resistors and readout chain gain variation are analyzed. Calibration coefficient for each channel is calculated and normalized against a single channel.

TABLE II
PERFORMANCE COMPARISON OF EIT SYSTEMS

	Target	[20]	[4]	[21]	[22]	This Work
AFE form factor	ASIC	Multiple COTS	Multiple COTS	ASIC	ASIC	ASIC
Frequency (kHz)	1-1000	10-1000	1-1000	45-1000	11	0.5-1000
SNR (dB)	65-90; 55-73	45-82	84-100	48-54	83	66-76
# Channels	16-20	32 (max 48)	16	16	16	16 (max 20)

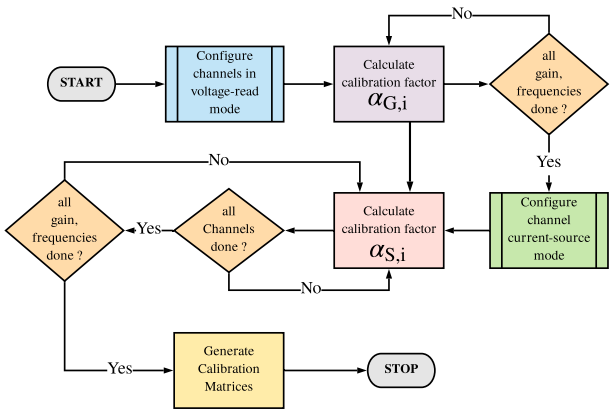

Fig. 24. Calibration procedure flowchart to calculate the calibration coefficients for the EIT system.

of Defense CDMRP Grant Nos. W81XWH-15-1-0572 and W81XWH-15-1-0571.

References

[1] S. Loeb, M. A. Bjurlin, J. Nicholson, T. L. Tammela, D. F. Penson, H. B. Carter, P. Carroll, and R. Etzioni, "Overdiagnosis and overtreatment of prostate cancer," pp. 1046–1055, 2014.

[2] E. K. Murphy, X. Wu, and R. J. Halter, "Fused-data transrectal EIT for prostate cancer imaging," *Physiological Measurement*, vol. 39, no. 5, p. 054005, May 2018.

[3] R. J. Halter, A. Schned, J. Heaney, A. Hartov, and K. D. Paulsen, "Electrical Properties of Prostatic Tissues: I. Single Frequency Admittivity Properties," *Journal of Urology*, vol. 182, no. 4 SUPPL., pp. 1600–1607, Oct 2009.

[4] S. Khan, P. Manwaring, A. Borsic, and R. Halter, "FPGA-based voltage and current dual drive system for high frame rate electrical impedance tomography," *IEEE Transactions on Medical Imaging*, vol. 34, no. 4, pp. 888–901, Apr 2015.

[5] A. Mahara, S. Khan, E. K. Murphy, A. R. Schned, E. S. Hyams, and R. J. Halter, "3D Microendoscopic Electrical Impedance Tomography for Margin Assessment During Robot-Assisted Laparoscopic Prostatectomy," *IEEE Transactions on Medical Imaging*, vol. 34, no. 7, pp. 1590–1601, Jul 2015.

[6] A. Borsic, A. Hartov, K. D. Paulsen, and P. Manwaring, "3D electric impedance tomography reconstruction on multi-core computing platforms," in *2008 30th Annual International Conference of the IEEE Engineering in Medicine and Biology Society*. IEEE, Aug 2008, pp. 1175–1177.

[7] W. R. B. Lionheart, J. Kaipio, and C. N. McLeod, "Generalized optimal current patterns and electrical safety in EIT," in *Physiological Measurement*, vol. 22, no. 1. IOP Publishing, feb 2001, pp. 85–90.

[8] R. D. Cook, G. J. Saulnier, D. G. Gisser, J. C. Goble, J. C. Newell, and D. Isaacson, "ACT3: A High-Speed, High-Precision Electrical Impedance Tomograph," *IEEE Transactions on Biomedical Engineering*, vol. 41, no. 8, pp. 713–722, Aug 1994.

[9] A. Hartov, R. A. Mazzarese, F. R. Reiss, T. E. Kerner, K. S. Osterman, D. B. Williams, and K. D. Paulsen, "A multichannel continuously selectable multifrequency electrical impedance spectroscopy measurement system," *IEEE Transactions on Biomedical Engineering*, vol. 47, no. 1, pp. 49–58, Jan 2000.

[10] R. J. Halter, A. Hartov, and K. D. Paulsen, "A broadband high-frequency electrical impedance tomography system for breast imaging," *Biomedical Engineering, IEEE Transactions on*, vol. 55, no. 2, pp. 650–659, 2008.

[11] A. Rao, Y. C. Teng, C. Schaef, E. K. Murphy, S. Arshad, R. J. Halter, and K. Odame, "An Analog Front End ASIC for Cardiac Electrical Impedance Tomography," *IEEE Transactions on Biomedical Circuits and Systems*, vol. 12, no. 4, pp. 729–738, aug 2018.

[12] A. J. Rao, E. K. Murphy, M. Shahghasemi, and K. M. Odame, "Current conveyor based wide-band current driver for electrical impedance tomography," *Physiological Measurement*, vol. 40, no. 3, p. 034005, apr 2019.

[13] Y.-C. Teng and K. M. Odame, "A 10 MHz 85 dB dynamic range instrumentation amplifier for electrical impedance tomography," *2014 IEEE Biomedical Circuits and Systems Conference (BioCAS) Proceedings*, pp. 632–635, Oct 2014.

[14] E. Sackinger and W. Guggenbuhl, "A high-swing, high-impedance MOS cascode circuit," *IEEE Journal of Solid-State Circuits*, vol. 25, no. 1, pp. 289–298, 1990.

[15] A. Zeki and H. Kuntman, "Accurate and high output impedance current mirror suitable for CMOS current output stages," *Electronics Letters*, vol. 33, no. 12, p. 1042, 1997.

[16] E. K. Murphy, M. Takhti, J. Skinner, R. J. Halter, and K. Odame, "Signal-to-Noise Ratio Analysis of a Phase-Sensitive Voltmeter for Electrical Impedance Tomography," *IEEE Transactions on Biomedical Circuits and Systems*, vol. 11, no. 2, pp. 360–369, Apr 2017.

[17] R. H. Walden, "Analog-to-digital converter survey and analysis," *IEEE Journal on Selected Areas in Communications*, vol. 17, no. 4, pp. 539–550, Apr 1999.

[18] M. Takhti and K. Odame, "Structured Design Methodology to Achieve a High SNR Electrical Impedance Tomography," *IEEE Transactions on Biomedical Circuits and Systems*, vol. 13, no. 2, pp. 364–375, Apr 2019.

[19] E. K. Murphy, A. Mahara, and R. J. Halter, "Absolute Reconstructions Using Rotational Electrical Impedance Tomography for Breast Cancer Imaging," *IEEE Transactions on Medical Imaging*, vol. 36, no. 4, pp. 892–903, 2017.

[20] Y. Yang and J. Jia, "A multi-frequency electrical impedance tomography system for real-time 2D and 3D imaging," *Review of Scientific Instruments*, vol. 88, no. 8, Aug 2017.

[21] Y. Wu, D. Jiang, A. Bardill, R. Bayford, and A. Demosthenous, "A 122 fps, 1 MHz Bandwidth Multi-Frequency Wearable EIT Belt Featuring Novel Active Electrode Architecture for Neonatal Thorax Vital Sign Monitoring," *IEEE Transactions on Biomedical Circuits and Systems*, pp. 1–1, Jul 2019.

[22] M. H. Lee, G. Y. Jang, Y. E. Kim, P. J. Yoo, H. Wi, T. I. Oh, and E. J. Woo, "Portable multi-parameter electrical impedance tomography for sleep apnea and hypoventilation monitoring: Feasibility study," *Physiological Measurement*, vol. 39, no. 12, Dec 2018.